博士論文

マイクロ波放電式中和器の性能向上及びプラズマ計測

Performance Enhancements and Plasma Diagnostics of Microwave Discharge Cathode

森下貴都

Takato Morishita

A dissertation submitted in partial fulfillment of the requirements
for the degree of Doctor of Engineering

Department of Aeronautics and Astronautics
The University of Tokyo, Japan
March 2022

Abstract

The microwave ion thruster μ10 was first demonstrated in space by the Japanese asteroid explorer Hayabusa. In its successor Hayabusa2, the thrust was increased by 25%. To apply ion thrusters to future missions, it is necessary to increase the ion current of the ion sources, which in turn requires the electron current of the microwave discharge cathode to be increased.

In this dissertation, two types of performance enhancements are reported. Firstly, the performance was improved by weakening the magnetic field at the cathode's nozzle using a coil. It was confirmed that when the axial magnetic field of the plume of the microwave discharge cathode is weakened to 14 mT in this way, the anode current increases from 180 mA to 260 mA at a constant anode voltage of 37 V. Secondly, the magnetic field intensity and mirror ratio in the discharge chamber were increased. By increasing the magnet field intensity by 10 mT and the mirror ratio from 2.0 to 8.3, the electron current was increased from 300 mA to 560 mA.

To investigate the plasma inside and outside the microwave discharge cathode, a microwave discharge cathode with a small optical window was developed. It was confirmed that the I–V characteristics of the developed viewable cathode matches that of the flight-model of Hayabusa2 within 7% accuracy. Laser-induced fluorescence (LIF) spectroscopy was performed on the cathode under nominal conditions. The axial and radial ion velocity distribution functions (IVDFs) in the plume region and the axial IVDFs inside the cathode were measured and found to exhibit multimodal characteristics. The measured functions, which represent the number density of Xe II $(^3\mathrm{P}_2)6\mathrm{p}[3]_{5/2}$, were compared to a previously reported relative number density of xenon ions measured by an electrostatic probe on the plume. In order to discuss the multimodal characteristics, anode current oscillation and radiated emission measurements were conducted. Theoretical models based on the measured current oscillation support the multimodal characteristics. Finally, LIF measurements were conducted on the improved cathodes with the performance enhancements applied. In both improved cathodes, it was confirmed that the density was twice that of the nominal model in the plume, suggesting that the dense plasma contributes to the improvements.

Contents

List of Figures

3.4 Schematic diagram of microwave discharge cathode measurement setup for axial LIF spectroscopy. For the radial measurement, the microwave discharge cathode was rotated 90° with respect to the Y axis. 60
3.5 Photograph of microwave discharge cathode measurement setup for axial LIF spectroscopy. 61
3.6 Schematic diagram of measurement point. 61
3.7 Measurement points of LIF spectroscopy. 63
3.8 Diode laser. 64
3.9 Controller for diode laser. 64
3.10 Optical amplifier. 65
3.11 Wavelength meter TQ8325 for 600–1,600 nm. 65
3.12 Lock-in amplifier. 66
3.13 Mechanical chopper. 67
3.14 Photograph of signal detection system. 67
3.15 Schematic diagram of signal detection system. 68
3.16 DC discharge reference cell for xenon. 69
3.17 Fiber coupler. 69
3.18 Example of axial LIF signal varying the laser frequency at X = 0 mm, Z = -11 mm. 70
3.19 Comparison of LIF signals when the angle between the reference cell and laser was changed. 71
3.20 Design of the microwave discharge cathode with an optical window. 73
3.21 Photograph of the microwave discharge cathode with an optical window. . . . 74
3.22 Photograph of the microwave discharge cathode with an optical window in diode mode operation. 75
3.23 Comparison of I–V characteristics between the microwave discharge cathode with an optical window and the Hayabusa2 flight model for various values of microwave power P_m (6, 8, and 10 W) at $\dot{m}_\mathrm{c}$ = 0.7 sccm. 8 W (red) is the nominal microwave power for Hayabusa2. 60,000 hours ground endurance test model is also compared (green). 76
3.24 Duration test of the developed cathode at P_m = 8 W, $\dot{m}_\mathrm{c}$ = 0.7 sccm, I_a =180 mA. 77
3.25 Comparison of LIF signals measured before and after the experiment. 77
3.26 Photograph of optical observation near the antenna. 79
3.27 Static magnetic field analysis inside the discharge chamber by Finite Element Method Magnetics. 80

A.2 Three types of flux on wall. (a) Ion current, (b) Secondary electron emission by ions, (c) Secondary electron emission by Auger de-excitation of metastable molecules. 148
A.3 Comparison of flux between Mo and La-W nozzle models. 149

B.1 Combinations of magnetic fields formed by a microwave discharge cathode and Hall thruster. The left figures are schematics and the right figures are fields measured by a teslameter. 153
B.2 Ignition process of Hall thruster - microwave discharge cathode system. . . . 154
B.3 I_{coil} vs. V_{cg} comparison between type A and B magnetic fields at $V_{\mathrm{ath}} = 150$ V. 155
B.4 Comparison of thrust F, specific impulse I_{sp}, potential difference between the cathode and ground V_{cg}, anode current I_{a}, and thrust efficiency between the microwave discharge cathode and hollow cathode at $I_{\mathrm{coil}} = 2.0$ A 158
B.5 Comparison of ion energy distribution (left) and ion beam profile (right) at $I_{\mathrm{coil}} = 2.0$ A,$V_{\mathrm{ath}} = 250$ V 160
B.6 Comparison of four efficiencies, acceleration efficiency η_a, propellant utilization efficiency η_{u}, beam energy efficiency η_{E}, and beam divergence efficiency η_{div} at $I_{\mathrm{coil}} = 2.0$ A. 161
B.7 Comparison of plasma production region between a hollow cathode and microwave discharge cathode 162

C.1 Experimental setup for measurement of neutralization current density. 167
C.2 Time history of charge neutralization using 0.2 sccm xenon. 168
C.3 Experimental setup for measurement of neutralization current density. 171
C.4 Schematic diagram of microwave discharge plasma sources of neutralization current density. 172
C.5 Photograph of microwave discharge plasma sources of neutralization current density. 173
C.6 Comparison of charge neutralization current density. 174
C.7 Experimental setup for charge neutralization in film transfer simulator. 175
C.8 Photograph of the experimental setup for charge neutralization in film transfer simulator. 176
C.9 Time history of charge neutralization in film transfer simulator. 176
C.10 Developed microwave discharge plasma neutralization system. ©Copyright 2019 Kasuga Denki, Inc. 178

D.1 Schematic diagram of experimental setup for charged dust removal. 183

List of Tables

Nomenclature

$\bar{v}_{\mathrm{X}}$	Radial mean ion velocity
$\bar{v}_{\mathrm{Z}}$	Axial mean ion velocity
$\boldsymbol{\nu}$	Particle velocity vector
$\Delta\nu$	Photon frequency shift
Δv_0	Oscillation amplitude
$\dot{m}_{\mathrm{a}}$	Anode mass flow rate
$\dot{m}_{\mathrm{c}}$	Cathode mass flow rate
η_{a}	Acceleration efficiency
η_{div}	Beam divergence efficiency
η_{E}	Beam energy efficiency
η_{g}	Gas utilization efficiency for cathode
η_{multi}	Multi-charged ion efficiency
η_{P}	Electrical efficiency
η_{T}	Thrust efficiency
η_{u}	Propellant utilization efficiency
ν_{q}	Quenching frequency
ν_0	Photon frequency
ν	Collision frequency
Ω	Collection angle
ω_{c}	Electron cyclotron angular frequency
ω_i	Anode current oscillation frequency at the i-th harmonic
ϕ	Work function
σ	Cross section
$\mathbf{k}$	Photon wave vector
θ	Angle between probe and thruster center axis
θ_{m}	Pitch angle
θ_i	Anode current oscillation phase at the i-th harmonic
ε_0	Electric constant

A	Richardson constant
a	Laser beam radius
A_{21}	Einstein A coefficient
B	Magnetic field intensity
$B_{\max}$	Maximum magnetic field intensity
$B_{\min}$	Minimum magnetic field intensity
B_{12}	Einstein B coefficient
c	Speed of light in a vacuum
C_{i}	Ion production cost
C_{n}	Neutralization cost
C_{s}	Electrostatic capacity of spacecraft
e	Elementary charge
E_{m}	Mean beam energy
F	Thrust force
f	Ion velocity distribution function
f_{e}	Electron cyclotron frequency
g	Standard gravity
G_i	Relative spectrum magnitude at the i-th harmonic of anode oscillation
I_{a}	Anode current
I_{beam}	Beam current
I_{c}	Cathode current
I_{coil}	Inner coil current
I_{ex}	Laser intensity
I_{i}	Ion current
I_{k}	Keeper current
I_{n}	Neutralization current
I_{sp}	Specific impulse
J	Current density measured by probe
J_{f}	Current density by Richardson-Dashman law
J_{si}	Space-charge-limited current density
k	Boltzmann constant
L	Distance between thruster exit and probe
L_{s}	Distance between electrodes
M	Xenon ion mass
m_{e}	Electron mass
N	Particle density in two-level system

n_{i}	Ion density
n_{n}	Neutral density
P	Total power consumption in thruster system
P_{a}	Anode consumption power
P_{c}	Cathode consumption power
P_{coil}	Coil consumption power
P_{d}	Discharge power
P_{m}	Head microwave power
Q	Quenching rate
Q_{s}	Electric charge of spacecraft
R^2	Coefficient of determination
R_{m}	Mirror ratio
r_0	Outer radius of thruster channel
S	Fluorescence intensity
S_{p}	Cross-section in plume region
T	Temperature on surface
t	Time
T_{e}	Electron temperature
T_{i}	Ion temperature
u_{e}	Exhaust velocity
v	Ion velocity
$v_{0\mathrm{c}}$	Oscillation center velocity
V_{a}	Anode voltage
V_{Ac}	Accelerator voltage
V_{ath}	Anode voltage of thruster
V_{b}	Beam acceleration voltage
V_{c}	Cathode voltage
V_{cg}	Potential difference between ground and cathode
V_{d}	Discharge voltage
V_{f}	Floating probe potential
V_{k}	Keeper voltage
V_{p}	Plasma potential
V_{s}	Potential of spacecraft
V_{Sc}	Screen voltage
V_{si}	Potential distance between electrodes
V_{signal}	Collection volume

v_{X}	Radial ion velocity
v_{Z}	Axial ion velocity
v_0	Instantaneous bulk velocity

Chapter 1

Introduction

1.1 Electric propulsion

There are mainly two types of spacecraft propulsion: chemical propulsion and electric propulsion. The nozzle converts propellant at high temperature and high pressure into thrust. As detailed later, the exhaust velocity is an order of magnitude lower than that of electric propulsion, but the thrust density is large due to the large propellant mass. Therefore, it is suitable for launch rockets that require large thrust density and attitude control for quick response. However, it has a lower specific impulse than electric propulsion and is not suitable for deep space exploration that requires a large ΔV.

On the other hand, electric propulsion has a low thrust density due to its small exhaust mass, but has a large specific impulse. This is because the ionized propellant is directly affected by electromagnetic and electrostatic forces used to accelerate the spacecraft. Due to these characteristics, it is not suitable for spacecraft that require a large force in a relatively short time. However, it is suitable for spacecraft that require a large ΔV with low fuel consumption, such as for deep space exploration. In other words, it is possible to increase the payload ratio of a spacecraft and increase the degrees of freedom of a mission using electric propulsion.

Electric propulsion can be classified into three types, electrothermal, electromagnetic, and electrostatic, depending on the acceleration mechanism. The characteristics of each and the thrusters used for each are summarized in Table 1.1.

1.2 Principle of ion thruster

An ion thruster consists of two major components: an ion source and a neutralizer cathode. Ions generated in the ion source are accelerated by two or three grids and form an ion beam.

In the discharge chamber of an ion source, neutral particles are discharged, as described later. The ions are accelerated by fields applied by the grids and generate a thrust force. An ion thruster achieves a relatively higher exhaust velocity (10s to 100s of km/s) than other

Table 1.1: Types and thrusters in electric propulsion

Type	Characteristics	Thrusters
Electrothermal	Aerodynamic acceleration by high-temperature gas generated by electrical heating	DC arcjet Resist jet
Electromagnetic	Electromagnetic acceleration by ionized gas	MPD thruster Hall thruster
Electrostatic	Electrostatic acceleration of ionized gas	Hall thruster Ion thruster

types of electric propulsion, and a high specific impulse of 3,000–10,000 s. However, the ion beam current density is limited by the Child–Langmuir law, and the thrust density is relatively low compared with other types of electric propulsion. Figure 1.1 shows a schematic diagram of an ion thruster.

As shown in the figure, an ion thruster consists of three major components:

1. Ion production
2. Electrostatic acceleration
3. Neutralization

Each component will be described in detail in the next section.

1.2.1 Ion production

In the ion production part, the propellant is discharged and ions are generated. In general, the ions are generated through the following steps.

1. Generation of energetic electrons with enough energy to discharge the propellant
2. Energetic electrons confined by a magnetic field
3. Collisions between energetic electrons and neutrals, generating ions
4. Transport of the ions to the electrostatic acceleration part

It is necessary to reduce the power consumption for ion production as much as possible because the power does not directly contribute to the thrust force. Therefore, ions should be generated with high efficiency, and ion loss should be suppressed.

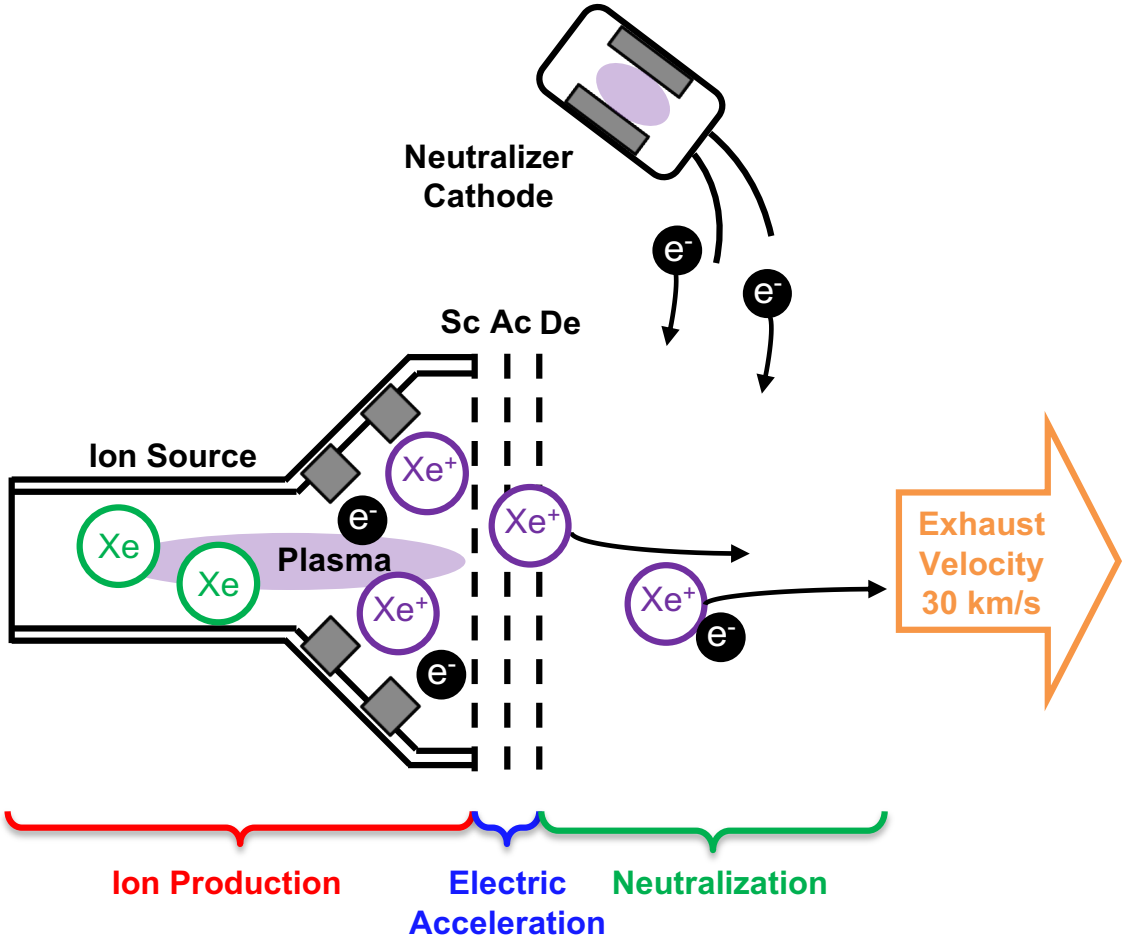

Figure 1.1: Schematic diagram of ion thruster.

1.2.2 Electrostatic acceleration

The grids are porous electrodes. They are installed to electrostatically accelerate and expel ions to generate a thrust force. Figure 1.2 shows a schematic diagram of ion acceleration. Two or three grids with a large number of holes with diameters of several millimeters are installed at intervals of several millimeters. The grid on the ion production part is called a screen grid, and a positive voltage of about 1 kV is generally applied. An accelerator grid is installed downstream of the screen grid. A negative potential of -300 to -500 V is generally applied to the accelerator grid, and ions are accelerated by the potential difference relative to the screen grid. The accelerator grid also plays a role in preventing back-flow of electrons from the neutralizer cathode. Downstream of the screen grid, low-energy ions generated by charge exchange collisions between high-energy ions and low-energy neutrals cause erosion of the accelerator grid. Therefore, a "grounded" discell grid is often installed downstream of the accelerator grid. As the grid material, molybdenum, titanium, or a cabon-carbon composite

material, which has a low coefficient of thermal expansion and a low sputtering rate, is used.

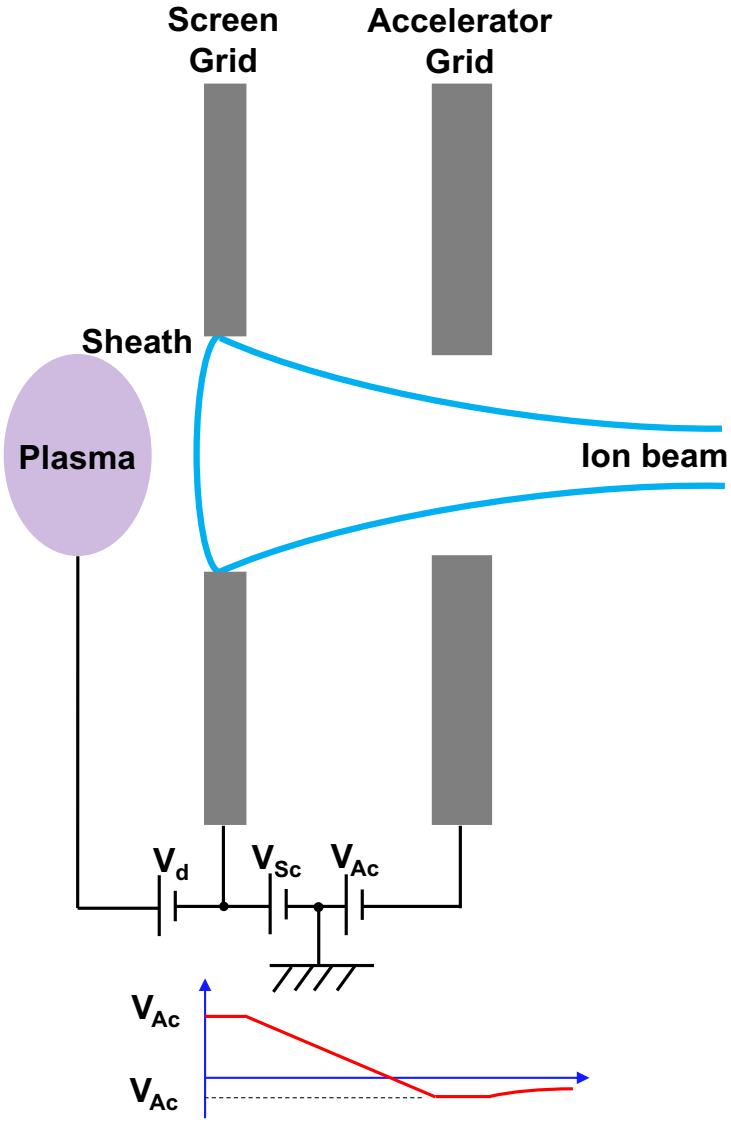

Figure 1.2: Schematic diagram of ion acceleration.

1.2.3 Neutralization

If only positive ions are extracted from the ion source, the spacecraft will be negatively charged to −10s of kV in a few milliseconds and ion acceleration will be immediately interrupted. The neutralizer cathode emits electrons at the same rate as that at which the ions are accelerated, to avoid an electrostatic charge imbalance between the spacecraft and the space plasma. Reduction of gas and power consumption is important because the cathode does not contribute to the thrust force. The neutralizer cathode is placed near the ion beam, but not directly in the beam path in order to avoid sputtering by the energetic ion beam. The electrons are extracted to the ion beam by the potential difference between the cathode and ion beam. Hollow cathodes are commonly used as neutralizer cathodes, as described in detail later.

1.3 Types of ion thrusters

Ion thrusters can also be classified into several types according to the plasma generation method. In this section, specifications are compared between DC, RF, and microwave discharge thrusters, the latter being the type considered in this study. The specifications are summarized in Table 1.2.[1][2][3][4]

1.3.1 DC ion thruster

Figure 1.3 shows a schematic diagram of a DC ion thruster. For DC discharge, a hollow cathode is installed in the discharge chamber, and the electrons emitted from the cathode are accelerated by the potential difference from the plasma potential, and the propellant is ionized by collisions with energetic electron. A magnetic field is applied to increase the collision frequency between electrons and neutrals, to reduce the cost of ion generation. The ions are efficiently transported because the magnetic field forms a diffuse shape in the electrostatic acceleration region. In addition, the ion density is uniformly distributed because the magnetic field is relatively weak in the region surrounded by the ion production region and the electrostatic acceleration region. However, because a hollow cathode is generally used as the cathode, DC ion thrusters can be prone to oxidization and low durability of the heater, as will be described in detail later.

Table 1.2: Comparison of ion thruster specifications

Thruster	μ 10 (this study)	T5	XIPS-13	ETS-III Kaufmann	RIT-10
Plasma generation	Microwave discharge	DC	DC	DC	RF
Beam diameter, cm	10	10	13	12	10
Thrust, mN	10	18	17.2	20.9	15
Specific impulse, s	3200	3400	2507	2402	3300

1.3.2 RF ion thruster

Figure 1.4 shows a schematic diagram of an RF ion thruster. RF thrusters also need a hollow cathode to ignite the plasma in the discharge chamber. Electrons entering the ion source are accelerated by radio-waves, which also keep the RF plasma in the discharge chamber. The discharge chamber is made of alumina, a dielectric material. The antenna system is enclosed in a metal plasma shield to avoid electron collection from space plasma.

1.3.3 Microwave discharge ion thruster

Our laboratory previously developed a microwave discharge ion thruster μ10, which was the main propulsion system for the asteroid sample return mission Hayabusa and its successor Hayabusa2.[5][6][7][8] The second-generation model of the thruster, which increased the thrust force from 8 to 10 mN, was used in the Hayabusa2 probe, which launched in December 2014 and returned to Earth in December 2020 (an extended mission is planned). The latest model of the thruster, which has a 12-mN thrust force, is planned to be used in the comet fly-by mission DESTINY$^+$.[9]

Figure 1.5 shows a schematic diagram of a microwave discharge ion thruster. The microwave discharge ion thruster requires a DC block that insulates the microwave system and provides a high potential to the thruster system. Xenon gas is injected into the discharge chamber and 4.25-GHz microwaves are transmitted from the antenna into the discharge chamber. A magnetic circuit generates an azimuthal mirror magnetic field. Electron cyclotron resonance (ECR) heating occurs where the magnetic field intensity is 0.15 T. During ECR heating, high-energy electrons exhibit three types of motion: Larmor motion around the magnetic field lines, reciprocating motion between the magnetic mirrors, and azimuthal motion due to the curvature and grad-B drift.

No electrodes are used to generate plasma in the microwave discharge ion thruster and, therefore, a long life is expected in principle. In the case of the microwave discharge ion thruster μ10, the ion source and neutralizer cathode use the same plasma generation method.

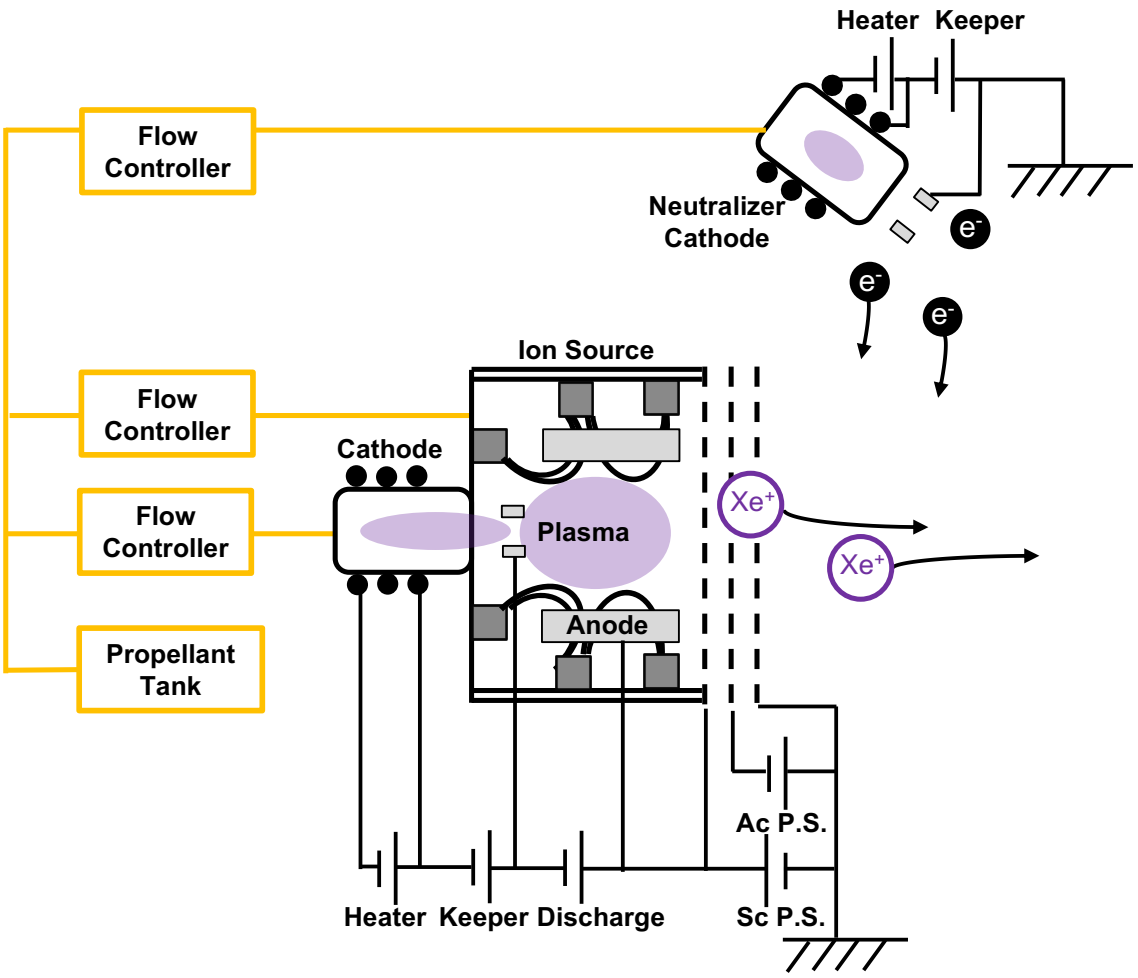

Figure 1.3: Schematic diagram of DC ion thruster.

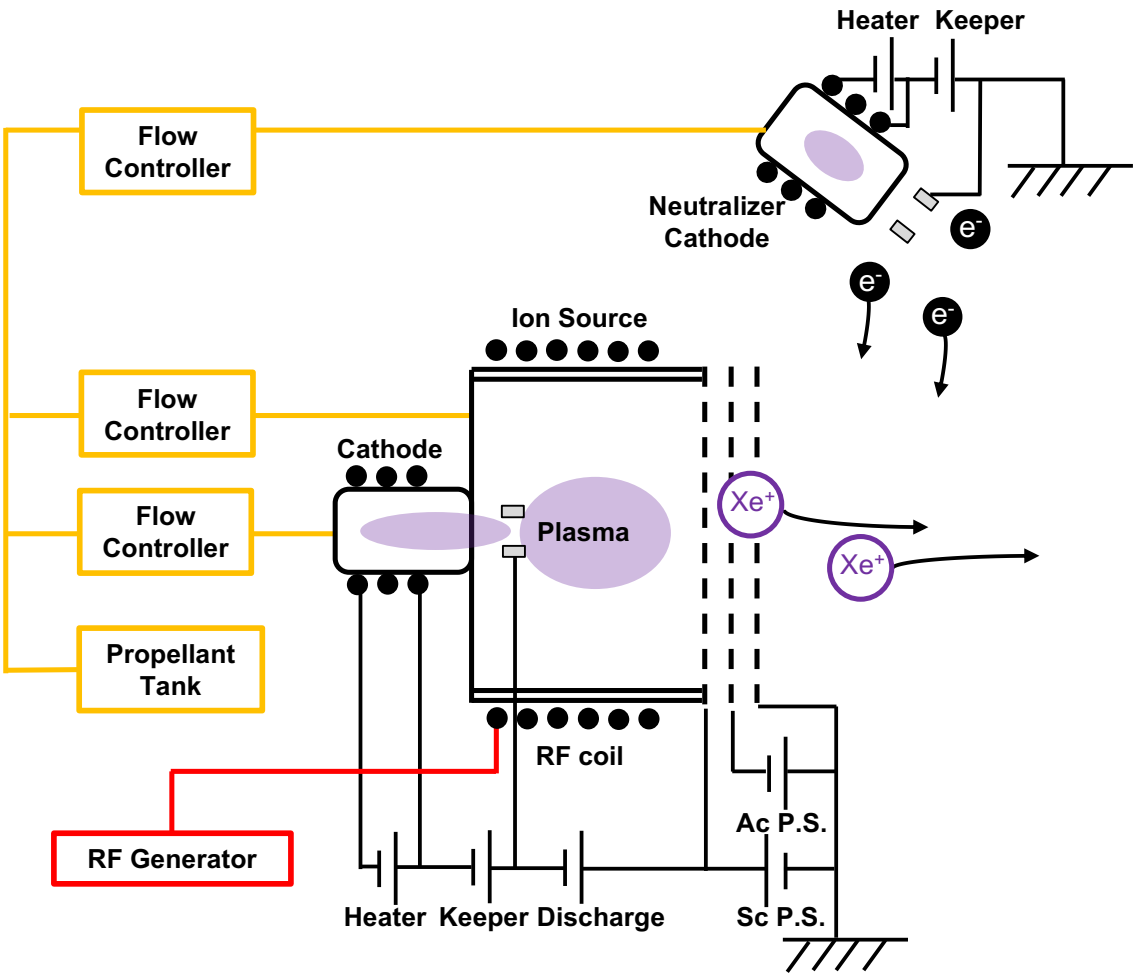

Figure 1.4: Schematic diagram of RF ion thruster.

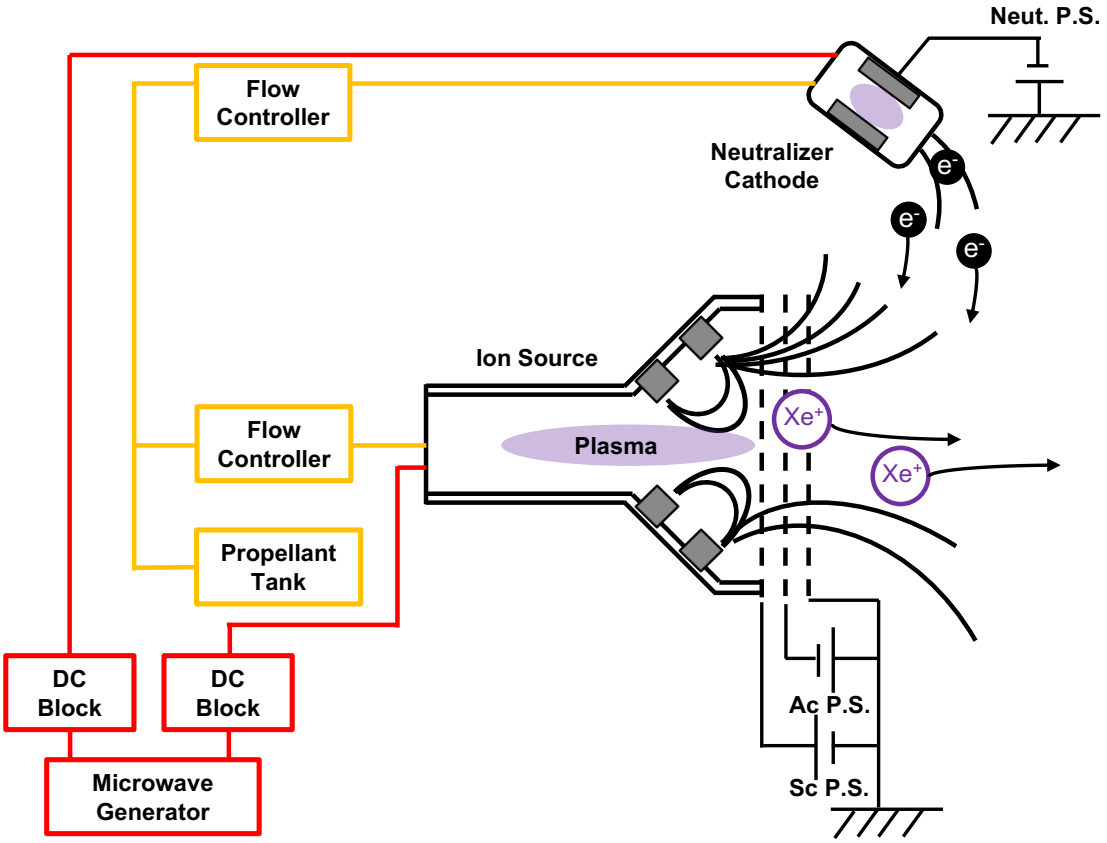

Figure 1.5: Schematic diagram of microwave discharge ion thruster μ10.

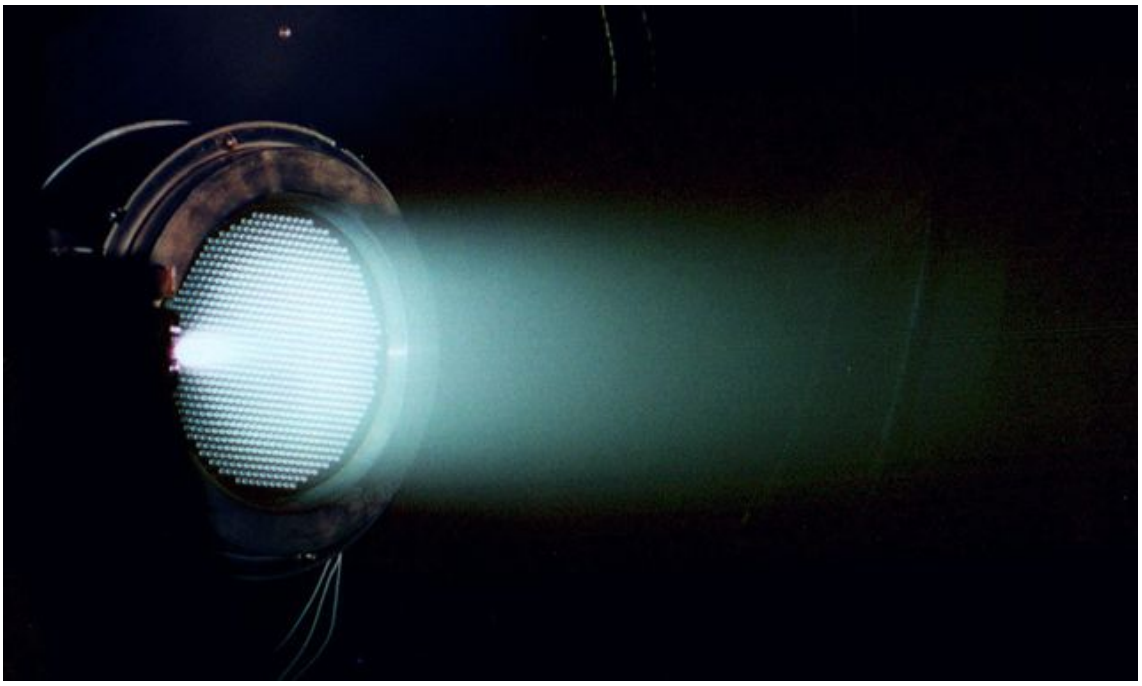

Figure 1.6: Photograph of microwave discharge ion thruster μ10. ©Copyright 2002 JAXA

1.4 Ion thruster performance

Thrust, specific impulse, ion production cost, propellant utilization efficiency, electrical efficiency, and thrust efficiency are used to evaluate the characteristics of an ion thruster. The definition of each parameter is described below.

1.4.1 Thrust

Eq. 1.1 is the thrust calculation formula.

$$F = \eta_{\mathrm{div}}\eta_{\mathrm{multi}} I_{\mathrm{beam}} \sqrt{\frac{2MV_{\mathrm{b}}}{e}} \tag{1.1}$$

As shown in Eq. 1.1, the thrust F is proportional to the beam current I_{beam}. However, as shown by Eq. 1.2, the beam current of the ion thruster is limited by the Child–Langmuir law.

$$J_{\mathrm{si}} = \frac{4}{9}\varepsilon_0 \sqrt{2e} M \frac{V_{\mathrm{s}}^{3/2}}{L_{\mathrm{s}}^2} \tag{1.2}$$

For example, when the potential difference V_{s} is 1.5 kV and the distance between the electrodes L_{s} is 1 mm, the current density is 28 mA/cm^2. Because the thrust of the ion thruster is small, it is difficult to directly measure it with sufficient accuracy. Therefore, the thrust is calculated from the ion beam current. It has been confirmed that this calculated thrust is equivalent to the actual thrust obtained through operation of Hayabusa and Hayabusa2.

1.4.2 Specific impulse

Specific impulse I_{sp} is defined in Eq. 1.3.

$$I_{\mathrm{sp}} = \frac{F}{\dot{m}g} = \eta_{\mathrm{div}}\eta_{\mathrm{multi}}\eta_{\mathrm{u}} \frac{u_e}{g} = \frac{\eta_{\mathrm{div}}\eta_{\mathrm{multi}}\eta_{\mathrm{u}}}{g} \sqrt{\frac{2eV_{\mathrm{b}}}{M}} \tag{1.3}$$

The product of I_{sp} and the standard gravity g can be considered to be the average exhaust velocity. Xenon is generally used as the propellant because it has a high molecular weight and is easy to handle.

1.4.3 Propellant utilization efficiency

Eq. 1.4 is the definition of the propellant utilization efficiency η_{u}.

$$\eta_{\mathrm{u}} = \frac{MI_{\mathrm{beam}}}{e\dot{m}_a} \tag{1.4}$$

However, note that Eq. 1.4 assumes that all the ions are singly charged. When η_{u} is low, I_{sp} decreases. In addition, the number of charge exchange collisions increases, so the amount of erosion on the accelerator grid increases. This is an important parameter that greatly affects the propellant flow rate in the actual operation of a spacecraft.

1.4.4 Ion production cost

Eq. 1.5 is the definition of the ion production cost C_{i}, which is the power consumption for the production of an ion.

$$C_{\mathrm{i}} = \frac{P_{\mathrm{d}}}{I_{\mathrm{beam}}} \tag{1.5}$$

For a DC discharge ion thruster, C_{i} is the ratio of the discharge voltage at the ion source to the total power consumption, and is also called the discharge loss. For a microwave discharge ion thruster, C_{i} is the microwave power divided by the beam current. C_{i} should be reduced as much as possible while considering the balance with η_{u}.

1.4.5 Electrical efficiency

Eq. 1.6 is the definition of the electrical efficiency η_{P}, which is the ratio of the power consumption for thrust to the total power consumption of the ion thruster.

$$\eta_{\mathrm{P}} = \frac{I_{\mathrm{beam}} V_{\mathrm{b}}}{I_{\mathrm{beam}} V_{\mathrm{b}} + P_{\mathrm{d}} + P_{\mathrm{c}}} \tag{1.6}$$

For a DC discharge ion thruster, η_{P} is generally about 80%. For example, in the case of XIPS-25, it is 88 %. For a microwave discharge ion thruster, η_{P} is about 70% because it is limited by the microwave amplifier loss and transmission loss.

1.4.6 Thrust efficiency

Eq. 1.7 is the definition of the thrust efficiency η_{T}, which is the ratio that pertains to kinetic energy generation.

$$\eta_{\mathrm{T}} = \frac{\frac{1}{2}\dot{m}u_{\mathrm{e}}^2}{P} = \frac{\frac{1}{2}FgI_{\mathrm{sp}}}{P} = \eta_{\mathrm{div}}^2 \eta_{\mathrm{multi}}^2 \eta_{\mathrm{u}} \eta_{\mathrm{P}} \tag{1.7}$$

As shown in Eq. 1.7, η_{T} increases for high I_{sp} and gradually approaches η_{u}, but decreases as I_{sp} decreases.

1.5 Neutralizer cathode

This section outlines the neutralizer cathode used in electric propulsion. As described above, the neutralizer cathode is important for electrical neutralization of the ion beam.

If the ion beam is not neutralized, the spacecraft will be negatively charged, as shown by Eq. 1.8.

$$\frac{dV_{\mathrm{s}}}{dt} = \frac{1}{C_{\mathrm{s}}} \frac{dQ_{\mathrm{s}}}{dt} \ \frac{I_{\mathrm{beam}}}{C_{\mathrm{s}}} \tag{1.8}$$

Here, V_{s} is the potential of the spacecraft, C_{s} is the electrostatic capacity of the spacecraft, and the Q_{s} is the electric charge on the spacecraft. For example, when $C_{\mathrm{s}} = 10$ pF and

$I_{\text{beam}} = 100$ mA, the spacecraft will generate a potential of -10 kV in 1 ms. Therefore, when operating the ion thruster, an electron source called a neutralizer cathode is used to electrically neutralize the ion beam.

As shown in Figure 1.7, there are four methods of supplying electrons for neutralization.

(a) Filament cathode outside the ion beam
(b) Filament cathode inside the ion beam
(c) Electron gun ejecting electrons into the ion beam
(d) Plasma bridge

In method (a), to supply enough electrons to a low-density ion beam, an applied potential of -50 V to -100 V should be applied to the filament. The short lifetime of the filament is a serious problem with this method.

In method (b), if the filament is inserted at a position where the ion density is high, sufficient electron current is emitted even with a relatively small bias voltage. However, the durability of the filament due to ion beam sputtering when inserted into the plume is a serious problem. Early ion thrusters such as SERT1 used this method, but the filament deteriorated due to repeated thermal cycles, and the lifetime of the filament limited the operating time of the thruster system.

Method (c) exhibits problems with the complicated structure of the propulsion system and high power consumption.

In recent years, method (d) has been generally used. Plasma is generated in the cathode, and electrons are selectively extracted by an applied field. Hollow cathodes and microwave discharge cathodes, which will be described later, are classified as method (d).

1.5.1 Filament cathode

The filament cathode is an electron source that utilizes thermionic emission. Free electrons are emitted when the thermal energy exceeds the work function of the material. Eq. 1.7 is the Richardson–Dushman law.

$$J_f = AT^2 \exp(-\frac{\phi}{kT}) \tag{1.9}$$

Here, T is the surface temperature, ϕ is the work function of the filament material, A is the Richardson coefficient, and k is the Boltzmann coefficient.

The filament cathode is a simple system and is often used in ground tests and preliminary experiments, though sputtering and degradation by heating are serious problems.

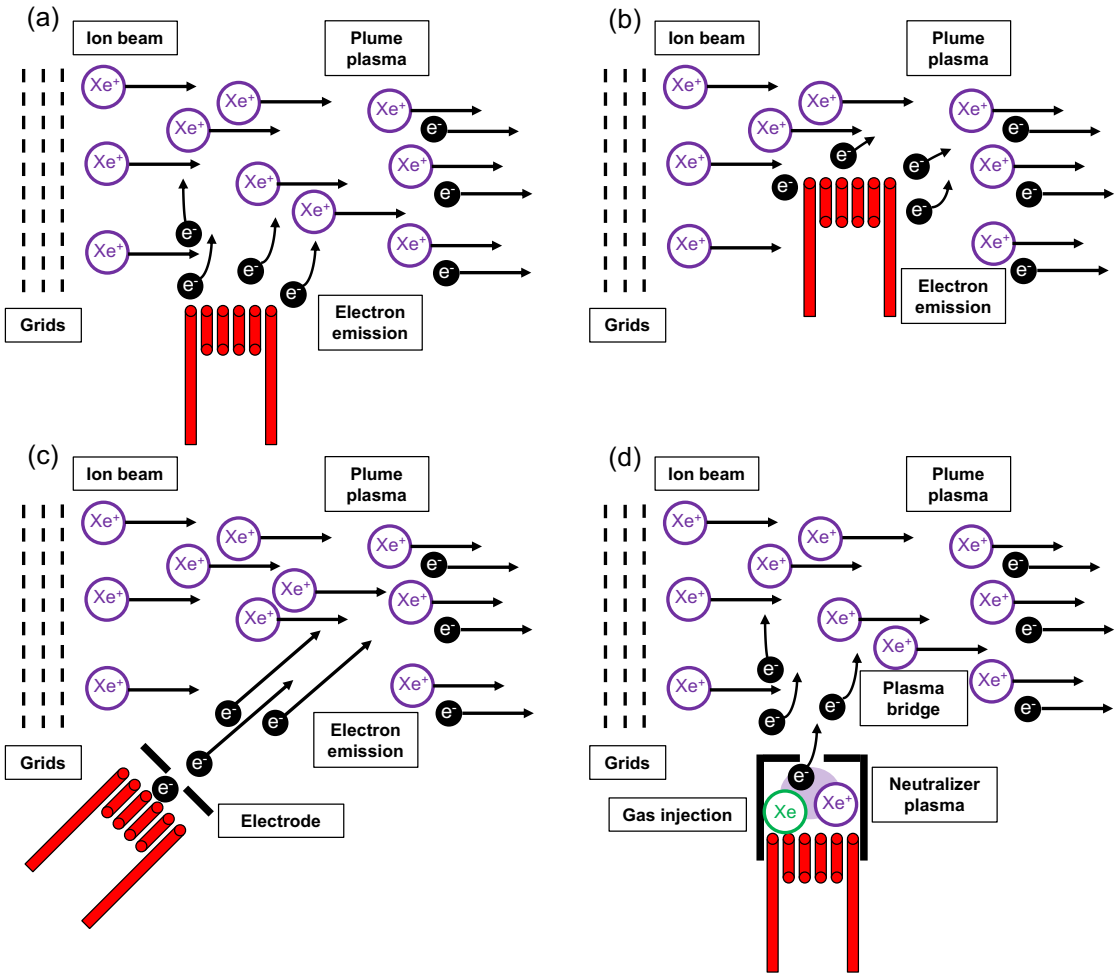

Figure 1.7: Neutralization methods. (a) Filament cathode outside the ion beam. (b) Filament cathode inside the ion beam. (c) Electron gun ejecting electrons into the ion beam. (d) Plasma bridge.

1.5.2 Hollow cathode

Hollow cathodes are often used as cathodes for electric propulsion satellites.[10] Figure 1.8 shows the schematic diagram of hollow cathode. Hollow cathode generates thermionic electrons by heating a low work function material called an insert. Hollow cathode generate plasma by the arc discharge between the keeper electrode and cathode. The insert material is generally BaO or LaB_6.

However, a hollow cathode has some disadvantages comparing with the microwave discharge cathode which is explained in the next section. Table 1.3 shows the comparison of characteristics of a microwave discharge cathode and hollow cathode. A hollow cathode needs to be heated to about 1,000°C by a heater and a high voltage must be applied to a keeper

at the start of ignition operation,[11] which makes it relatively difficult to handle. Also, there is a cathode failure mode due to repeated cycling of the heater.[12] Furthermore, due to the characteristics of the electron emitting material, hollow cathodes cannot be exposed to atmospheric conditions for as long as a few thousand hours. For ion thrusters of 500 W or less, the discharge current of the hollow cathode is 1 A or less, and the heat flux is not sufficient to maintain a self-heating mode. Therefore, the efficiency is poor because it needs power for the keeper and heater to maintain discharge.[13][14][15]

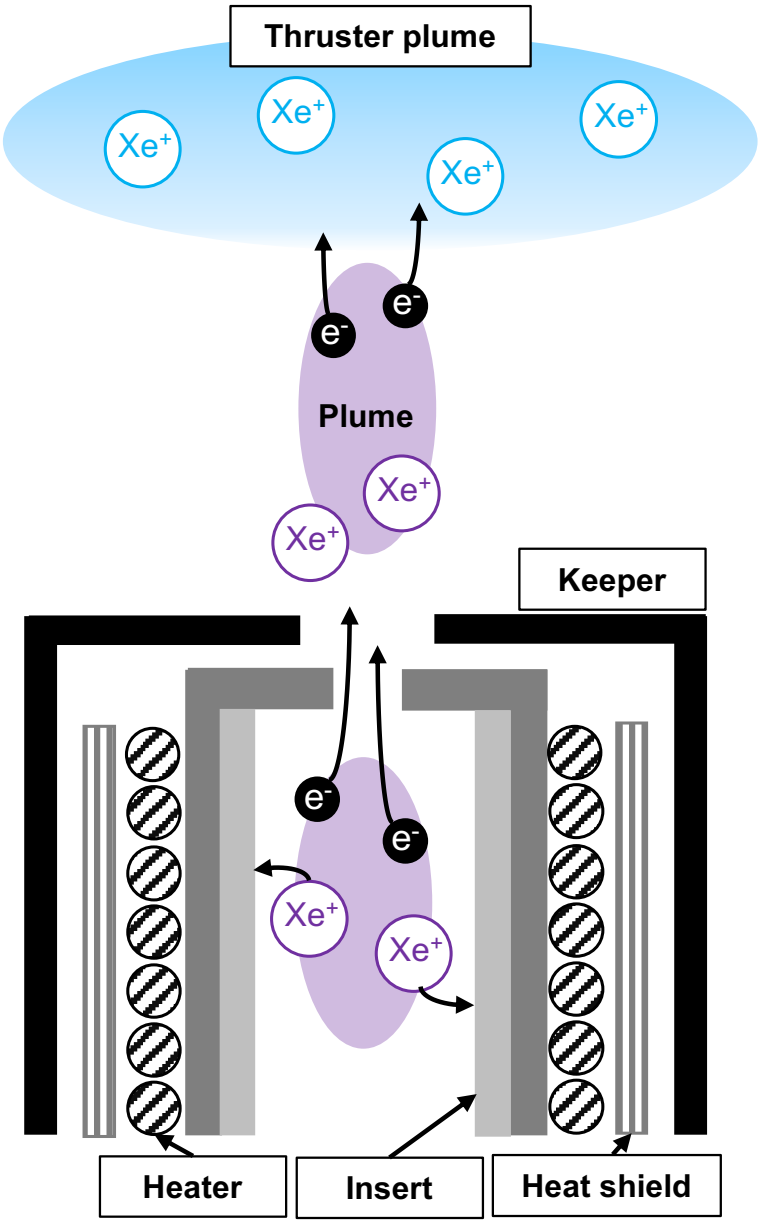

Figure 1.8: Schematic diagram of hollow cathode.

1.5.3 Microwave discharge cathode

Figure 1.9 shows the schematic diagram of microwave discharge cathode. The cathode consists of permanent magnets, magnetic circuits, a discharge chamber, an antenna, and a nozzle. As shown in the figure, electrons are generated via two methods. In the first electron generation method, collisions between neutral particles and high-energy electrons heated by ECR at electron cyclotron frequency, as shown in Eq. 1.10, are used.[16]

$$f_{\mathrm{e}} = \frac{\omega_e}{2\pi} = \frac{eB}{2\pi m_e} \tag{1.10}$$

Microwaves at a frequency of 4.25 GHz are transmitted from the antenna into the discharge chamber. A magnetic circuit generates an azimuthal mirror magnetic field, within which a region with a field strength of 0.15 T gives rise to ECR heating. Xenon is injected into the discharge chamber, where electrons are continuously accelerated by microwave electrical oscillations and trapped by a mirror magnetic field due to ECR. Through electron-neutral collisions, ECR plasma is generated. During ECR heating, high-energy electrons exhibit three types of motion, namely Larmor motion around the magnetic field lines, reciprocating motion between the magnetic mirrors, and azimuthal motion due to the curvature and grad-B drift.

In the second electron generation method, called DC discharge, the potential difference drives the electrostatic acceleration of electrons from the cathode plasma to the ion beam. The acceleration is sufficient to drive the electron impact ionization of neutrals and produces electrons for ion beam neutralization.

The microwave discharge cathode generates plasma from which electrons are emitted into the ion beam by the negative applied voltage at the cathode. Ions, generated at the same rate as the ejected electrons, bombard the interior of the cathode, completing the electrical circuit.

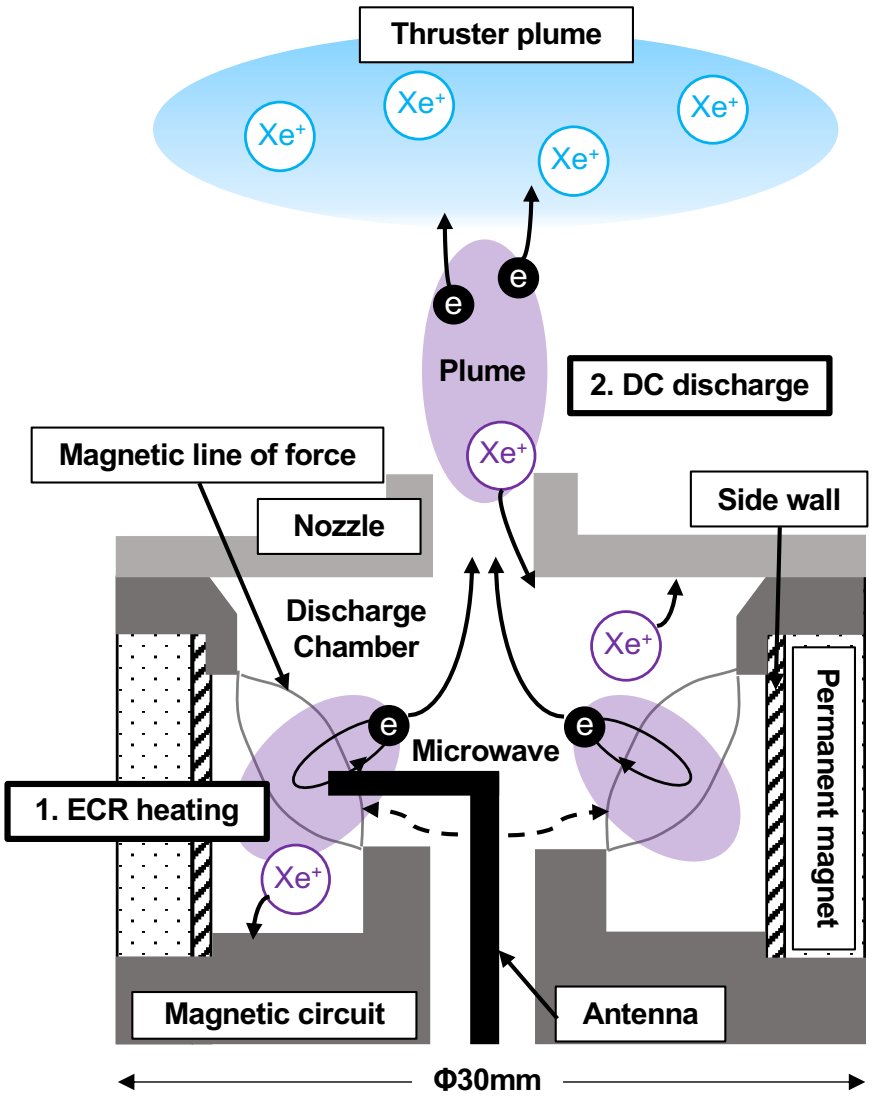

Figure 1.9: Schematic diagram of the microwave discharge cathode.

Table 1.3: Comparison of characteristics of a microwave discharge cathode and hollow cathode.

	Microwave discharge cathode	Hollow cathode
Advantages	·Quick ignition ·Easy handling ·Heaterless	·Wide current range ·Efficient in self-heating mode (>a few amperes)
Disadvantages	·Small current (<1 A) ·Microwave power for plasma generation is required(<20 W) ·Microwave oscillator and amplifier are required	·Difficulty in self-heating mode at ≤1 A ·Preheating is required ·For heaterless cathode, high voltage is required at ignition ·Prone to oxidization (BaO) ·Low durability of heater
Magnetic field	Yes	No

1.5.4 Performance evaluation

The performance of a neutralizer cathode is evaluated based on two parameters: the neutralization cost C_{n} and the propellant utilization efficiency η_{u}. The neutralization cost is the power required to emit a neutralization current of 1 A. For a hollow cathode, Eq. 1.11 gives C_{n}. Here, a hollow cathode is assumed to operate in the current range of self-heating mode.

$$C_{\mathrm{n}} = \frac{I_{\mathrm{k}} V_k + I_{\mathrm{n}} V_{\mathrm{c}}}{I_{\mathrm{n}}} \tag{1.11}$$

For a microwave discharge cathode, microwave power is considered instead of keeper power, and the neutralization cost is Eq. 1.12.

$$C_{\mathrm{n}} = \frac{P_{\mathrm{m}} + I_{\mathrm{n}} V_{\mathrm{c}}}{I_{\mathrm{n}}} \tag{1.12}$$

η_{u} is given by Eq. 1.13 for both a hollow cathode and a microwave discharge cathode.

$$\eta_{\mathrm{g}} = \frac{I_{\mathrm{n}}}{\dot{m}_{\mathrm{c}}} \tag{1.13}$$

Figure 1.10 shows a comparison between a microwave discharge cathode and a hollow cathode using these evaluations.[17][18] A high-performance cathode has a high η_{u} and a low C_{n}. In other words, the higher the performance, the lower the right side of the plot. As shown in the figure, a microwave discharge cathode is better than a hollow cathode. This is because the neutralization current is small. Therefore, enhancing the neutralization current is a major research objective for microwave discharge cathodes.

In DubaiSat2, the μ20-class microwave discharge cathode achieved a neutralization current of 500 mA.[19][20][21] This high neutralization current was achieved by increasing the microwave power. However, as shown in Figure 1.10, this is not an efficient method to improve performance. Figure 1.11 shows the relationship between the microwave power and the potential difference between ground and cathode $|V_{\mathrm{cg}}|$. Figure 1.12 shows the relationship between the microwave power and C_{n}. These figures show that it is difficult to improve C_{n} by increasing the microwave power. In addition, since the cathode must be operated at 47 V or less, which is the threshold voltage for sputtering, the cathode operates in the region on the right side of the dotted line in Figure 1.12. This leads to an increase in C_{n}, which is not recommended considering the low microwave power supply efficiency of 55% and heat problems in antennas and coaxial cables. Therefore, considering other approaches is important.

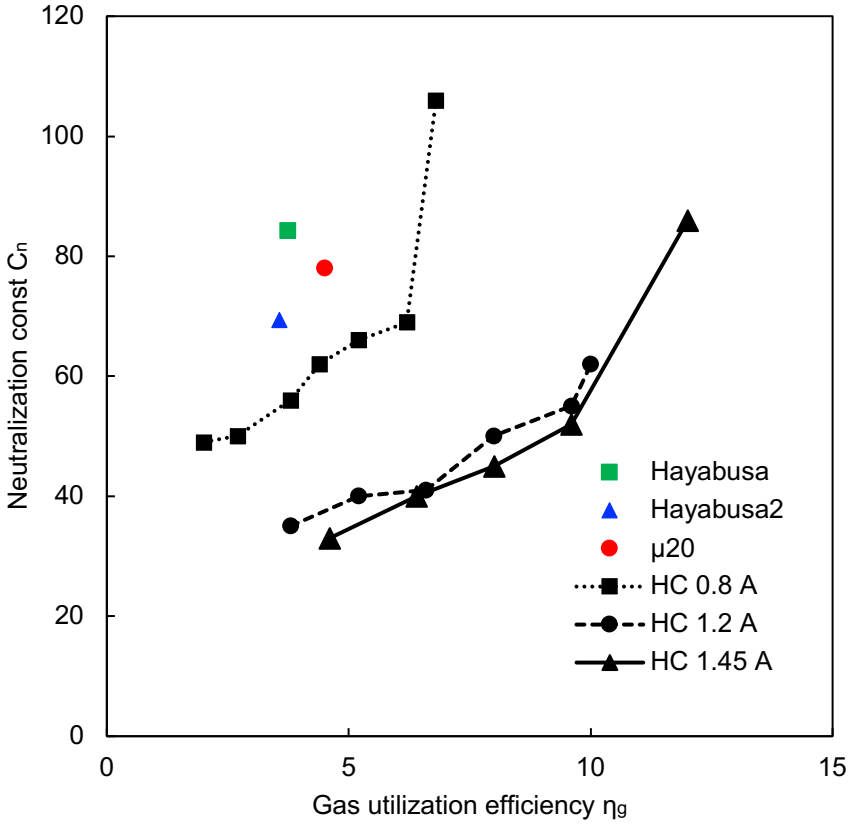

Figure 1.10: Neutralization cost C_{n} and propellant utilization efficiency η_{g} comparison between microwave discharge cathode and hollow cathode.

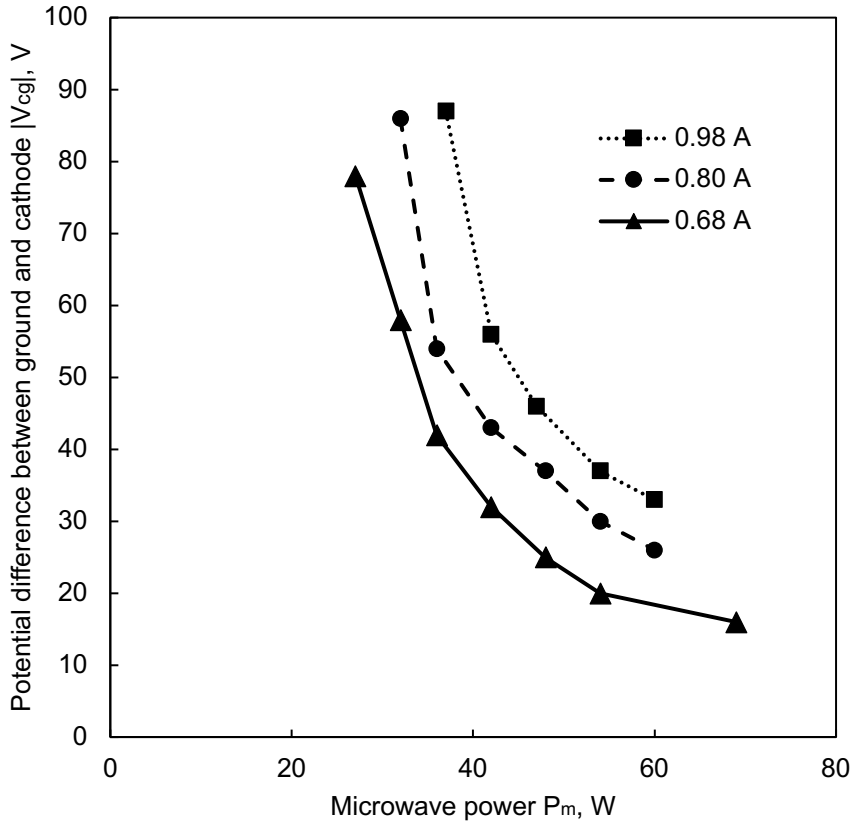

Figure 1.11: Relationship between microwave power P_{m} and potential difference between ground and cathode $|V_{\mathrm{cg}}|$ in DubaiSat2 cathode.

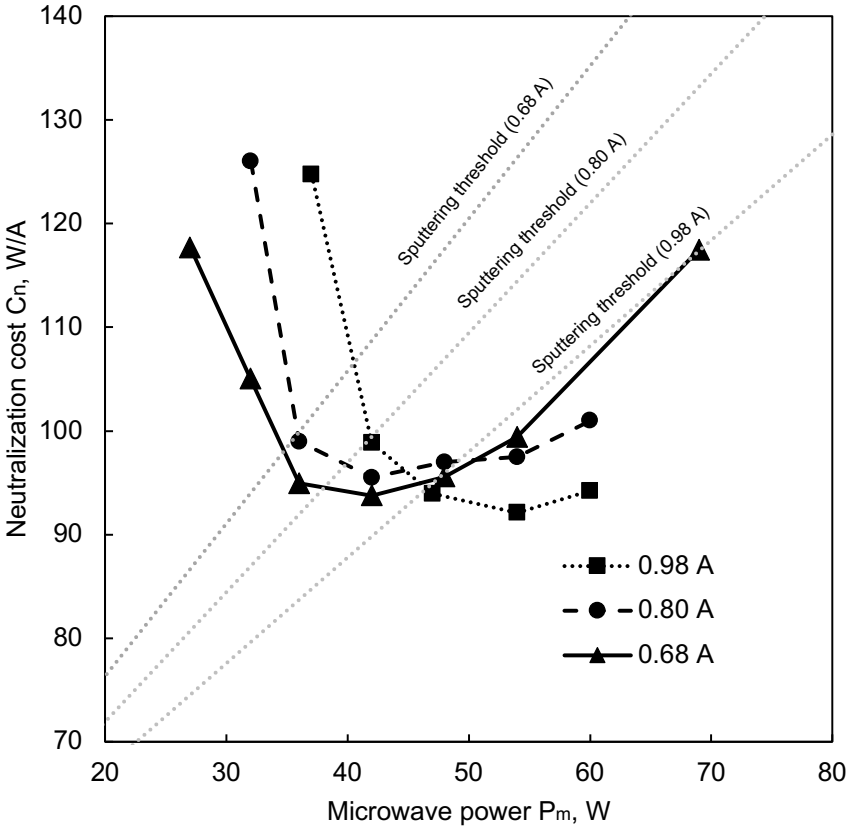

Figure 1.12: Relationship between microwave power P_{m} and neutralization cost C_{n} for DubaiSat2 cathode.

1.6 Background

1.6.1 Previous studies on microwave discharge cathode

This section provides a quick history of previous studies on microwave discharge cathodes and their improvement. In 1997, Suzuki developed an improved prototype microwave discharge cathode (40–50 mA class).[22] In 1998, Funaki and Satori measured the inside of a prototype model using an electrostatic probe [23][24] and significantly redesigned the discharge chamber and magnetic field configuration to improve the electron current. This redesign was the basis for the magnetic field and discharge chamber of the current model (100 mA class). In 1999, Onodera investigated a prototype using an electrostatic probe and laser absorption spectroscopy. However, to investigate the interior plasma, the discharge chamber was significantly modified.[25] In 2001, Funaki conducted a parametric study of the microwave power and flow rate.[26] In 2004, Koizumi applied a microwave discharge cathode for DubaiSat2, as described above (500 mA class).[18] In 2011, Ohmichi investigated the degradation mechanism.[27] In 2014, Tani investigated the flow rate dependence of doubly ionized xenon.[28] Tani also developed the hybrid model cathode with thermionic emission.[17] The causes of the degradation in the Hayabusa mission were analyzed by Ohmichi, but the hypotheses have not been fully validated in space.[29] Ohmichi also investigated the internal plasma using parts inside the cathode as probes.[29] In 2017, Morita tried to measure contamination and sputtering using a quartz crystal microbalance, but accurate measurements were difficult due to heat problems.[30]

As described above, the microwave discharge cathode interior has been investigated several times. However, the probes have had problems with reliability due to electromagnetic disturbances in the microwave electric field. In addition, for small plasma sources such as microwave discharge cathodes, probe measurements have low spatial resolution. Therefore, it is necessary to measure the internal plasma with low disturbance and high reliability.

1.6.2 Previous studies on viewable plasma sources

In previous research, some plasma sources have been visualized to investigate the plasma inside the discharge chamber. However, it is difficult to view a discharge chamber under plasma generation conditions. In 1994, a prototype μ10 ion source was visualized. [31] In 2000, it was reported that the ion production cost decreases by 20% for a viewable DC ion source. [32] In 2014, the accelerator current for a viewable microwave discharge ion source was increased by 15% compared to the original.[33] In 2015, a DC ion source was visualized, providing a different plasma density distribution and electron temperature than those for the original model, as well as a different ion beam current, which was investigated as part of the study. [34]

1.6.3 Cathodes for 200–300 W class Hall thruster

OneWeb constellation has 384 satellites with low-power xenon-fed Hall thrusters on December 2021.[35] As of January 2022, Starlink constellation already has 1,469 active satellites equipped with krypton-fed Hall thrusters.[36] In recent years, as small satellites have attracted increasing interest by government agencies, industries, and universities, the demand low-power thrusters has increased.[37] For this purpose, a Hall thruster system operating at 200–300 W is a promising candidate.[38][39] Figure 1.13 shows the current range for a microwave discharge cathode, a BaO cathode, and a LaB_6 hollow cathode. As described above, a microwave cathode emits a smaller electron current than a hollow cathode. While a hollow cathode emits a relatively large flux of electrons due to the Richardson–Dushman law, a microwave cathode emits electrons as a counterpart to ion collection on the inner wall of the discharge chamber. Ion collection is rate-limiting for the electron emission capability of a microwave cathode. The performance of a microwave discharge cathode and hollow cathode is similar for currents of about 500–1,000 mA, which is in the range of a 200–300-W class Hall thruster, and it is not yet clear which type of cathode is superior in this operating range, as shown in Figure 1.13.[40] [41]

For a high electron emission current, a microwave discharge cathode is easier to handle than a hollow cathode, and hence the microwave discharge cathode is a candidate for the neutralizer cathode of a Hall thruster system. Therefore, an increased current is required in the 500–1,000 mA region for microwave discharge cathodes.

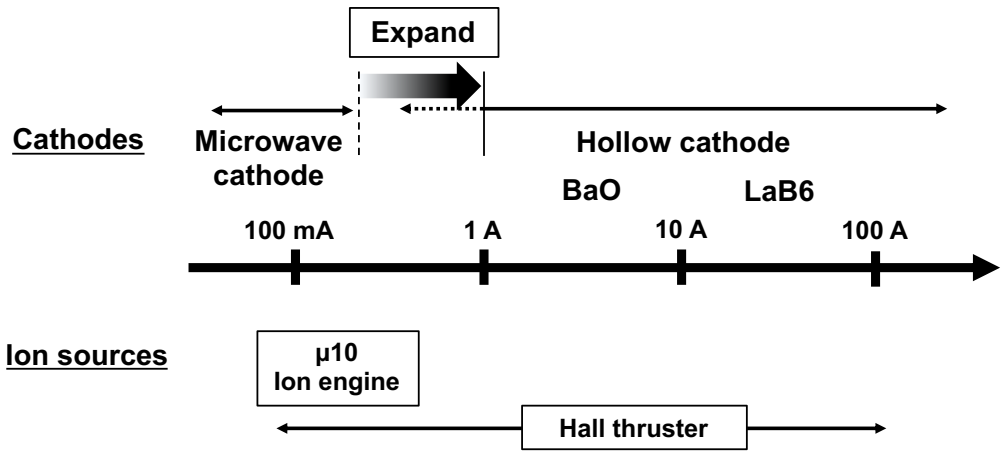

Figure 1.13: Current range for microwave discharge cathode, BaO, cathode and LaB_6 hollow cathode.

1.6.4 Space applications

As described above, our laboratory previously developed a microwave discharge cathode as the neutralizer cathode for a microwave discharge ion thruster μ10, which was the main propulsion system for the asteroid sample return mission Hayabusa and its successor Hayabusa2. Prior to the first mission, the microwave discharge ion thruster μ10 completed a 20,000-hour lifetime endurance test at a ground facility. Although the mission was a success, it was observed that the microwave discharge cathode of μ10 degraded faster than it did in the ground endurance test. The second-generation model of the thruster, which increased the thrust force from 8 to 10 mN and had modified microwave discharge cathodes, was used in the Hayabusa2 probe, which launched in December 2014. The latest model of the thruster, which has a 12-mN thrust force, is planned to be used in the comet fly-by mission DESTINY$^+$.[9]

Table 1.4 and Figure 1.14 summarize the history and future plans for space exploration using microwave discharge ion thruster systems. In the asteroid explorer Hayabusa, the electron current was 135 mA. In its successor Hayabusa2, the electron current was increased to 180 mA by enhancing the magnetic field intensity in the discharge chamber. For the future DESTINY$^+$ mission, an electron current of 220 mA is needed.

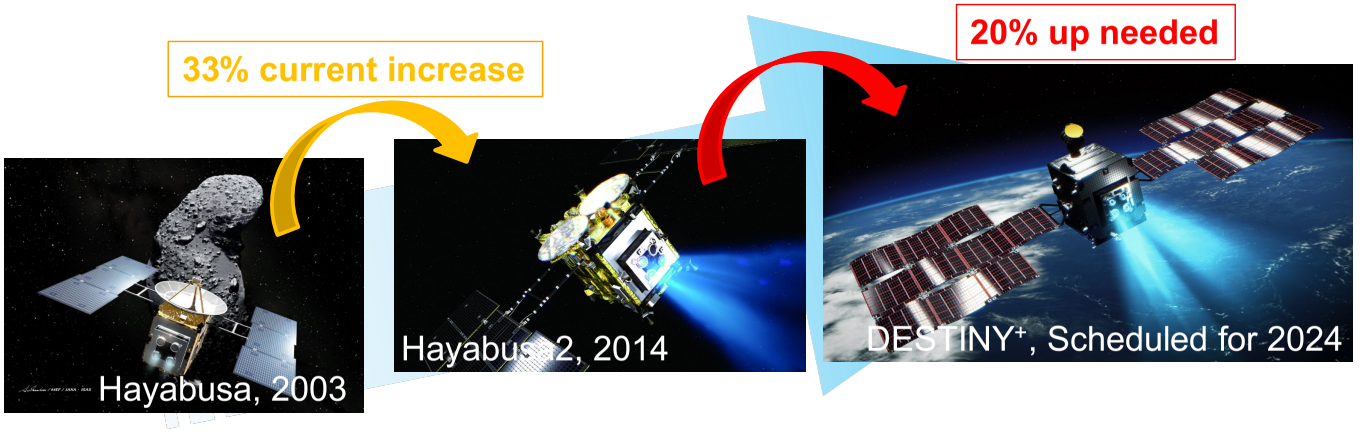

Figure 1.14: JAXA's explorers with microwave discharge ion thruster systems. ©Copyright 2009 JAXA and Akihito Ikeshita.

Table 1.4: Previous improvements and future plans for microwave discharge cathodes.

Application	Launch	Improvement	Neutralization current, mA
Hayabusa	2003	-	135
DubaiSat2	2013	Microwave power increased	500
Hayabusa2	2014	Magnetic field intensity enhanced	180
DESTINY$^+$	Scheduled for 2024	Detailed in this study	220

1.7 Objectives

1.7.1 Objectives of this study

As described in the background section, performance improvements are needed for future microwave discharge ion thrusters. Therefore, the objective of this study is to improve the performance of microwave discharge cathodes, and the following studies are performed: performance enhancements in the two current ranges of 200 mA and 500 mA, developing a viewable microwave discharge cathode for optical measurements, making a plasma diagnosis in a flight-model class viewable cathode, and making a plasma diagnosis in the improved cathodes. The following studies are detailed in the appendix: performance enhancement using a low-work-function material, performance analysis and discussion of microwave discharge cathode–200-W Hall thruster system with a comparison to a hollow cathode, application as a plasma source for charge removal in high vacuum, and application for charged dust removal.

1.7.2 Outline of the content

Two approaches for performance enhancements for microwave discharge cathodes are reviewed in Chapter 2. Plasma diagnosis of a microwave discharge cathode is described in Chapter 3. The conclusions obtained by this study are given in Chapter 4.

The objective of the study described in Chapter 2 is to improve the performance using two different approaches. Firstly, to improve the performance in the 200-mA class current range, the effect of a magnetic field at the nozzle on performance was investigated in diode mode operation. To change the field intensity, a coil was installed at the nozzle. The difference in the I–V characteristics was measured between the nominal model and the model with a coil. In addition, a magnetic shield that reproduces the effect observed with the coil was designed and the I–V characteristics of the cathode were measured. Secondly, to improve the performance in the 500-mA class current range, the mirror ratio and magnetic field intensity were increased. The difference in the I–V characteristics was measured between the nominal model and the developed model in diode mode operation. To investigate the I–V characteristics in coupling operation, a 200-W class Hall thruster was coupled. In addition, to evaluate the validity of the developed microwave discharge cathode, a hollow cathode was coupled with the thruster and investigated. The thrust performance and beam profile are discussed in Appendix B.

In Chapter 3, plasma diagnostics of both the nominal and improved cathode are discussed. Firstly, a microwave discharge cathode was developed with a small optical window in the discharge chamber that provides visual access to the cathode interior. To investigate the actual conditions for the Hayabusa2 onboard cathode, it is necessary to develop a viewable

microwave discharge cathode with an optical window that has I–V characteristics equivalent to those of the flight model. The difference in the I–V characteristics were measured between the nominal model and the viewable cathode to verify the reproductivity. Laser-induced fluorescence (LIF) spectroscopy was applied to the cathode due to its low plasma and electromagnetic disturbance. The axial and radial ion velocity distribution functions (IVDFs) in the plume region and the axial IVDFs inside the cathode were measured. The measured functions, which represent the relative number density of XeII $(^3P_2)6p[3]_{5/2}$, were compared to the previously reported ion density measured by an electrostatic probe in the plume region. In the plume, the two-dimensional spatial velocity vector was calculated by axial and radial LIF measurements. To discuss the velocity vector, the plasma potential distribution was measured by an emissive probe. Parametric measurements of axial LIF were conducted in the viewable cathode. To investigate the effect of laser reflection on IVDFs inside the cathode, a black-painted viewable cathode was measured by LIF. To discuss multimodal IVDFs inside the cathode, anode current oscillation and radiated emission were measured. A theoretical model based on the measured current oscillation was compared to the measured IVDFs. LIF measurements were conducted for the improved models. The LIF intensity distribution was compared to the nominal model to investigate the performance difference.

In Appendix A, the effect of the nozzle material on the I–V characteristics is discussed. Materials with a lower work function emit more electrons at lower energy. Mo and Th-W were compared in diode mode operation to investigate this effect.

In Appendix B, the 500-mA class improved model was coupled with a 200-W class Hall thruster. A hollow cathode was also coupled with the thruster to compare the performance. Firstly, the effect of the magnetic field polarity on the ignition characteristics was investigated. Secondly, the thrust, ion energy distribution function and beam profiles were measured by an inverted thrust stand, a retarding potential analyzer, and an ion collector, respectively. Using these results, the thrust was measured and a deficiency analysis was performed. The differences between these results and the trade-off point between the microwave discharge cathode and hollow cathode are discussed.

In Appendix C, a microwave discharge cathode was applied in a charge neutralizer in a high vacuum environment of 10^{-1}–10^{-4} Pa. Firstly, the time constants for charge neutralization were measured. Secondly, the distribution of the charge neutralization current density was measured. The anode and orifice were changed and the distributions were compared. Thirdly, the charge neutralization effect was demonstrated using a film transfer simulator.

In Appendix D, the microwave discharge cathode was applied in a charged dust remover in a high vacuum. Firstly, charged dust adhering to the surface was exposed to a microwave discharge plasma. The charging potential and the amount of adhered dust were measured.

Secondly, the effect of the microwave discharge plasma on the mitigation of dust adhesion was investigated. Thirdly, a charged particle was levitated by an electrostatic levitation furnace. The effect of the microwave discharge plasma on the levitated particle was investigated.

Chapter 2

Performance Enhancements of Microwave Discharge Cathode

In Chapter 2, the two types of performance enhancements that were implemented and described in detail. This chapter is partially reproduced from published articles[42][43], with the permission of Elsevier.

2.1 Effect on performance of a magnetic field at a nozzle

Firstly, a magnetic field was applied at the nozzle by a coil. Secondly, to realize the same magnetic field intensity achieved in the first experiment without any additional power consumption, a magnetic shield was developed.

2.1.1 Experimental setup

As shown in Figure 2.1, experiments were conducted in a diode mode in which an anode plate was placed in front of the cathode instead of an ion beam potential from an ion source. The microwave discharge cathode system was composed of a propellant supply system and microwave supply system. The xenon tank and mass flow controller supplied a constant mass flow of xenon. The microwave supply system was composed of an oscillator, amplifier, and matching circuit. The system produced microwaves of 4.25 GHz and then amplified them to a determined intensity. The microwaves were introduced into the cathode through the matching circuit.

The experimental conditions are summarized in Table 2.1. The propellant was xenon and was operated at a gas flow rate of 0.7 sccm, a microwave power of 8 W, and a cathode current of 180 mA, as the nominal conditions. The distance between the cathode and the anode plate

was 11 mm. This is consistent with the ground durability test of the Hayabusa2. A coil was wrapped around the nozzle of this cathode and the performance difference was investigated by changing the coil current. The nozzle has a convex shape and the coil can be wound around it.

The anode voltage V_a was measured when the external magnetic field of the cathode was changed by the coil current. The direction of the magnetic field was fixed so that downstream from the cathode was a South pole. In this study, the direction of the magnetic force that strengthens the external magnetic field is defined as the positive direction. The magnetic flux density was measured at 1.5-mT increments from 7.5 mT to 37.5 mT. The anode current I_a was also measured when V_a was fixed at 37 V. The relationship between I_a and magnetic flux density controlled by the coil was measured. The anode voltage V_a was measured by changing I_a at 140, 180, and 220 mA. In addition, the dependence of the gas flow rate $\dot{m}_c$ of the cathode was investigated. The gas flow rates $\dot{m}_c$ were 0.5, 0.7, and 1.5 sccm.

Table 2.1: Experimental conditions for I–V characteristic measurements with coil or magnetic shield.

Parameter	Value
Microwave frequency	4.25 GHz
Microwave power, P_m	8 W
Xenon flow rate, $\dot{m}_c$	0.5 sccm, 0.7 sccm, 1.5 sccm (0.049 mg/s, 0.069 mg/s, 0.088 mg/s)
Anode current, I_a	0 mA, 140 mA, 180 mA, 220 mA in Constant Current
Anode voltage, V_a	37 V in Constant Voltage
Microwave antenna	Flight model (Hayabusa2)
Background pressure	3×10^{-3} Pa at 0.7 sccm Xe
Nominal condition	$P_m = 8$ W, $\dot{m}_c = 0.7$ sccm, $I_a = 180$ mA

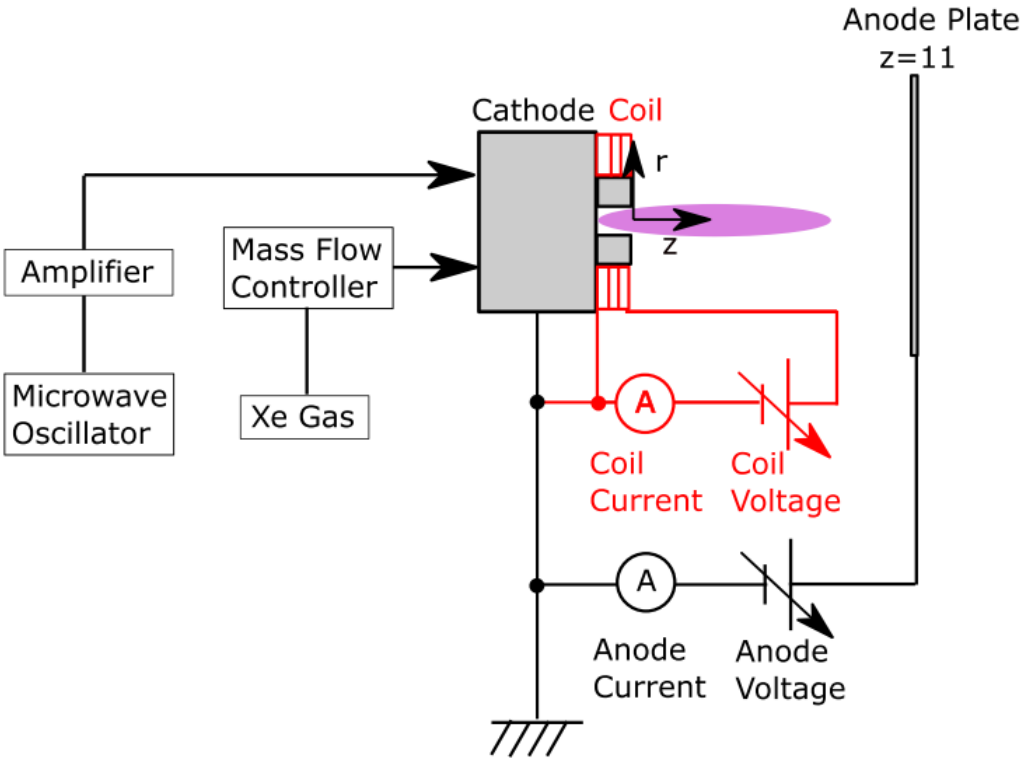

Figure 2.1: Experimental setup for the diode mode operation with a coil. An axial magnetic field is applied by an external coil around the nozzle.

2.1.2 Application of magnetic field using a coil

The measurement results of I_a at a constant voltage operation of 37 V are shown in Figure 2.2. Even in this case it can be seen that I_a has increased due to a weakening magnetic field. The anode current I_a increased by 80 mA over that of a conventional cathode when the magnetic field intensity was weakened to 15 mT at the nozzle. For a further weakening of the magnetic field, V_a suddenly increased, reducing I_a.

Figure 2.3 shows the relationship between V_a and magnetic flux density at the nozzle. Even when the external magnetic field was strengthened, V_a did not change much, but when the external magnetic field was weakened, V_a decreased. When I_a was 180 mA which is same as Hayabusa 2 condition, V_a decreased by 10 V when the magnetic field intensity was weakened to 14 mT. When we further weakened the magnetic field, V_a suddenly increased. We consider the effect of changing the parameters of the cathode. Figure 2.3 also shows the result when I_a is changed. When I_a was increased, the characteristic curve was shifted, increasing V_a. When I_a was decreased, V_a decreased in the high magnetic flux density region.

Figure 2.4 shows the results of changing $\dot{m}_c$. When $\dot{m}_c$ was increased, the magnetic flux density dependency on V_a decreased.

To investigate the plasma in the near-nozzle plume, we measured the plasma by an electrostatic probe of tungsten wire of ϕ0.3 mm and an exposed length of 1 mm covered with an alumina tube of ϕ2 mm. As shown in Figure 2.5, the probe was measured at positions of z = 2, 6, and 8 mm in the downstream direction of the cathode. The probe was inserted in the plume vertically. The plasma measurements were carried out for four values of magnetic flux density at the nozzle of the microwave discharge cathode, 11 mT, 15 mT, 18 mT, and 23 mT, the same as the Hayabusa2 cathode. The relationship between the electron number density and magnetic flux density for the coil is shown in Figure 2.6. If the external magnetic field is weakened by the coil up to 15 mT, the electron number density increases. However, the electron number density decreases at 11 mT. Comparing Figure 2.2 and Figure 2.3, when V_a decreased and I_a increased, the electron number density increased.

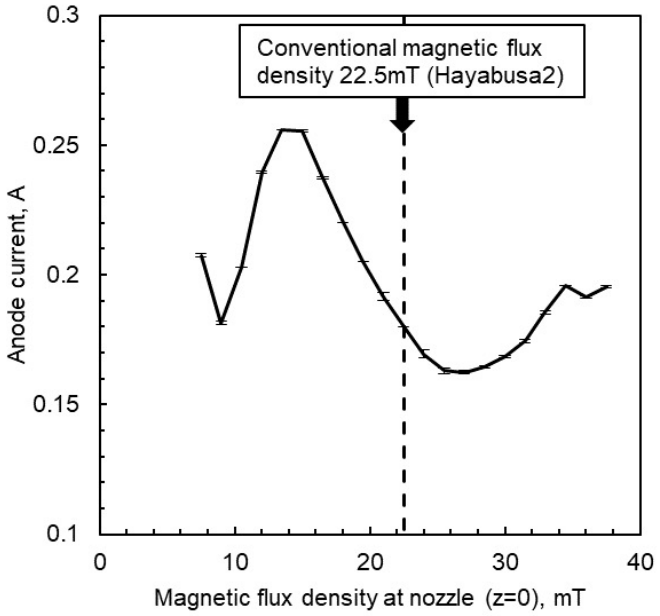

Figure 2.2: Anode current transition with respect to the magnetic flux density at the nozzle at $I_a = 0.7$ sccm, $V_a = 37$ V.

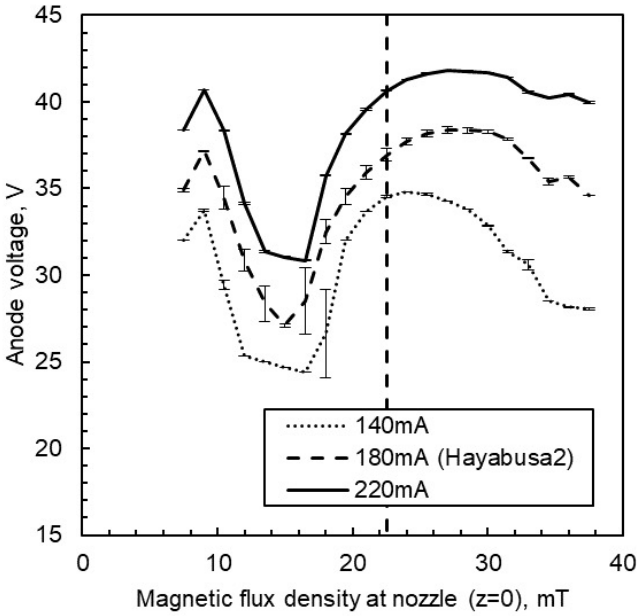

Figure 2.3: Anode voltage transition with respect to the magnetic flux density at $\dot{m}_c = 0.7$ sccm. The anode current is 140, 180, 220 mA.

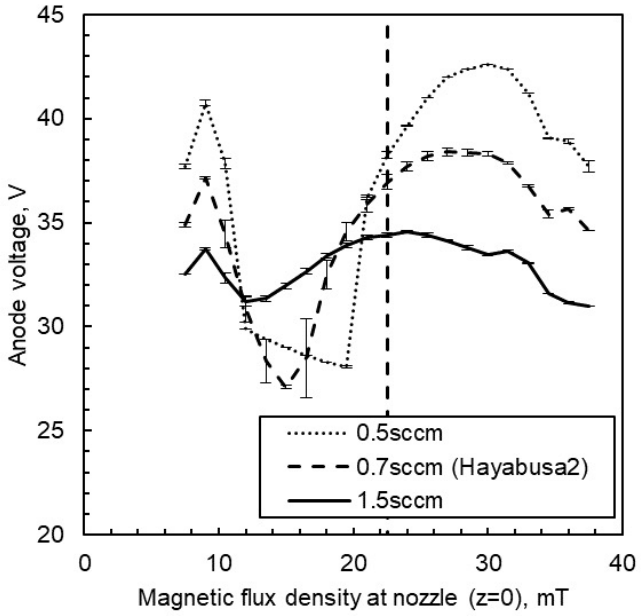

Figure 2.4: Voltage transition of the anode plate with respect to the magnetic flux density at $\dot{m}_c$ of 0.5, 0.7, 1.5 sccm. The anode current is 180 mA.

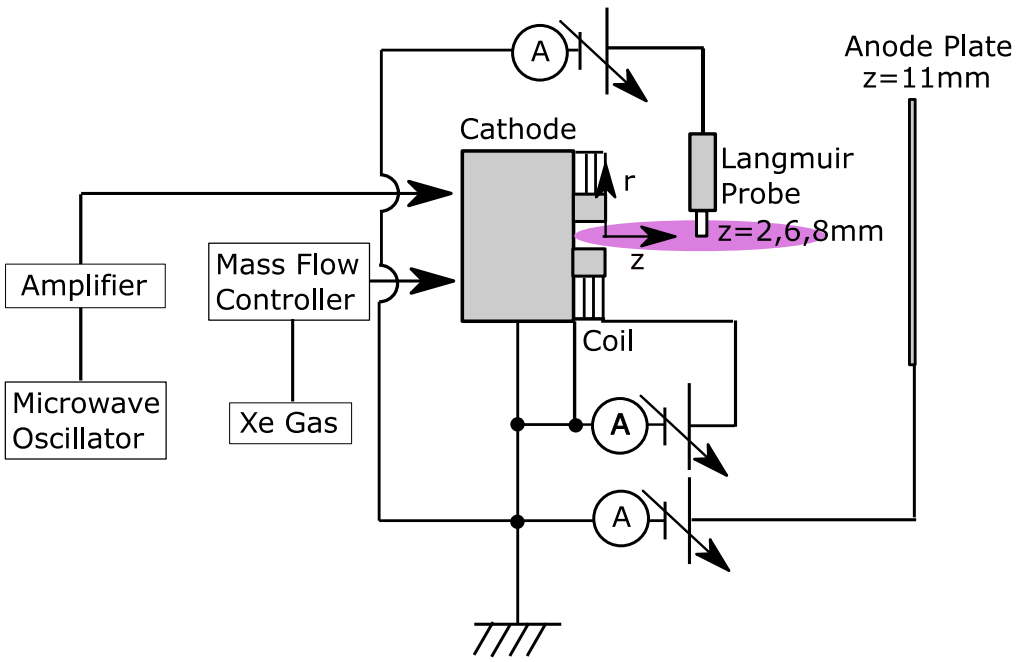

Figure 2.5: Experimental setup for the electron number density measurements using an electrostatic probe. The probe is set at 2, 6, and 8 mm from the exit of the nozzle along the centre axis.

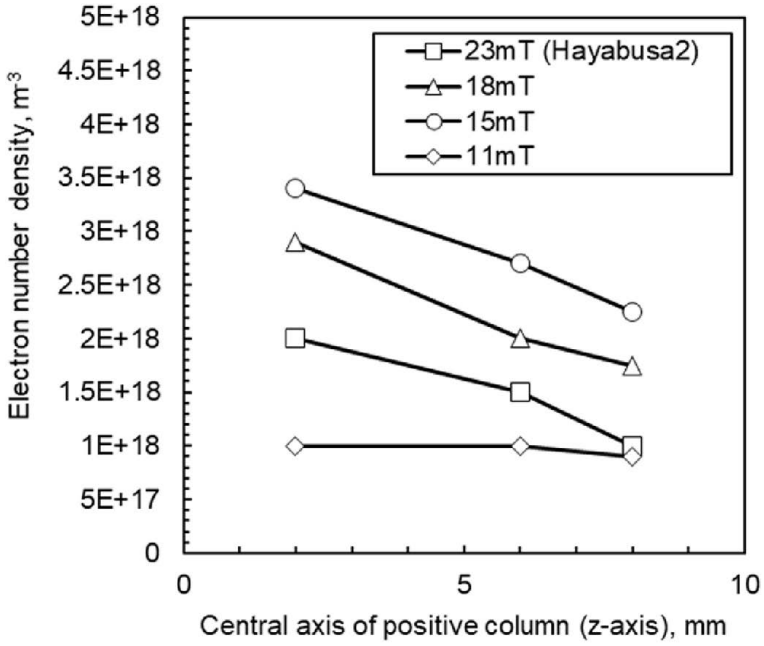

Figure 2.6: Relationship between the electron number density and magnetic flux density. The anode voltage is 40 V.

2.1.3 Magnetic shield

In the previous section, it was confirmed that V_a was decreased by using a coil. By using a coil, it is possible to continuously change the magnetic field in the plume, which is convenient in terms of finding the optimum value. However, when applied to spacecraft, an additional power supply system for the coil is required, which increases the payload. Simplification and weight reduction of the system are required for deep space exploration. There is also a disadvantage in that electric power for the coil is required, but resources are limited in a space mission. There is also the problem of robustness. It is possible that the wire of the coil may become disconnected. Therefore, we aim to mechanically reproduce the same magnetic field as the optimum magnetic field formed by the coil. The magnetic field inside the cathode and the plume is analyzed using the magnetic field analysis software "Finite Element Method Magnetics". Based on this, we formulated a method to increase I_a without a coil power supply by installing a simple magnetic shield.

The magnetic field reproducing the coil was determined by numerical analysis and reproduced by a magnetic shield made from iron. To verify the effectiveness of this reproduction, the magnetic shield was attached as shown in Figure 2.7. The other conditions were the same as in the previous section.

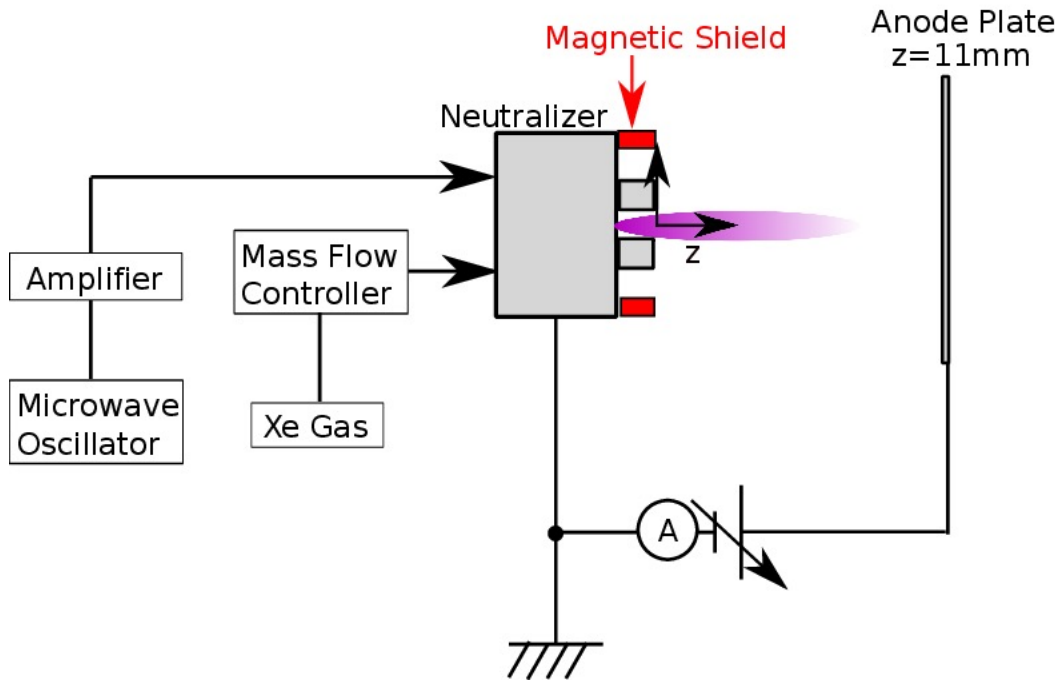

Figure 2.7: Experimental setup for the diode mode operation with a shield for demagnetization at the nozzle.

As shown in Figure 2.2 and Figure 2.3, since V_a decreased around 14 mT to 16 mT, this region is a target to reproduce. The magnetic shield was designed as shown in Figure 2.8, with an absolute magnetic flux density $|B|_{(r=0)}$ distribution for the magnetic shield at 14 mT at the nozzle (z = 0 mm).

A performance comparison for the cases with and without the magnetic shield is shown in Figure 2.9. A good performance shows a high current transport with a small anode voltage, or in other words, a tendency towards the lower right in Figure 2.9. The figure confirms that V_a with the shield was reduced by 3-5 V compared with a conventional cathode. In addition, a current increase of about 20-50 mA was confirmed.

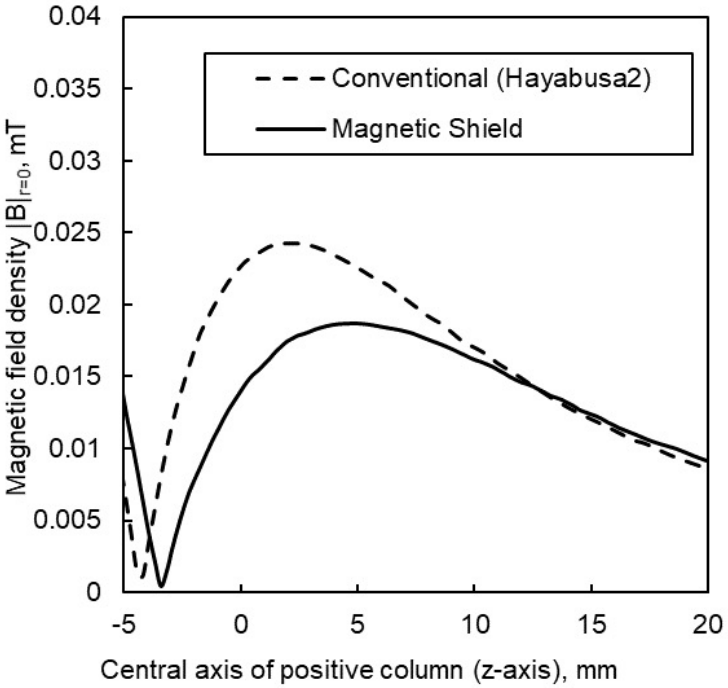

Figure 2.8: Comparison of magnetic field density between the conventional and magnetic shield model along the central axis

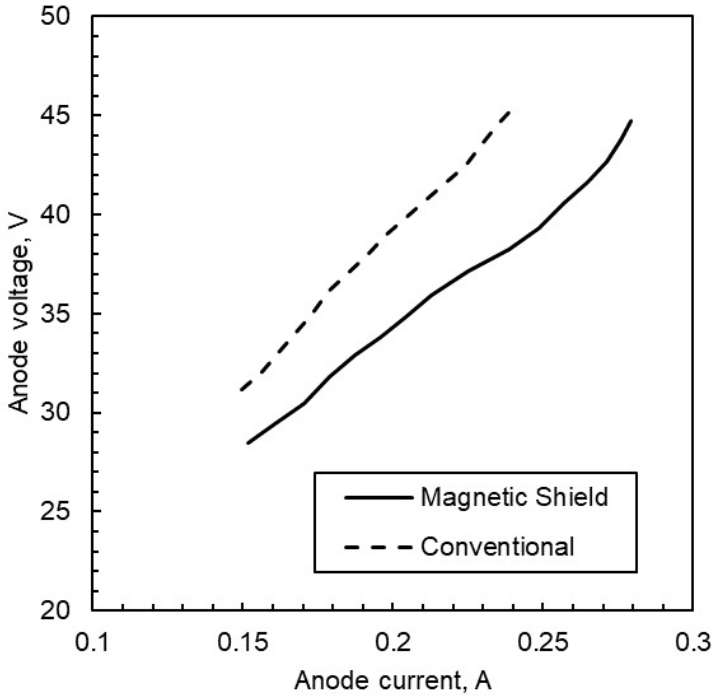

Figure 2.9: Comparison of I–V characteristics between conventional and magnetic shield model at $P_{\mathrm{m}} = 8$ W, $\dot{m}_{\mathrm{c}} = 0.7$ sccm.

2.1.4 Discussion

In a plasma with a magnetic field, if the cyclotron frequency is sufficiently larger than the collision frequency, the classical diffusion coefficient $D_\perp$ in the direction perpendicular to the magnetic field B can be written by the following approximate Eq.2.1.[16]

$$D_\perp = \frac{mkT\nu}{e^2}\frac{1}{B^2} \tag{2.1}$$

From Eq. 2.1, it can be seen that $D_\perp$ is inversely proportional to the square of the magnetic flux density B. This is because the charged particles move in a spiral around the magnetic field lines with Larmor radius r inversely proportional to the magnetic flux density B due to the Lorentz force. Where the magnetic flux density B is weak, $D_\perp$ is large.

Figure 2.10 shows the comparison of electron transport between conventional and improved magnetic field. In the conventional magnetic field, because the magnetic field is stronger, relatively trapped electrons are increased around the nozzle. Therefore, the electrons are prevented from being emitted to the outside through the nozzle. On the other hand, in the improved magnetic field, transported electrons are increased because the nozzle magnetic field is relatively weak. It is presumed that the applied magnetic field facilitates the detachment of magnetic lines by the electrons inside the microwave cathode, resulting in a reduction of V_a.

Figure 2.9 confirms that V_a was reduced by 3-5 V, demonstrating that the magnetic shield reproduces the magnetic field of the coil. However, V_a was larger than for the case when a coil was used. This is believed to be because the magnetic field in the cathode was also weakened by the magnetic shield. By analysing the magnetic field, it was confirmed that the magnetic field of the discharge chamber was reduced to about 10 mT compared to the case when a coil was used. Weakening the magnetic field density in the cathode likely decreases plasma generation by ECR, which would be why V_a was not small compared with the case when a coil was used.

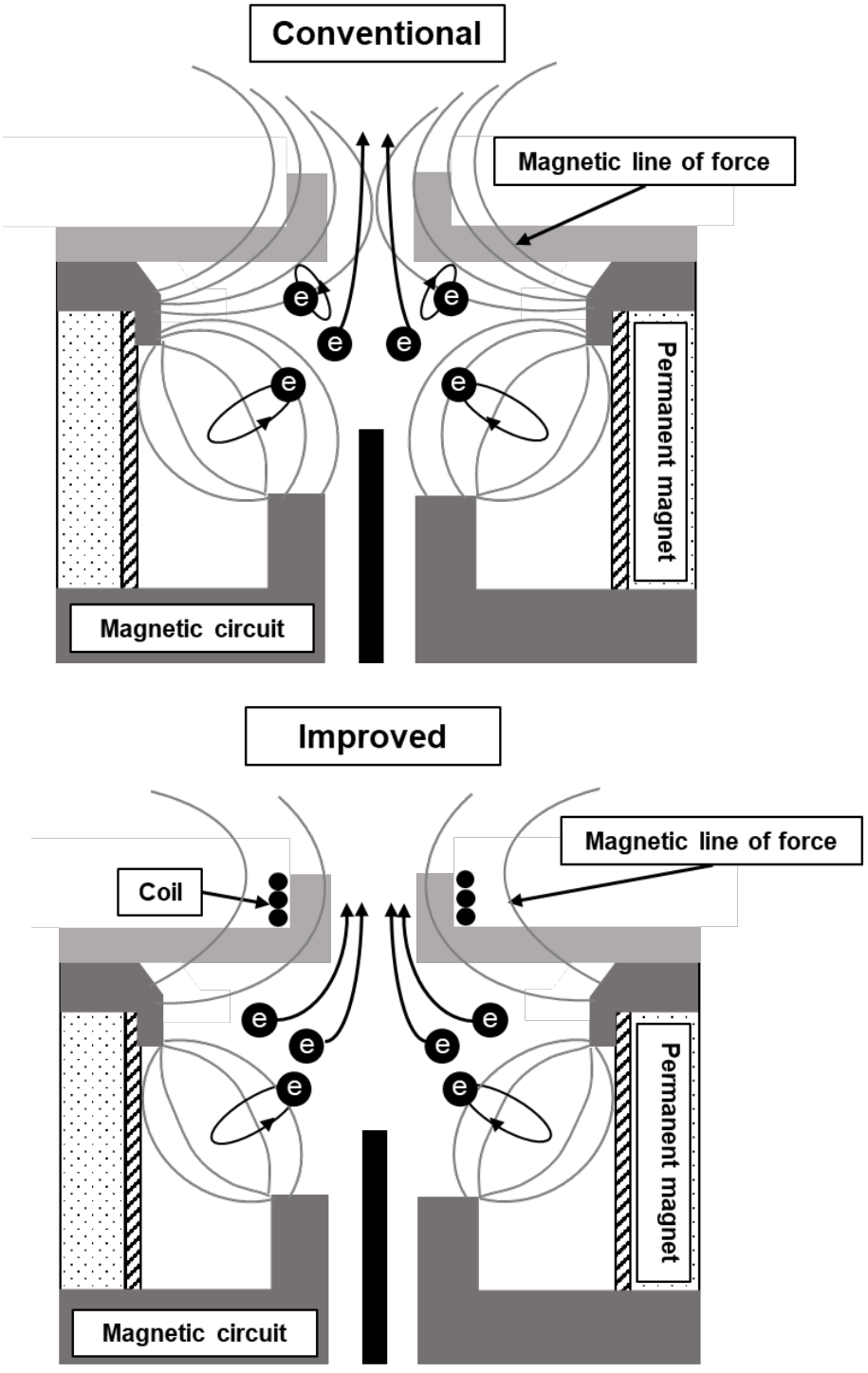

Figure 2.10: Comparison of electron transport between conventional and improved magnetic field.

2.1.5 Summary

The experimental approach described in this section focused on the performance of a microwave discharge cathode by controlling the magnetic field intensity and its subsequent application for space operation. The results are summarized as follows:

1. It was found that when the axial magnetic field of the plume of the microwave discharge cathode was weakened by a coil, the anode current I_a increased by 80 mA more than the conventional cathode operated at a constant anode voltage V_a of 37 V. This is a 44% increase. Operating at a constant I_a of 180-mA, V_a decreased by as much as 10 V, which is a 27% decrease.
2. It was found that the magnetic shield reproduced the effect observed with the coil of producing lower V_a at a fixed current and higher I_a at a fixed voltage. Because the impedance of the discharge changed, it was suggesting easier transport across the B-field lines inside the cathode. Concretely, when the magnetic shield was attached, I_a increased by 30 mA over that of a conventional cathode operated at a constant V_a of 37 V. This is a 17% increase. Operating at a constant I_a of 180-mA, V_a decreased by as much as 5 V, a 14% decrease.

2.2 Increase of mirror ratio and magnetic field intensity

This section firstly describes the mirror ratio, magnetic field intensity redesign and the I–V characteristics measurements in the diode mode operation. Secondly, an improved microwave discharge cathode was coupled with a 200-W class Hall thruster for measuring the I–V characteristics in coupling test operation. In addition, to evaluate the improved microwave discharge cathode as an alternative to hollow cathodes, the I–V characteristics were compared with a hollow cathode in coupling operation.

The thrust performance characteristics and beam profiles were also measured and the differences in these characteristics were analyzed, with the results discussed in Appendix B.

2.2.1 Redesign of magnetic circuit

To increase the electron current, two parts of the magnetic circuit were redesigned using "Finite Element Method Magnetics".[44] Firstly, the magnetic field intensity in the discharge chamber was enhanced by increasing the number of permanent magnets, which increased the magnetic field intensity by an average of 10 mT inside the discharge chamber, as shown in the "Field enhanced" plot in Figure 2.11. Secondly, the mirror field was redesigned. In the nominal model, which has the same magnetic design as DubaiSat2 and Hayabusa2, the magnetic field lines do not match on either two side of the magnetic yoke edges, which leads to relatively weak magnetic confinement. Therefore, by ensuring the magnetic field lines match, the mirror ratio R_{m} was increased. R_{m} is defined in Eq. 2.2.

$$R_{\mathrm{m}} = \frac{B_{\max}}{B_{\min}} = \frac{1}{\sin^2 \theta_{\mathrm{m}}} \tag{2.2}$$

Here, $B_{\max}$ is the maximum density on a magnetic field line, $B_{\min}$ is the minimum density on the magnetic field line, and θ_{m} is the pitch angle of the loss-cone. Eq.2.2 shows that as R_{m} increases, the loss at the edges of the magnetic yokes decreases and the electron confinement time increases. By redesigning the inner diameter of the lower yoke, R_{m} was increased from 2 to 8.3, as shown in the "Nominal" and "High mirror ratio yoke" plots in Figure 2.11. The "Field enhanced with high mirror yoke" plot in Figure 2.11 is a combination of "High mirror ratio yoke" and "Field enhanced". Figure 2.12 shows a schematic diagram of Figure 2.11.

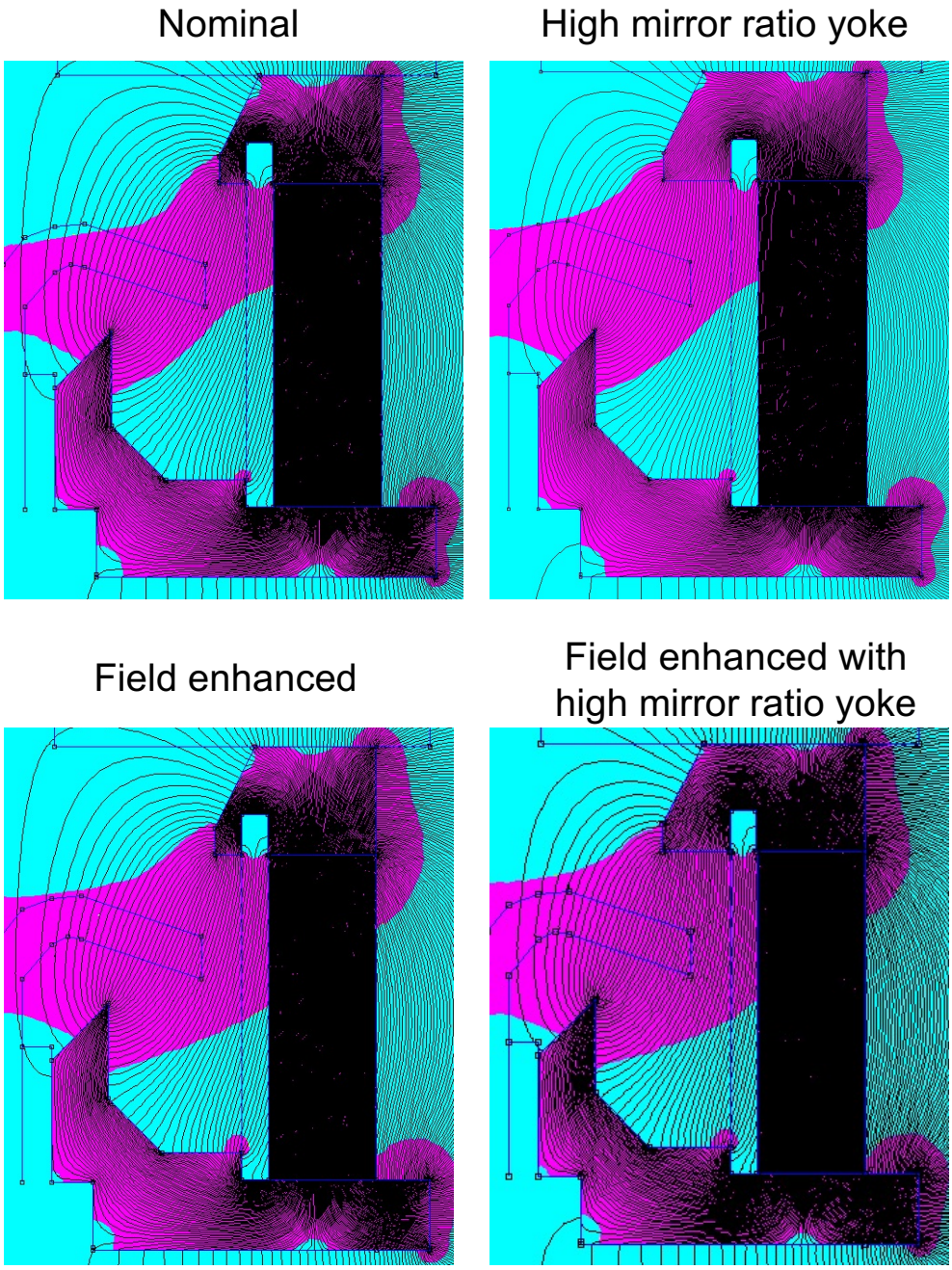

Figure 2.11: Comparison of redesigned magnetic field calculated by Finite Element Method Magnetics.

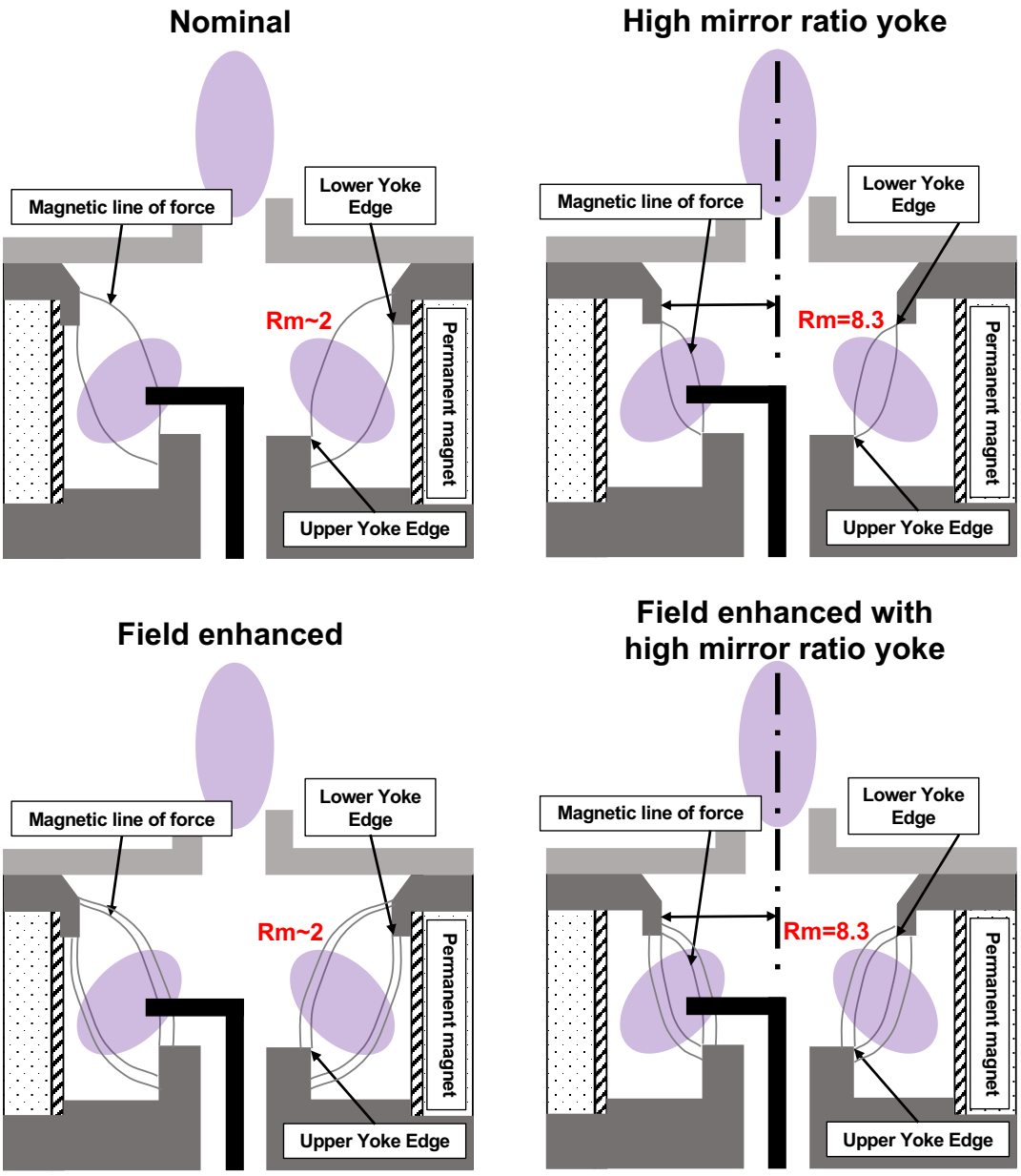

Figure 2.12: Schematic diagram of the redesigned magnetic field shown in Figure 2.12.

2.2.2 Experimental setup for diode mode operation

Figure 2.13 shows the experimental setup for the I–V characteristic comparison between the conventional and improved models in diode mode operation. The experimental conditions are summarized in Table 2.2. The gas flow rate $\dot{m}_c$ was fixed at 1.5 sccm. The microwave power was also fixed at 20 W.

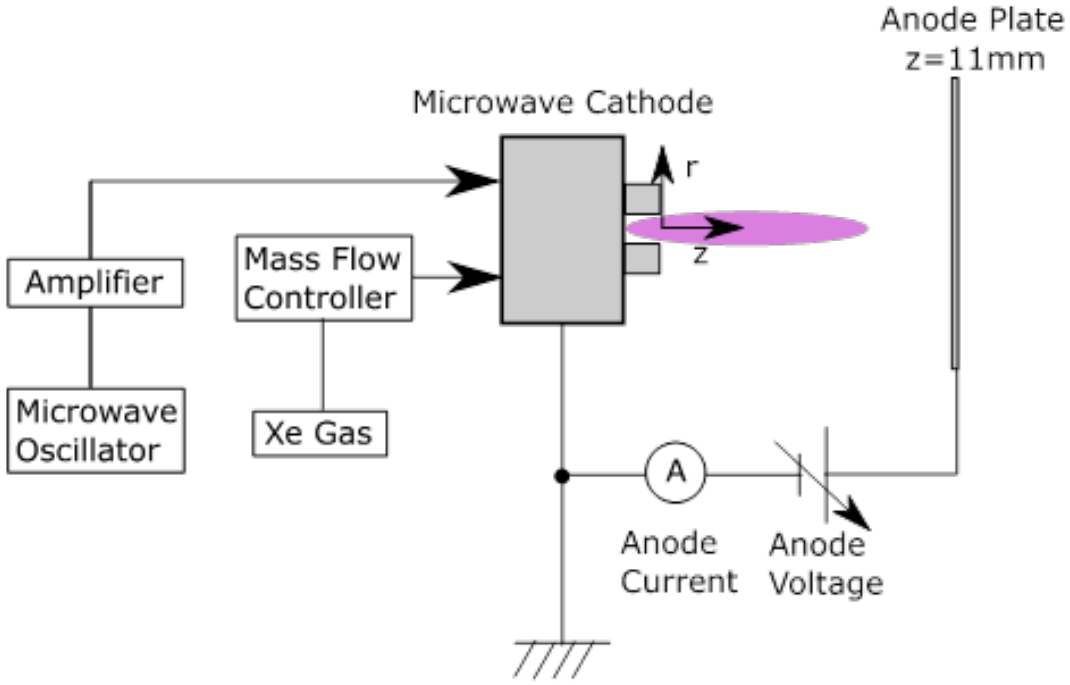

Figure 2.13: Experimental setup for I–V characteristic comparison between conventional and improved models in diode mode operation.

Table 2.2: Experimental conditions for microwave discharge cathode in diode mode operation.

Parameter	Value
Microwave frequency	4.25 GHz
Microwave power, P_m	20 W
Xenon flow rate, $\dot{m}_c$	1.5 sccm (0.15 mg/s)
Microwave antenna	Flight model (Hayabusa2)
Background pressure	4×10^{-5} Pa without Xe 1×10^{-3} Pa at 1.5 sccm Xe

2.2.3 Results and discussion for diode mode operation

Figure 2.14 compares the I–V characteristics of the nominal and improved models in diode mode. The nominal model operated at 26 V at 100 mA, which increased to 46 V at 300 mA. The "High mirror ratio yoke" model decreased the anode voltage by 2–5 V and increased the anode current by 10–50 mA compared to the nominal model. The "Field enhanced" model decreased the anode voltage by 8–11 V and increased the anode current by 90–100 mA compared to the nominal model. The "Field enhanced with high mirror ratio yoke" model decreased the anode voltage by 8–12 V and increased the anode current by 90–120 mA compared to the nominal model. In the "Field enhanced with high mirror ratio yoke" model, the anode current increased from 300 mA to 560 mA when the anode voltage was 37 V compared to the nominal model.

The results suggest that the electron emission capacity of the microwave discharge cathode was improved by the enhanced magnetic field and the improvement in R_{m}, which implies that the electron confinement time increased and consequently the amount of plasma generation increased. In addition, the high mirror yoke generated a dense plasma near the nozzle and electrons moved to the nozzle relatively easily. This is discussed in Section 3.10.2.

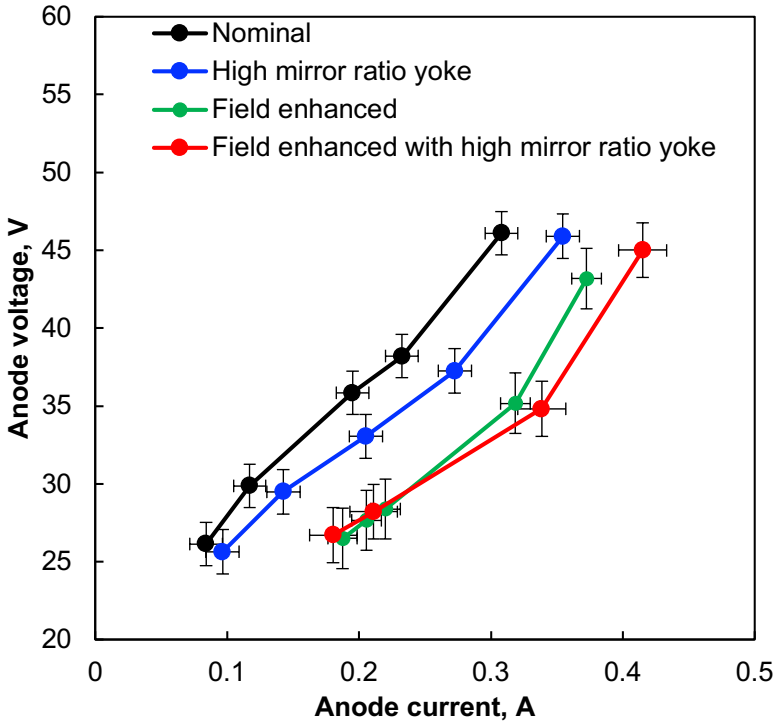

Figure 2.14: Comparison of I–V characteristics of conventional and improved models in diode mode.

2.2.4 Experimental setup for coupling operation with 200-W class Hall thruster

To investigate the I–V characteristics, coupling operation of the microwave discharge cathode–Hall thruster system was performed. In addition, to evaluate whether the improved microwave discharge cathode is a viable alternative, the I–V characteristics were compared with those for a hollow cathode. In this experiment, the "Field enhanced with high mirror ratio yoke" model was used as the improved model. The experiments were conducted in the space science chamber at the Institute of Space and Astronautical Science (ISAS) of the Japan Aerospace Exploration Agency (JAXA). The Hall thruster was a magnetic layer type developed by Kyushu University.

The experimental setup is shown in Figure 2.15. Figure 2.16 shows the photograph of 200-W class Hall thruster with microwave discharge cathode in operation. The microwave discharge cathode was placed 15 mm in the downstream direction and 65 mm in the radial direction with respect to the Hall thruster. As parameters, the inner coil current I_{coil} and anode voltage of the thruster V_{ath} were changed. The outer coil current was set to be 4 times I_{coil}. We measured the anode current I_{a} and cathode current I_{c} using a current probe, as well as the potential difference between the cathode and ground V_{cg}.

As described in Appendix B, to investigate the thruster performance and beam profile, a retarding potential analyzer (RPA) and ion collector were placed 950 mm downstream of the Hall thruster. They were then moved ±500 mm along the r-direction. As a benchmark, these same measurements were conducted for a general hollow cathode (Ion Tech HCN252).

Table 2.3 shows the experimental conditions during coupling operation. The cathode power consumption, $P_{\mathrm{c}} = 20$ W, and xenon flow ratio for the cathode, $\dot{m}_{\mathrm{c}} = 1.5$ sccm, were set to minimize V_{cg} and the power consumption.

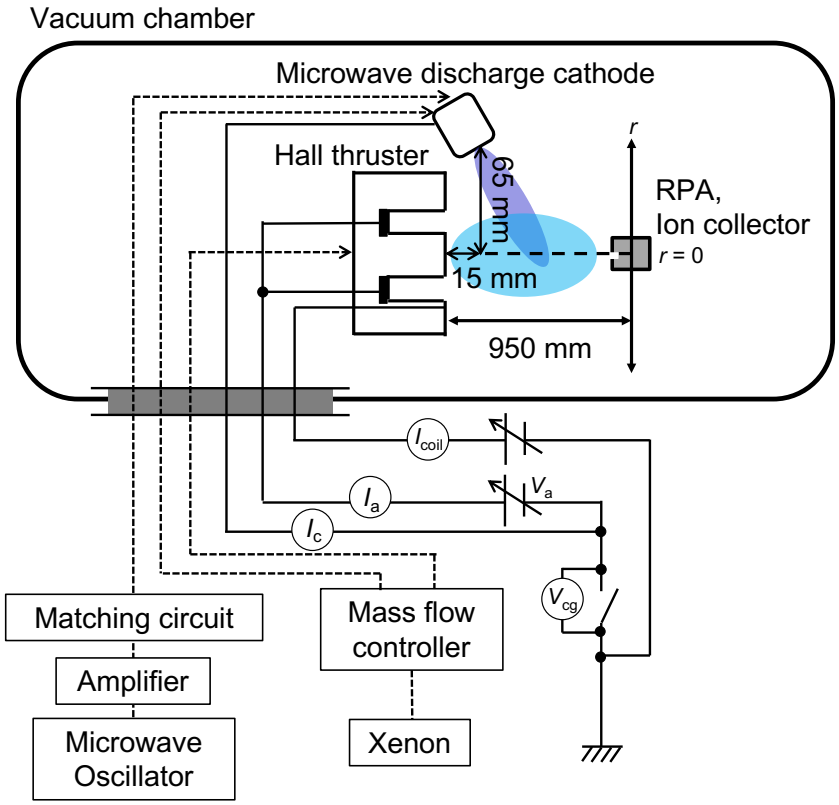

Figure 2.15: Experimental setup for coupling operation of Hall thruster and microwave discharge cathode.

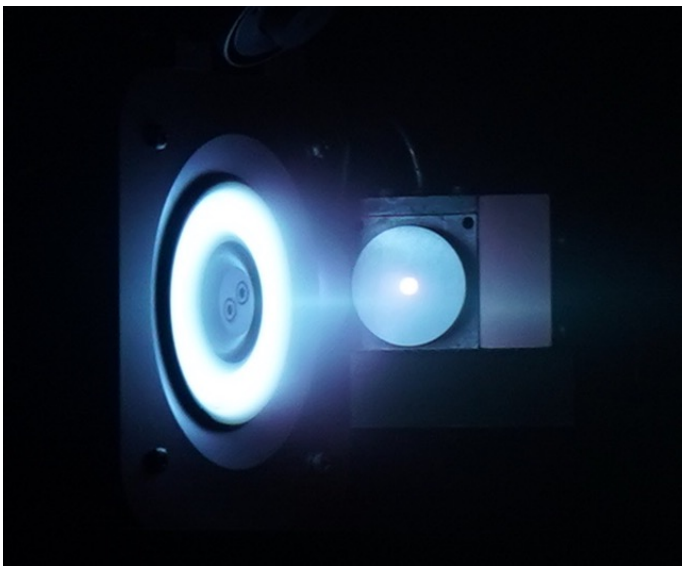

Figure 2.16: Photograph of 200-W class Hall thruster with microwave discharge cathode in operation.

Table 2.3: Experimental conditions for the coupling test of microwave discharge cathode - Hall thruster system.

Parameter	Value
Microwave frequency	4.25 GHz
Microwave power, P_c	20 W
Xenon flow rate for microwave discharge cathode	1.5 sccm (0.15 mg/s)
Heater and keeper power	20 W
Xenon flow rate for hollow cathode	1.5 sccm (0.15 mg/s)
Xenon flow rate for anode, $\dot{m}_a$	7.0 sccm (0.069 mg/s)
Inner coil current, I_{coil}	1.5 A, 2.0 A, 2.5 A
Anode voltage of thruster, V_{ath}	150 V, 200 V, 250 V, 300 V
Microwave antenna	Flight model (Hayabusa2)
Background pressure	4×10^{-5} Pa without Xe 3×10^{-3} Pa at 10 sccm Xe

2.2.5 Results for coupling operation with 200-W class Hall thruster

Figure 2.17 compares the I–V characteristics for the nominal and improved models for both diode and coupling test operation. It should be noted that diode mode operation was also conducted in the ISAS/JAXA space science chamber, which is different to the previous diode mode operation chamber. As shown in Figure 2.17, in diode mode, the anode current increases from 300 mA to 560 mA compared with the nominal model when the anode voltage was 37 V. In coupling operation, the microwave discharge cathode can supply a higher electron current than in the diode mode. This is thought to be due to the neutral particles and plasma supplied by the Hall thruster. However, it is also considered that the plasma potential in the plume offsets V_{cg}.

Figure 2.18 shows the I_a–V_{cg} characteristics including all parameters, such as I_{coil} and V_{ath} of Table 2.3. At $I_a = 600$ mA and above, the microwave discharge cathode showed different characteristics than the hollow cathode. This indicates that the electron emission capability of the microwave discharge cathode is comparable to that of the hollow cathode up to 600 mA, while above that, the hollow cathode is preferable. However, this trade-off point should be smaller for an optimized low-current hollow cathode.

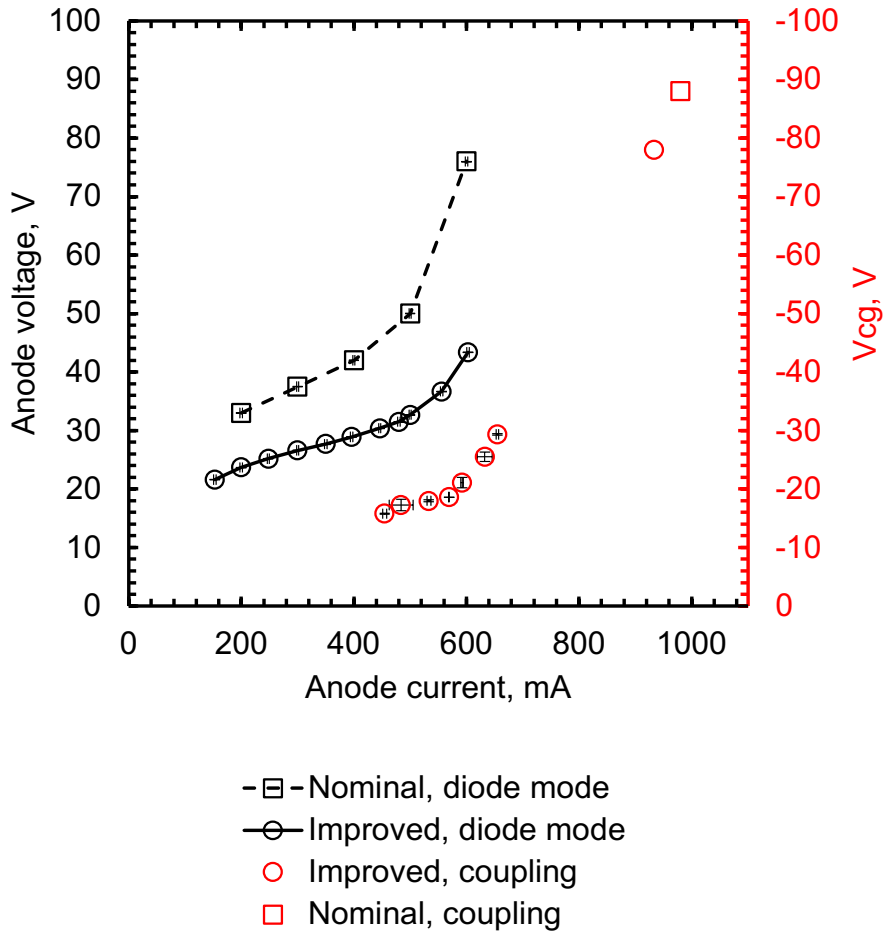

Figure 2.17: Comparison of I–V characteristics of nominal and improved models for diode and coupling test operation.

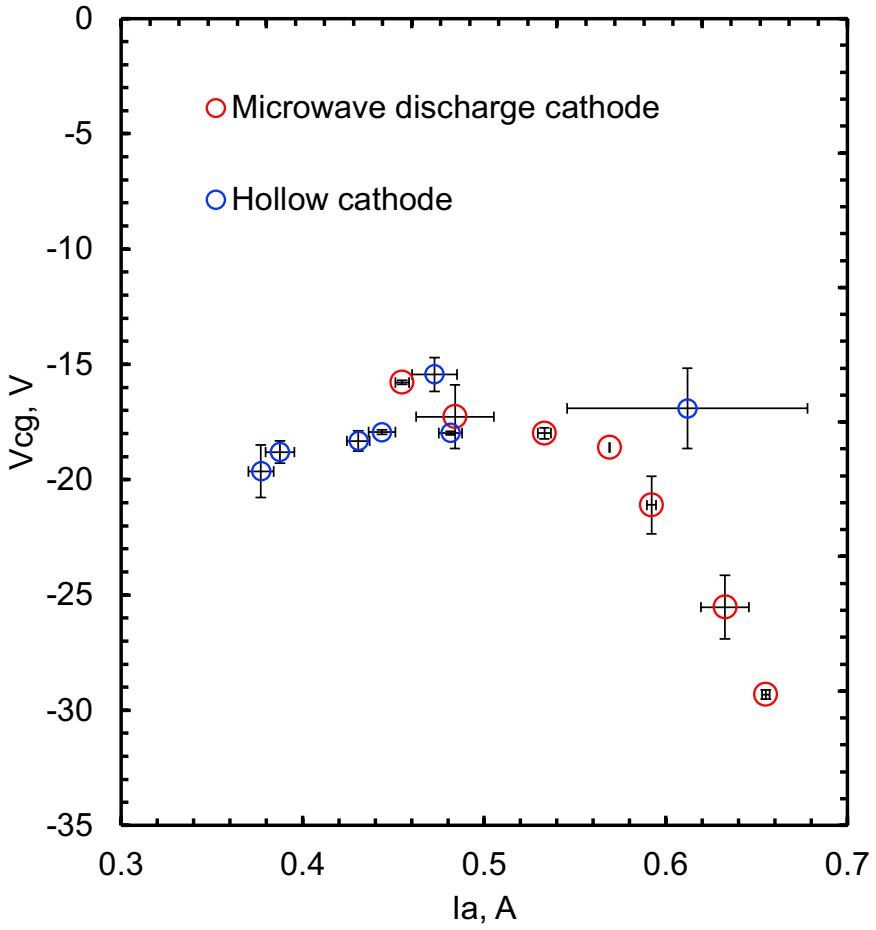

Figure 2.18: Comparison of I–V characteristics of microwave discharge cathode and hollow cathode.

2.2.6 Summary

In order to increase the electron current, the mirror ratio and magnetic field intensity were increased. In addition, to evaluate whether the improved microwave discharge cathode is a viable alternative, the I–V characteristics are compared with those for a hollow cathode in coupling operation. The results can be summarized as follows:

1. By increasing the magnet field intensity and mirror ratio from 2.0 to 8.3 for the microwave discharge cathode, the electron current increased from 300 mA to 560 mA when the anode voltage was 37 V.
2. It was found that in coupling operation, the microwave discharge cathode can supply a higher electron current than in diode mode. The anode voltage was 22 V when the anode current was 600 mA. This is thought to be due to the effects of neutral particles, plumes, and magnetic fields supplied by the Hall thruster.
3. Since V_{cg} rapidly drops above 600 mA in the microwave discharge cathode, it was found that the performance trade-off point between the two cathodes is about 600 mA.

Chapter 3

Plasma Diagnostics Inside and Outside a Microwave Discharge Cathode

Chapter 3 is partially reproduced from published article[45], with the permission of AIP Publishing.

3.1 Principle of laser-induced fluorescence spectroscopy

Laser-Induced Fluorescence Spectroscopy, LIF is an optical measurement method based on the resonant absorption of laser radiation by particles such as atoms and molecules. The particles spontaneously emit photons due to de-excitation in the transition probability time (on the order of nanoseconds). This fluorescence is isotropically radiated from the particles and can thus be measured from any direction. The absorption frequency depends on the particle velocity in the direction of the laser beam due to the Doppler effect. The frequency shift $\Delta\nu$ is calculated using Eq. 3.1.

$$\frac{\Delta\nu}{\Delta\nu_0} = -\frac{\boldsymbol{\nu}}{c} \cdot \frac{\mathbf{k}}{|\mathbf{k}|} \tag{3.1}$$

Here, $\boldsymbol{\nu}$ is the particle velocity vector and $\mathbf{k}$ is the photon wave vector. The target particle velocity distribution function along the laser direction is obtained by varying the laser frequency. In this study, a two-level energy model is considered as shown in Figure 3.1.[46] The mathematical relationship between fluorescence intensity S and particle density N is described by Eq. 3.2.

$$S = \frac{A_{21}B_{12}I_{\mathrm{ex}}}{c(A_{21}+Q)+2B_{12}I_{\mathrm{ex}}}\frac{\Omega}{4\pi}N \tag{3.2}$$

Here, the quenching Q by ion - atom collision is negligible. In this study, ion velocity v is up

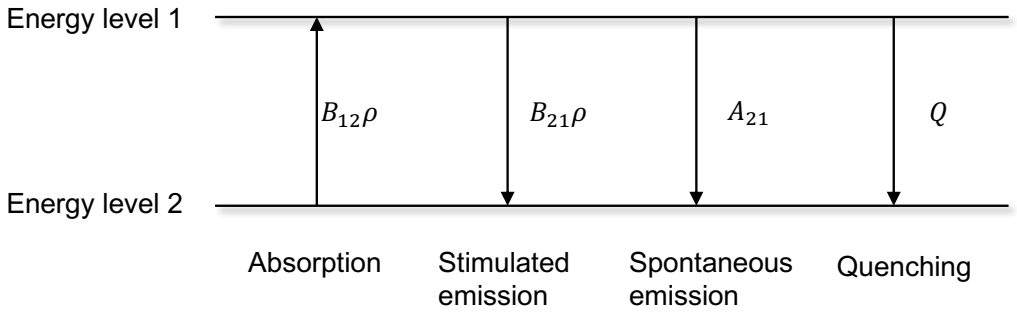

Figure 3.1: Two level model for laser absorption and line emission.

to 5 km/s, neutral density n_{n} is up to $10^{21}\mathrm{m}^{-3}$[46], and cross section σ is $10^{-19}\mathrm{m}^2$. Therefore, quenching frequency $\nu_{\mathrm{q}} = n_{\mathrm{n}}\sigma v \sim 10^5\mathrm{s}^-1$. This is much lower than the spontaneous de-excitation rate ($A_{21} > 10^7\mathrm{s}^-1$).[47] In this study, the laser intensity I_{ex} is constant in the sweep range and other coefficients are independent of N and n_{n}. Therefore, the N is proportional to S.

In previous research, LIF spectroscopy was applied to study plasma sources such as Hall thrusters, [48][49][50][51][52][53] hollow cathodes,[54][55][32] and ion thrusters.[56][57][58] In the present study, the time averaged LIF measurement of the Xe II $(^3P_2)5d[4]_{7/2} \rightarrow (^3P_2)6p[3]^0_{5/2}$ transition at 834.7 nm is conducted in the plume region and inside the microwave discharge cathode with an optical window. Figure 3.2 shows the partial Grotrian diagram of Xe II.

Here, the evaluation of line broadening is discussed. The beam is σ-polarized (π-polarized) when the laser beam is perpendicular (parallel) to the magnetic field due to the Zeeman effect. In the $(^3P_2)5d[4]_{7/2} \rightarrow (^3P_2)6p[3]_{5/2}$ transition, π-polarized splitting effects are negligible whereas σ-polarized splitting effects are not.[59] For the axial IVDF measurements in this study, the magnetic field component perpendicular to the laser beam is up to 0.01 T, the Zeeman splitting is $\sim$ 200 MHz, and is 3-10% of the typical full width at half maximum (FWHM) of 2 - 7 GHz. For the radial IVDF measurements, the magnetic field is up to 0.02 T, and the Zeeman splitting is 6-20% of the typical FWHM. To evaluate saturation broadening, a saturation study is conducted. As shown in Figure 3.3, an operating regime of laser power is between the saturation and weak pumping In order to evaluate the broadening, a two-level energy model is used, following previous studies.[60] [61] [62] [63] For a Gaussian line shape corresponding to the typical FWHM in this study, the saturation broadening is estimated to cause an overestimation of the FWHM of 5-20 %. Natural broadening is 17 MHz and the laser line width is up to $\sim$ 500 kHz; these values are negligible.[64] Stark broadening is neglected because its effects are only apparent at high heavy particle density and electron density.[65][66]

For example, Stark broadening for the 541.9 nm transition is $\sim$ 20 MHz for an electron density of $10^{19}\mathrm{m}^{-3}$, which is the maximum electron density in the microwave discharge cathode.[46][67] Xenon gas has 9 stable isotopes.[68] It is thus difficult to calculate the isotopic splitting for complicated atoms such as xenon. Therefore, it was measured experimentally. The hyperfine splitting constants are not fully known for the $(^3P_2)5d[4]_{7/2} \rightarrow (^3P_2)6p[3]_{5/2}$ transition, and were thus estimated experimentally. In previous research, the calculation model was deconvolved out of the LIF signal with known parameters of hyperfine and isotopic splitting.[67] However, the $(^3P_2)5d[4]_{7/2} \rightarrow (^3P_2)6p[3]_{5/2}$ transition is not fully deconvolved.[66] In previous research, even for a narrow FWHM of 1 GHz, the broadening was within 10%, which is negligible for the wider IVDF obtained under the typical conditions of the present study.[65][66]

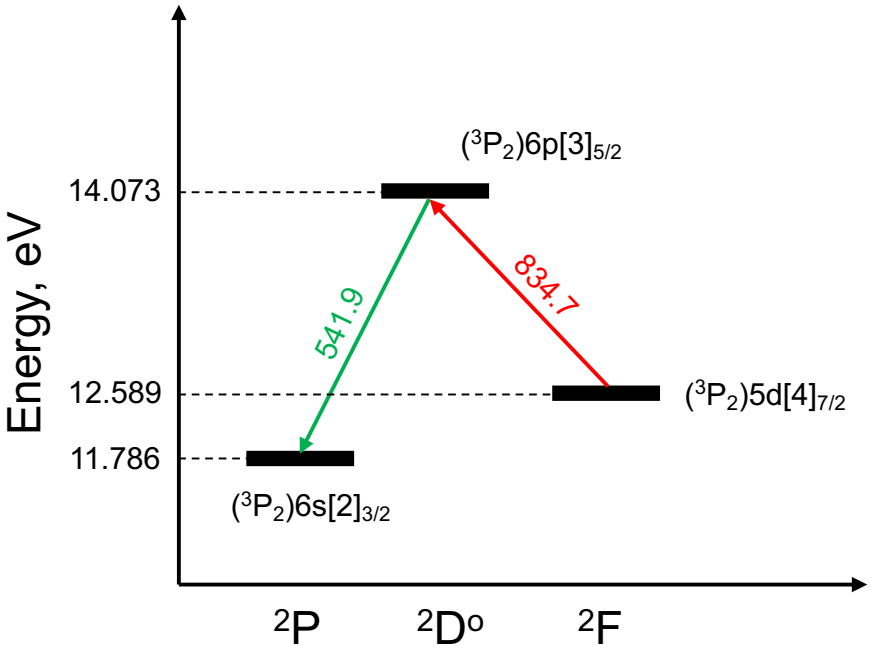

Figure 3.2: Partial Grotrian diagram of Xe II.

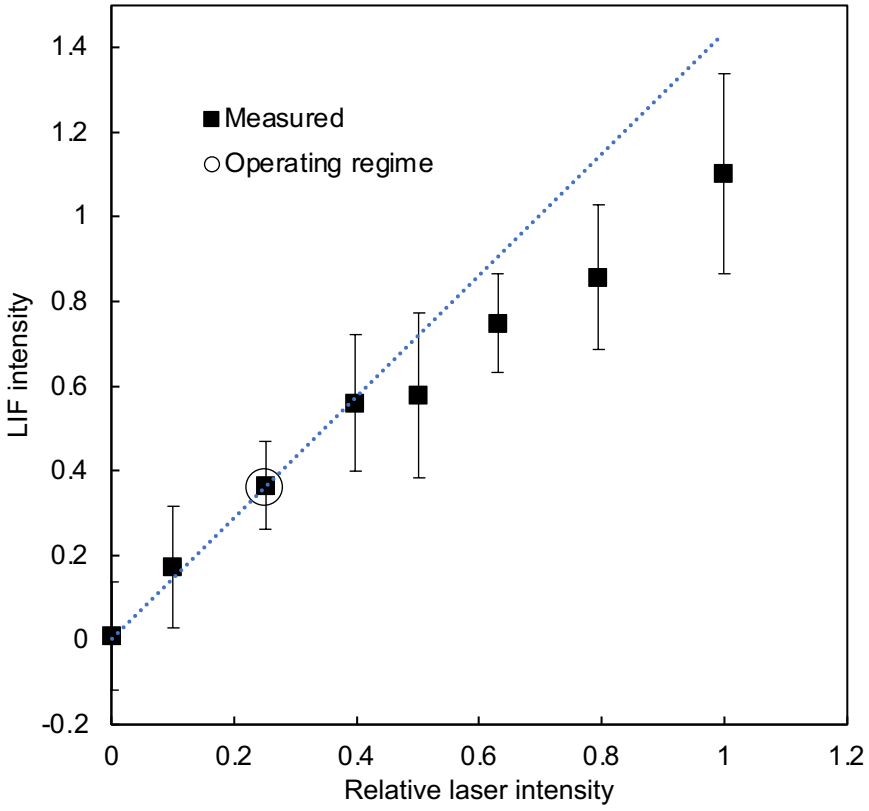

Figure 3.3: Effect of laser saturation on LIF intensity.

3.2 Experimental setup for LIF measurements

Figure 3.4 shows the experimental setup for LIF spectroscopy. The photograph of the setup is shown in Figure 3.5. The laser beam was emitted by a continuous wave diode laser "TOPTICA Photonics DL100" and amplified to the specified power. The laser beam was chopped at 6 kHz and input to the vacuum chamber via fiber coupling. In the vacuum chamber, the microwave discharge cathode was operated in diode mode. In the LIF measurements, a laser beam with a diameter of ϕ1.8 mm was input through an anode to the interior of a viewable microwave discharge cathode. As shown in Figure 3.6, the signal collection diameter was also ϕ1.8 mm. Therefore, the collection volume V_{signal} can be calculated using Eq. 3.3.

$$V_{\mathrm{signal}} = \frac{16}{3}a^3 \tag{3.3}$$

Here, $a = 0.9$ mm in this setup. The laser power was set to 40 mW at the measurement point. The microwave discharge cathode was installed on a two-axis stage, which allowed the two-dimensional distribution to be measured. For the radial direction measurement, the microwave discharge cathode was rotated 90° with respect to the Y axis and the laser beam was input between the anode and the cathode. LIF was detected by a photomultiplier tube (PMT) "Hamamatsu Photonics K.K. H11462-031". The signal was amplified by a lock-in amplifier. To measure the Doppler shift, we compared the results to those for a xenon reference cell.

In this LIF setup, the signal-to-noise ratio (SNR) had to be improved because of the small size of the microwave discharge cathode. In addition, a relatively high spatial resolution is required to measure the plasma distribution inside the cathode. Therefore, the signal collection system required a small V_{signal} and a sufficient SNR. Due to the redesign of the focal length, V_{signal} decreased. The main problem was the input efficiency at the fiber coupling. Therefore, a 6-axis alignment coupler was constructed and the lens was redesigned to minimize chromatic aberration to increase the input laser power and fluorescence. The spatial resolution was improved five-fold and the coupling efficiency was doubled compared to those of the original setup.[56][57] As described above, the laser saturation effected the FWHM of the IVDFs. However, due to the doubled laser power, the FWHM was up to 2% larger than that for the previous setup. Therefore, the improved setup was used because of its high SNR despite the small saturation effect.

The experimental conditions are shown in the Table 3.1. The parameters are microwave power P_{m}, xenon flow rate $\dot{m}_{\mathrm{c}}$, anode current I_{a} and type of microwave antenna. Figure 3.7 shows the measurement points for the axial and radial direction. For the radial direction measurement, for sufficient SNR, the parameters of PMT and lock-in amplifier were changed. The

results of this measurement were therefore examined only in terms of the velocity. Although it was difficult to measure the inside of the microwave discharge cathode with sufficiently high SNR and spatial resolution, the axial direction measurement was successful.

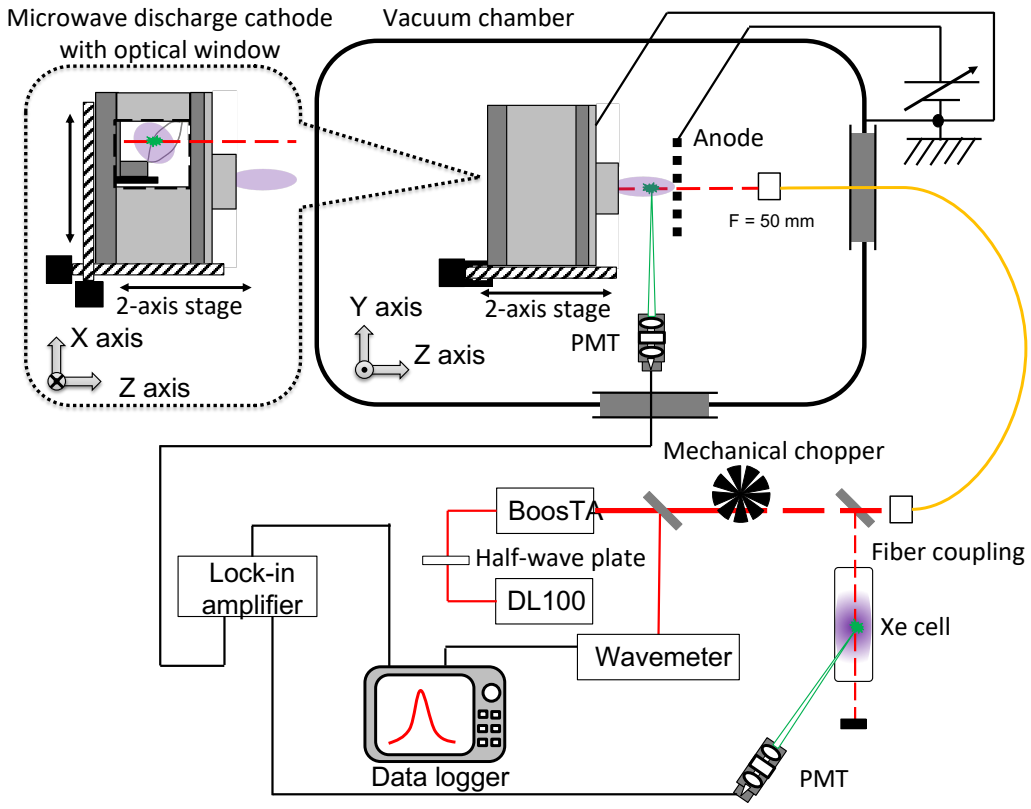

Figure 3.4: Schematic diagram of microwave discharge cathode measurement setup for axial LIF spectroscopy. For the radial measurement, the microwave discharge cathode was rotated 90° with respect to the Y axis.

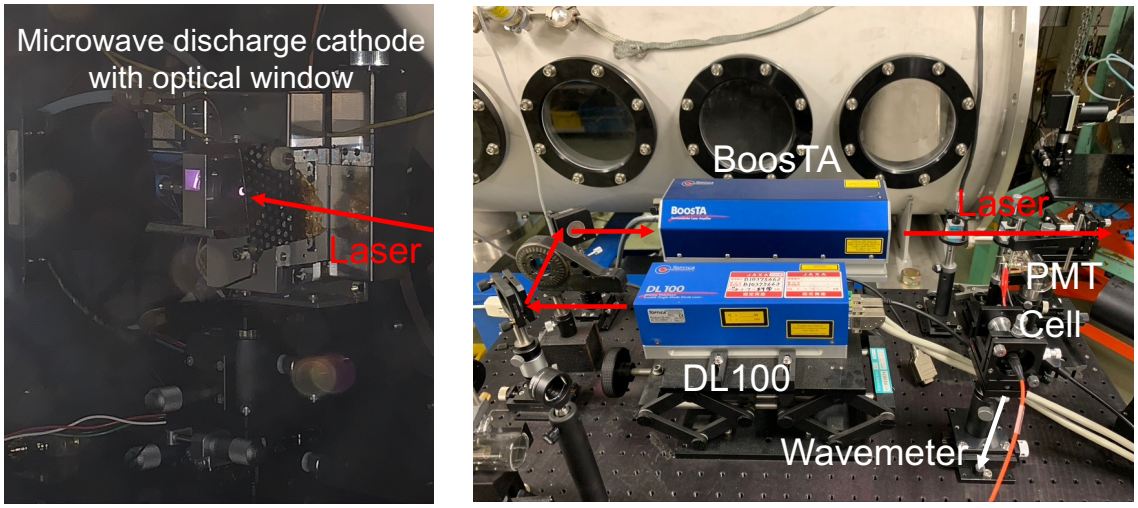

Figure 3.5: Photograph of microwave discharge cathode measurement setup for axial LIF spectroscopy.

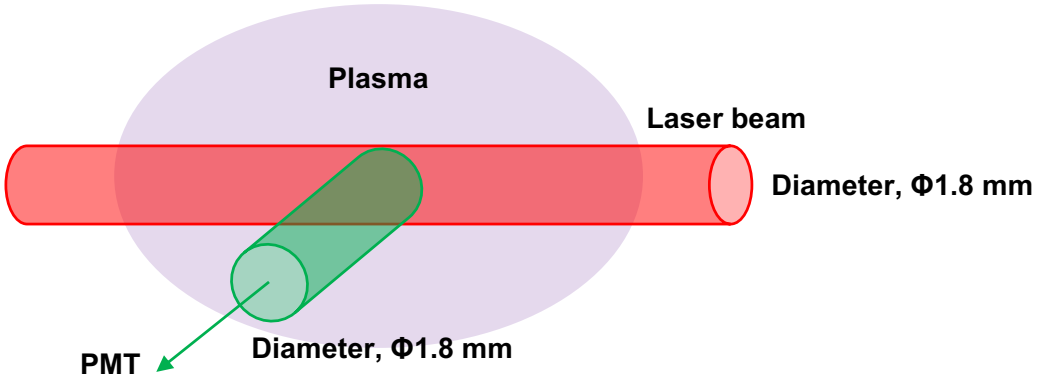

Figure 3.6: Schematic diagram of measurement point.

Table 3.1: Experimental conditions of the microwave discharge cathode for LIF measurements.

Parameter	Value
Microwave frequency	4.25 GHz
Microwave power, P_{m}	6 W, 8 W, 10 W
Xenon flow rate, $\dot{m}_{\mathrm{c}}$	0.5 sccm, 0.7 sccm, 0.9 sccm (0.049 mg/s, 0.069 mg/s, 0.088 mg/s)
Anode current, I_{a}	0 mA, 135 mA, 180 mA, 220 mA in constant-current mode
Microwave antenna	Flight model (Hayabusa2) Black antenna to suppress laser refrection
Background pressure	9×10^{-5} Pa without Xe 7×10^{-4} Pa at 1-sccm Xe
Nominal conditions	$P_{\mathrm{m}} = 8$ W, $\dot{m}_{\mathrm{c}} = 0.7$ sccm, $I_{\mathrm{a}} = 180$ mA, flight model antenna

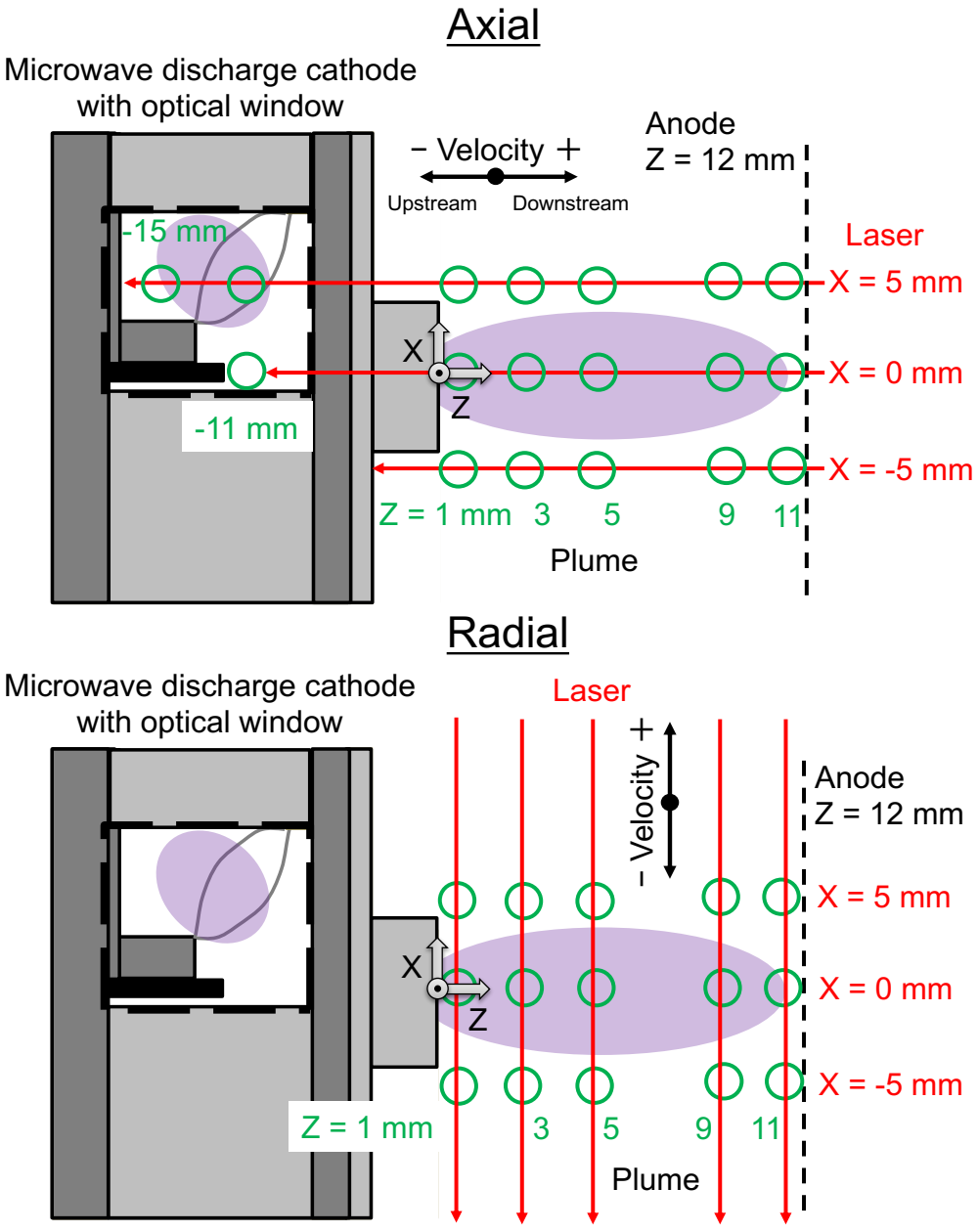

Figure 3.7: Measurement points of LIF spectroscopy.

3.2.1 Diode Laser

In the study, an external cavity diode laser (TOPTICA DL100) was used for LIF measurements, as shown in Figure 3.8. Compared with conventional lasers, such as a CO_2 laser or a dye laser, the cavity diode laser has a lower cost, a wider wavelength range, and is easier to handle. As shown in Figure 3.9, a temperature and current controller was used for the laser head.

Figure 3.8: Diode laser.

Figure 3.9: Controller for diode laser.

3.2.2 Optical amplifier

To obtain sufficient laser power, the laser beam emitted from the diode laser was amplified by an optical amplifier (TOPTICA BoosTA), as shown in Figure 3.10. In this study, the laser power was amplified from 30 mW to 500 mW by the optical amplifier.

Figure 3.10: Optical amplifier.

3.2.3 Wavelength meter

Figure 3.11 shows the wavelength meter (ADVANTEST TQ8325) used for LIF measurements of Xe II at 834.954 ±0.050 nm. It offers high resolution and accuracy, and a repeatability of less than 1 pm, although it requires high power for measurements.

Figure 3.11: Wavelength meter TQ8325 for 600–1,600 nm.

3.2.4 Lock-in amplifier

Figure 3.12 shows the lock-in amplifier (AMETEK 7270). Figure 3.13 shows the mechanical chopper (THORLABS MC1F60). A lock-in amplifier measures the amplitude and phase of a target signal by comparing with a reference signal. This technique is called phase sensitive detection (PSD). The lock-in amplifier increases the SNR of a target signal by averaging the signal over time. In this study, the reference signal was generated by a mechanical chopper at 6.0 kHz. Two lock-in amplifiers were used for the cathode plasma and reference cell.

3.2.5 Signal detection system

Figure 3.14 shows a photograph of the signal detection system, and Figure 3.15 shows its schematic diagram. The LIF signal passed through two lenses and a band-pass filter (THORLAB FL543.5 10 CWL=543.5). The band-pass filter passed wavelengths of 543.5 ±2 nm. The filtered signal was detected by a photomultiplier tube (HAMAMATSU H11462-031).

Figure 3.12: Lock-in amplifier.

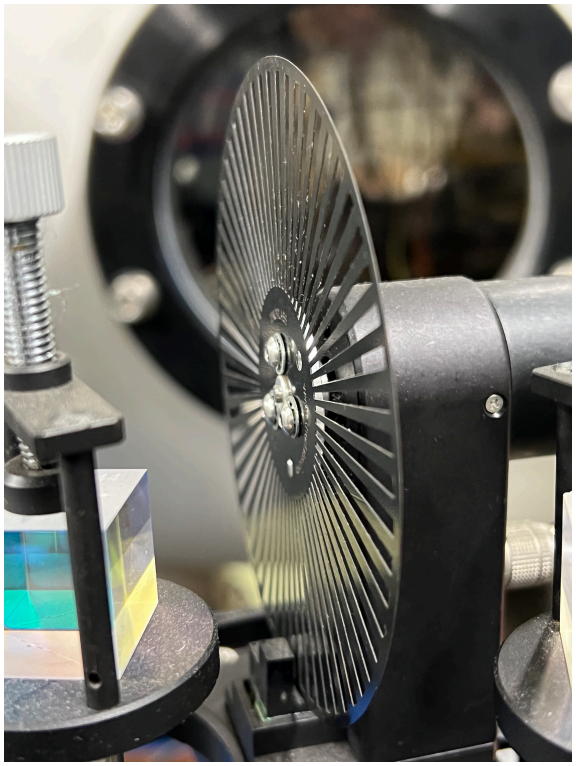

Figure 3.13: Mechanical chopper.

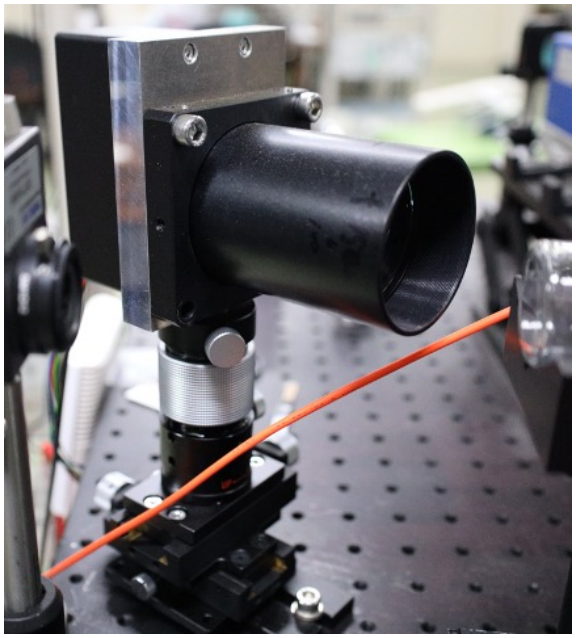

Figure 3.14: Photograph of signal detection system.

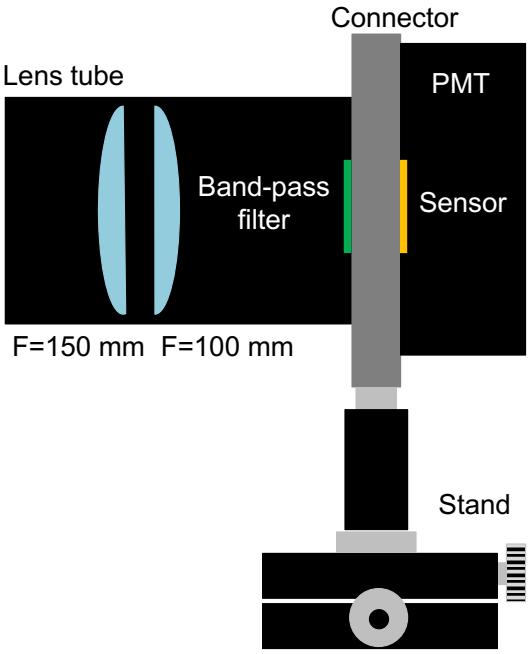

Figure 3.15: Schematic diagram of signal detection system.

3.2.6 Other optics

Figure 3.16 shows the DC discharge reference cell for 1-Torr xenon. Figure 3.17 shows a fiber coupl. The laser beam was focused by a near-infrared (NIR) objective lens (SIGMAKOKI PAL-20-NIR-HR-LC00).

3.2.7 Effect of angle between reference cell and laser in velocity measurements

The LIF signal was measured by varying the laser frequency as shown in Figure 3.18. As described above, a reference cell was used to determine the zero value in the velocity measurements. The velocity error when the angle of the reference cell was changed was evaluated. In the LIF measurements, the angle between the reference cell and the laser beam was 0°, so that the beam passed through the electrodes on the central axis of the reference cell. The LIF signal was measured when the angle was changed to 30° to compare the velocity measurements under the same conditions. Figure 3.19 shows a comparison of the LIF signal when the angle between the reference cell and laser was changed. The LIF signals were measured at X = 0 mm, Z = 1 mm in the plume and in the reference cell. The velocity difference is within 30 m/s. This is smaller than the value of 50–100 m/s for the standard error in the LIF measurements.

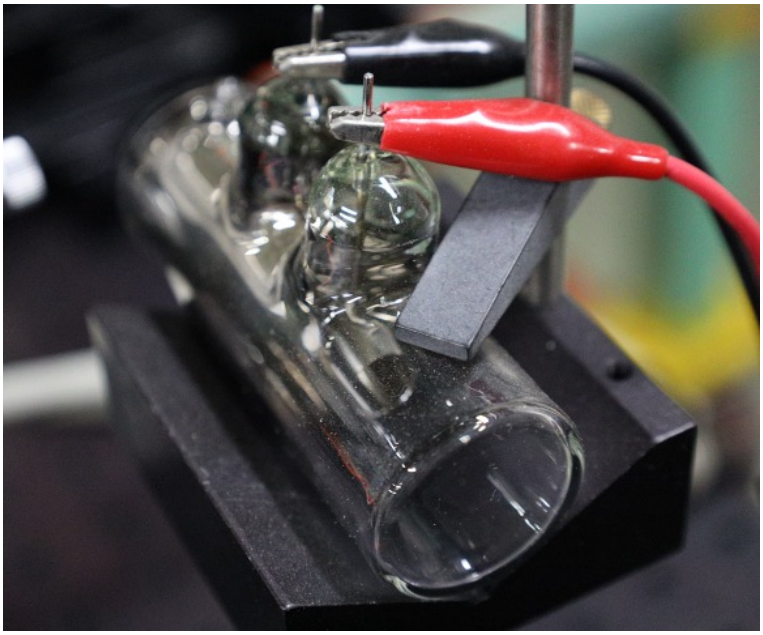

Figure 3.16: DC discharge reference cell for xenon.

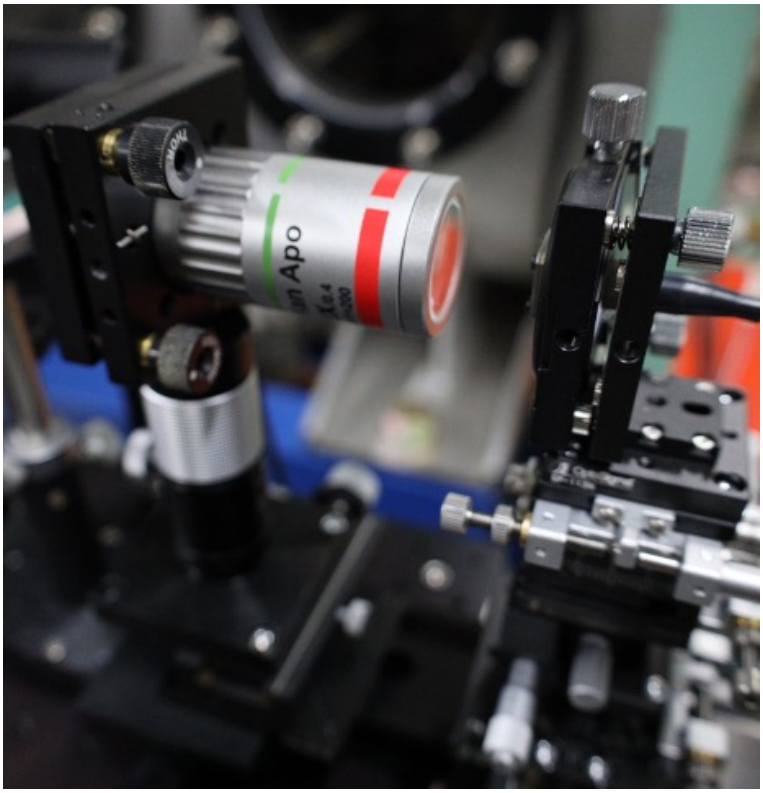

Figure 3.17: Fiber coupler.

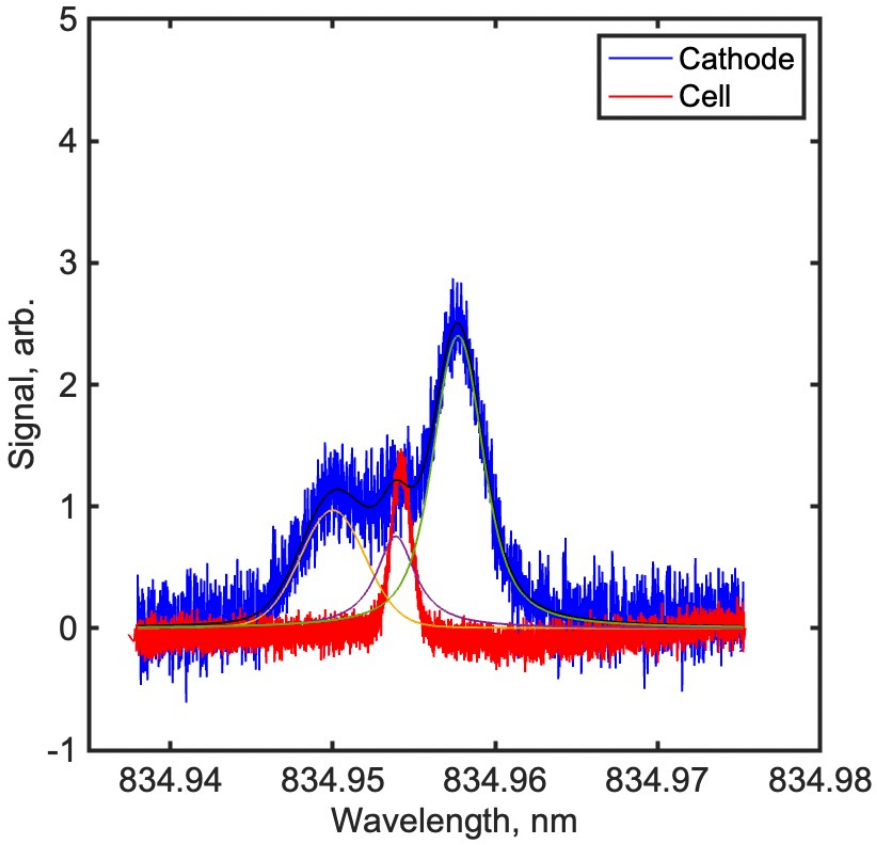

Figure 3.18: Example of axial LIF signal varying the laser frequency at X = 0 mm, Z = -11 mm.

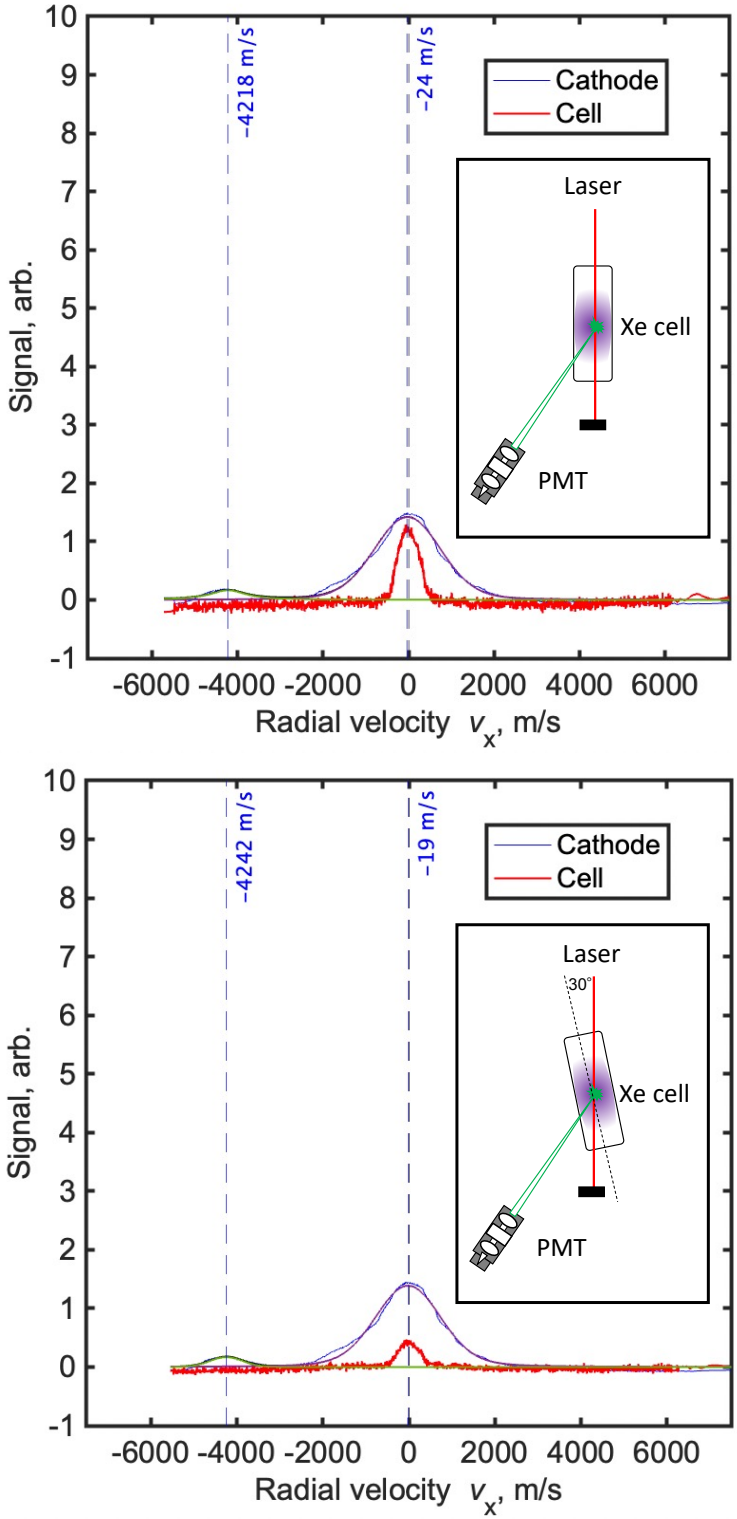

Figure 3.19: Comparison of LIF signals when the angle between the reference cell and laser was changed.

3.3 Microwave discharge cathode with optical window

It is difficult to measure plasma parameters inside a cathode without affecting its performance. Because optical windows are insulators, they interfere with the absorption of ions, which are the counterparts of the emitted electrons. Optical windows thus degrade cathode performance. To investigate the actual conditions of the Hayabusa2 onboard cathode, we needed to develop a viewable microwave discharge cathode with an optical window that has I–V characteristics equivalent to those of the flight model. As described in section 1.6.2, it is difficult in general to view the inside while maintaining the I–V characteristics. Therefore, in this study, the design requirements were as follows:

1. The I–V characteristics of the developed cathode are equivalent to those of the flight model.
2. Minimize changes in the shape of the discharge chamber.
3. Allow observations near the antenna, nozzle, and the mirror magnetic field.

To allow the microwave discharge cathode to be visually monitored, we replaced part of the side wall with a SiO_2 plate, as shown in Figures 3.20 and 3.21. The magnet was moved in the circumferential direction, but the total magnetic flux was guaranteed to be the same as the nominal. The magnetic circuit supported circumferential uniformity of the magnetic field. In addition, the orifice nozzle was partially visible through the SiO_2 plate to allow introduction of a laser beam. To suppress the disturbance caused by the SiO_2 wall, the SiO_2 wall area was set to be as small as possible. The entire discharge chamber could be observed by rotating the antenna, gas port, and nozzle. Figure 3.22 shows a photograph of the microwave discharge cathode in diode mode operation. As shown, a high-density plasma was distributed along the central axis. This microwave discharge cathode can be used to continuously measure the plume region and the interior of the cathode.

Figure 3.23 compares the I–V characteristics of the microwave discharge cathode with an optical window and the Hayabusa2 flight model in diode mode operation for various values of microwave power P_{m}. Under the nominal conditions for Hayabusa2, the electron current was 180 mA and $P_{\mathrm{m}} = 8$ W. As shown in the figure, the performance of the developed microwave discharge cathode was very similar to that of the flight model under Hayabusa2 conditions (anode voltage error within 2%). Under other conditions, the anode voltage error was at most 7%. LIF spectroscopy experiments were thus conducted on the developed cathode.

Figure 3.24 shows the anode voltage difference in the duration test of the developed cathode. In the LIF measurements, it took up to 12 hours to measure the two-dimensional map of the IVDF. As shown in the figure, it was confirmed that the anode difference is not significant in

a period of 12 hours.

To evaluate the reproducibility of the LIF signal, the LIF signals were measured under the same conditions at the start and end of the experiments. The time interval was 8 hours. Figure 3.25 shows a comparison of the LIF signals measured before and after the experiments. The two signals closely match ($R^2 = 0.97$). The intensity difference is 3%. The result suggests that the condition of the optical window was maintained during the experiment.

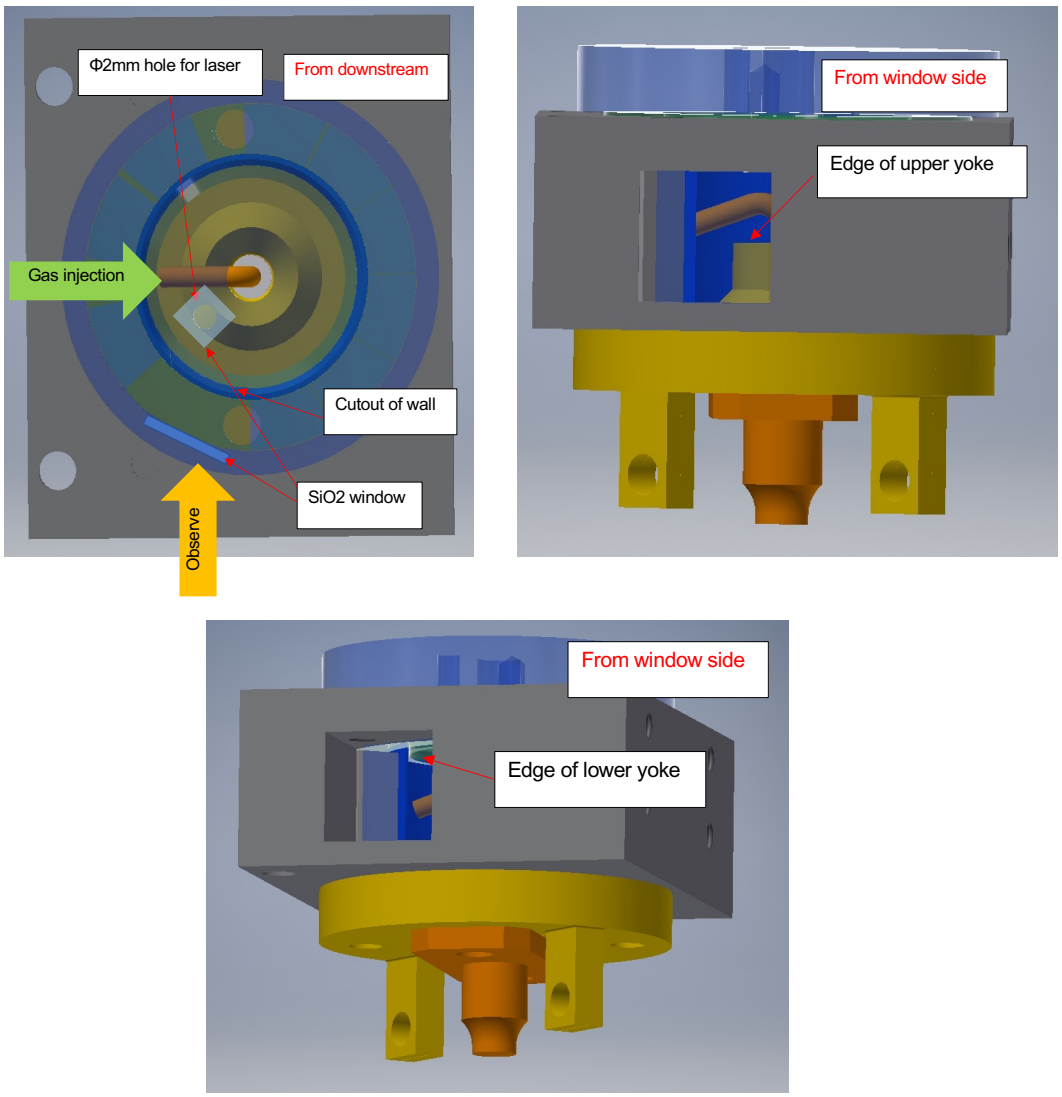

Figure 3.20: Design of the microwave discharge cathode with an optical window.

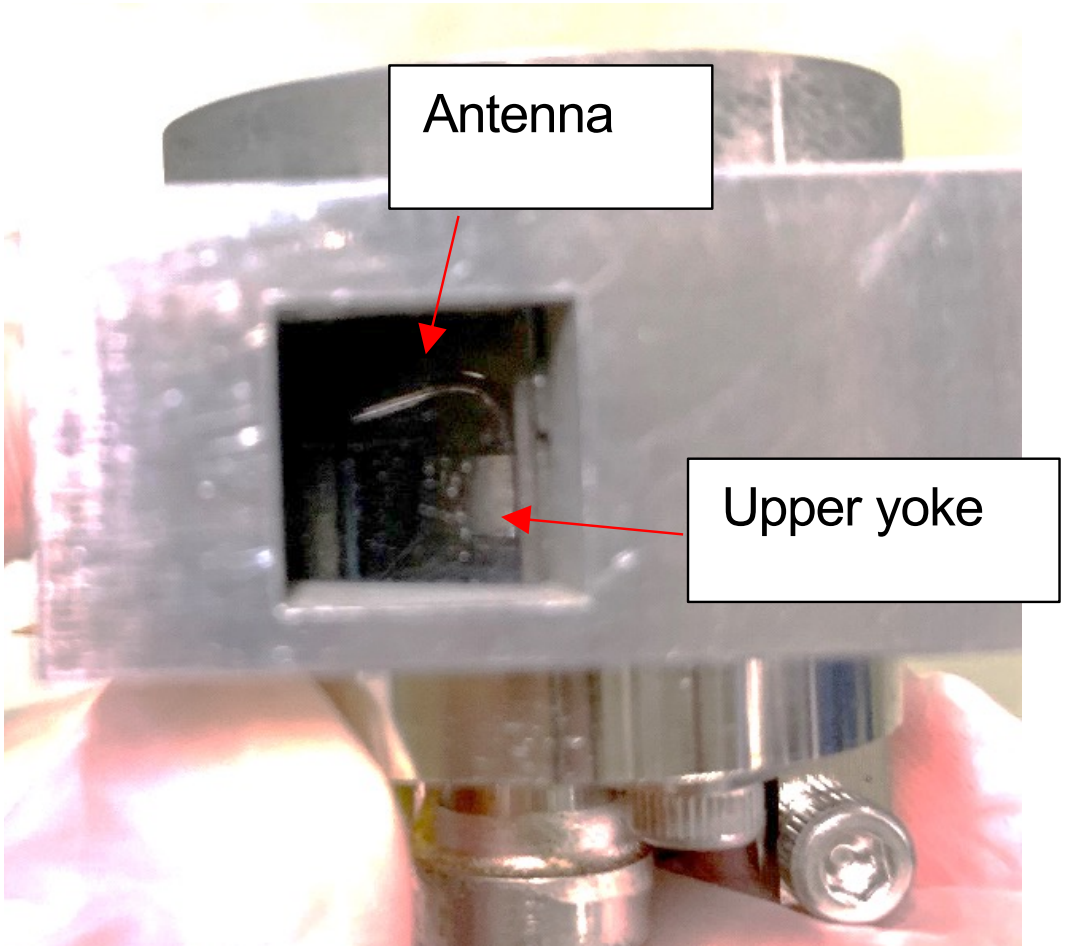

Figure 3.21: Photograph of the microwave discharge cathode with an optical window.

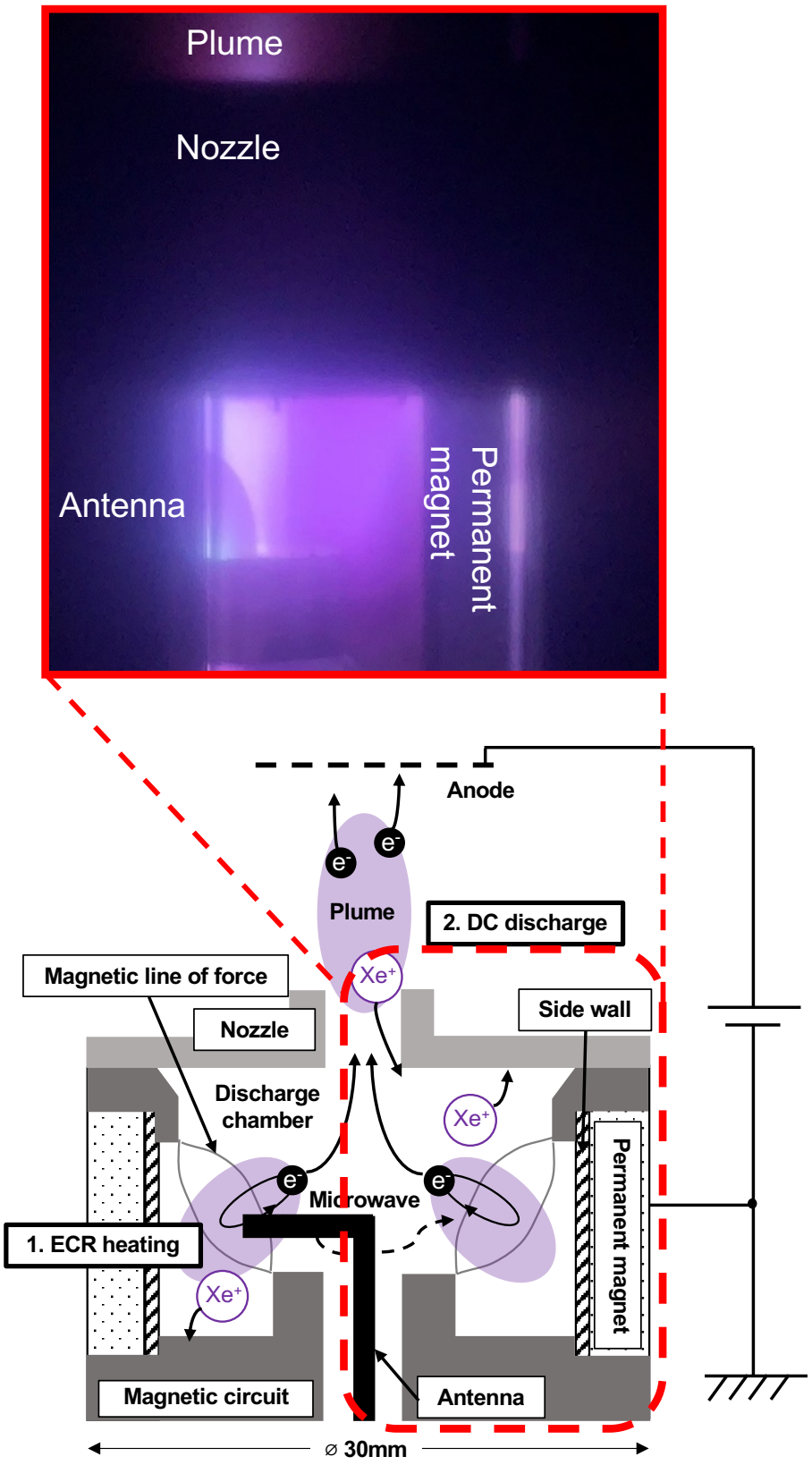

Figure 3.22: Photograph of the microwave discharge cathode with an optical window in diode mode operation.

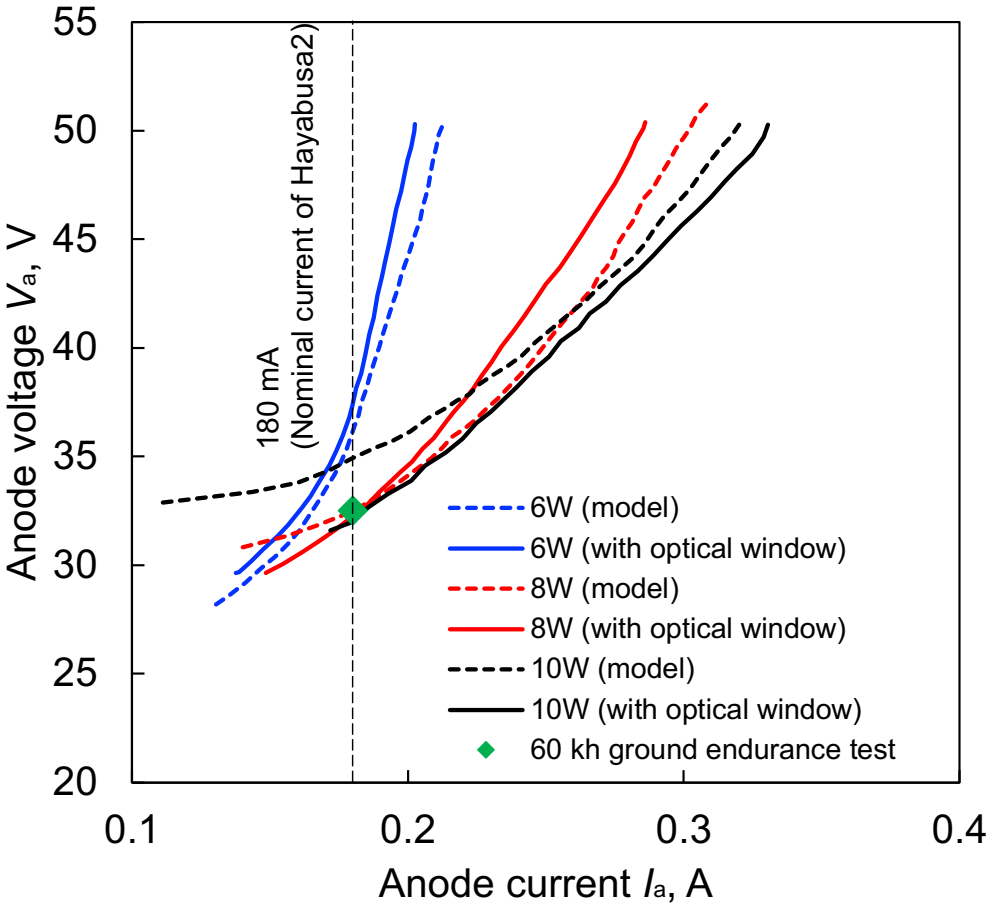

Figure 3.23: Comparison of I–V characteristics between the microwave discharge cathode with an optical window and the Hayabusa2 flight model for various values of microwave power P_{m} (6, 8, and 10 W) at $\dot{m}_{\mathrm{c}} = 0.7$ sccm. 8 W (red) is the nominal microwave power for Hayabusa2. 60,000 hours ground endurance test model is also compared (green).

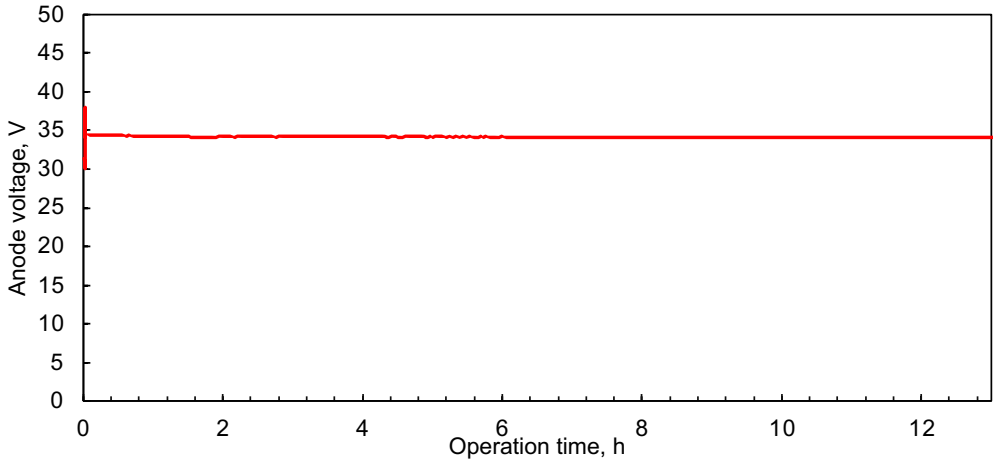

Figure 3.24: Duration test of the developed cathode at $P_{\mathrm{m}} = 8$ W, $\dot{m}_{\mathrm{c}} = 0.7$ sccm, I_{a} =180 mA.

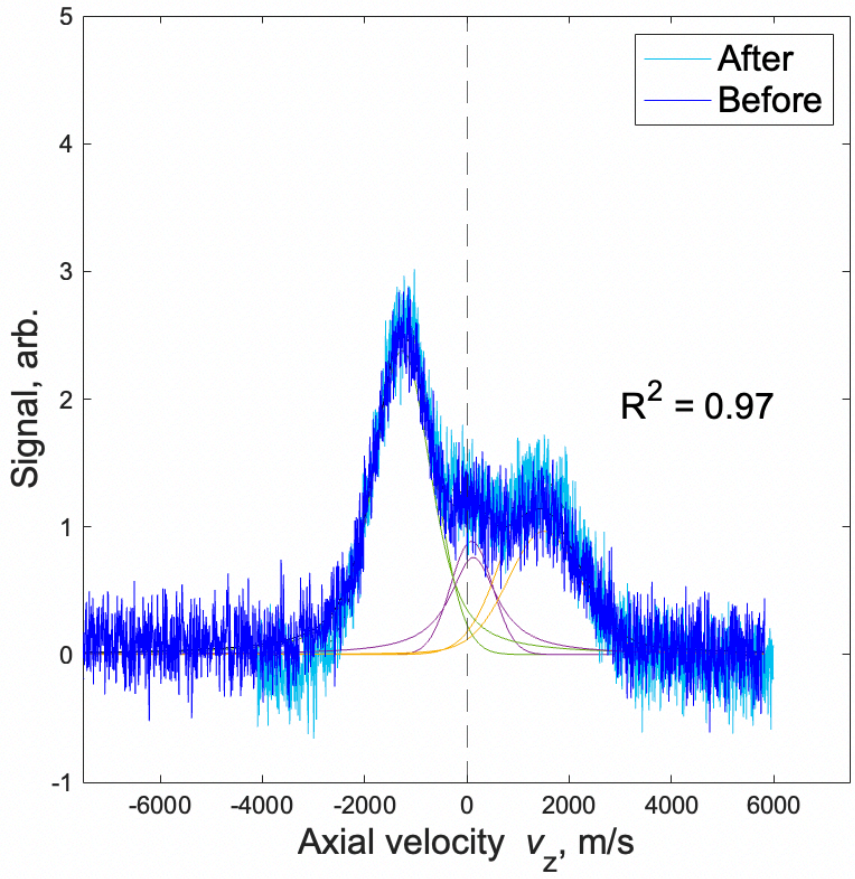

Figure 3.25: Comparison of LIF signals measured before and after the experiment.

3.3.1 Optical observation

Figure 3.26 shows a photograph of the optical observation near the antenna. Figure 3.27 shows the results of a static magnetic field analysis inside the discharge chamber by Finite Element Method Magnetic. High intensity emission was distributed in the magnetic mirror magnetic field near the root of the antenna and the edge of the yoke. Ions were generated by high energy electron collisions with neutrals in the mirror magnetic field. In addition, high intensity was confirmed in the mirror magnetic field in the direction in which the antenna was facing. A boundary line was observed in the area, considered to be the ECR region based on static magnetic field analysis.

Figure 3.28 shows a comparison between the cases of $I_{\mathrm{a}} = 180$ mA and 0 mA for nominal conditions. In the case of $I_{\mathrm{a}} = 0$ mA, the intensity was weak in the discharge chamber and plasma was reddish purple, which is characteristic of a low electron temperature.

Figure 3.29 shows the optical observation of the internal plasma with the antenna facing the optical window for nominal conditions. Similar to Figure 3.22, high-density plasma was distributed along the central axis. A high intensity region was observed especially at the bent inner root of the antenna and at the edge of the mirror magnetic field.

Figure 3.30 shows burning ceramic near the root of the antenna for high microwave power conditions ($I_{\mathrm{a}} = 180$ mA, $\dot{m}_{\mathrm{c}} = 0.7$ sccm, and $P_{\mathrm{m}} = 25$ W). When $P_{\mathrm{m}} = 25$ W, the ceramic antenna cap glowed red. After this operation, the antenna cap was partially sublimated. These result suggest that $P_{\mathrm{m}} = 20$ W is the maximum power that can be operated stably in the coupling operation, although the flow rate was different.

Figures 3.31 and 3.32 show comparisons of the discharge chamber plasma for various values of the parameters P_{m}, $\dot{m}_{\mathrm{c}}$, and I_{a}, for the nominal and improved models, respectively. The improved model had a high mirror ratio yoke and a nominal magnetic intensity. The magnetic intensity was nominal because the number of magnets was not increased to observe the internal plasma. The details are described in Section 2.2. A larger P_{m} led to a higher intensity in both cathodes. In addition, a larger I_{a} led to a higher intensity in the mirror magnetic field in both cathodes. In the case of the improved cathode, the high intensity region was closer to the nozzle compared to the nominal model in all conditions. At $P_{\mathrm{m}} = 15$ W, $\dot{m}_{\mathrm{c}} = 1.5$ sccm, $I_{\mathrm{a}} = 300$ mA, it was confirmed that dense plasma distributes near both edges of the mirror field in both models. Figures 3.33 and 3.34 compare histograms of Figures 3.31 and 3.32, respectively, for various parameters. These histograms were calculated in same area to compare with both models. As shown in Figures 3.33 and 3.34, there were two populations. The lower luminance population was from the antenna. The higher luminance population was from the red-purple region and pale region. The high mirror ratio yoke model had up to 22% higher luminance in higher luminance population.

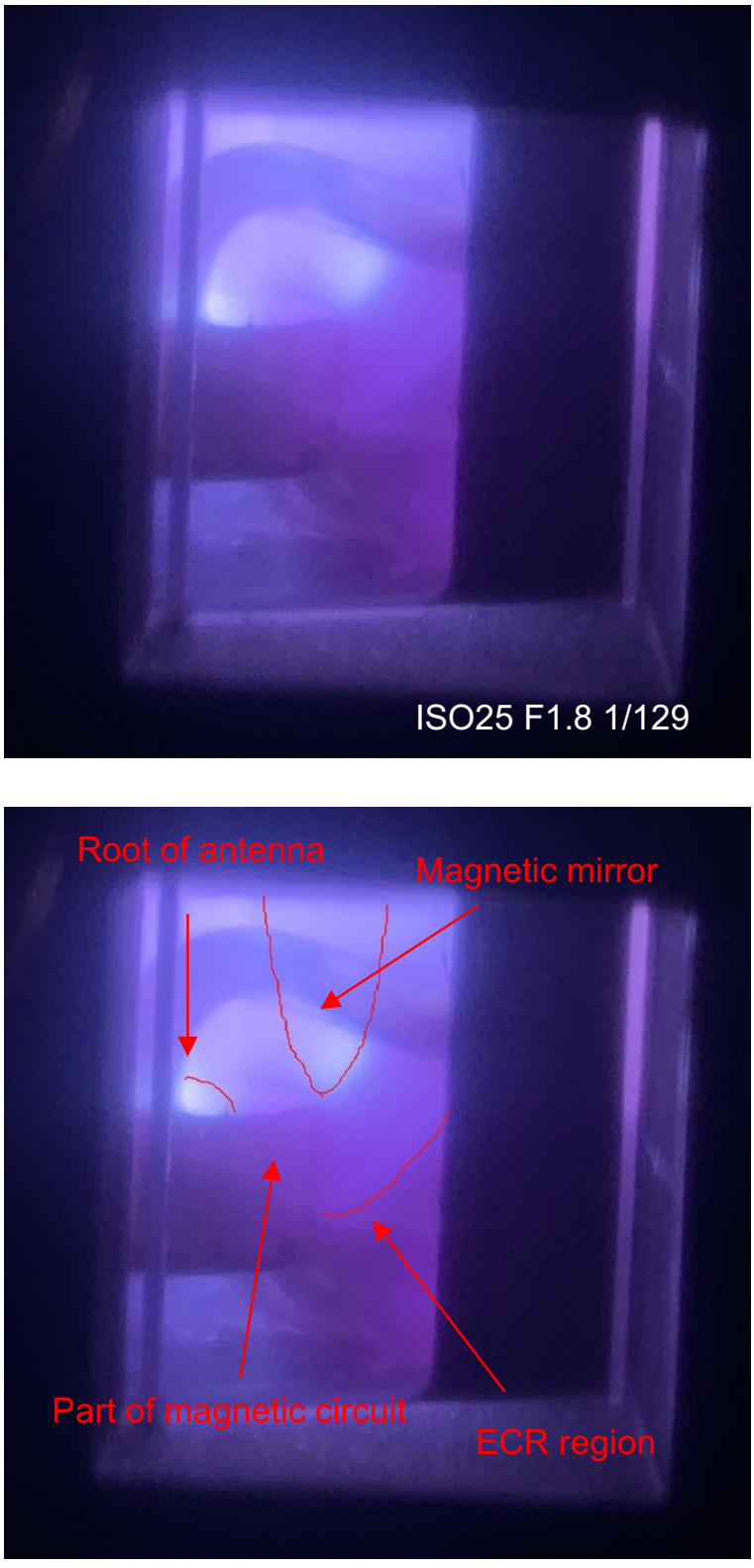

Figure 3.26: Photograph of optical observation near the antenna.

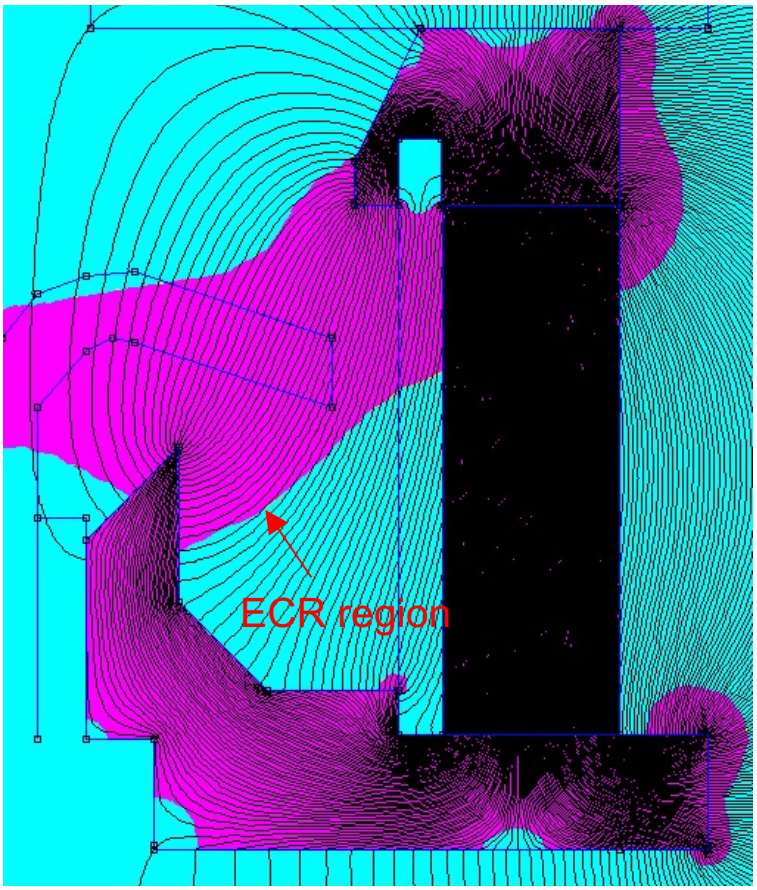

Figure 3.27: Static magnetic field analysis inside the discharge chamber by Finite Element Method Magnetics.

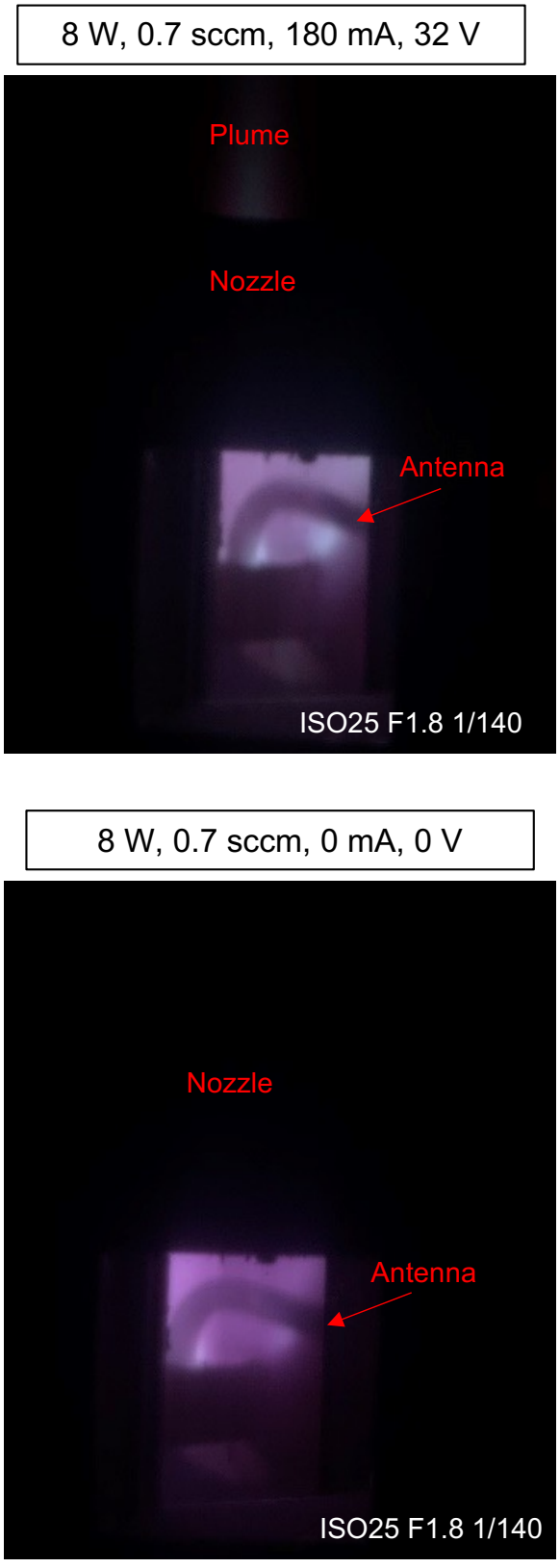

Figure 3.28: Comparison between the cases of $I_a = 180$ mA and 0 mA for nominal conditions.

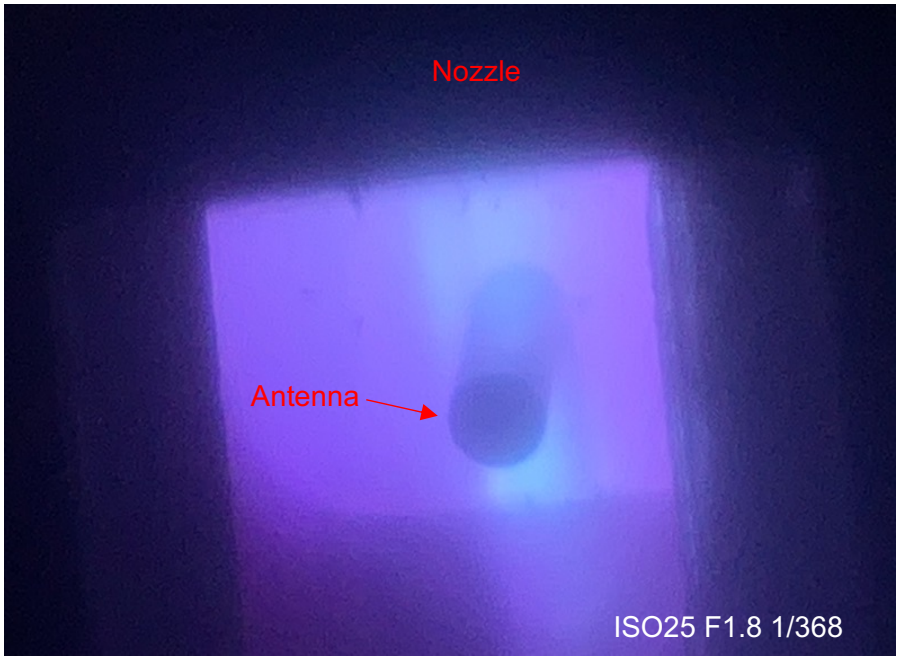

Figure 3.29: Optical observation of internal plasma with the antenna facing the optical window for the nominal conditions.

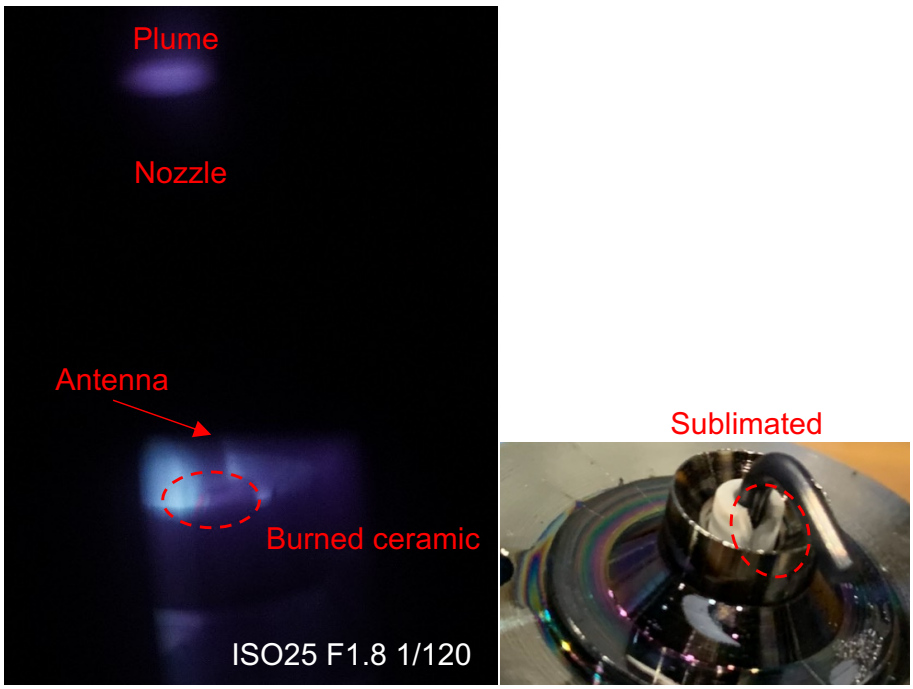

Figure 3.30: Burning ceramic near the root of the antenna at $I_a = 180$ mA, $\dot{m}_c = 0.7$ sccm, and $P_m = 25$ W.

(a) Nominal, 180 mA, 0.7 sccm, 8 W

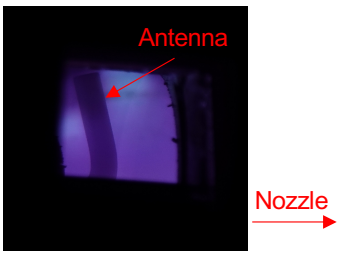

(b) Nominal, 180 mA, 0.7 sccm, 6 W

(c) Nominal, 180 mA, 0.7 sccm, 10 W

(d) Nominal, 180 mA, 0.5 sccm, 8 W

(e) Nominal, 180 mA, 0.9 sccm, 8 W

(f) Nominal, 0 mA, 0.7 sccm, 8 W

(g) Nominal, 135 mA, 0.7 sccm, 8 W

(h) Nominal, 220 mA, 0.7 sccm, 8 W

(i) Nominal, 300 mA, 1.5 sccm, 15 W

Figure 3.31: Comparison of discharge chamber plasma with varying parameters (I_a, $\dot{m}_c$, and P_m) for the nominal model. (F4.0 1/500 ISO100 600 mm)

(a) Improved, 180 mA, 0.7 sccm, 8 W

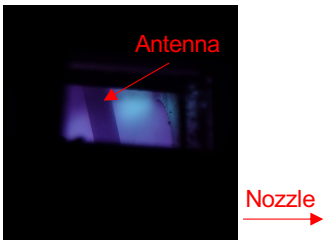

(b) Improved, 180 mA, 0.7 sccm, 6 W

(c) Improved, 180 mA, 0.7 sccm, 10 W

(d) Improved, 180 mA, 0.5 sccm, 8 W

(e) Improved, 180 mA, 0.9 sccm, 8 W

(f) Improved, 0 mA, 0.7 sccm, 8 W

(g) Improved, 135 mA, 0.7 sccm, 8 W

(h) Improved, 220 mA, 0.7 sccm, 8 W

(i) Improved, 300 mA, 1.5 sccm, 15 W

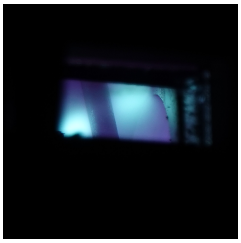

Figure 3.32: Comparison of discharge chamber plasma with varying parameters (I_a, $\dot{m}_c$, and P_m) for the improved model with high mirror ratio yoke. (F4.0 1/500 ISO100 600 mm)

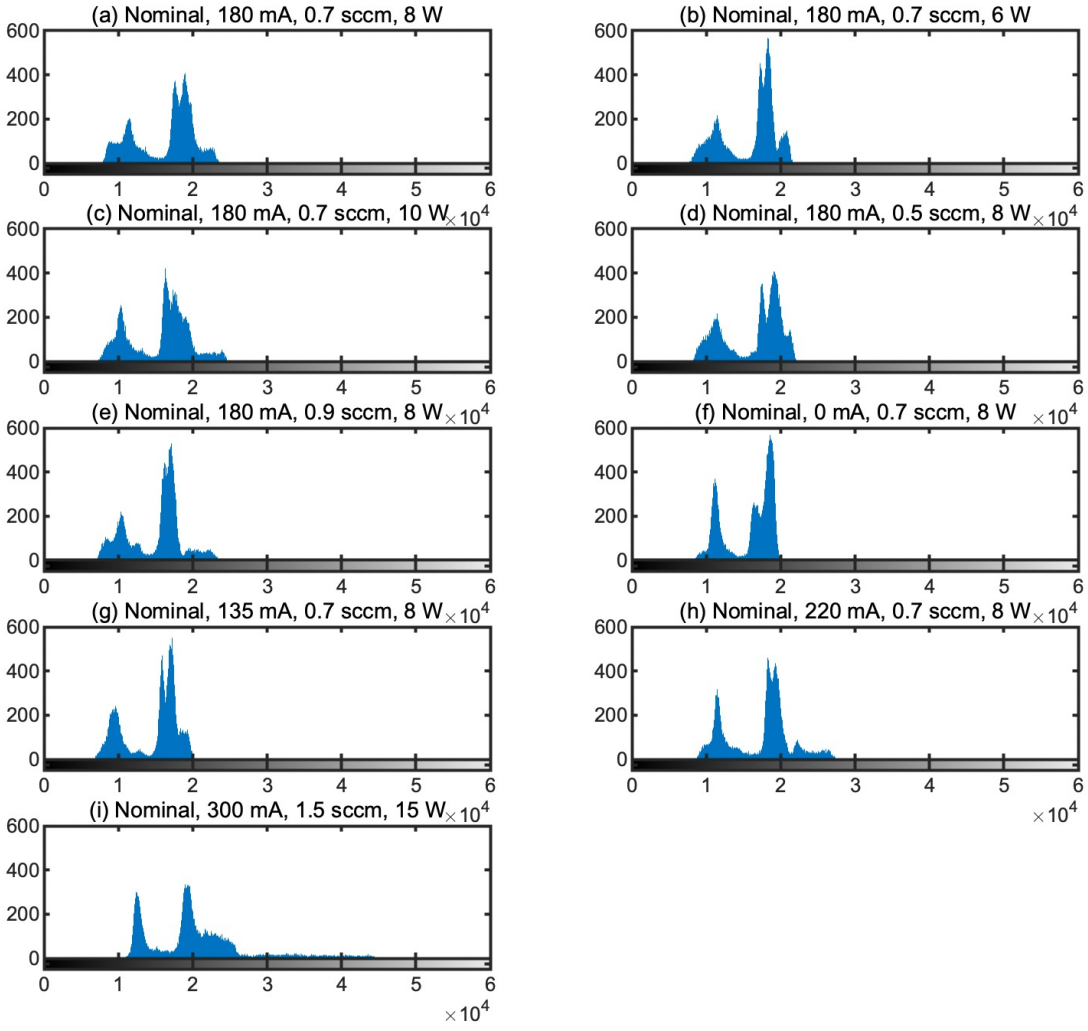

Figure 3.33: Comparison of histograms of Figure 3.31 with varying parameters (I_a, $\dot{m}_c$, and P_m) for the nominal model.

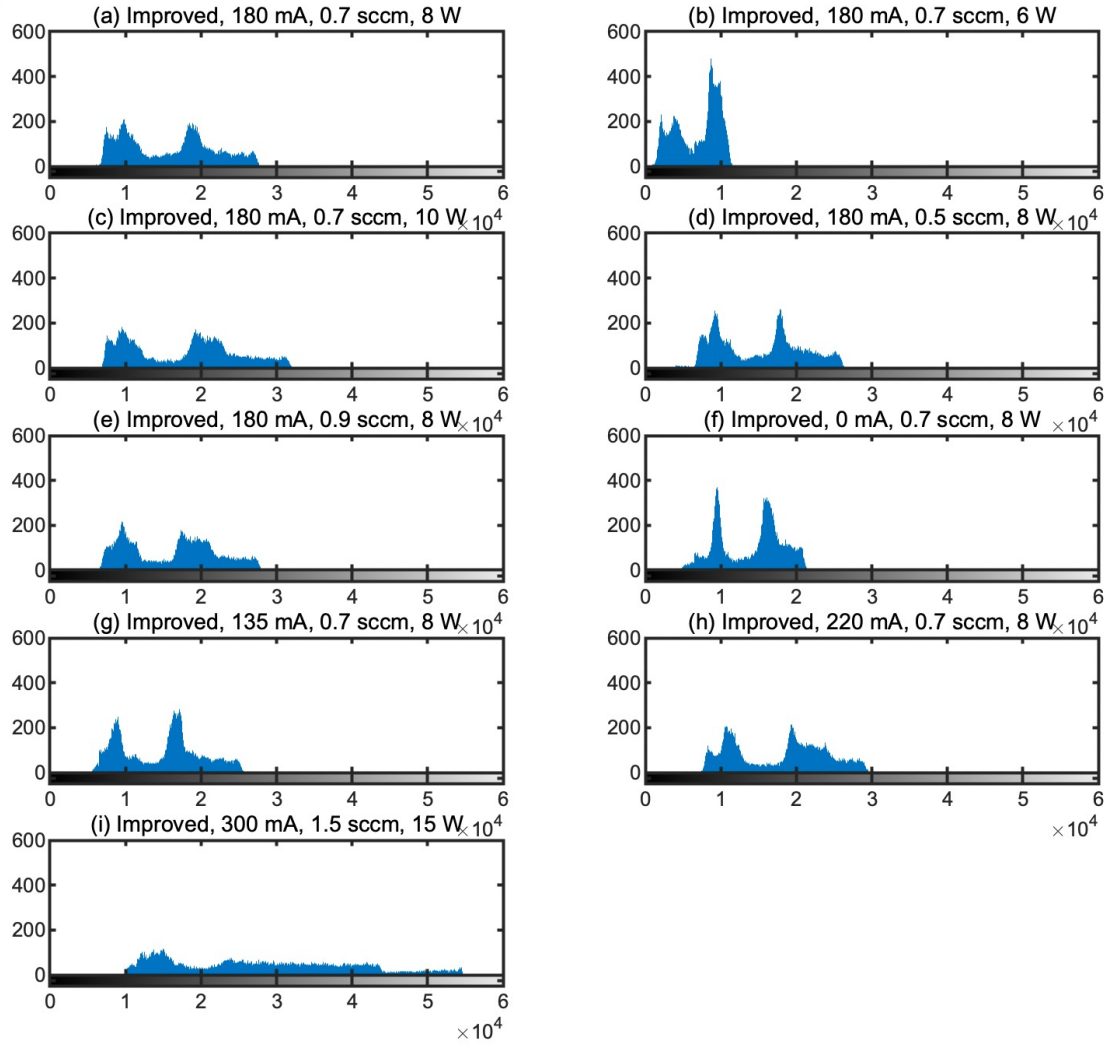

Figure 3.34: Comparison of histogram of Figure 3.32 with varying parameters (I_{a}, $\dot{m}_{\mathrm{c}}$, and P_{m}) for the improved model with high mirror ratio yoke.

3.4 Axial IVDF in plume region

Figure 3.35 shows the axial IVDF in the plume region. A bimodal IVDF is confirmed. It is also confirmed that the population ratio is different between the central axis and the off axis. On the central axis, the mean velocity is toward the cathode. At X = ±5 mm, the mean velocity is toward the anode. A comparison of the results at X = -5 mm and X = 5 mm reveals different SNR values. The excited ion density on the central axis is about 5 to 10 times higher than that at X = ±5 mm.

Figure 3.36 shows the spatial distribution of axial LIF intensity obtained by fitting results in Figure 3.35. A raw data is measured 10 times and fitted by Voigt function. The color contour shows the LIF signal intensity of the IVDF (arbitrary unit). On the central axis, the mean velocity of ions is toward the inside of the discharge chamber; these ions serve as current carriers. The excited ion density is high near the nozzle and gradually decreases toward the anode. In addition, it is confirmed that there are bimodal IVDF on the plume, and the results are discussed in Section 3.8. In previous research, the plume was measured using an electrostatic probe.[42] Figure 3.37 compares the plasma density slope between the previous probe measurement and the LIF measurement. Although the comparison is between relative values, with a proper calibration value and the assumption of uniform electron temperature T_e in the previous research,[25] the slope of the density distribution is reasonable compared to the probe measurement. (R^2 = 0.96) The excited ion density at the root of the antenna is about 3 times higher than that at the nozzle outlet (the results for the discharge chamber are shown in Section 3.6).

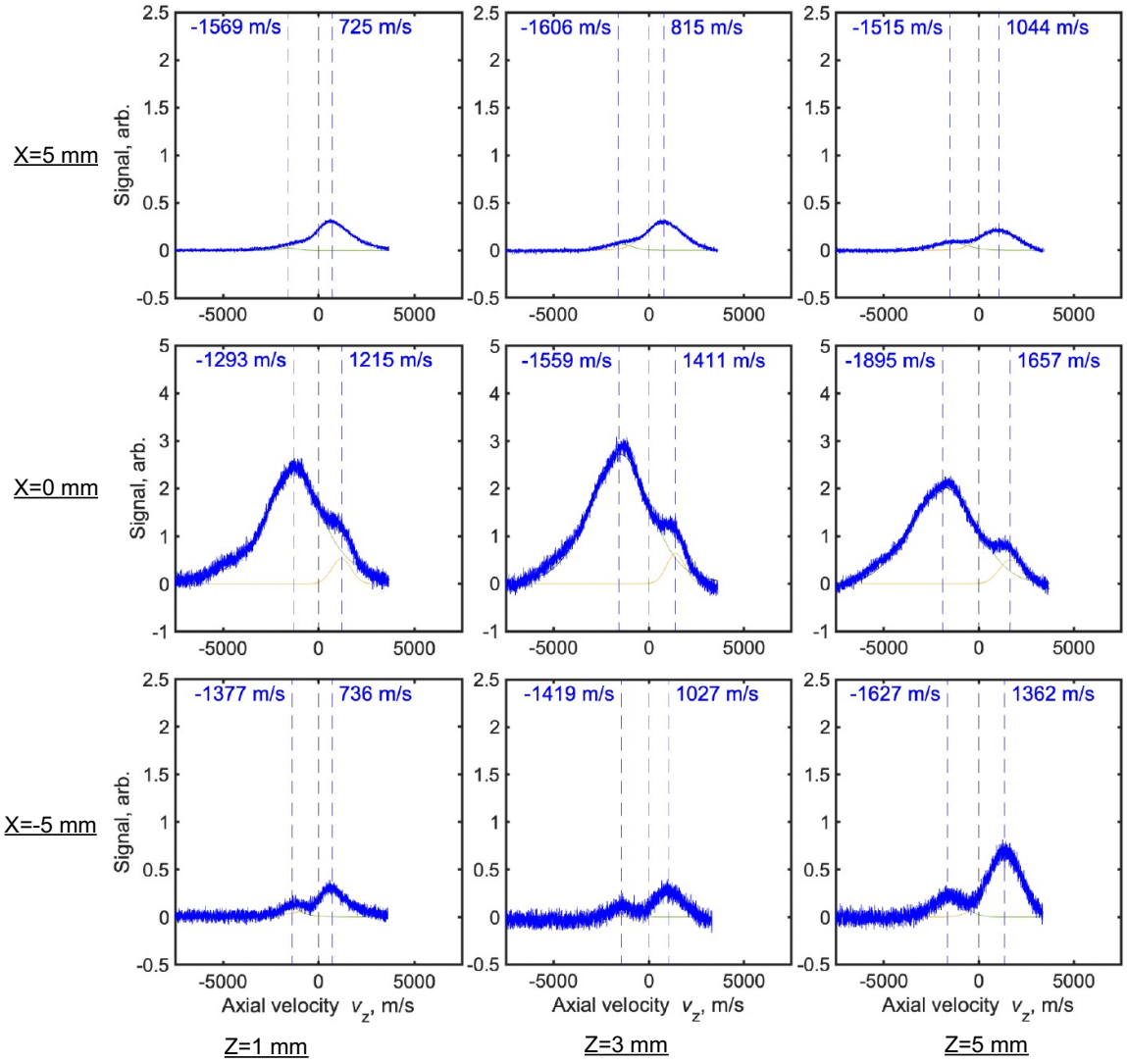

Figure 3.35: Axial results of LIF spectroscopy in plume region at $P_{\mathrm{m}} = 8$ W, $\dot{m}_{\mathrm{c}} = 0.7$ sccm, $I_{\mathrm{a}} = 180$ mA.

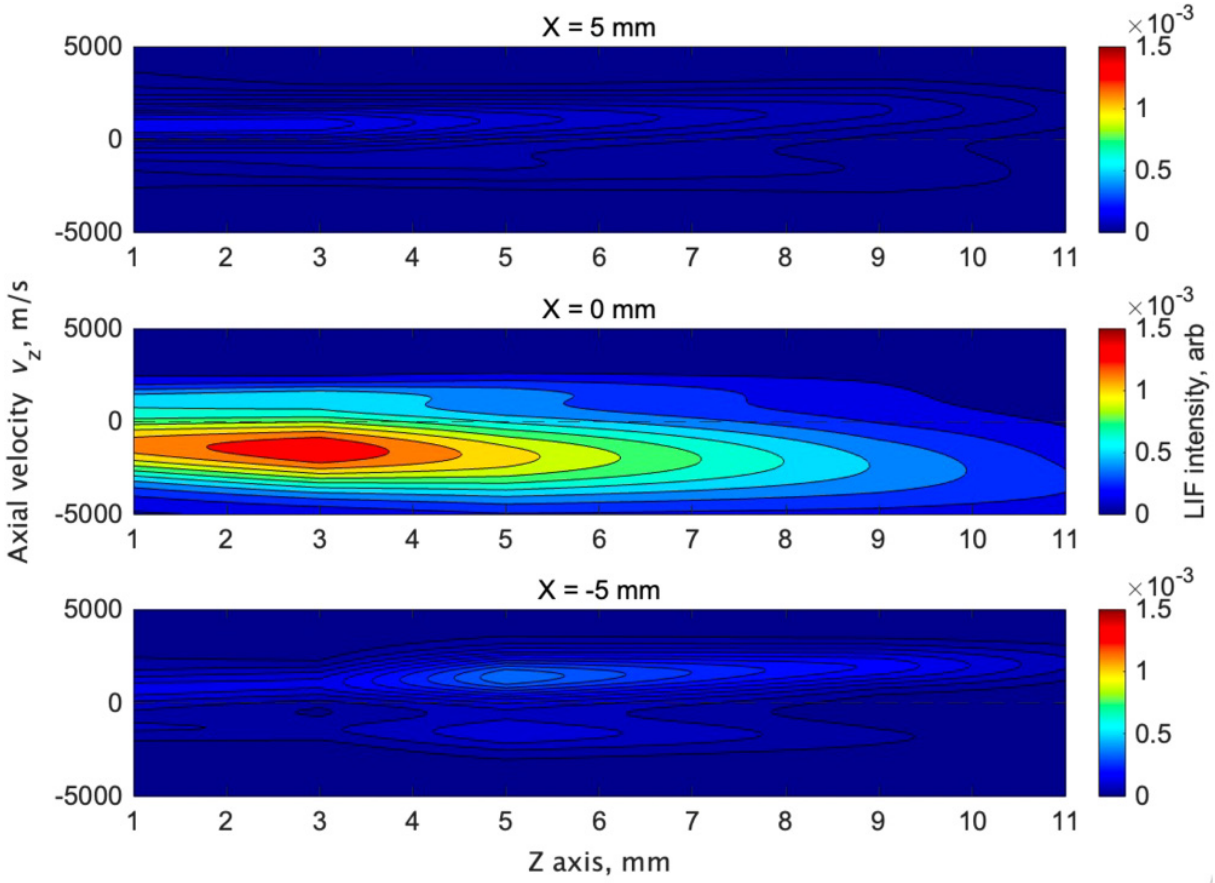

Figure 3.36: Spatial distribution of axial LIF signal at $P_{\mathrm{m}} = 8$ W, $\dot{m}_{\mathrm{c}} = 0.7$ sccm, $I_{\mathrm{a}} = 180$ mA.

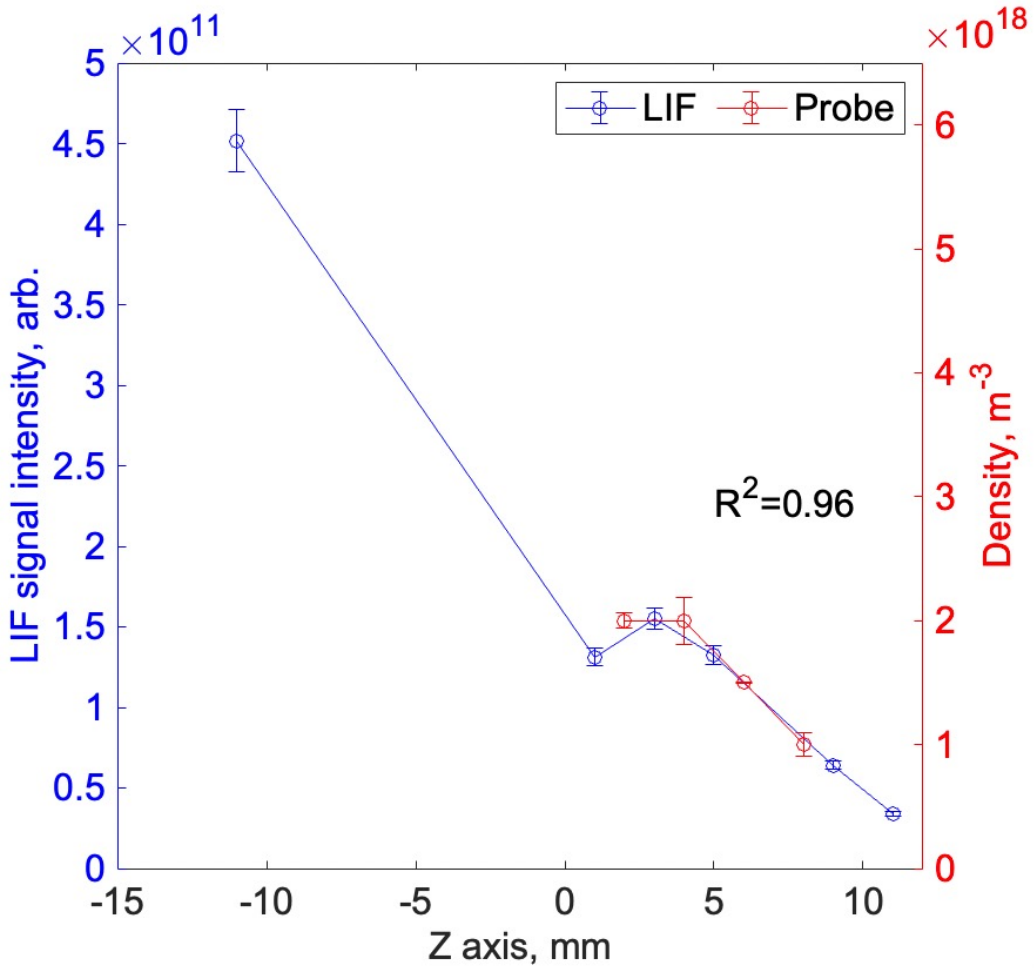

Figure 3.37: Number density comparison of Xe II $(^3P_2)6p[3]_{5/2}$ measured by LIF and xenon ion measured using electrostatic probe at $P_\mathrm{m} = 8$ W, $\dot{m}_\mathrm{c} = 0.7$ sccm, $I_\mathrm{a} = 180$ mA.

3.5 Radial IVDF in plume region

Figure 3.38 shows the radial IVDF on the central axis and ±5 mm from the central axis at the plume. As described above, for radial direction measurements, we changed the parameters for the PMT and lock-in-amplifier to obtain a sufficient SNR. However, when the Z position was not changed, the parameters for the PMT and lock-in-amplifier were the same. The results of radial direction measurements could then be analyzed for velocity. At Z = 1 mm, the peak velocity was positively biased. At Z = 3 mm, velocity symmetry with respect to the X-axis was found and a weak peak at about −3,000 m/s was observed. In addition, as shown in Figure 3.19, a similar weak peak at about −4,200 m/s was observed in the plume region, while the peak was not found in the reference cell. Therefore, it was suggested that the weak peak did not generated by a hyperfine structure. At Z = 9 mm, the peak velocity converged on the central axis.

Figure 3.39 shows the spatially two-dimensional velocity vector on the plume obtained by the axial and radial LIF measurements in Figures 3.35 and 3.38. As shown in Figure 3.35, an axial bimodal IVDF was found on the plume, and therefore the velocity in Figure 3.39 was calculated as the mean velocity. The mean velocity $\bar{v}_{\mathrm{X}}$ and $\bar{v}_{\mathrm{Z}}$ are defined in Eq. 3.4 and Eq. 3.5, respectively.

$$\bar{v}_{\mathrm{X}} = \int_{-\infty}^{+\infty} v_{\mathrm{X}} f(v_{\mathrm{X}}) \mathrm{d}v_{\mathrm{X}} \tag{3.4}$$

$$\bar{v}_{\mathrm{Z}} = \int_{-\infty}^{+\infty} v_{\mathrm{Z}} f(v_{\mathrm{Z}}) \mathrm{d}v_{\mathrm{Z}} \tag{3.5}$$

As shown in Figure 3.39, the mean velocity on the central axis was directed toward the cathode. The mean velocity was largest near the anode and decreased as it approached the cathode. Between Z = 3 mm and 5 mm, the mean velocity decreased by about 300 m/s. At X = ±5 mm, the mean velocity was directed toward the anode. The radial velocity was up to about 300 m/s, which was much smaller than the axial velocity. These results are discussed in Section 3.9.

In the LIF measurement in the plume region of a hollow cathode, it was reported that ions flow mainly in the downstream direction but flow back near the nozzle.[69][70] The ion flow difference may be due to differences in anode shape, presence or absence of a keeper, and plasma generation method. For a hollow cathode, a cylindrical anode is used and ions easily flow to the downstream. In diode mode operation with a plate anode, it was reported that ion velocities were lower compared to those for a cylindrical anode.[71] The cylindrical anode has a smaller effect on the neutral flow downstream of the nozzle. Therefore, the neutral density is lower compared to that for the plate anode. Lower collision probabilities lead to larger

velocity. In addition, because the keeper of the hollow cathode is kept floating or positively biased during cathode operation, most ions flow toward the anode, with only a small fraction of highly energetic ions moving toward the keeper. In contrast, for a microwave discharge cathode in diode mode, the anode is a meshed plate (diameter: 3.0 mm; pitch: 5.0 mm; aperture ratio: 32.6%) and it is possible for the field generated by the anode to affect ion flow. In addition, a microwave discharge cathode requires ion absorption on the wall to emit electrons. Therefore, there are differences in the ion flow between a hollow cathode and a microwave discharge cathode.

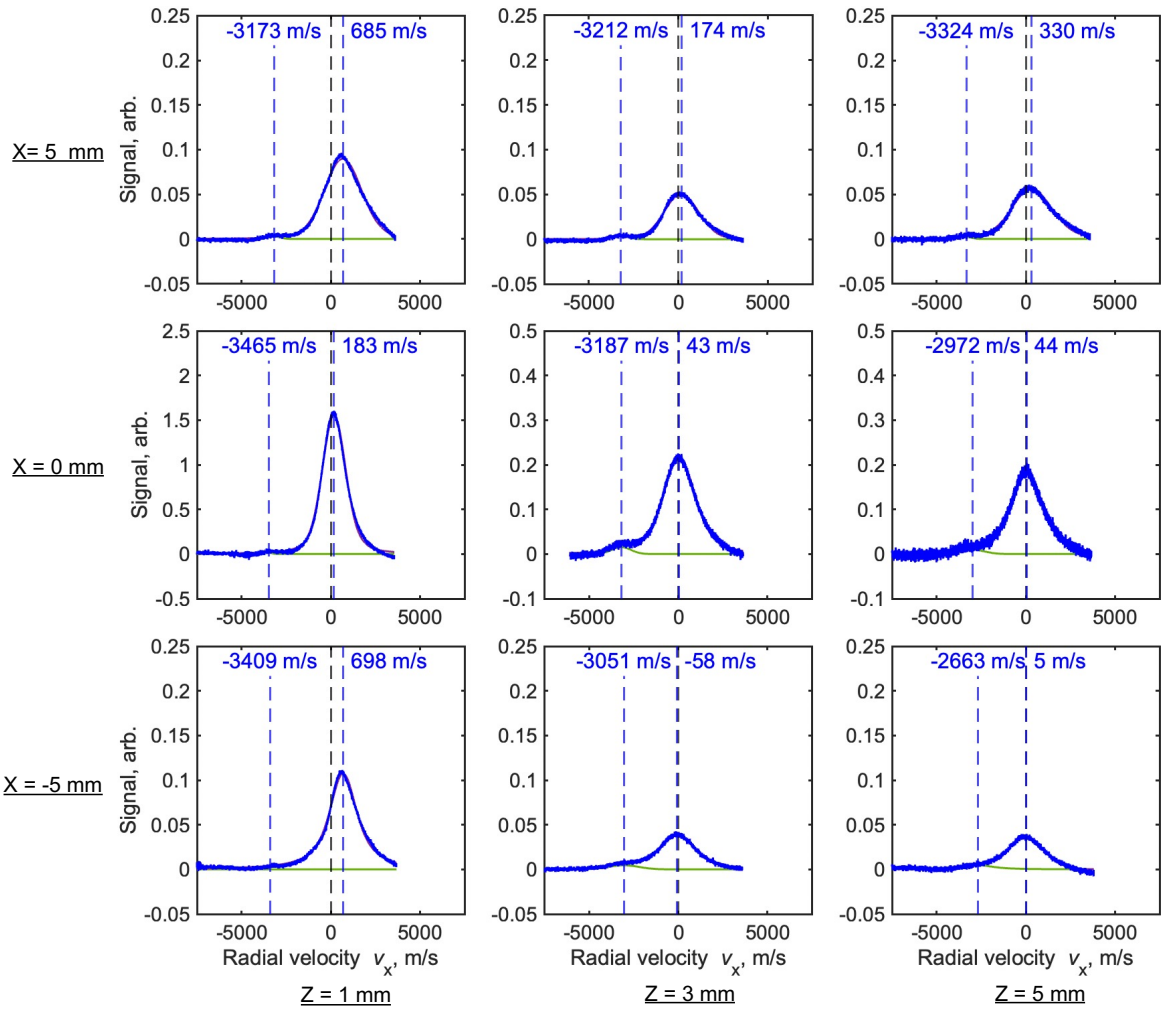

Figure 3.38: Radial results of LIF spectroscopy in plume region at $P_m = 8$ W, $\dot{m}_c = 0.7$ sccm, $I_a = 180$ mA.

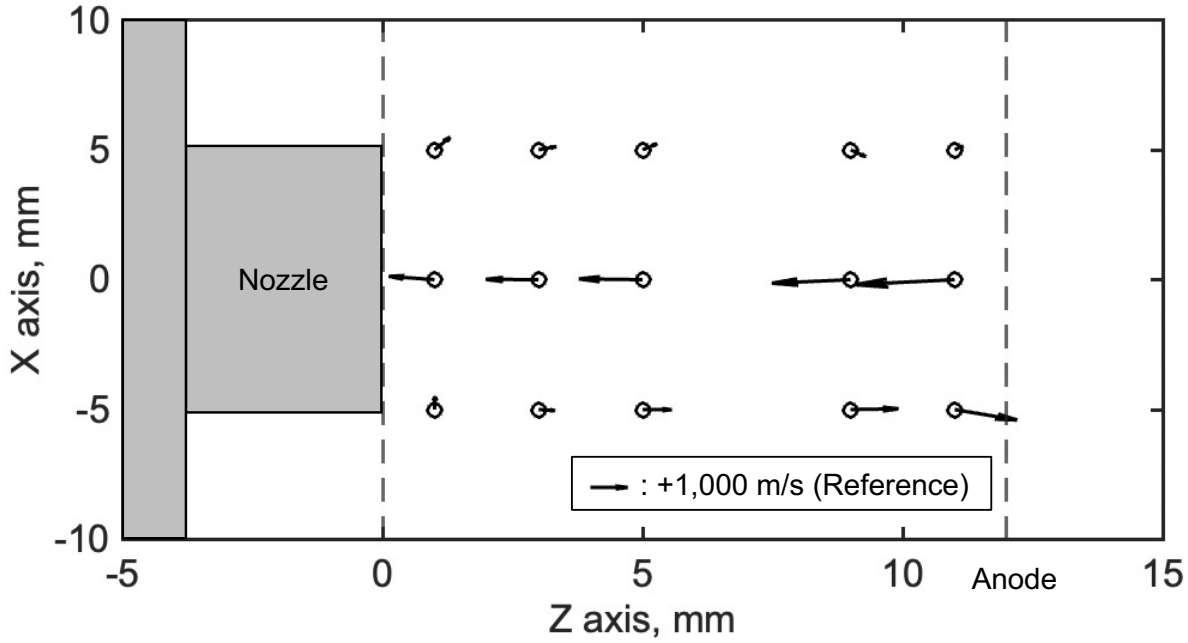

Figure 3.39: Mean xenon ion velocity vectors in plume region at $P_{\mathrm{m}} = 8$ W, $\dot{m}_{\mathrm{c}} = 0.7$ sccm, $I_{\mathrm{a}} = 180$ mA.

3.6 Axial IVDF in viewable microwave discharge cathode

In this section, the results of a diagnosis inside the viewable microwave discharge cathode are compared based on the parameters in Table 3.1.

Figure 3.40 shows the axial IVDF at $P_{\mathrm{m}} = 8$ W, $\dot{m}_{\mathrm{c}} = 0.7$ sccm, $I_{\mathrm{a}} = 180$ mA, which are the nominal conditions for Hayabusa2. The numbers in the figure indicate the intensity of each velocity population normalized by the intensity at X = 0 mm, Z = -11 mm under nominal conditions. The numbers in brackets indicate the ratios normalized by the total intensity for the given condition. The populations include a negative-velocity population toward the upstream called "Population A" (green), a near-zero-velocity population called "Population B" (red), a positive-velocity population toward the downstream called "Population C" (orange), and the total signal (blue). As shown in Figure 3.40, a trimodal IVDF is confirmed at X = 0 mm, Z = -11 mm. At other positions, a bimodal IVDF is observed. At X = 5 mm, Z = -15 mm, the most upstream measurement point in this study, the peak velocity of Population A (about -1,700 m/s) is the largest. At other positions, the peak velocity of Population A is -1,200 to -1,300 m/s. As shown in Figure 3.40, the highest intensity is distributed at X = 0 mm, Z = -11 mm. At other positions, the density is about 15% of the intensity at X = 0 mm, Z = -11 mm. At X = 0 mm, Z = -11 mm, the intensity ratio is 55% for Population A, 15% for Population B, and 30% for Population C. At other conditions, Figure 3.41 – 3.47 show the axial IVDF inside microwave discharge cathode at $P_{\mathrm{m}} = 6$ W, $\dot{m}_{\mathrm{c}} = 0.7$ sccm, $I_{\mathrm{a}} = 180$ mA; $P_{\mathrm{m}} = 10$ W, $\dot{m}_{\mathrm{c}} = 0.7$ sccm, $I_{\mathrm{a}} = 180$ mA; $P_{\mathrm{m}} = 8$ W, $\dot{m}_{\mathrm{c}} = 0.5$ sccm, $I_{\mathrm{a}} = 180$ mA; $P_{\mathrm{m}} = 8$ W, $\dot{m}_{\mathrm{c}} = 0.9$ sccm, $I_{\mathrm{a}} = 180$ mA; $P_{\mathrm{m}} = 8$ W, $\dot{m}_{\mathrm{c}} = 0.7$ sccm, $I_{\mathrm{a}} = 0$ mA; $P_{\mathrm{m}} = 8$ W, $\dot{m}_{\mathrm{c}} = 0.7$ sccm, $I_{\mathrm{a}} = 135$ mA; $P_{\mathrm{m}} = 8$ W, $\dot{m}_{\mathrm{c}} = 0.7$ sccm, $I_{\mathrm{a}} = 220$ mA, respectively. The intensity ratio and peak velocity of each velocity population are similar for a given position.

Figure 3.48 shows an LIF intensity comparison of the microwave power P_{m}, xenon flow rate $\dot{m}_{\mathrm{c}}$, and anode current I_{a} at X = 0 mm, Z = −11 mm. The larger P_{m}, the higher the total intensity. A 2-W microwave increase enhanced the total intensity by about 20%. In contrast, the larger $\dot{m}_{\mathrm{c}}$, the lower the total intensity, while the larger I_{a}, the higher the total intensity. As shown in the Figures 3.41– 3.47, the same trends were observed at other positions.

Figure 3.49 shows a comparison of the axial LIF signal intensity ratio and peak velocity at X = 0 mm, Z = −11 mm for $P_{\mathrm{m}} = 8$ W, $\dot{m}_{\mathrm{c}} = 0.7$ sccm, $I_{\mathrm{a}} = 180$ mA, calculated using the results shown in Figures 3.41– 3.47. As shown in Figure 3.49, for other parameter values (P_{m}, $\dot{m}_{\mathrm{c}}$, and I_{a}), the intensity ratio and peak velocity of each velocity population were not very different for the same positions. It is noted that the same trends were observed for $I_{\mathrm{a}} =$ 0 mA.

Figure 3.50 summarizes a comparison of the axial LIF intensity normalized by the intensity at X = 0 mm, Z = −11 mm for nominal conditions. The intensity in the discharge chamber increased or decreased uniformly as the parameters were changed. No local changes were confirmed for these parameters, such as an intensity increase or decrease only in the mirror magnetic field.

Figure 3.51 shows a photograph and schematic diagram of a black antenna model. Figure 3.52 shows an axial IVDF comparison for the microwave antenna condition at X = 0 mm, Z = −11 mm. The black antenna model was used to suppress reflection of the laser beam. The surface resistance was 5-10 Ω, measured using a digital multimeter. The anode voltage V_a of the black antenna model increases by 20 V because the carbon black coating deteriorated the microwave transmission characteristics.

As shown in Figure 3.52, there is not much difference in the velocity at each peak with respect to the antenna type. As before, the peak velocity of Population A is about -1,300 m/s and that of Population C is about 1,500 m/s. However, the intensity ratio of each peak is different due to the type of microwave antenna. The intensity of Population A decreases by 50% and that of Population C decreases by 30% compared to the former results; the mean velocity decreases as a result. The intensities decrease because the plasma density decreases due to the microwave emission performance degradation caused by the black antenna, as shown by the V_a increase of 20 V. Although the total intensity decreases, the intensity ratio of Population C increases. Therefore, it is inferred that Population C is not a reflected Population A caused by laser reflection at the antenna or wall.

As shown in Figure 3.52 and Figure 3.45, it is noted that the total intensity at I_a = 0 mA is higher than that of black antenna model. Therefore, black-painted model require to generate higher density plasma on the plume to compensate for performance deterioration in the discharge chamber. Therefore, the anode voltage V_a increases by 20 V.

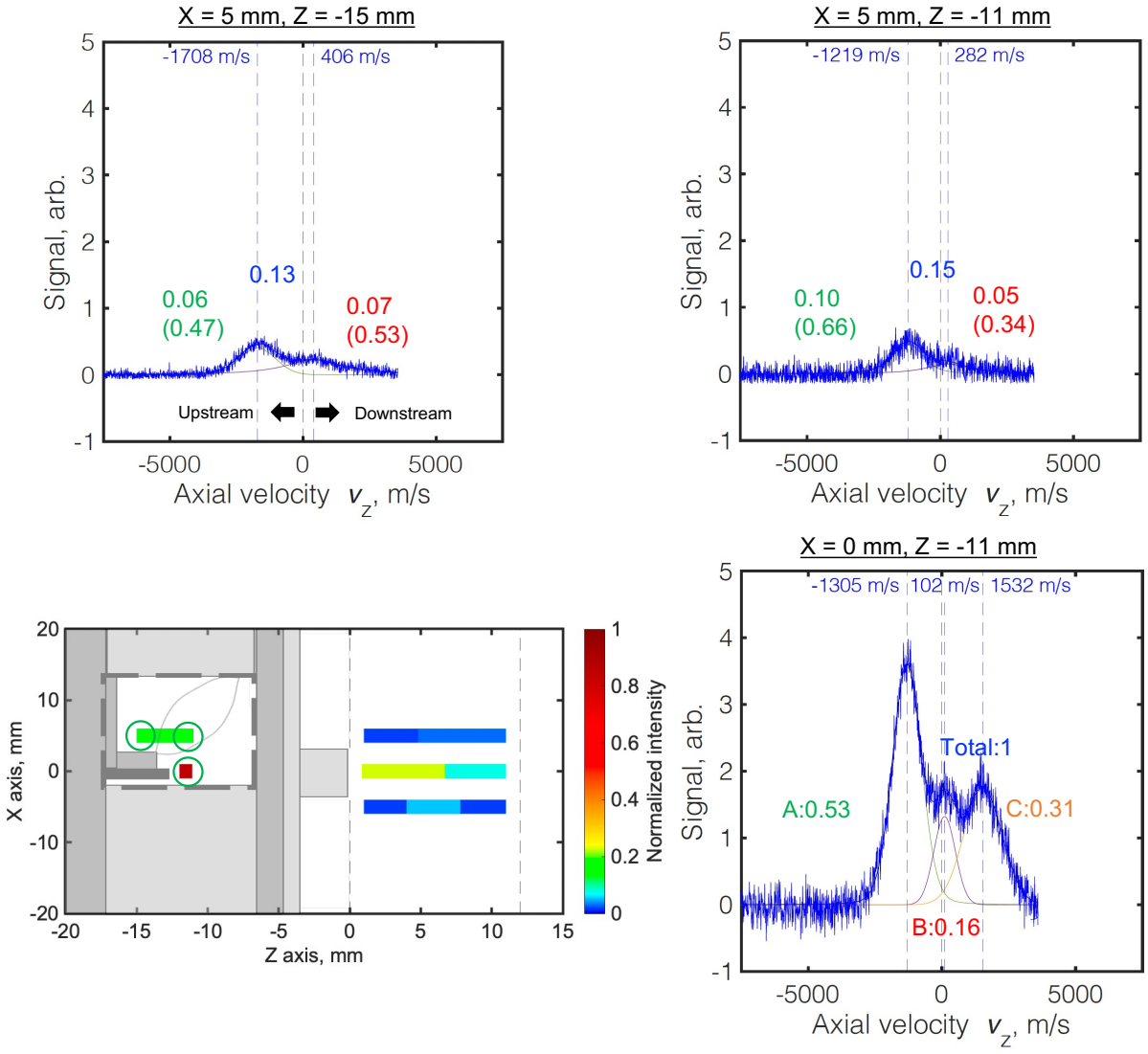

Figure 3.40: Axial results of LIF spectroscopy inside microwave discharge cathode at $P_{\mathrm{m}} = 8$ W, $\dot{m}_{\mathrm{c}} = 0.7$ sccm, $I_{\mathrm{a}} = 180$ mA.

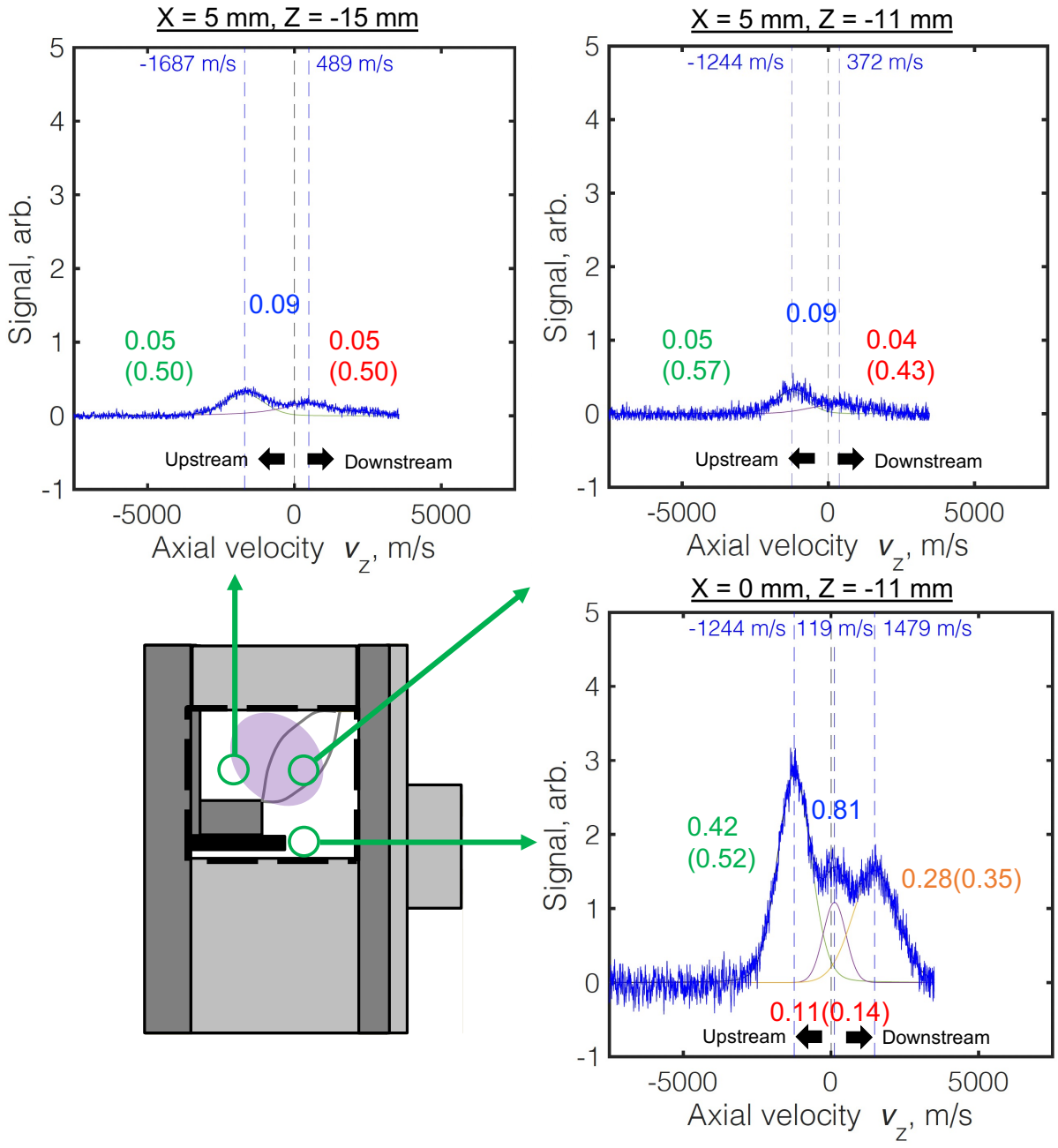

Figure 3.41: Axial results of LIF spectroscopy inside microwave discharge cathode at $P_{\mathrm{m}} = 6$ W, $\dot{m}_{\mathrm{c}} = 0.7$ sccm, $I_{\mathrm{a}} = 180$ mA.

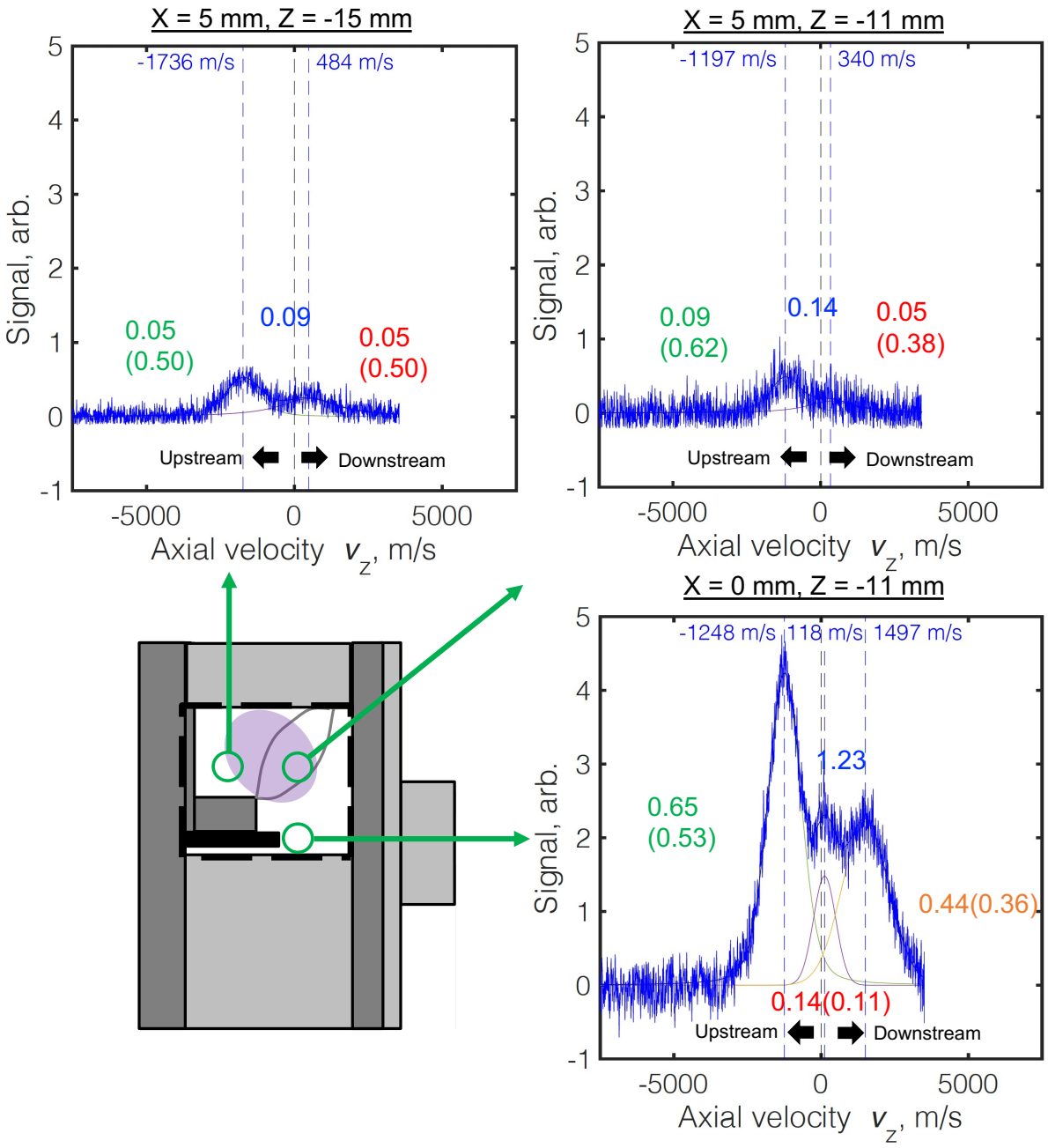

Figure 3.42: Axial results of LIF spectroscopy inside microwave discharge cathode at $P_{\mathrm{m}} = 10$ W, $\dot{m}_{\mathrm{c}} = 0.7$ sccm, $I_{\mathrm{a}} = 180$ mA.

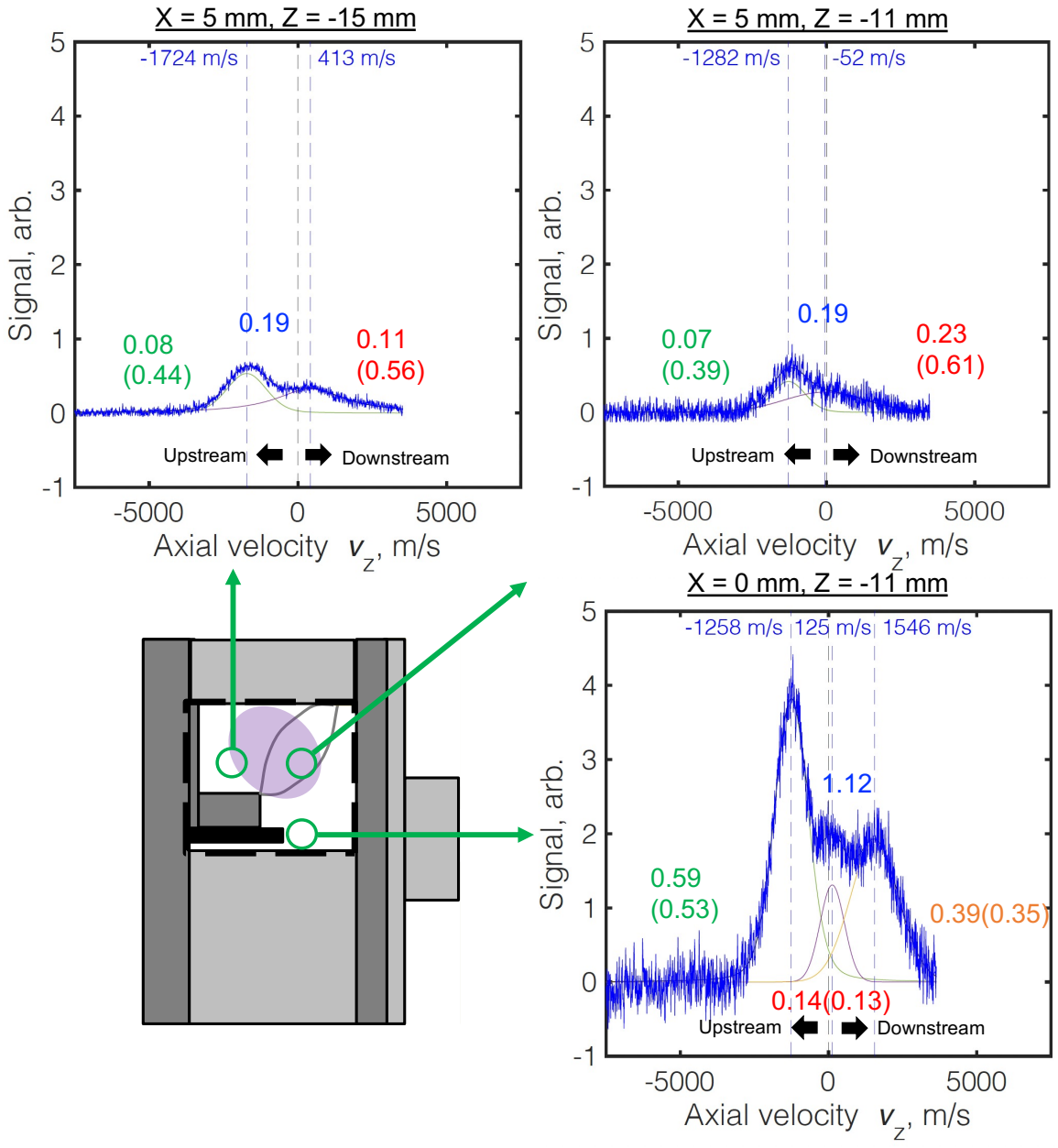

Figure 3.43: Axial results of LIF spectroscopy inside microwave discharge cathode at $P_{\mathrm{m}} = 8$ W, $\dot{m}_{\mathrm{c}} = 0.5$ sccm, $I_{\mathrm{a}} = 180$ mA.

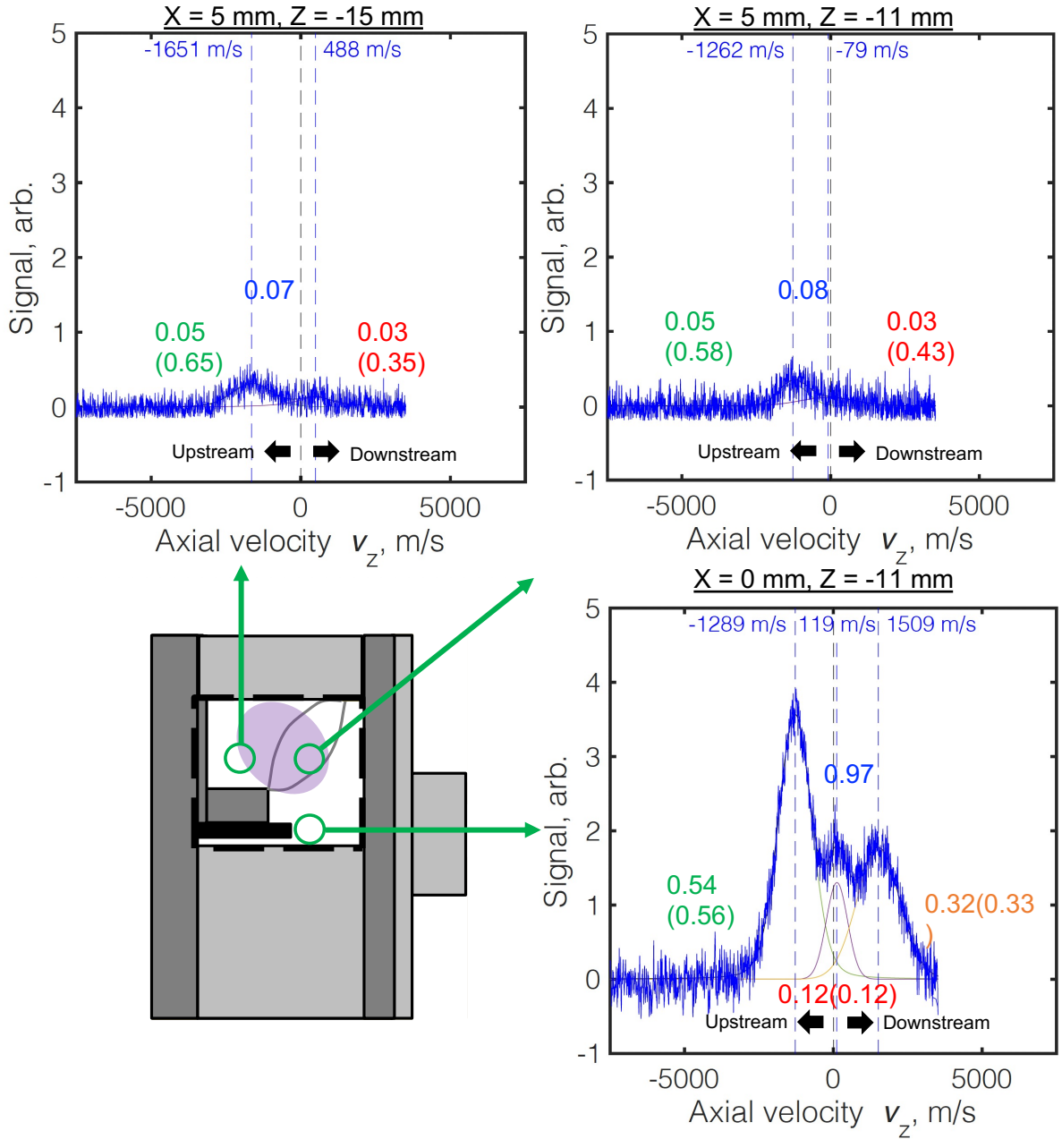

Figure 3.44: Axial results of LIF spectroscopy inside microwave discharge cathode at $P_{\mathrm{m}} = 8$ W, $\dot{m}_{\mathrm{c}} = 0.9$ sccm, $I_{\mathrm{a}} = 180$ mA.

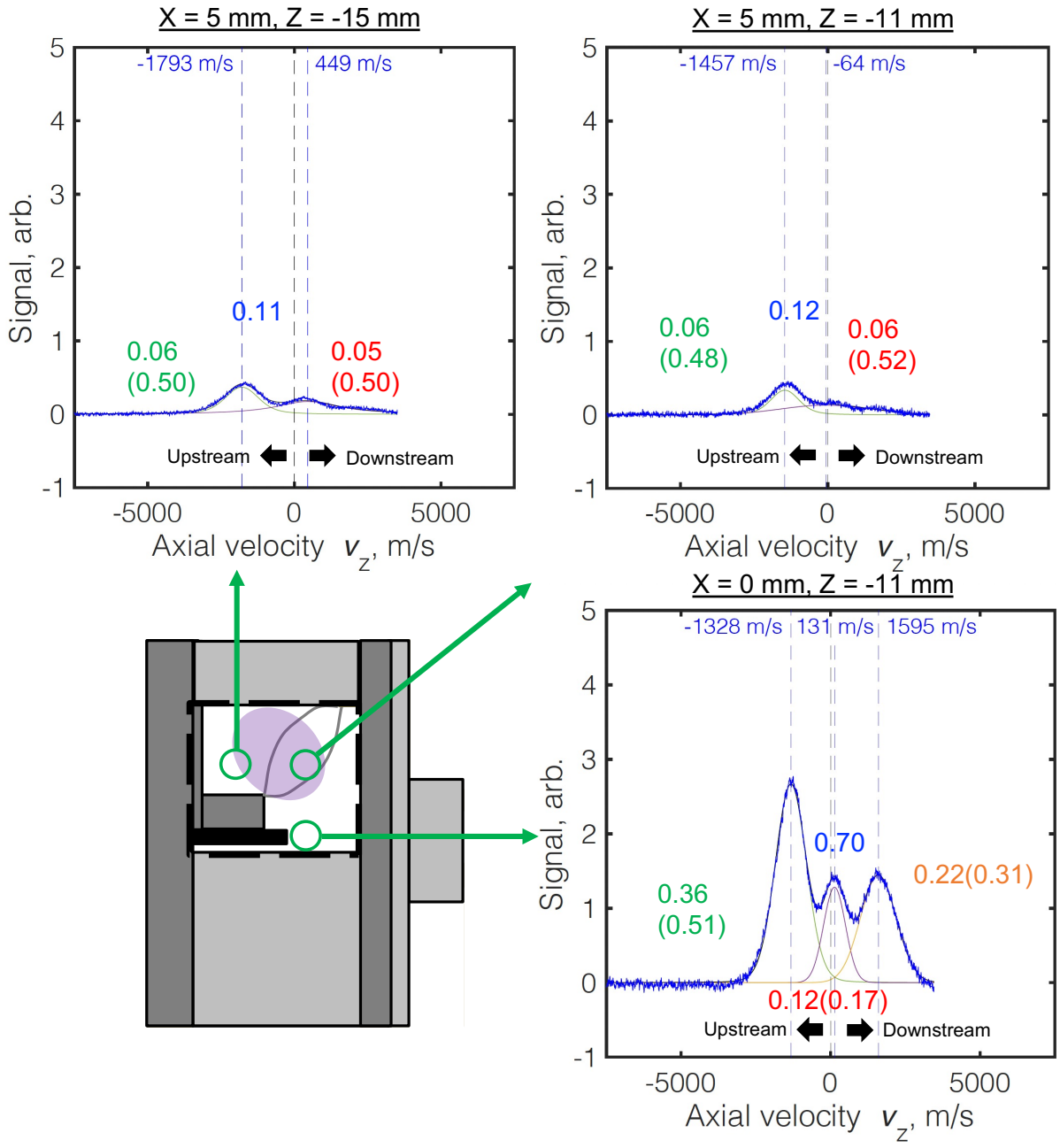

Figure 3.45: Axial results of LIF spectroscopy inside microwave discharge cathode at $P_{\mathrm{m}} = 8$ W, $\dot{m}_{\mathrm{c}} = 0.7$ sccm, $I_{\mathrm{a}} = 0$ mA.

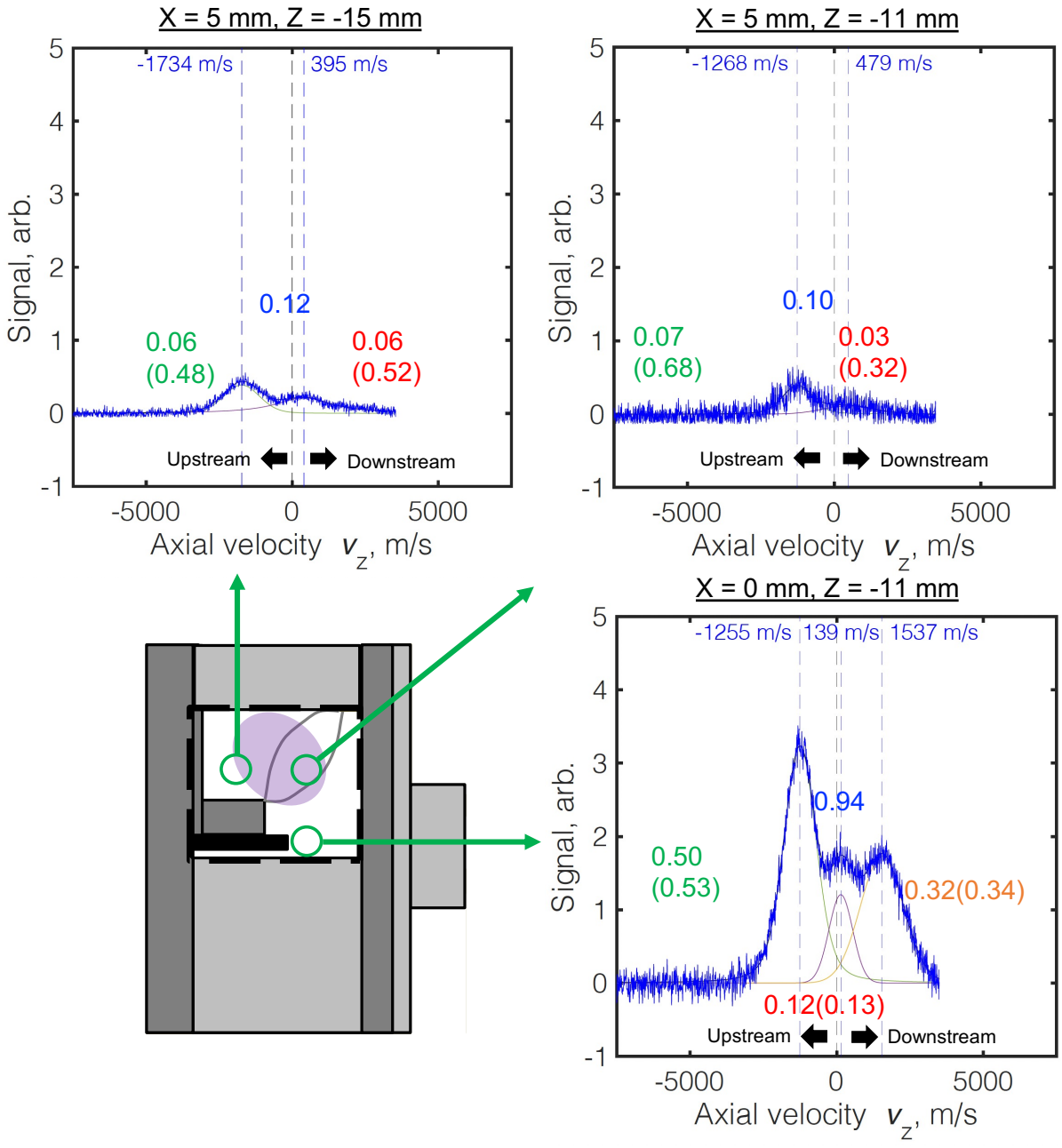

Figure 3.46: Axial results of LIF spectroscopy inside microwave discharge cathode at $P_{\mathrm{m}} = 8$ W, $\dot{m}_{\mathrm{c}} = 0.7$ sccm, $I_{\mathrm{a}} = 135$ mA.

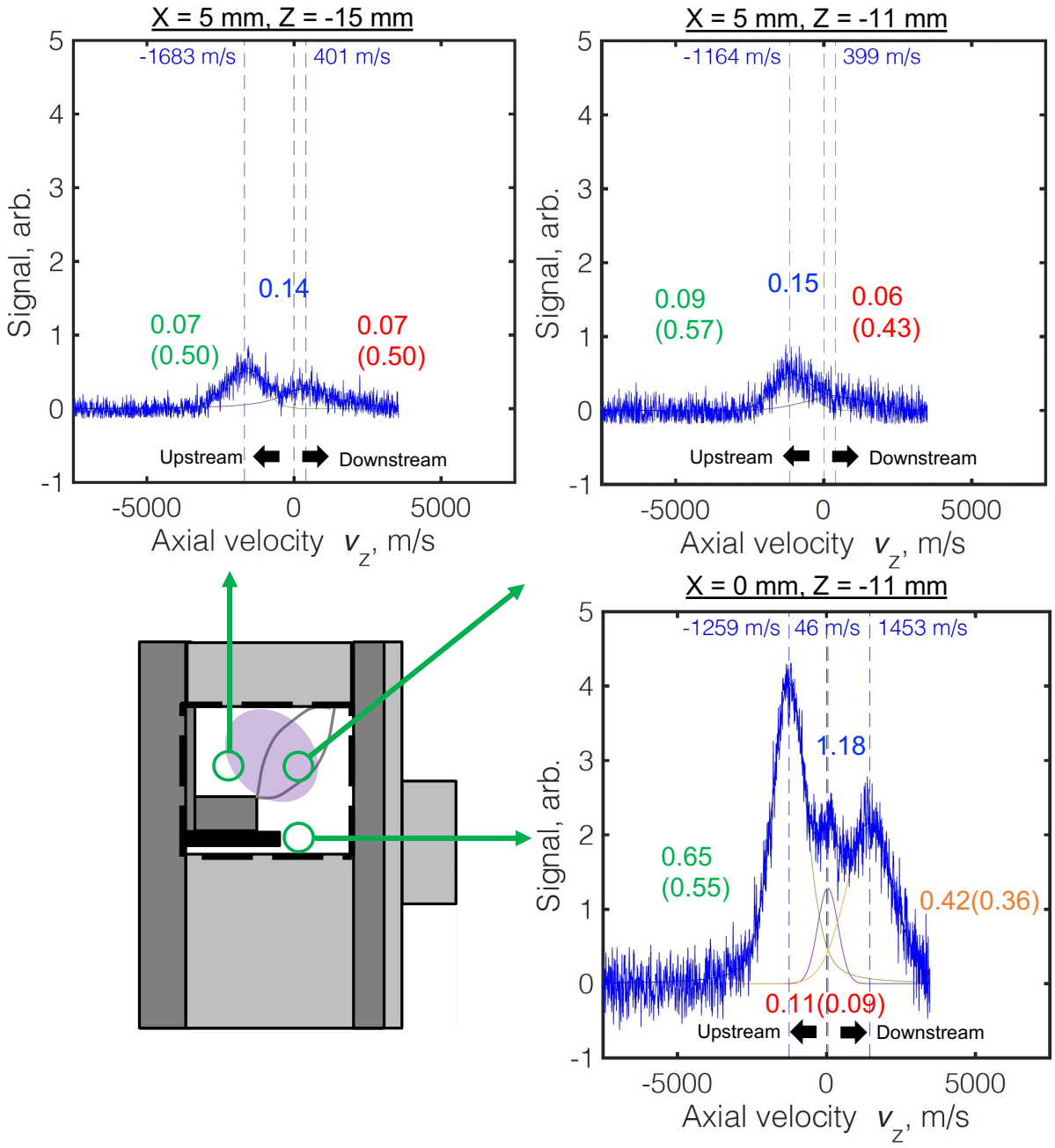

Figure 3.47: Axial results of LIF spectroscopy inside microwave discharge cathode at $P_{\mathrm{m}} = 8$ W, $\dot{m}_{\mathrm{c}} = 0.7$ sccm, $I_{\mathrm{a}} = 220$ mA.

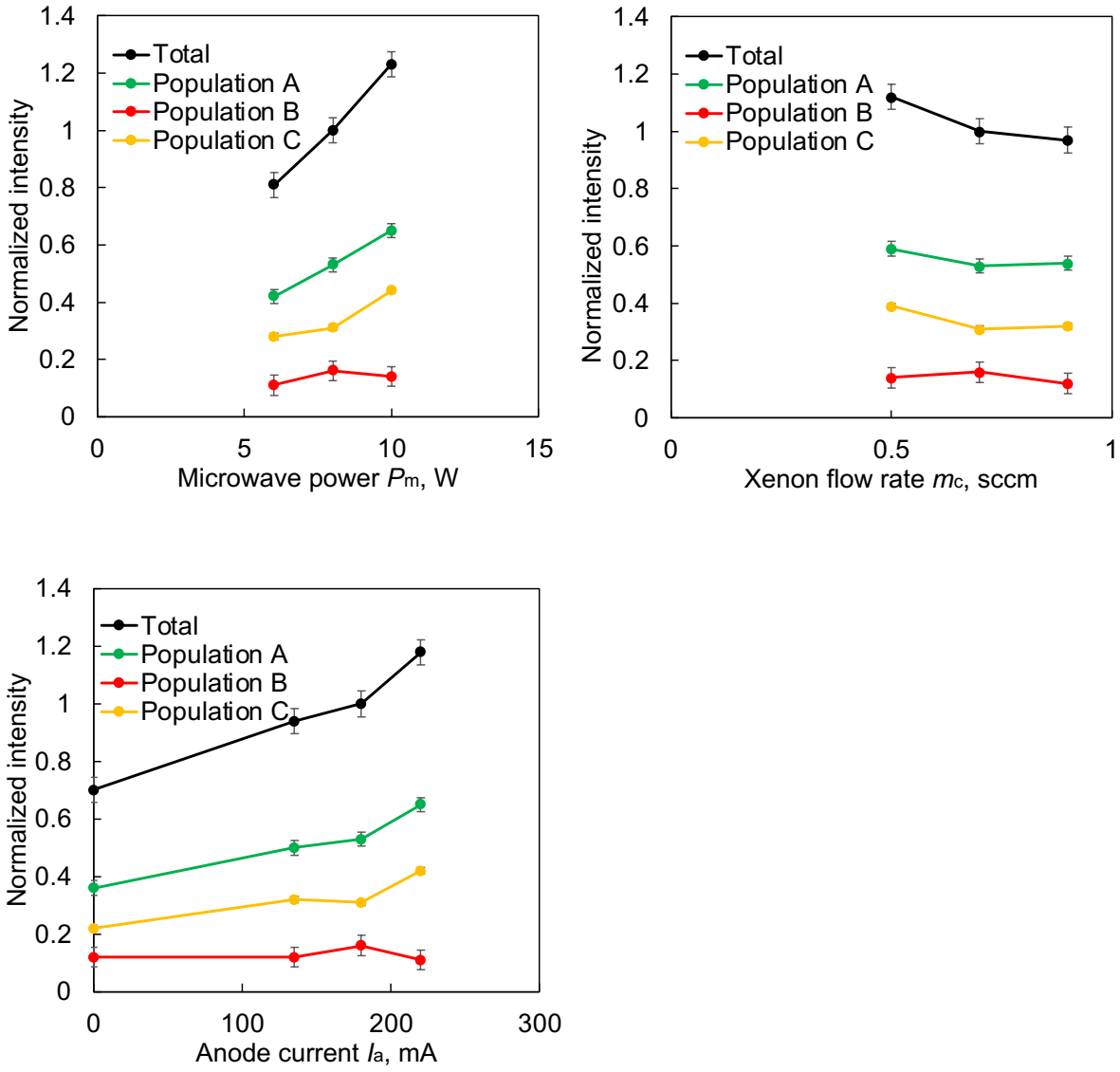

Figure 3.48: Comparison of axial LIF intensity for each population (A, B, C), near the antenna (X = 0 mm, Z = −11 mm).

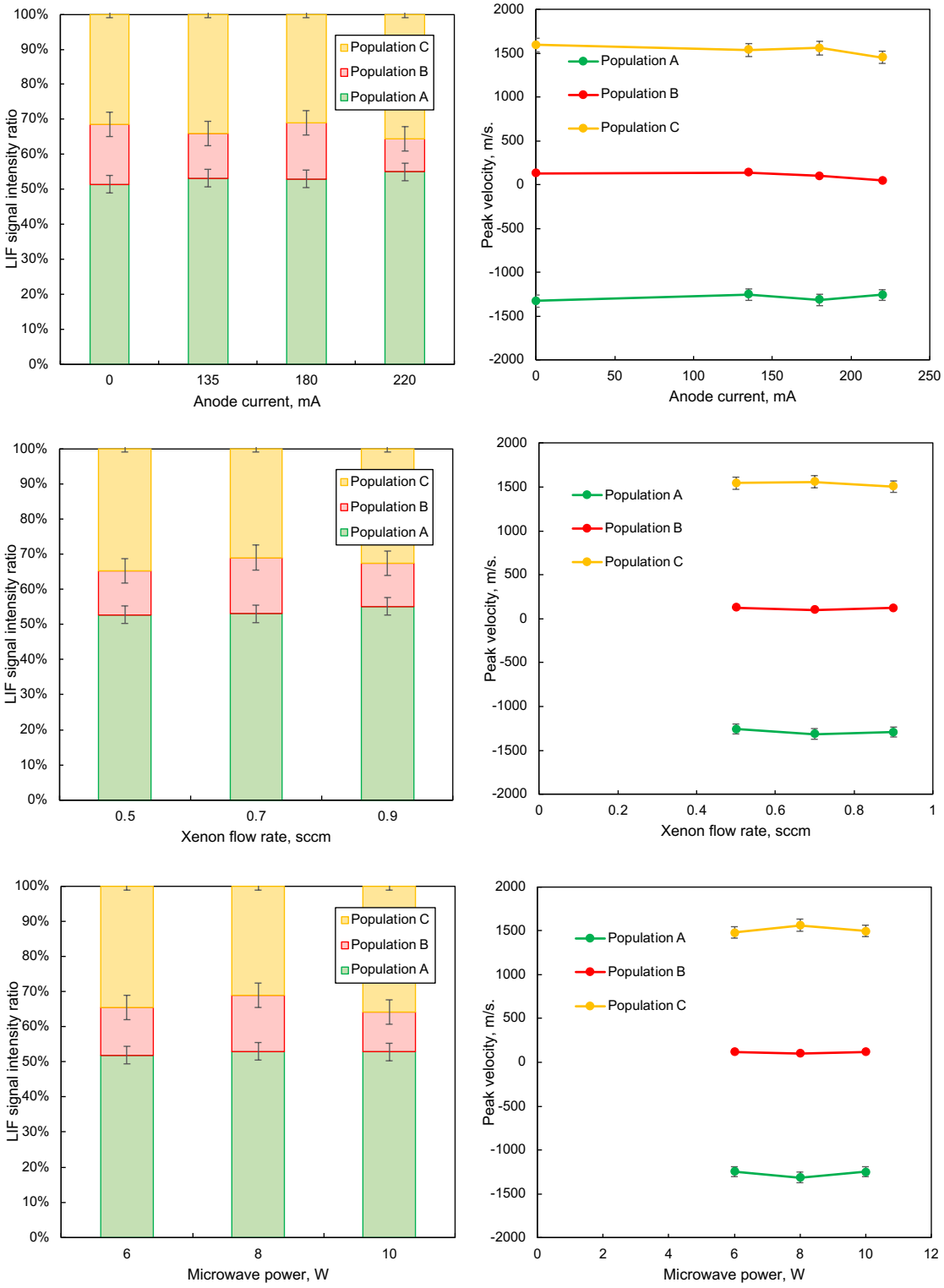

Figure 3.49: Comparison of axial LIF signal intensity ratio and peak velocity at X = 0 mm, Z = −11 mm for $P_{\mathrm{m}} = 8$ W, $\dot{m}_{\mathrm{c}} = 0.7$ sccm, $I_{\mathrm{a}} = 180$ mA.

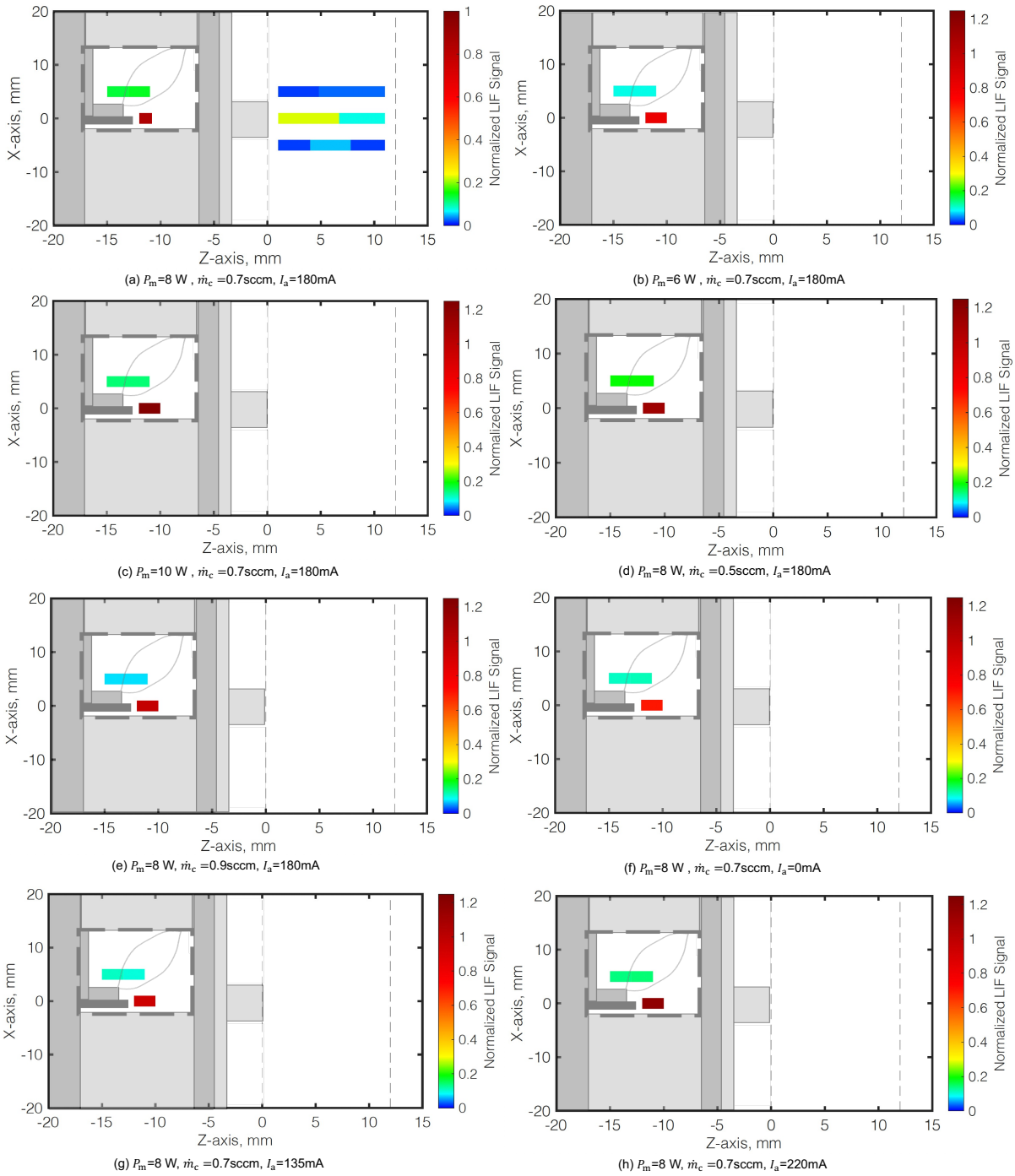

Figure 3.50: Comparison of axial LIF intensity normalized by intensity at X = 0 mm, Z = −11 mm for the nominal conditions in (a).

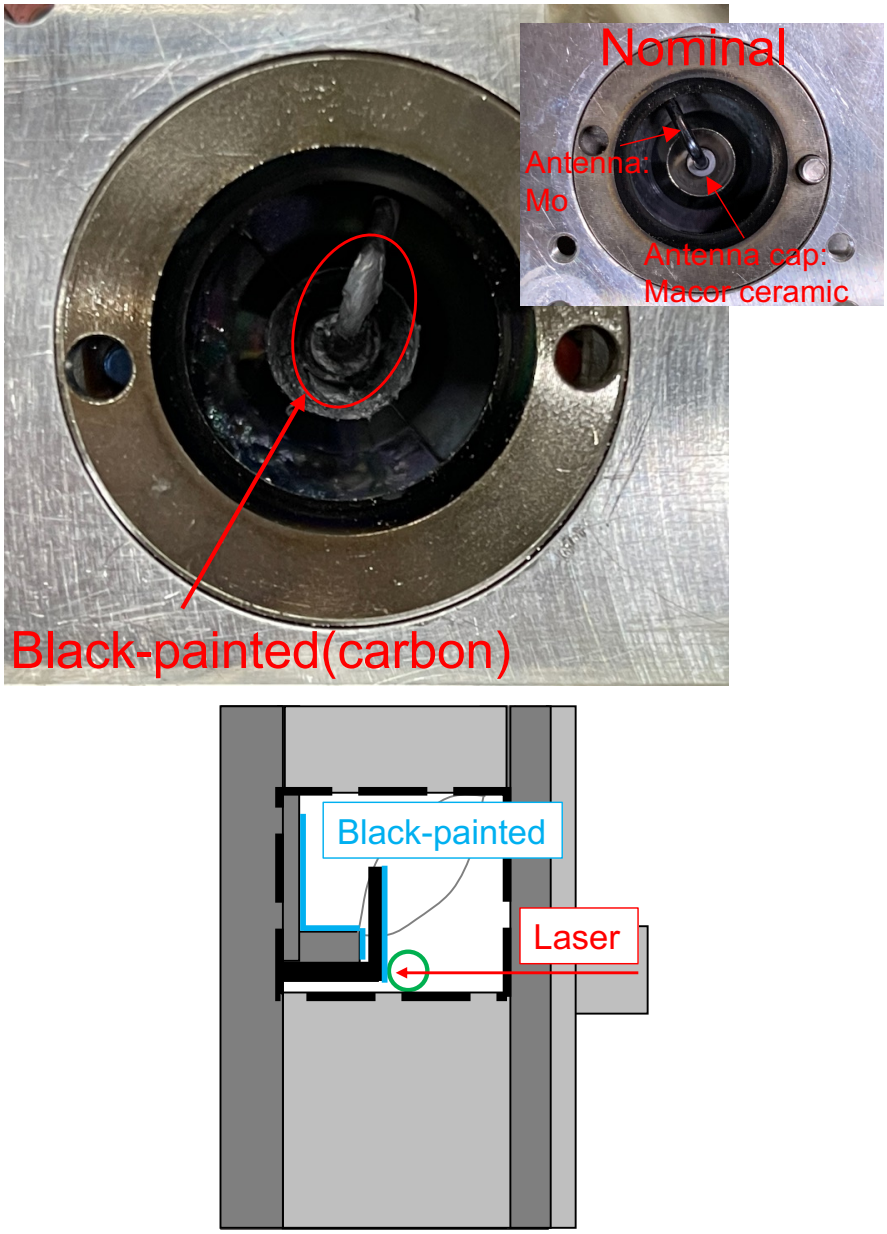

Figure 3.51: Photograph and schematic diagram of black antenna model.

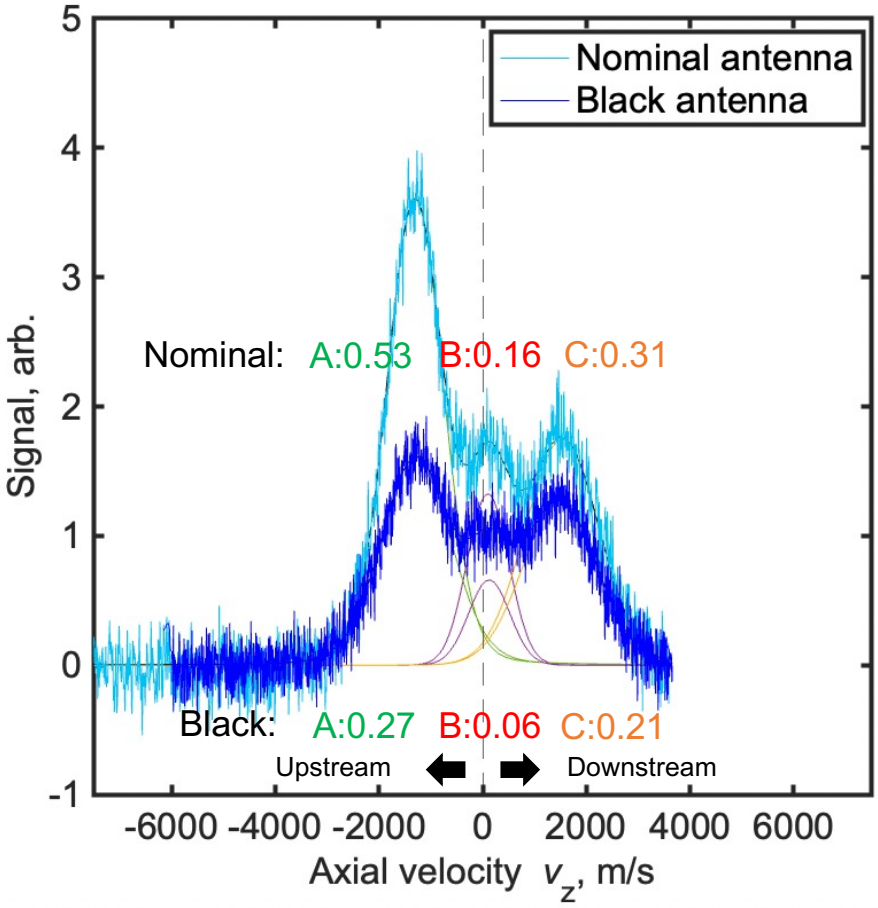

Figure 3.52: Comparison of axial IVDF and its populations (A, B, C) between nominal antenna (cyan) and black antenna (blue) (painted to suppress laser beam reflection) near antenna (X = 0 mm, Z = -11 mm). The numbers indicate the intensity normalized by that for the nominal conditions.

3.7 Anode current oscillation and radiated emission measurements

In the LIF measurement of Hall thrusters, it was reported that ion oscillation affects the IVDF in the time-averaged LIF.[72][73] The relationship between ion oscillation and time-averaged IVDFs has been discussed.[74] In addition, it was reported that the integrated time-resolved LIF signal is comparable to the time-averaged LIF signal.[75] In this study, the results suggest a similar phenomenon for a microwave discharge cathode.

3.7.1 Experimental setup

To investigate the relationship between the IVDF and ion oscillation, the anode current oscillation and the radiated emission are measured using a current probe "YOKOGAWA 700937" and a conical log spiral antenna "RAVEN ENGINEERING 93491-2", respectively. Photograph of conical log spiral antenna is shown in Figure 3.54. To measure the radiated emission, the microwave discharge cathode is installed in a glass chamber, as shown in Figure 3.53. The radiated emission was measured from the axial and radial directions. Experimental conditions are summarized in Table 3.2. This experiment is conducted in diode mode under nominal conditions (P_{m} = 8 W, $\dot{m}_{\mathrm{c}}$ = 0.7 sccm, I_{a} = 180 mA). In previous research, the radiated emission measurement was conducted before cathode improvement for Hayabusa2, and a fundamental frequency of 160 kHz as well as harmonics up to the fifth harmonic were confirmed.[76] Therefore, we conducted a radiated emission measurement for the developed cathode for comparison with the anode oscillation measurement using a current probe.

Table 3.2: Experimental conditions for measurements of anode current oscillation and radiated emission.

Parameter	Value
Microwave frequency	4.25 GHz
Microwave power, P_{m}	8 W
Xenon flow rate, $\dot{m}_{\mathrm{c}}$	0.7 sccm (0.069 mg/s)
Anode current, I_{a}	180 mA
Anode voltage, V_{a}	32 V
Microwave antenna	Flight model (Hayabusa2)
Background pressure	3×10^{-3} Pa at 0.7 sccm Xe
Nominal conditions	P_{m} = 8 W, $\dot{m}_{\mathrm{c}}$ = 0.7 sccm, I_{a} = 180 mA

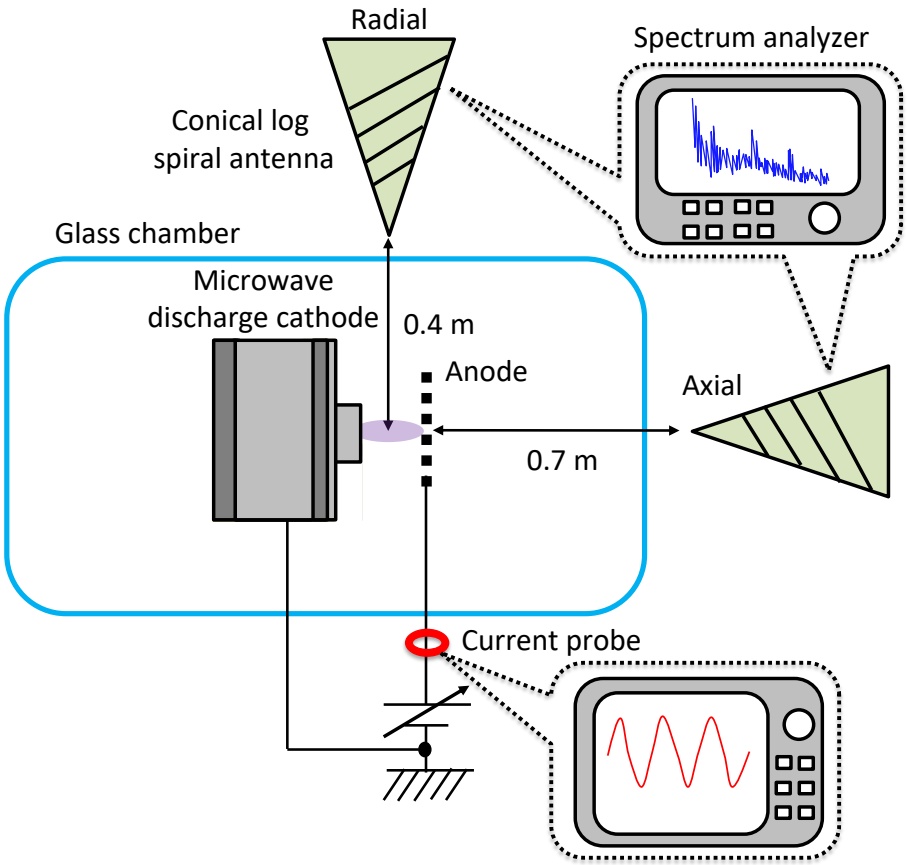

Figure 3.53: Experimental setup for anode current oscillation and radiated emission measurement.

Figure 3.54: Conical log spiral antenna.

3.7.2 Results

Figures 3.55(a)-(c) respectively show the current waveform obtained by the current probe, its fast Fourier transform (FFT), and the radiated emission in diode mode operation at nominal conditions. Table 3.3 summarizes the results shown in Figure 3.55. Figure 3.55(b) shows a fundamental frequency of about 180 kHz and harmonics up to the fourth harmonic. Similarly, Figure 3.55(c) shows a fundamental frequency of about 180 kHz and harmonics up to at least the third harmonic. It is found that the measurement direction did not significantly affect the results. Additionally, the fundamental frequency is within 2% of that derived from the current probe results. This fundamental frequency has a difference of about 20 kHz from that reported in previous research because of differences in the cathode conditions.

Table 3.4 shows a comparison of the amplitude of the fundamental frequency for different mass flow rates with $P_{\mathrm{m}} = 8$ W, $I_{\mathrm{a}} = 180$ mA. The amplitudes of the anode oscillations were not significantly different, but the amplitude was largest at $\dot{m}_{\mathrm{c}} = 0.7$ sccm, while $\dot{m}_{\mathrm{c}} = 0.9$ sccm was the second largest and 0.5 sccm was the third largest. These characteristics were also confirmed in previous research.[76]

Table 3.3: Experimental results from anode current probe and radiated emission measurements.

	Anode current probe			Radiated emission
Degree of harmonics, i	ω_i, kHz	θ_i, rad	G_i	ω_i, kHz
1	183	25.2	1	187
2	373	20.0	0.39	375
3	553	1.8	0.21	560
4	739	-14.6	0.11	-

Table 3.4: Comparison of the amplitude of the fundamental frequency for different mass flow rates with $P_{\mathrm{m}} = 8$ W, $I_{\mathrm{a}} = 180$ mA.

Xenon flow rate, $\dot{m}_{\mathrm{c}}$	Amplitude of fundamental frequency, dB
0.5	−4.8
0.7	5.0
0.9	3.0

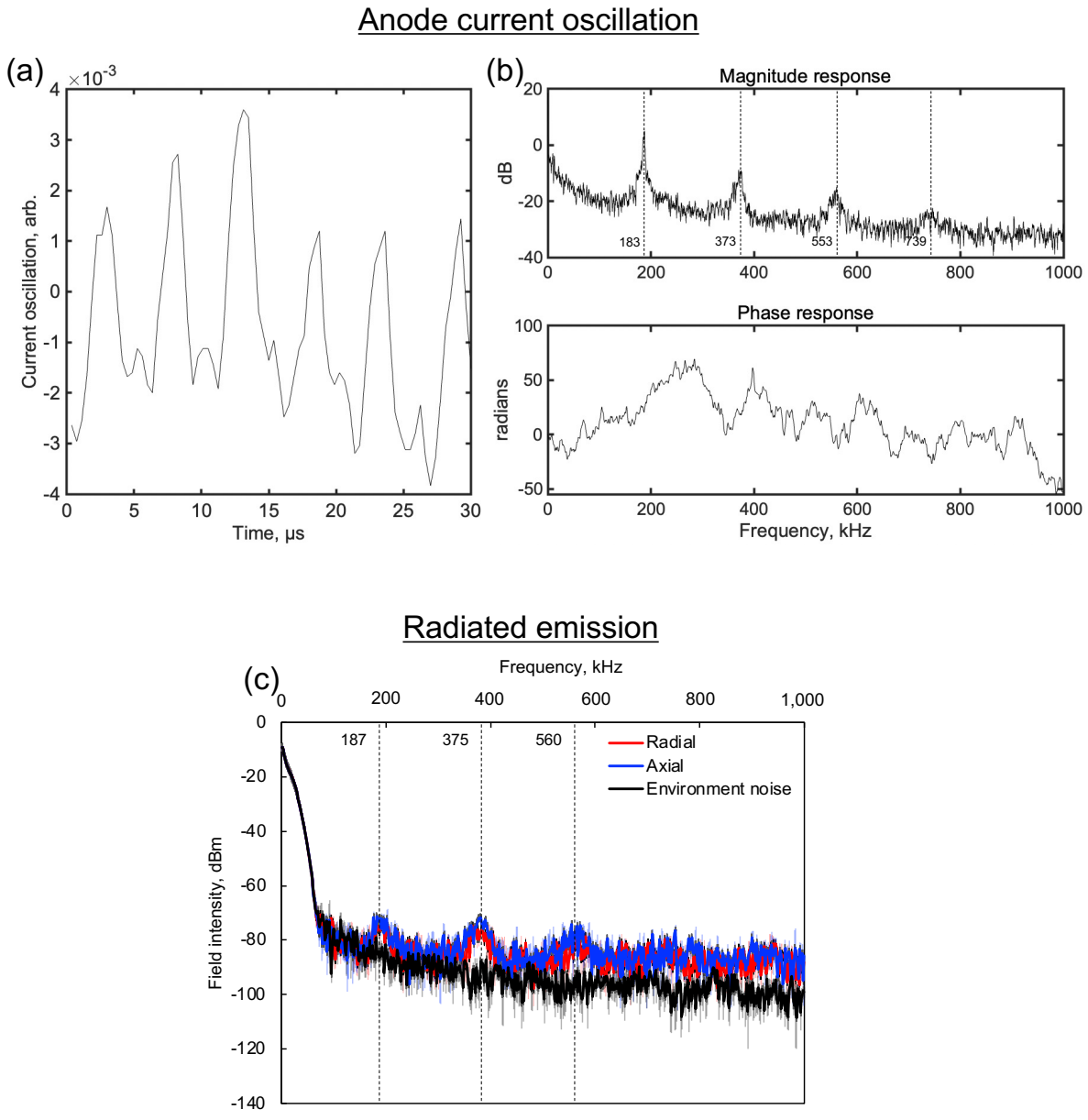

Figure 3.55: (a) Current waveform obtained using current probe and (b) its FFT. (c) Radiated emission in diode mode operation at $P_{\mathrm{m}} = 8$ W, $\dot{m}_{\mathrm{c}} = 0.7$ sccm, $I_{\mathrm{a}} = 180$ mA.

3.8 Discussion of multimodal IVDF

The results of the LIF measurements can be summarized as follows:

- Multimodal IVDFs were measured inside the cathode and in the plume region.
- Changing the parameters (P_{m}, $\dot{m}_{\mathrm{c}}$, I_{a}) did not affect the fluorescence intensity ratio for a given population.
- The black antenna model showed a significantly degraded performance and changed the LIF intensity ratio for each peak, while the intensity ratio for Population C increased.

In this study, we obtained a time-averaged LIF signal that integrated the instantaneous velocity function over the wavelength sweep time of the laser. When the plasma oscillated, the time averaged LIF signal included a multimodal IVDF.

To discuss the possibility of multimodal IVDFs, a simple model is introduced. For simplicity, the Maxwellian distribution is that expressed in Eq. 3.6

$$f(v) = A \exp\left\{ \frac{M(v - v_0)^2}{2kT_{\mathrm{i}}} \right\} \tag{3.6}$$

Here, we assume that the instantaneous bulk velocity v_0 has the oscillation components shown in Eq. 3.7,

$$v_0(t) = v_{0\mathrm{c}} + \Delta v_0 \sum_i G_i \sin(\omega_i t + \theta_i) \tag{3.7}$$

Here, i is the degree of the fundamental wave and harmonics. As an example, Figure 3.56 shows the case of simple oscillation at $T_{\mathrm{i}} = 423$ K, $v_{0\mathrm{c}} =$ -200 m/s, and $\Delta v_0 =$ 2,000 m/s. The ion temperature T_{i} is taken to be the cathode wall temperature (423 K). Figure 3.56(a) shows the instantaneous bulk velocity with simple oscillation. Figure 3.56(b) shows the single 423-K Maxwellian distribution. Figure 3.56(c) shows the IVDF simulated using the model. The single Maxwellian distribution moves to the negative- or positive-velocity region depending on the probability distribution, which is determined by the instantaneous bulk velocity v_0 oscillation.

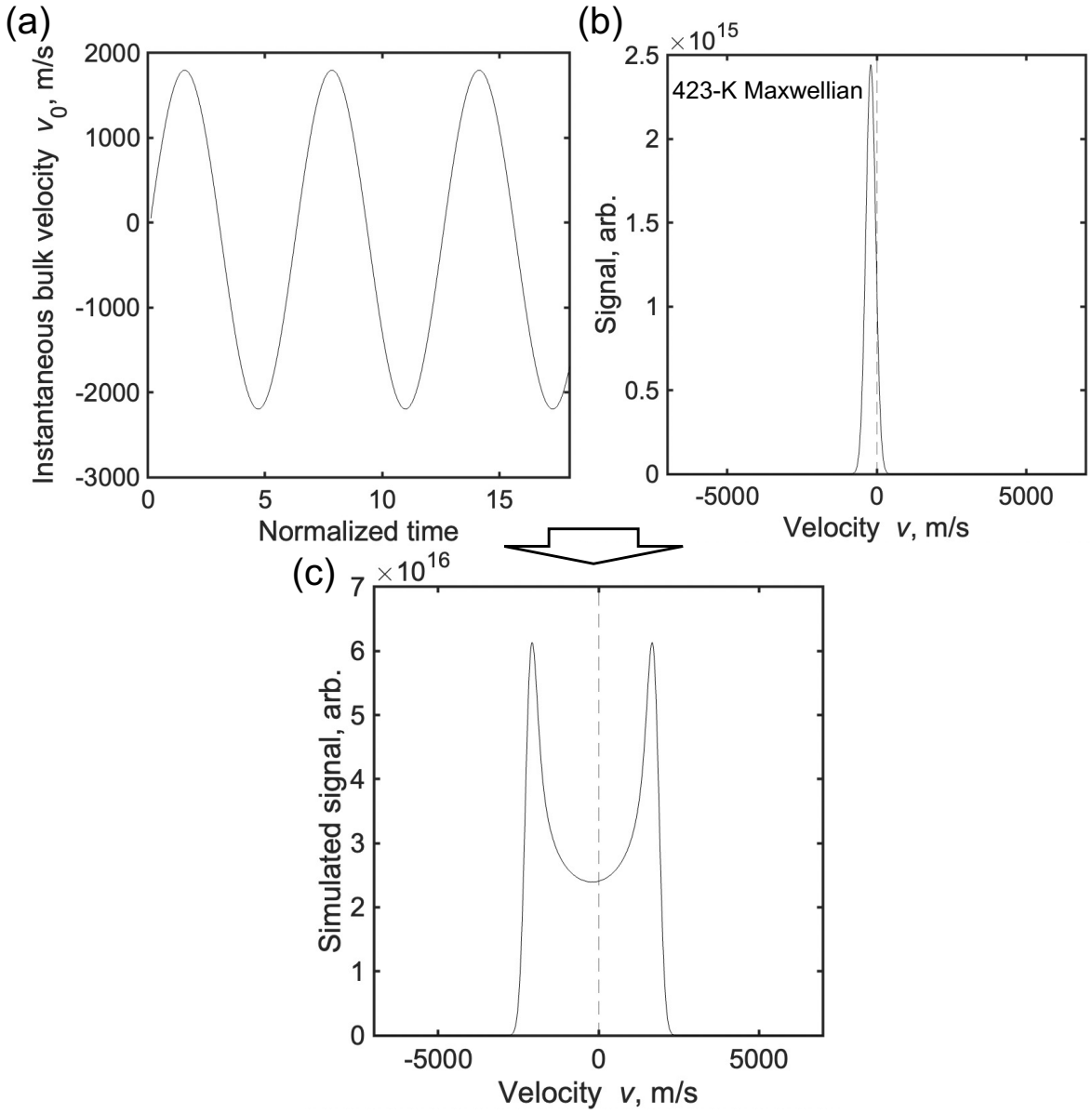

Figure 3.56: Effect of ion oscillation on IVDF. (a) Instantaneous bulk velocity with simple oscillation, (b) single 423-K Maxwellian distribution, and (c) IVDF simulated using model.

The actual ion oscillation is more complicated. Therefore, it is possible that the asymmetry of a multimodal IVDF depends on phase θ, intensity G, and frequency ω. From the results in Figure 3.55(a), we simply simulated the signal in the time-averaged LIF using Eq. 3.6. As described above, the anode current oscillates and the radiated emission shows the same spectrum characteristics. We assume that the electric field and ions oscillate in the same manner. The normalized waveform in Figure 3.55(a) was substituted into Eq. 3.6. Figure 3.57 shows a normalized comparison between the simulated asymmetric IVDF at at $T_{\mathrm{i}} = 423$ K and $\Delta v_0 = 2{,}000$ m/s and the measured IVDF at X = 0 and Z = 1mm in Figure 3.35. As an example, we compare the LIF signal at X = 0 and Z = 1mm in Figure 3.35 because this point shows dense plasma and should significantly affect the results of current oscillation and radiated emission. The measured IVDF is 30%-40% wider than the simulated IVDF. This is because the simulated IVDF was derived from a Maxwellian distribution, whereas the measured IVDF includes Lorentzian broadening (especially Zeeman splitting and saturation broadening), as described above. As shown in Figure 3.57, the simulated IVDF well matches the measured IVDF, with an R^2 value of 0.82. Therefore, the asymmetry of the multimodal IVDF is considered to be due to ion oscillation.

In order to consider the total effect of Gaussian (f of Eq. 3.6) and Lorentzian ($\equiv l$) functions, both functions were convolved as follows.

$$W = (f * l)(v_{\mathrm{Z}}) \tag{3.8}$$

Here, the Lorentzian broadening was assumed to be 40%. Figure 3.58 shows the case for a Lorentzian broadening of 40% of that of the Gaussian broadening. The figure shows that the R^2 value of 0.94 was higher than that in Figure 3.57. The IVDF was smoothed by the Lorentzian broadening, but a bimodal characteristic was observed.

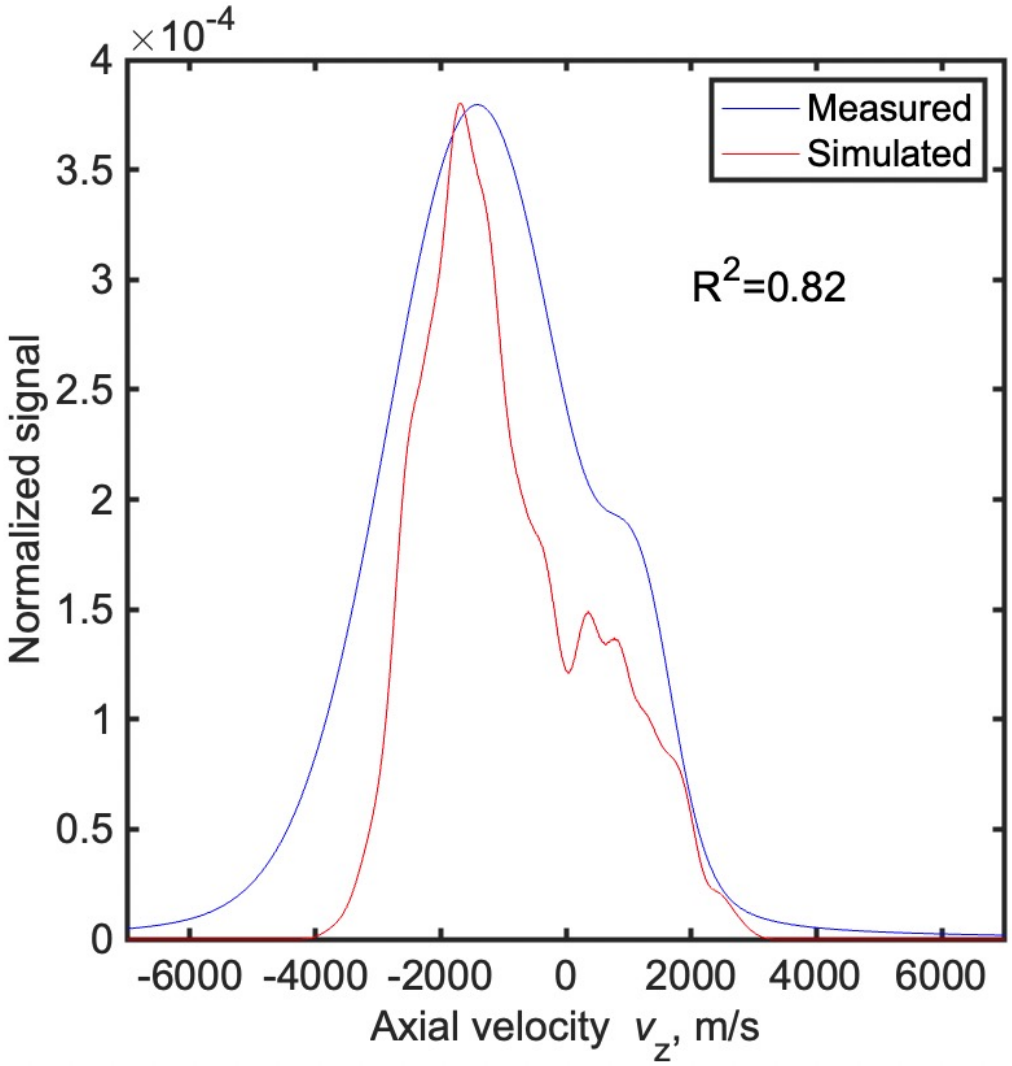

Figure 3.57: Comparison of measured IVDF at X = 0 and Z = 1 mm (blue) and simulated IVDF at T_i = 423 K, Δv_0 = 2,000 m/s (red). The peak value for the model is normalized with respect to the measured data.

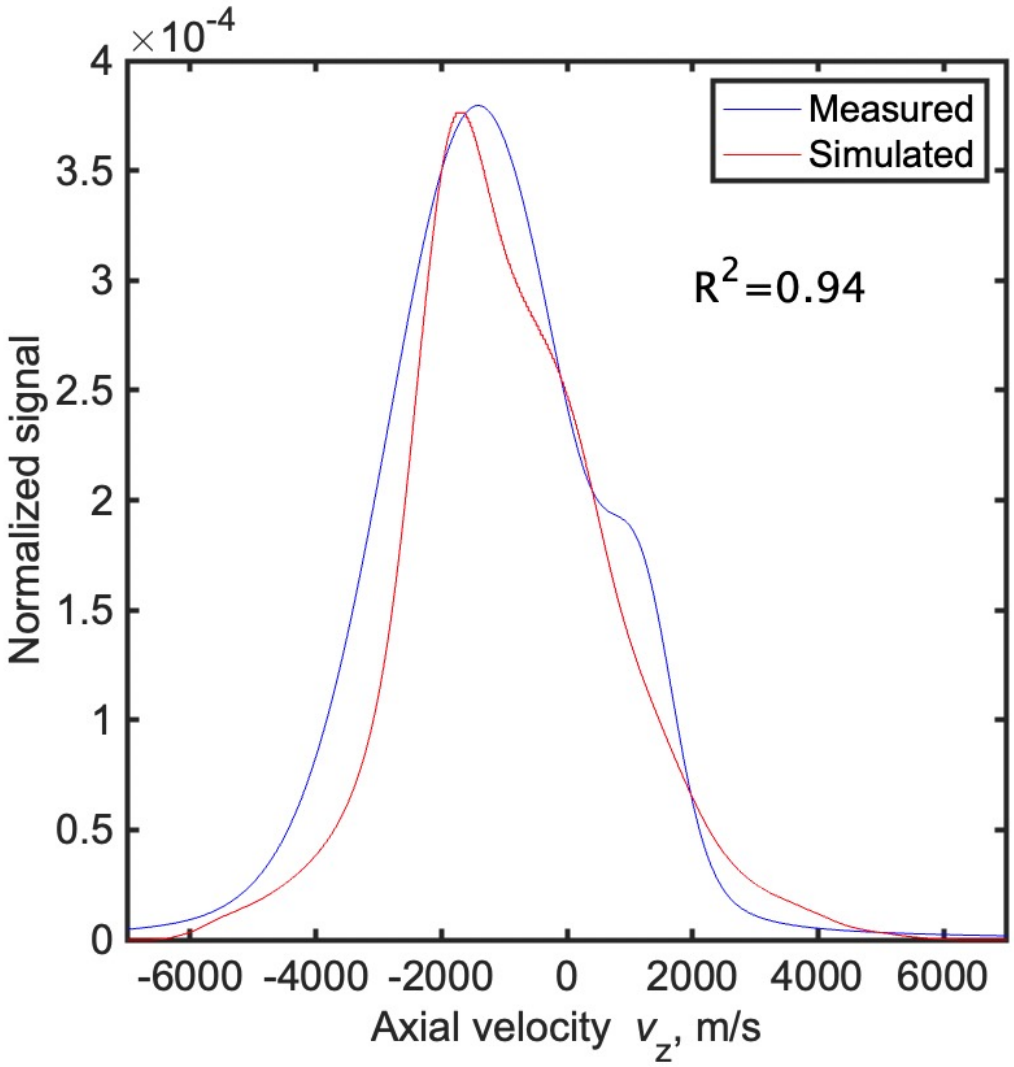

Figure 3.58: Comparison of measured IVDF at X = 0 mm, Z = 1 mm (blue) and simulated IVDF at T_i = 423 K, Δv_0 = 2,000 m/s (red) with 40% Lorentzian broadening. The peak value for the model is normalized with respect to the measured data.

3.9 Plasma potential measurements

As shown in Figure 3.39, ions flow from the anode to the nozzle on the central axis. The mean velocity was largest near the anode and decelerated as the ions approached the cathode. To investigate why this is the case, we measured the plasma potential in the plume region. In previous research, the plasma potential was measured on the central axis of the prototype cathode,[29] whereas the current measurement examined the plasma potential in two-dimensions.

3.9.1 Experimental setup

To measure the plasma potential, we used an emissive probe. Figure 3.59 shows a schematic diagram of the emissive probe and Figure 3.60 shows a photograph of the probe. Figure 3.61 shows the experimental setup for the plasma potential measurements. The emissive probe was inserted from the radial direction. Figure 3.62 shows the measurement points. A total of 56 measurement points, X = 0–9 mm and Z = 3–10 mm, were taken, and were selected so that the change in anode voltage was 1 V or less. Near the nozzle, the plume cannot be maintained, as this would require a significant increase in anode voltage. Due to physical interference between the probe holder and the cathode stage, only one side ($X \geq 0$) was measured with respect to the central axis.

Figure 3.63 shows the relationship between the probe potential and the heater current. The probe potential saturated above 5.5 A and the heater disconnected above 7 A. It was found that the change in the anode voltage during the heater current sweep was 0.1 V or less. Therefore, the heater current was set to 5.5 A. Experimental conditions are summarized in Table 3.5.

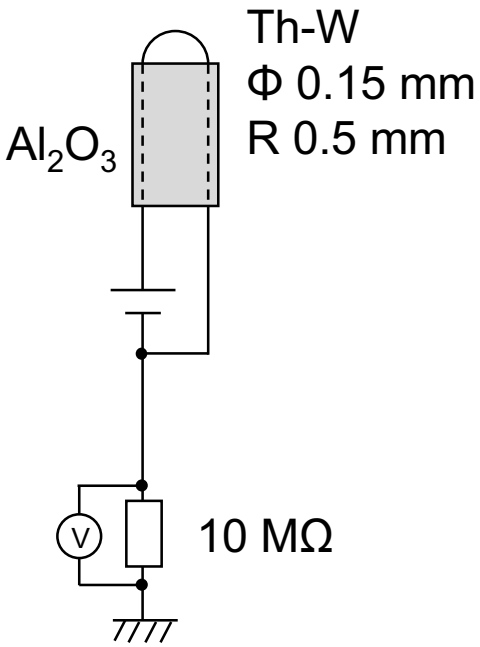

Figure 3.59: Emissive probe for plasma potential measurements.

Figure 3.60: Photograph of emissive probe.

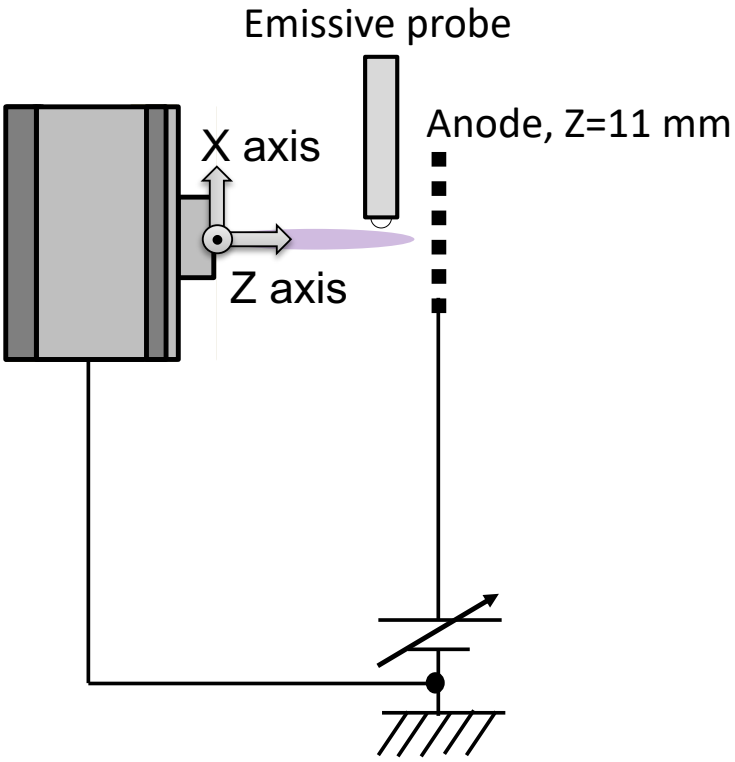

Figure 3.61: Experimental setup for plasma potential measurements.

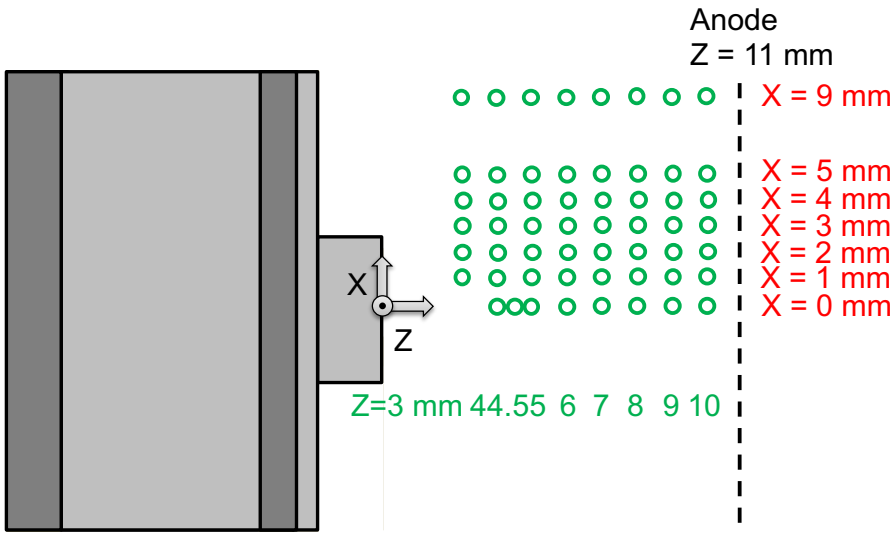

Figure 3.62: Plasma potential measurement points.

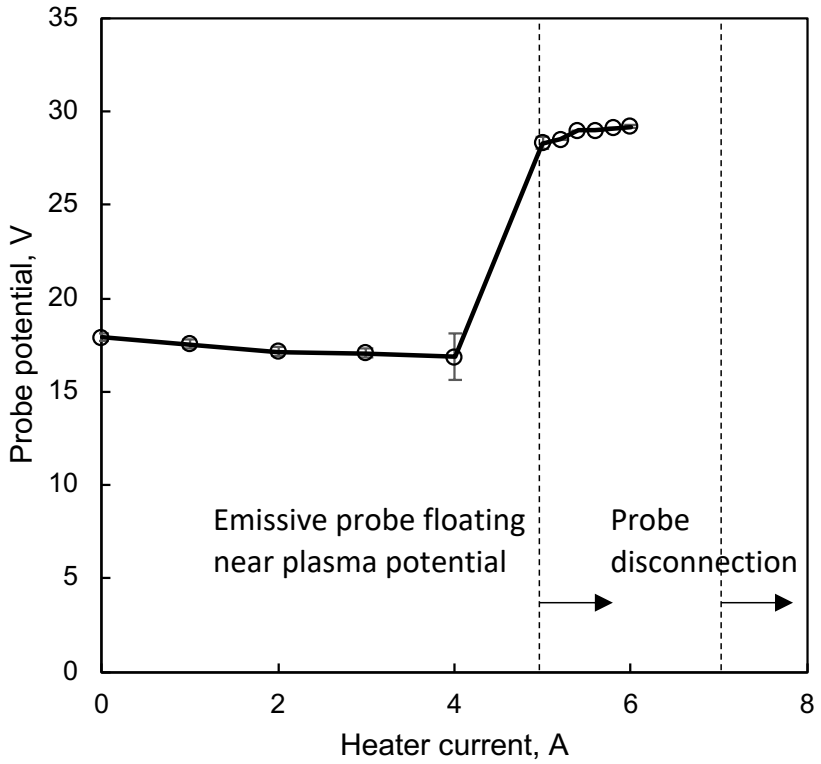

Figure 3.63: Relationship between probe potential and heater current.

Table 3.5: Experimental conditions for plasma potential measurements.

Parameter	Value
Microwave frequency	4.25 GHz
Microwave power, P_{m}	8 W
Xenon flow rate, $\dot{m}_{\mathrm{c}}$	0.7 sccm (0.069 mg/s)
Anode current, I_{a}	180 mA
Anode voltage, V_{a}	35 V
Microwave antenna	Flight model (Hayabusa2)
Heater current	5.5 A
Background pressure	3×10^{-4} Pa at 0.7 sccm Xe

3.9.2 Results

When the emission current from the probe surface becomes higher, a sufficient amount of electron cloud forms in front of the surface, which makes the zero electric field, and space-charge limited condition is reached. Because the space-charge effect exists in plasma potential measurements using emissive probe I-V characteristics, it affects the accuracy of the measurements. The difference between plasma potential V_p and probe potential V_f is known in Eq. 3.9.[77][78][79][80]

$$V_\mathrm{f} - V_\mathrm{p} \approx -T_\mathrm{e}/e \tag{3.9}$$

The probe potential V_f determines the plasma potential V_p with an accuracy of an order of T_e/e, and the accuracy does not depend on the plasma density. Therefore, the V_p is calculated by the Eq. 3.9 using a measured value of T_e in previous research.[30]

Figure 3.64 shows the results of the plasma potential measurements. Figure 3.65 shows a two-dimensional plot of the plasma potential. These figures show that there is a potential valley on the central axis. The plasma potential rises by 1 V between Z = 4 mm and 5 mm, which corresponds to a deceleration of about 500 m/s based on conservation of energy. As shown in Figure 3.39, the measured mean velocity decreases by about 300 m/s between Z = 3 and 5 mm, comparable to the results of the plasma potential measurements.

Notably, at X = 1 mm, the potential gradient is large in the deceleration direction. This potential gradient is the cause of ion deceleration near the nozzle. Away from the central axis, this potential gradient generates slow ions in the downstream direction.

In addition, the plasma potential increases in the radial direction, which is why the radial velocity is smaller than the axial velocity.

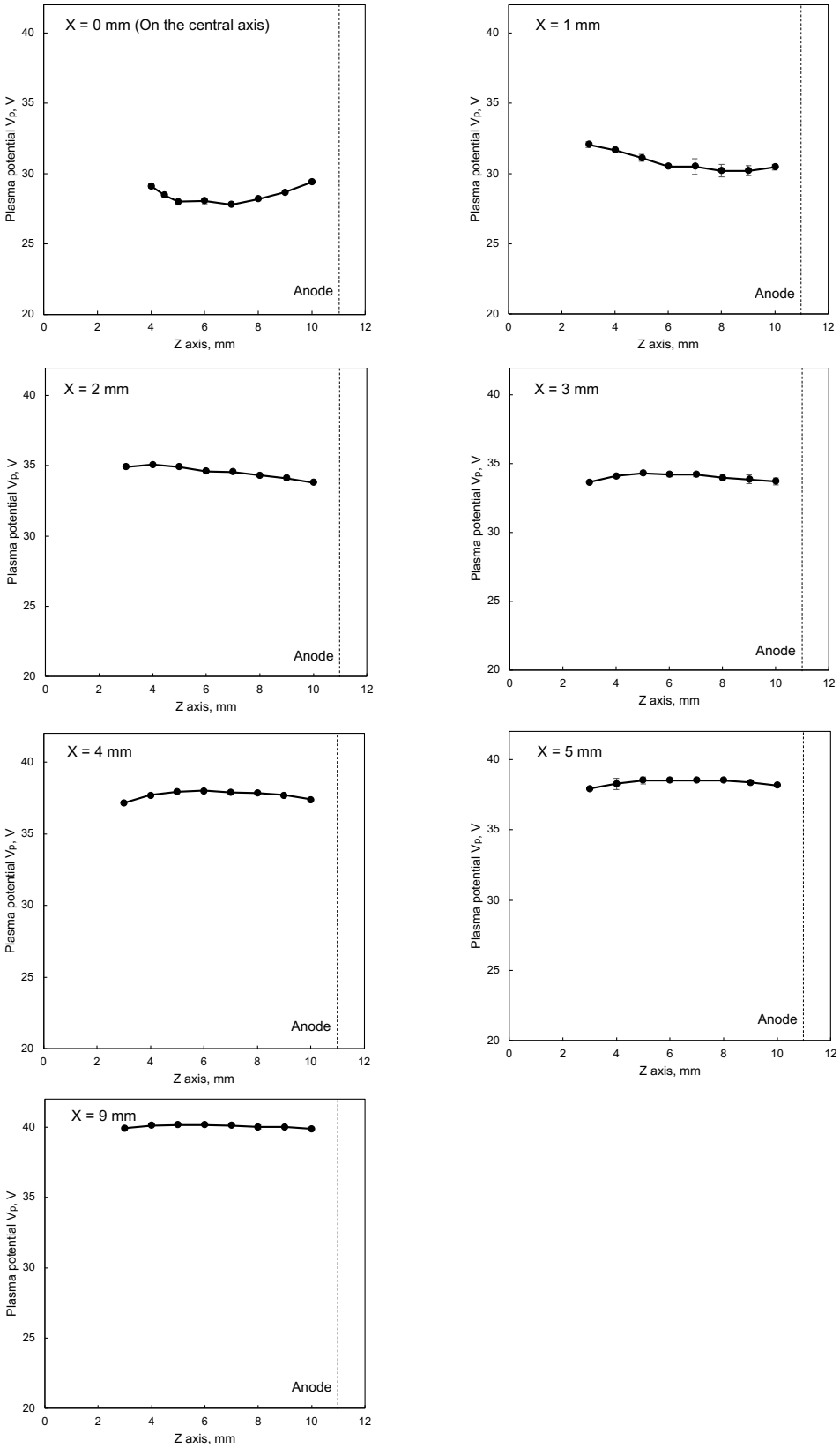

Figure 3.64: Plasma potential distribution measured by emissive probe in plume at $P_{\mathrm{m}} = 8$ W, $\dot{m}_{\mathrm{c}} = 0.7$ sccm, $I_{\mathrm{a}} = 180$ mA, $V_{\mathrm{a}} = 35$ V.

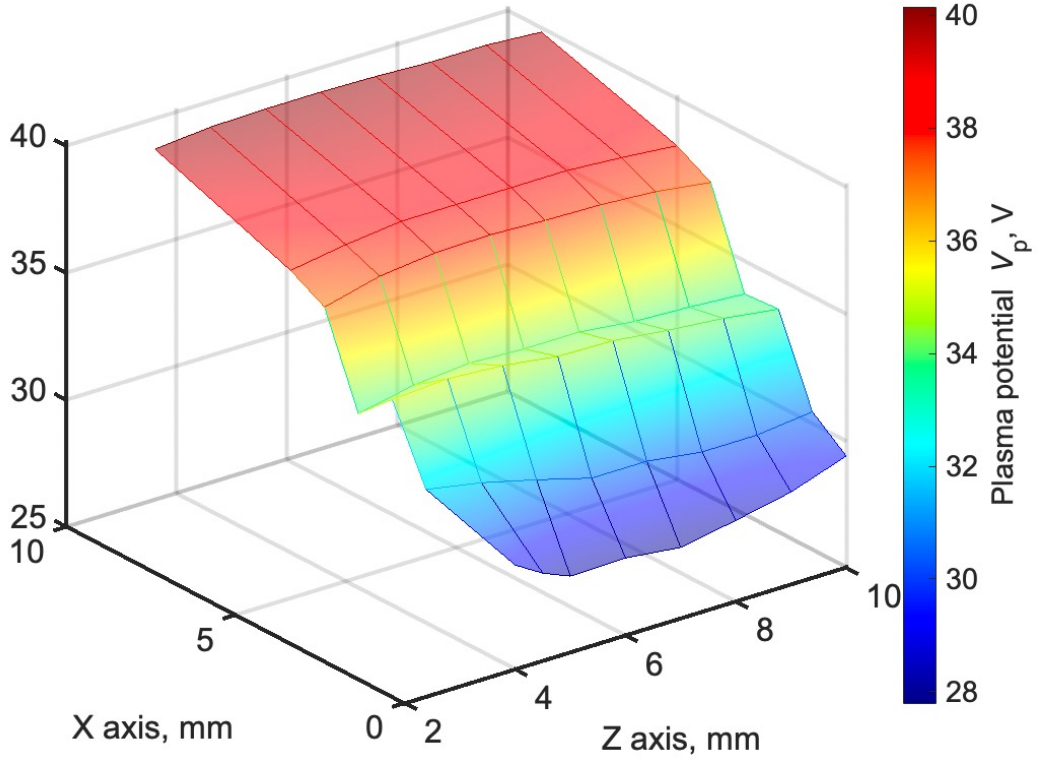

Figure 3.65: Two-dimensional plot of plasma potential shown in Figure 3.64.

3.10 LIF measurements for improved models

This section details LIF measurements conducted on the improved microwave discharge cathode described in Chapter 2.

3.10.1 Improvement by coil magnetic field

In Section 2.1, the nozzle magnetic field was redesigned and the performance was improved. In this section, we detail the measurements of the IVDF for the improved model on the plume.

Figure 3.66 shows the spatial distribution of the axial LIF intensity. Similarly, in the improved model, it was found that there were two peaks in the axial IVDF in the plume.

Figure 3.67 shows an intensity comparison between the improved model and the nominal model at $P_{\mathrm{m}} = 8$ W, $\dot{m}_{\mathrm{c}} = 0.7$ sccm, $I_{\mathrm{a}} = 180$ mA. It was found that the improved model had twice the intensity of the nominal model in the plume. It is suggested that the dense plasma was distributed in the plume due to the improvement of electron transportability by the weak magnetic field near the nozzle.

Figure 3.68 shows the mean xenon ion velocity vectors in the plume. The mean velocities differ by a maximum of several 100 m/s compared to the nominal model in the axial and radial directions.

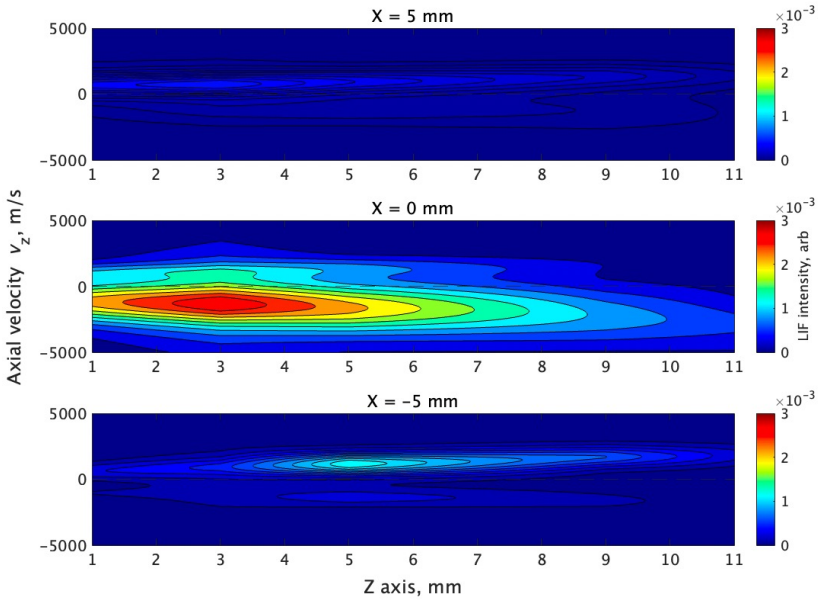

Figure 3.66: Spatial distribution of axial LIF signal for improved model with a coil at $P_{\mathrm{m}} = 8$ W, $\dot{m}_{\mathrm{c}} = 0.7$ sccm, $I_{\mathrm{a}} = 180$ mA.

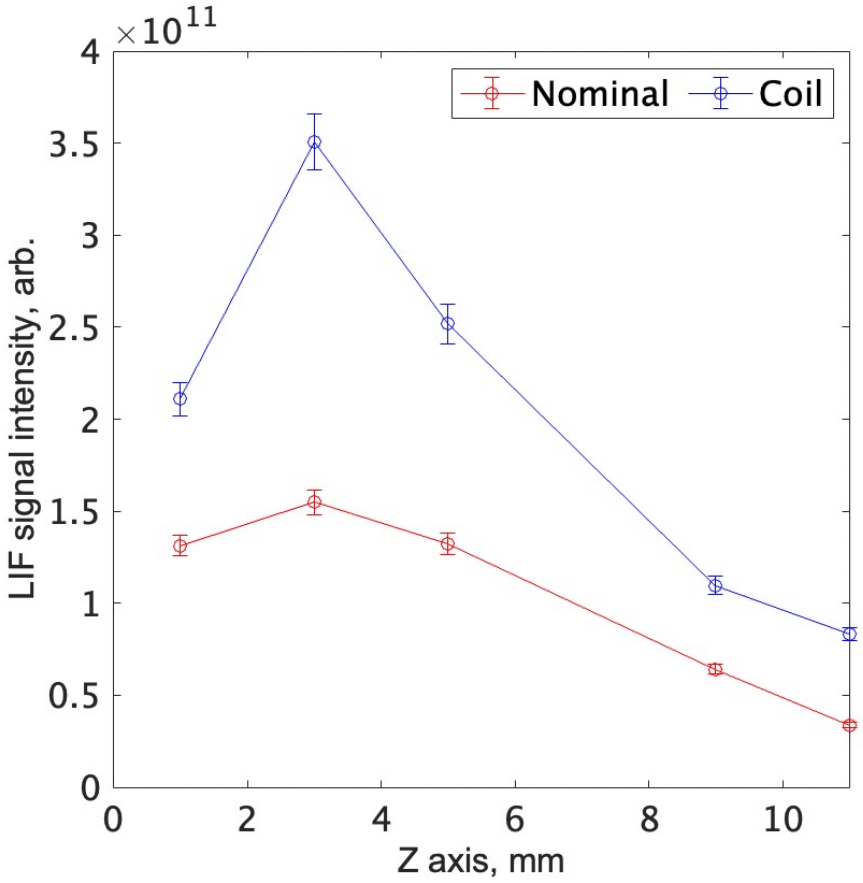

Figure 3.67: Intensity comparison between improved model with a coil and nominal model at $P_{\mathrm{m}} = 8$ W, $\dot{m}_{\mathrm{c}} = 0.7$ sccm, I_{a} =180 mA.

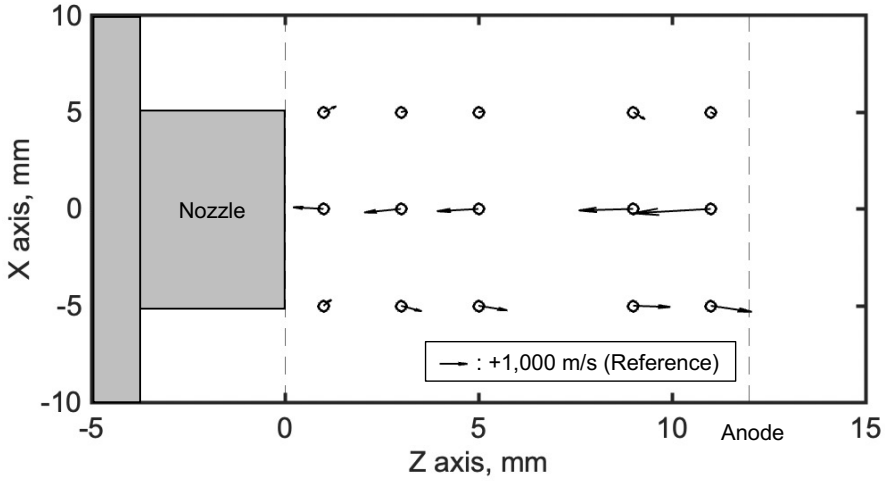

Figure 3.68: Mean xenon ion velocity vectors for improved model with a coil in the plume region at $P_{\mathrm{m}} = 8$ W, $\dot{m}_{\mathrm{c}} = 0.7$ sccm, $I_{\mathrm{a}} = 180$ mA.

3.10.2 Improvement of mirror ratio and enhancement of magnetic field intensity

In Section 2.2, the mirror ratio and the magnetic field intensity were increased by the redesign of the discharge chamber. In this section, the IVDF measurements using the improved model are described. The experimental conditions are shown in Table 3.6.

Figures 3.69 and 3.70 show the spatial distribution of the axial LIF intensity for the nominal and improved models, respectively. It is noted that the contour scale is different from Figures 3.36 and 3.66 because the parameters of the lock-in amplifier were different. As shown in these figures, the intensity was higher over the whole plume for the improved model.

Figure 3.71 and Figure 3.72 show results of LIF spectroscopy inside nominal and improved model at $P_{\mathrm{m}} = 15$ W, $\dot{m}_{\mathrm{c}} = 1.5$ sccm, $I_{\mathrm{a}} = 300$ mA. The improved model generated a 40% higher plasma density inside the cathode with peak velocities increased by 25%.

Figure 3.73 shows a fast Fourier transform (FFT) of the anode current oscillation for the improved model at $P_{\mathrm{m}} = 15$ W, $\dot{m}_{\mathrm{c}} = 1.5$ sccm, $I_{\mathrm{a}} = 300$ mA. A fundamental frequency of about 85 kHz is can be seen.

The same theoretical model as described in Section 3.8 was applied to these results. Figure 3.74 shows a normalized comparison between the simulated asymmetric IVDF at $T_{\mathrm{i}} = 423$ K and $\Delta v_0 = 2{,}000$ m/s and the measured IVDF of the improved model with high mirror ratio yoke and enhanced field at X = 0 and Z = 1mm. The measured IVDF was about 45% wider than the simulated IVDF. This is because the simulated IVDF was derived from a Maxwellian distribution, whereas the measured IVDF includes Lorentzian broadening, as described above. As shown in Figure 3.74, the simulated IVDF closely matches the measured IVDF, with an R^2 value of 0.88.

Figure 3.75 shows an intensity comparison between the nominal and improved model at $P_{\mathrm{m}} = 15$ W, $\dot{m}_{\mathrm{c}} = 1.5$ sccm, $I_{\mathrm{a}} = 300$ mA. It was found that the improved model produced twice the intensity of the standard model in the plume. The dense plasma contributed to the improved performance.

Figures 3.76 and 3.77 show the mean xenon ion velocity vectors for the nominal and improved models, respectively. Similarly, on the central axis, the mean velocity was toward the cathode. The mean velocity was largest near the anode and decreased nearer the cathode. At X = $\pm$5 mm, the mean velocity was toward the anode. As shown in these figures, there was no significant difference between the two models. Compared with the nominal conditions, as shown in Figure 3.39, the deceleration was large on the central axis. It is suggested that the higher neutral density increases collisions between ions and neutrals.

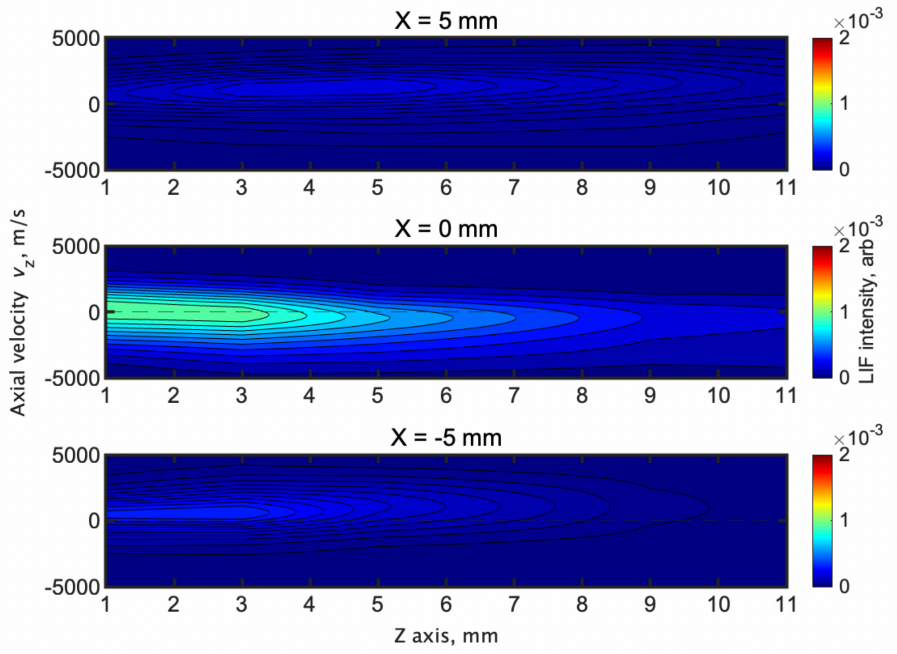

Figure 3.69: Spatial distribution of axial LIF signal for the nominal model at $P_{\mathrm{m}} = 15$ W, $\dot{m}_{\mathrm{c}} = 1.5$ sccm, $I_{\mathrm{a}} = 300$ mA.

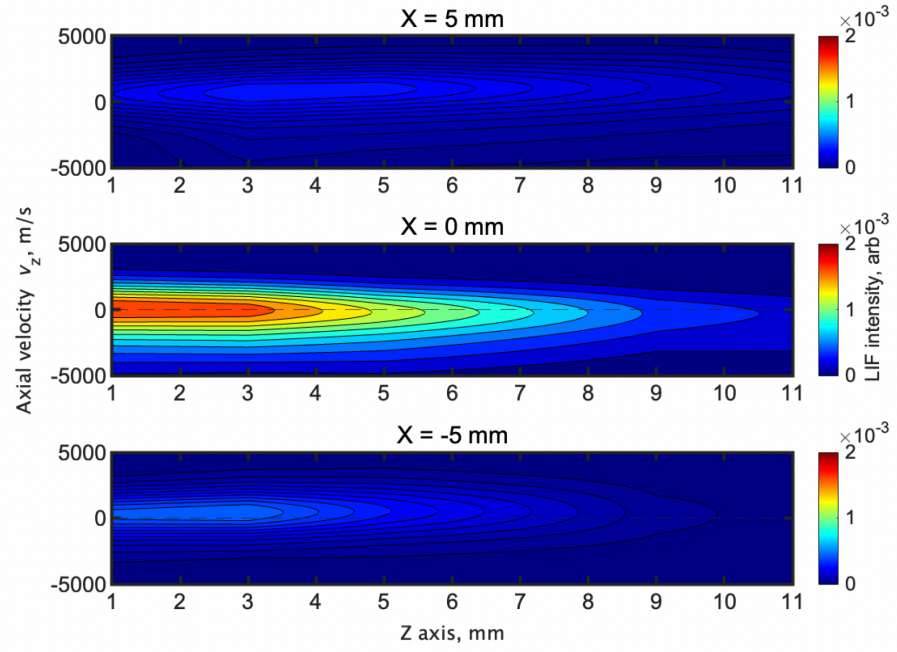

Figure 3.70: Spatial distribution of axial LIF signal for the improved model with high mirror ratio yoke and enhanced field at $P_{\mathrm{m}} = 15$ W, $\dot{m}_{\mathrm{c}} = 1.5$ sccm, $I_{\mathrm{a}} = 300$ mA.

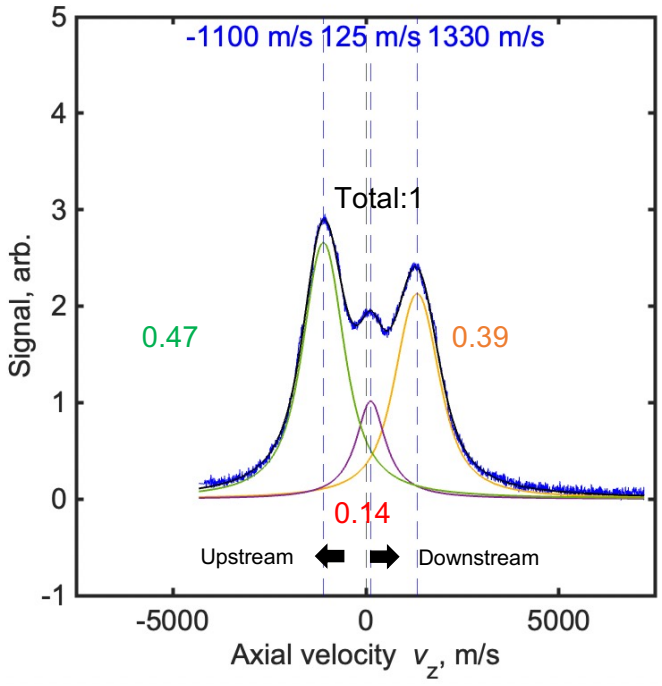

Figure 3.71: Axial result of LIF spectroscopy inside the nominal model at $P_{\mathrm{m}} = 15$ W, $\dot{m}_{\mathrm{c}} = 1.5$ sccm, $I_{\mathrm{a}} = 300$ mA.

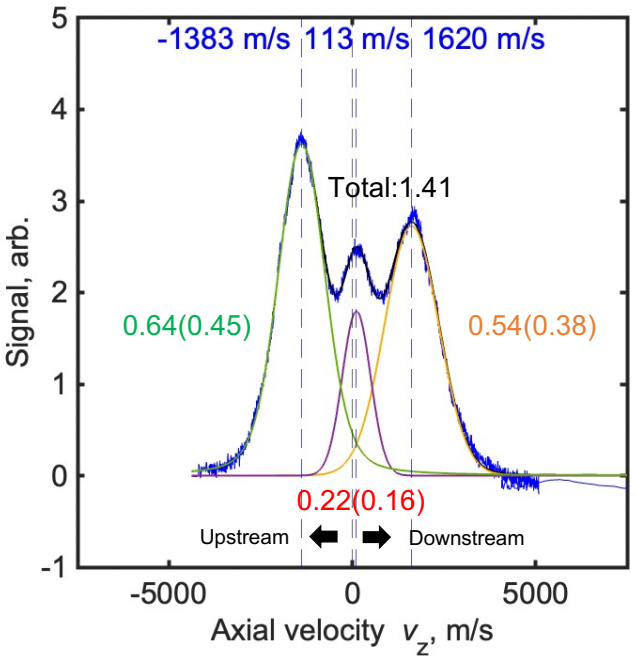

Figure 3.72: Axial result of LIF spectroscopy inside the improved model with high mirror ratio yoke and enhanced field at $P_{\mathrm{m}} = 15$ W, $\dot{m}_{\mathrm{c}} = 1.5$ sccm, $I_{\mathrm{a}} = 300$ mA.

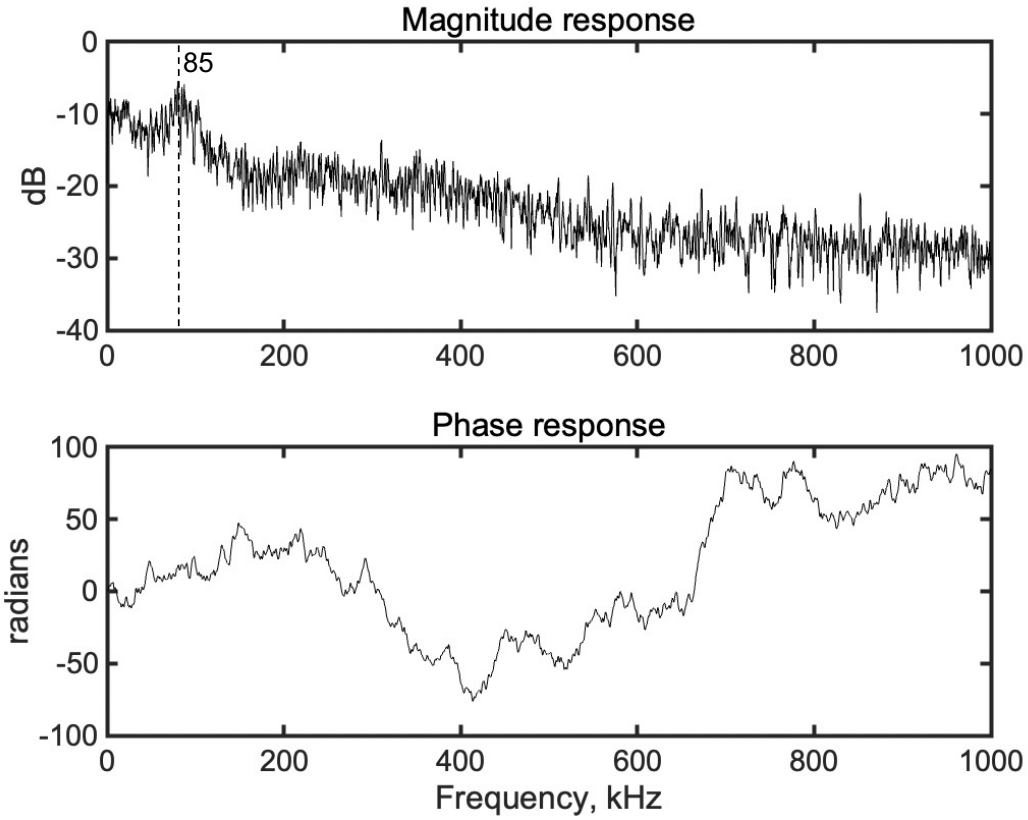

Figure 3.73: FFT of anode current oscillation for the improved model with high mirror ratio yoke and enhanced field at $P_{\mathrm{m}} = 15$ W, $\dot{m}_{\mathrm{c}} = 1.5$ sccm, $I_{\mathrm{a}} = 300$ mA.

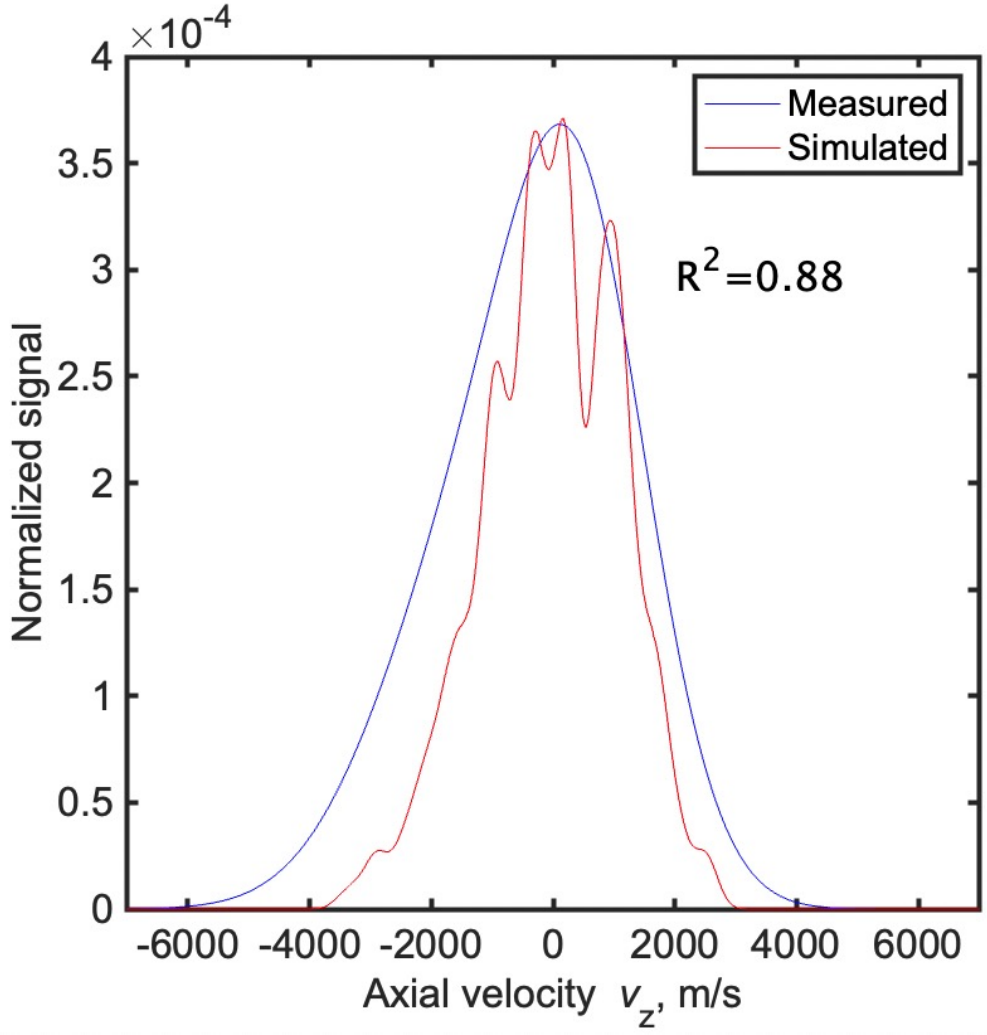

Figure 3.74: Comparison of measured IVDF of the improved model with high mirror ratio yoke and enhanced field at X = 0 and Z = 1 mm (blue) and simulated IVDF at T_i = 423 K, Δv_0 = 2,000 m/s, P_m = 15 W, $\dot{m}_\mathrm{c}$ = 1.5 sccm, I_a = 300 mA (red).

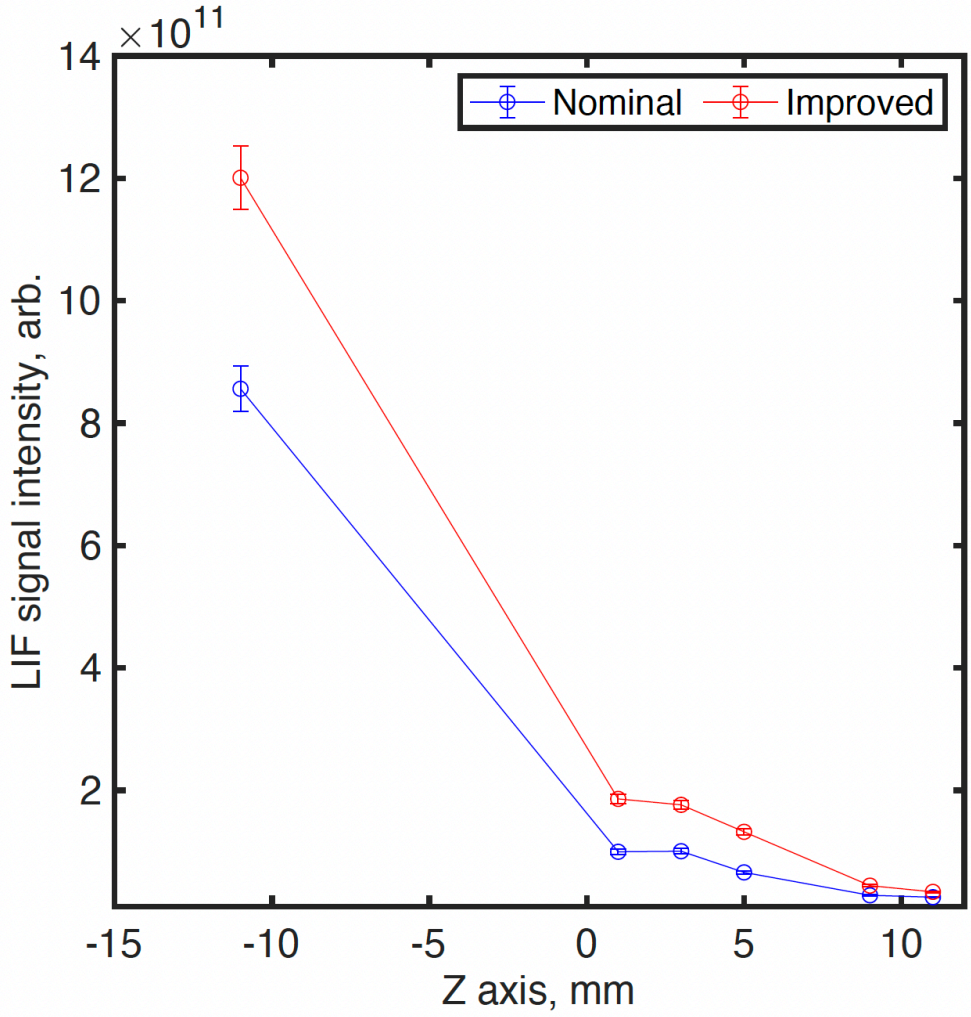

Figure 3.75: Intensity comparison between the nominal model and improved model with high mirror ratio yoke and enhanced field at $P_{\mathrm{m}} = 15$ W, $\dot{m}_{\mathrm{c}} = 1.5$ sccm, $I_{\mathrm{a}} = 300$ mA.

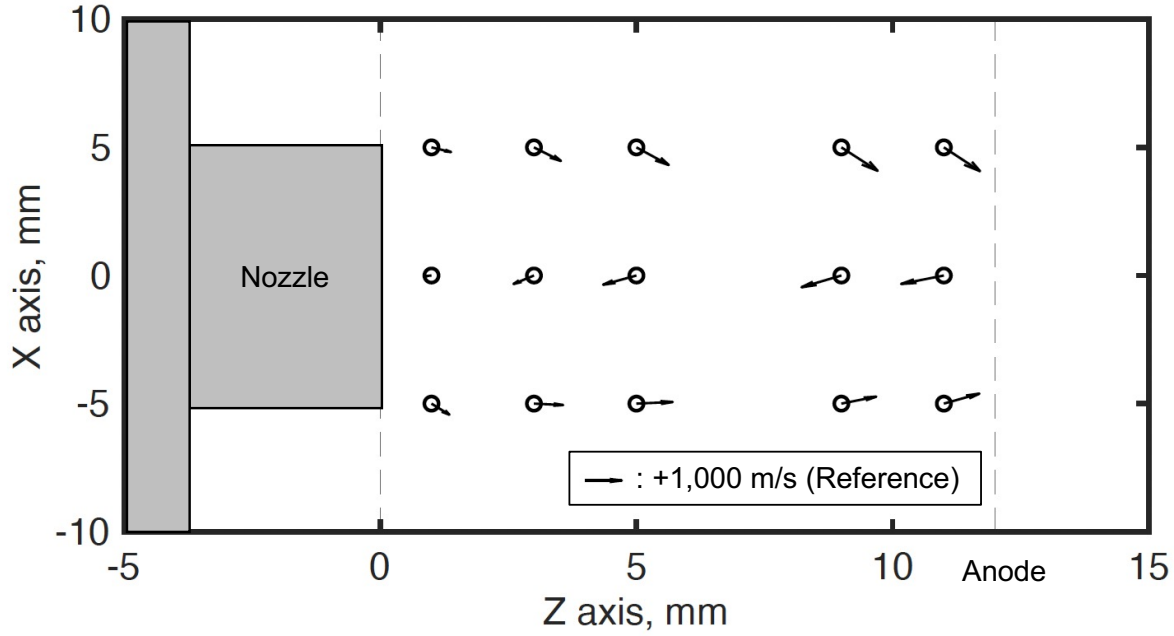

Figure 3.76: Mean xenon ion velocity vectors of the nominal model in the plume at $P_{\mathrm{m}} = 15$ W, $\dot{m}_{\mathrm{c}} = 1.5$ sccm, $I_{\mathrm{a}} = 300$ mA.

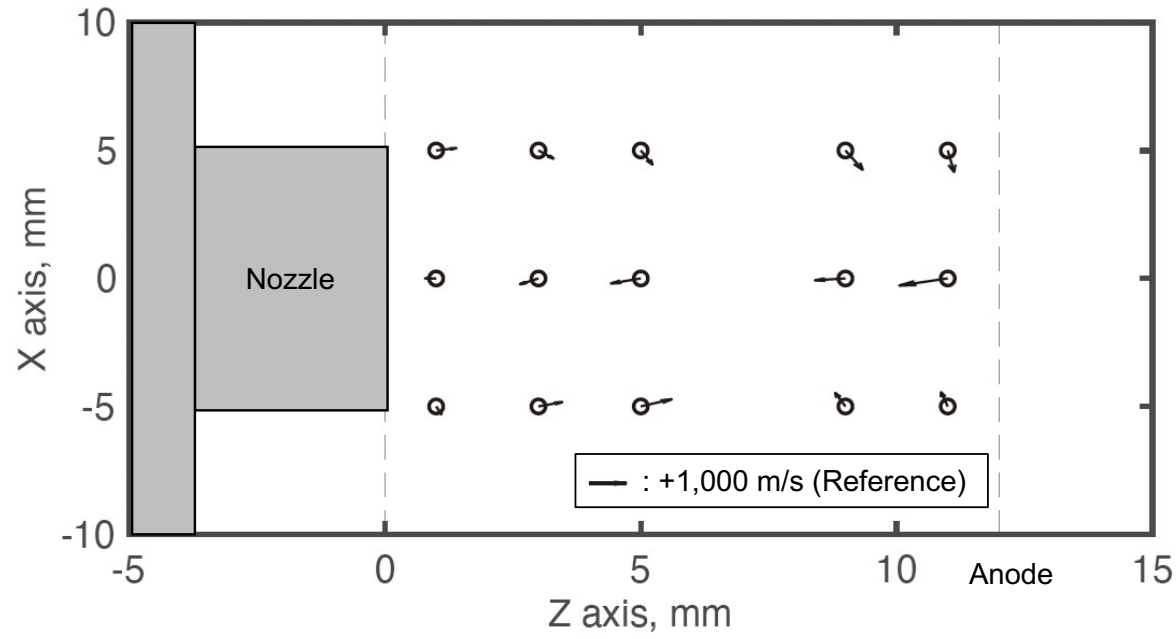

Figure 3.77: Mean xenon ion velocity vectors for the improved model with high mirror ratio yoke and enhanced field in the plume at $P_{\mathrm{m}} = 15$ W, $\dot{m}_{\mathrm{c}} = 1.5$ sccm, $I_{\mathrm{a}} = 300$ mA.

Table 3.6: Experimental conditions for improved microwave discharge cathode for LIF measurements.

Parameter	Value
Microwave frequency	4.25 GHz
Microwave power, P_{m}	15 W
Xenon flow rate, $\dot{m}_{\mathrm{c}}$	1.5 sccm (0.147 mg/s)
Anode current, I_{a}	300 mA
Anode volrage, V_{a}	Nominal: 45 V Improved: 35 V
Microwave antenna	Flight model (Hayabusa2)
Magnetic circuit	Nominal Improved (high mirror ratio yoke and enhanced field)
Background pressure	9×10^{-5} Pa without Xe 7×10^{-4} Pa at 1 sccm Xe

3.11 Ion current in plume region

In this section, ion current I_{i} in plume region is discussed. As shown in Eq. 3.10, I_{i} is calculated.

$$I_{\mathrm{i}} = en_{\mathrm{i}}\bar{v}_{\mathrm{Z}}S\mathrm{p} \tag{3.10}$$

Here, value of n_{i} was calculated by axial LIF results calibrated by the probe measurement results. A diameter of cathode nozzle was ϕ4 mm. For simplicity, I_{i} was calculated from X = -2 mm to X = 2mm. The parameters of $\bar{v}_{\mathrm{Z}}$ and n_{i} were measured values at X = 0 mm. For a simple model, they were assumed to be uniform from X = -2 mm to X = 2 mm.

Figure 3.78 shows I_{i} and its ratio in the plume region of nominal model. At Z = 3 mm and 5 mm, I_{i} was about 6 mA, and its ratio was 5%. In the case of improved model with a coil, as shown in Figure 3.79, they are 12 mA and 10%, respectively.

As shown in Figure 3.78 and Figure 3.78, the ratio of I_{i} to the anode current decreases toward the downstream. It was suggested that the erosion ratio by ions coming from the outside was not significant. The ion energy that affects the durability is mainly obtained in the ion sheath on the discharge chamber wall (however, it cannot be measured by the LIF in this study). It is known that a potential difference between the cathode and ion beam in coupling operation is larger than a potential difference between cathode and anode in diode mode. It was suggested that the difference in plasma parameters in the downstream region did not significantly affect the ion impact on the discharge chamber wall. In the future, the validity will be confirmed by LIF measurements in coupling operation.

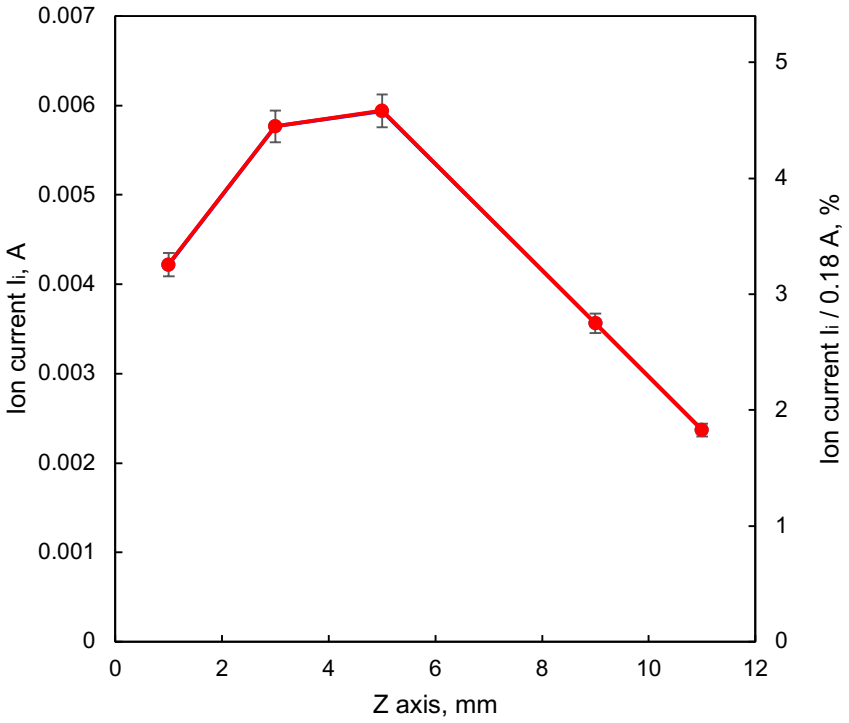

Figure 3.78: Ion current and its ratio in plume region of the nominal model.

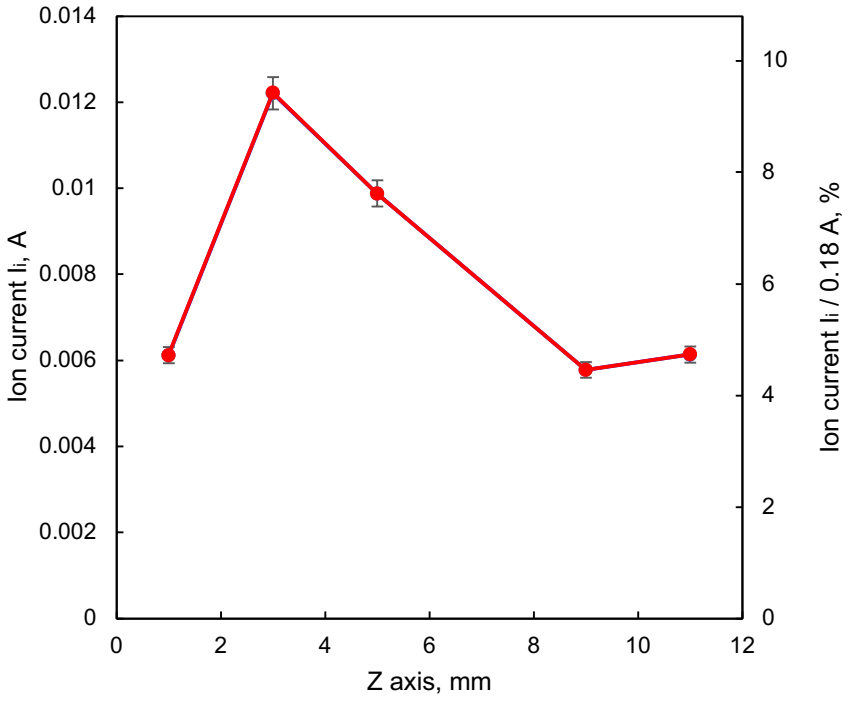

Figure 3.79: Ion current and its ratio in plume region of the improved model with a coil.

3.12 Summary

To investigate the plasma inside a microwave discharge cathode and in the plume region, LIF measurements were conducted during diode mode operation. For this, a microwave discharge cathode with a small optical window, with a performance similar to that of the flight model for Hayabusa2 (with an anode voltage error within 7%), was developed. The anode current oscillation and the radiated emission were measured to examine the relationship between ion oscillation and the IVDF. The results are summarized as follows:

1. It was confirmed that the spatial plume excited ion density distribution obtained from axial LIF measurements matches previous results obtained using an electrostatic probe ($R^2 = 0.96$).
2. On the central axis of the plume, mean ion flow was toward the cathode. It was confirmed that the mean ion flow off axis was toward the anode.
3. On plume region, the calculated ion current I_i was up to 6 mA, and its ratio to anode current was up to 5%. It was suggested that the erosion ratio by ions coming from the outside was limited. In addition, the difference in plasma parameters in the downstream region did not significantly affect the ion impact on the discharge chamber wall.
4. Near the microwave antenna, a trimodal IVDF was confirmed, with an upstream-velocity population (Population A), a near-zero-velocity population (Population B), and a downstream-velocity population (Population C). At other points inside the cathode and in the plume region, bimodal IVDFs were observed.
5. A parametric study showed that larger microwave power P_m and anode current I_a and a smaller xenon flow rate $\dot{m}_\mathrm{c}$ led to a higher total fluorescence intensity (integration of all velocity populations).
6. Near the microwave antenna, the peak velocity of Population A was -1,200 to -1,300 m/s and that of Population C was 1,400 to 1,600 m/s. The intensity ratio of Population A was 50% - 55%, that of Population B was 10% - 15%, and that of Population C was 30% - 35%. The results were the same for all values of parameters P_m, $\dot{m}_\mathrm{c}$, and I_a. However, the peak velocity and intensity ratio were different at different positions. These results suggest that the shape of the IVDF depends on the position rather than the values of P_m, $\dot{m}_\mathrm{c}$, and I_a.
7. A black antenna model, which increased the anode voltage by 20 V, was compared to evaluate the effect of laser reflection. The intensity of Population A decreased by 50% and that of Population C decreased by 30%. Therefore, Population C was not a reflected Population A caused by laser reflection at the antenna or wall.
8. Anode current oscillation and radiated emission measurements showed that the fun-

damental frequency was 180 kHz, and harmonics up to the third or fourth harmonic were observed. The error for both results is within 2%.

9. Relationship between the current oscillation and the measured IVDF were investigated. The IVDF simulated using the ion oscillation model well matched the measured IVDF ($R^2 = 0.82$). The measured IVDF was 30% - 40% wider because of broadening such as Zeeman splitting and saturation broadening. These results support that ion oscillation generated a bimodal IVDF.
10. The plasma potential was measured in the plume by an emissive probe. It was found that there was a potential valley on the central axis. The potential gradient causes ion deceleration near the nozzle.
11. LIF measurements for the improved models described in Chapter 2 were conducted. For the improved cathode using a coil, it was found that the improved model had twice the intensity of the nominal model in the plume. It was shown that the improved model, with an increased mirror ratio and enhanced magnetic field intensity, had twice the intensity. In the discharge chamber, a 40% higher plasma density was present. The dense plasma contributes to the improved performance.

Chapter 4

Conclusion

This study was performed to improve the performance of microwave discharge cathodes. In order to reach this goal, the following studies were conducted. Firstly, the performance was improved by redesigning the magnetic field in the 200-mA class and 500-mA class current ranges. Secondly, plasma diagnostics were conducted for the microwave discharge cathode. In order to measure the plasma inside and outside of the cathode, a viewable microwave discharge cathode was proposed. The major conclusions of this study are as follows.

Performance Enhancements

In Chapter 2, the microwave discharge cathode was improved by two approaches.

Firstly, the anode current was increased by 80 mA compared to the conventional cathode operated at an anode voltage of 37 V when the axial magnetic field of the plume was weakened to 14 mT by a coil. This was a 44% increase. Operating at a constant 180-mA anode current, the anode voltage decreased by as much as 10 V, which was a 27% decrease. In addition, it was found that a magnetic shield reproduced the effect observed with the coil. When the magnetic shield was attached, the anode current increased by 30 mA over that of a conventional cathode operated at a constant anode voltage of 37 V. This was a 17% increase. Operating at a constant 180-mA anode current, the anode voltage decreased by as much as 5 V, a 14% decrease.

Secondly, the mirror ratio and magnetic field intensity were increased in the discharge chamber. By increasing the magnet field intensity and the mirror ratio for the microwave discharge cathode from 2.0 to 8.3, the anode current increased from 300 mA to 560 mA for an anode voltage of 37 V. In coupling operation, the microwave discharge cathode supplied a higher anode current than in diode mode. The anode voltage was 22 V for an anode current of 600 mA. In addition, to evaluate whether the improved microwave discharge cathode is a viable alternative, the I–V characteristics were compared with those of a hollow cathode in coupling operation. It was found that V_{cg} rapidly drops above 600 mA in the microwave discharge cathode, indicating that the performance trade-off point between the two cathodes is about 600 mA.

Plasma Diagnostics

In Chapter 3, a microwave discharge cathode was optically measured by LIF spectroscopy in diode mode operation.

Firstly, a microwave discharge cathode with a small optical window was developed. It was found that the performance was similar to that of the flight model for Hayabusa2 (anode voltage error within 7%).

Secondly, axial and radial LIF measurements were conducted in the plume region. In the plume, bimodal IVDFs were observed. The spatial plume excited-ion density distribution obtained from the axial LIF measurements matched the previous results obtained using an electrostatic probe ($R^2 = 0.96$). Based on the axial and radial LIF measurements, the two-dimensional mean ion flow in the plume was calculated. On the central axis of the plume, the mean ion flow was toward the cathode and decreased nearer the cathode. It was also found that the off-axis mean ion flow was toward the anode. The plasma potential was measured in the plume by an emissive probe. A potential valley was identified on the central axis and it was suggested that the potential gradient was the cause of the ion deceleration near the nozzle. Ion current on plume region was calculated by the axial LIF results. The ion current was up to 6 mA, and its ratio to anode current was up to 5%. It was suggested that the erosion ratio by ions coming from the outside is limited. In addition, the difference in plasma parameters in the downstream region did not significantly affect the ion impact on the discharge chamber wall.

Thirdly, axial LIF measurements were conducted in the discharge chamber. Near the microwave antenna, a trimodal IVDF was confirmed, with an upstream-velocity population (called Population A), a near-zero velocity population (Population B), and a downstream-velocity population (Population C). At other points inside the cathode, bimodal IVDFs were observed. A parametric study found that a larger microwave power P_m and anode current I_a and a smaller xenon flow rate $\dot{m}_\mathrm{c}$ led to a higher total fluorescence intensity (integration of all velocity populations). In the parametric study, the intensity ratio and peak velocity were calculated. Near the microwave antenna, the peak velocity for Population A was -1200 to -1300 m/s and that for Population C was 1,400 to 1,600 m/s. The intensity ratio for Population A was 50–55%, that for Population B was 10–15%, and that for Population C was 30–35%. The results were the same for all values of the parameters P_m, $\dot{m}_\mathrm{c}$, and I_a. However, the peak velocity and intensity ratio were different at different positions. These results suggest that the shape of the IVDF depends on the position rather than the values

of P_{m}, $\dot{m}_{\mathrm{c}}$, and I_{a}. A black antenna model, which increased the anode voltage by 20 V, was compared to evaluate the effect of laser reflection and investigate the origin of Population C. The intensity of Population A decreased by 50% and that of Population C decreased by 30%, indicating that Population C was not a reflected Population A caused by laser reflection at the antenna or wall. To evaluate the effect of ion oscillation on the multimodal IVDFs, anode current oscillation and radiated emission measurements were conducted. These measurements showed that the fundamental frequency was 180 kHz, and harmonics up to the third or fourth harmonic were observed. The error for both results was within 2%. Based on the results of anode current oscillation, an IVDF was simulated using the ion oscillation model, and the results were found to be in good agreement with the measured IVDF ($R^2 = 0.82$). The measured IVDF was 30–40% wider because of broadening, such as Zeeman splitting and saturation broadening. These results support the conclusion that ion oscillation generated a bimodal IVDF. LIF measurements on the improved models described in Chapter 2 were conducted. For the improved cathode using a coil, it was found that the improved model had twice the intensity of the nominal model in the plume. The results also indicated that the improved model with an increased mirror ratio and enhanced magnetic field intensity had twice the intensity. In the discharge chamber, a 40% higher plasma density was produced. This dense plasma contributed to the improved performance.

Acknowledgements

In conducting this research and preparing this dissertation, I was supported by many people. In order to best show my gratitude, I would like to express the acknowledgments in my native language.

本研究は多くの方々のご支援があり完成させることができました。ここに謝意を表します。

はじめに、本研究を行う機会を与えて頂いた國中均宇宙科学研究所所長に深く感謝いたします。先生のイオンエンジン開発における、逆境から負の応援を糧とし 1 つのミッションを成し遂げた話に当時学部生だった私は感銘を受け、本研究室にて研究することを志望しました。配属後は熱心にご指導頂き、実際にモノを飛ばす宇宙工学者としてのエンジニアリングセンスには驚かされるばかりでした。また研究の議論において、物理的な解釈から直感的な理解に至るまで多くのことを学ばせて頂きました。実験手法においても先生の数多くのご経験から研究の核を捉えたアドバイスを頂き、先の課題を早く解決する事ができました。実験室に山のように積まれた機材には先生の作品が多くあり、解剖して多くのことを学ばせて頂きました。また新規研究のアイデアを頂くこともあり、学際的視野の広さや複眼的な思考を近くで学ばせて頂いたことは今後の研究者人生において大きな糧となることと思います。憧れである先生に師事できて光栄でした。西山和孝准教授には輪講で鋭い質問を頂き、工学的にも学術的にも多くのご助言を頂きました。宇宙機上のイオンエンジン運用を踏まえてアドバイスを頂き、常に宇宙探査という出口を意識して研究する姿勢を学ばせていただきました。また自由に研究を行う機会と多くの研究費を与えて頂き、指導教員として暖かく見守って頂いたことは大変感謝しております。研究に限らず、将来に関しても沢山相談させて頂き誠にありがとうございました。細田聡史研究員には、除電・除塵研究を通して多くのことを学ばせて頂きました。食事に連れて行って頂いたことも数知れず、宇宙への熱意を熱く語り合わせて頂いたことは良い思い出であり、進路を選択する上で大いに参考になりました。また共同研究においてプロジェクトマネジメントを一から教えて頂いたことは大変貴重なものです。研究費も多く工面頂き誠にありがとうございました。月崎竜童准教授には英語論文投稿の際に原稿チェックをして頂いたこと、成果発表における表現方法など多くのご指導を頂きました。学生に最も近い先生であり、イベント企画やウォーキング大会にご一緒し優勝したことは楽しい思い出です。船田美和子様には事務関係で大変お世話になりました。物品購入や学会参加等、事務処理が多かったことと存じますが、その都度迅速に手続き頂きありがとうございました。ホッとする差し入れや様々な相談をさせて頂いたこと、深く感謝申し上げます。神田大樹研究員には、研究室配属当初より実験において大変お世話になりました。配属後間もない時期にプラズマ物理や実験について一から教えて頂きありがとうございました。沢山飲みに行かせて頂きましたが、深夜の五次回までご一緒しそのままご自宅に泊まらせて頂いたことは良い思い出です。

またこの 5 年間を通して学生としては多くの共同研究を行ってきたと自負しています。その

分多くの研究者の方々と交流できたことは貴重な財産です。九州大学の山本直嗣教授には 200 W ホールスラスタとのカップリング研究にて大変お世話になりました。早朝から夜遅くまでお付き合い頂き、実験センスや考察力を鍛えることができました。実験をご一緒する中で、研究への鋭いご指摘や建設的なアドバイスを頂きました。また研究のみならず研究者人生についても相談させて頂くことも数多くありました。他大学の所属である私に共同研究の枠を超えて、親身に相談させて頂いたことに研究者としても教育者としても尊敬しています。JAXA の張科寅研究員、渡邊裕樹研究員には、200 W・100 W ホールスラスタ研究にてお世話になりました。研究のアドバイスや研究費のご提供も頂いたことに加え、JAXA における研究の進め方や進路の相談も親身にご対応頂き深く感謝申し上げます。名古屋大学の佐宗章弘副総長、杵淵紀世志准教授には将来の研究についてご相談させて頂きました。打ち合わせや学会等でお会いする度に、研究や研究者人生について沢山学ばせて頂きました。お忙しい御身でありながら、多くのお時間を頂き深く感謝申し上げます。春日電機の故野村様、最上様、峯村様には除電器の共同研究でお世話になりました。修士入学後の初めての研究であり強い思い入れがありますが、多くのことが初めての私に懇切丁寧に教えて頂きました。企業における研究者の在り方、スピード感を学ばせて頂きました。在学中にプロジェクトの立ち上げから製品化まで一貫して携わり達成できたこと、産学の両側を学ばせて頂いたことはかけがえのない経験です。JAXA の石川毅彦教授には、筑波宇宙センターにおいて静電浮遊炉を用いた除塵実験でお世話になりました。期間中は付き切りで手厚くご支援頂き感謝申し上げます。

工作グループの中坪様、故笛木様には工作の相談をさせて頂き感謝申し上げます。中和器は小型のため工作の難易度が高く沢山助けて頂きました。研究室で一緒に過ごした皆様にも沢山お世話になりました。谷さん、吉川さん、井出さん、Giulio さん、岡さん、森田さんには豊富な経験から数多くのアドバイスを頂きました。同期の江本君、清水君、山下君は研究室生活の支えとなりました。食事の度に将来について語り合ったのは良い思い出です。個性的な同期ばかりでしたが、皆さんとともに研究できたことを嬉しく思います。後輩の宮君、白川君、濃野君、服部さん、小磯君、高木君には少しでも力になれたのであれば嬉しいです。コロナ禍により交流が減った世代ですが、その分研究室イベントで楽しく話したことは良い思い出です。

最後に、宇宙研で研究するにあたり支えてくれた父母と姉、親戚に最大の感謝を捧げます。幼少に工夫することの楽しさを教えてくれた父は、研究者を志した原点です。研究について共に楽しく語り合ったことも数え切れないことと思います。分野を横断して常に新しいこと、楽しいことを探求しつづける研究者である父を誇りに思います。母は私の苦楽に最も近くで寄り添ってくれました。5 年間、良いこともあればつらいこともありました。その全てを自分のことのように受け止めて献身的に支えてくれたこと、言葉では言い尽くせないほどの感謝をしています。心労も多かったことと思いますがこれからは私が支え、恩返しをさせてください。姉には同じ学問の徒として沢山相談したと思います。同じ目線で貰うアドバイスには幾度となく助けられました。異分野の研究者からもらう指摘は時に鋭く、沢山の気づきを得ることができました。いつの日か、学際的な研究を共にできる日を夢見ています。また草葉の陰から見守ってくれた祖父母、遠方からいつも気にかけてくれた叔母に深く感謝致します。楽しく仲の良い家族に恵まれたことが最大の幸福です。

将来の我が国の、そして人類の宇宙探査に資することを願い本論文を捧げます

令和 4 年 3 月

博士（工学）　森下　貴都

Appendix A

Effect of Nozzle Material on I–V Characteristics

In appendix A, the investigation of the effect of nozzle material on the I–V characteristics in diode mode operation is detailed.

A.1 Experimental conditions

Table A.1 shows a comparison of the work function ϕ of the materials used. The work function is the minimum thermodynamic energy required to remove an electron from the surface to the outside. Materials with a lower work function emit more electrons at a lower energy. In this experiment, Mo and La-W were compared.

The experiment was conducted in nominal diode mode operation and the setup is the same as Figure 2.13. Table A.2 summarizes the experimental conditions.

A.2 Results

Figure A.1 shows a comparison of the I–V characteristics of Mo and La-W nozzles. The La-W nozzle model has a voltage that was 1–5 V lower than that for the Mo nozzle model. In addition, the La-W nozzle model had a 20–40 mA higher current. For example, at an anode voltage of 35 V, the anode current for the Mo nozzle model was 180 mA and that for the La-W model was 220 mA. The difference tended to be larger at higher current.

A.3 Discussion

As described above, a microwave discharge cathode emits electrons as counterparts of ion collection secondary electron emission on the inner wall of the discharge chamber. The charge

exchange on the wall is different for different materials, and three fluxes are discussed, as shown in Figure A.2.[25]

- Ion current
- Secondary electron emission by ion
- Secondary electron emission by Auger de-excitation of metastable molecules

Firstly, a flux of multi-charged ion current J_{n+} is considered. In this estimation, singly and doubly charged ions are considered.

$$J_{n+} = 0.61enN_{n+}\sqrt{\frac{kT_\mathrm{e}}{M}} \tag{A.1}$$

Secondly, a flux of secondary electron emission by ion $J_{\gamma n+}$ is considered.

$$J_{\gamma n+} = \frac{1}{n}\gamma_{n+}J_{n+} \tag{A.2}$$

$$\gamma_{n+} = 0.032(0.78E_n - 2\phi) \tag{A.3}$$

Eq. A.3 is the Baragiola approximation. E_n is the n-th ionization potential.

Thirdly, a flux of secondary electron emission by Auger de-excitation of metastable molecules $J_{\gamma\mathrm{m}}$ is considered.

$$\gamma_\mathrm{m} = \frac{e\gamma_1 N_\mathrm{m}}{4}\sqrt{\frac{8kT_\mathrm{n}}{\pi M}} \tag{A.4}$$

The parameters for the flux calculation are summarized in Table A.3.[25][28][29] In previous research, N_{1+} was measured in the plume. In this research, the density near the nozzle is estimated based on the results of the LIF measurements shown in Figure 3.37. Figure A.3 shows a comparison of the flux for the Mo and La-W nozzle models. The flux of secondary electron emission by singly charged ions showed the largest difference. The difference in the total current was 10 mA. This is reasonable compared with the results for the I–V characteristics including error bars shown in Figure A.1.

Table A.1: Comparison of work functions ϕ.

Material	Work function ϕ, eV
BaO-W	1.34
Th-W	2.63
La-W	2.8
W	4.55
Mo	4.6
Fe	4.6
Ni	5.15

Table A.2: Experimental conditions for evaluation of nozzle material differences.

Parameter	Value
Microwave frequency	4.25 GHz
Microwave power, P_{m}	8 W
Xenon flow rate, $\dot{m}_{\mathrm{c}}$	0.7 sccm (0.069 mg/s)
Microwave antenna	Flight model (Hayabusa2)
Background pressure	9×10^{-5} Pa without Xe input 7×10^{-4} Pa at 1 sccm Xe

Table A.3: Parameters for flux calculation.

Parameter	Value
Xe^{+} density, N_{1+}	8.7×10^{17} m^{-3}
Metastable molecule density, N_{m}	1.3×10^{17} m^{-3}
Electron temperature, T_{e}	3.2 eV
Neutral temperature, T_{n}	373 K
Doubly-charged ion ratio, ϵ	0.2%

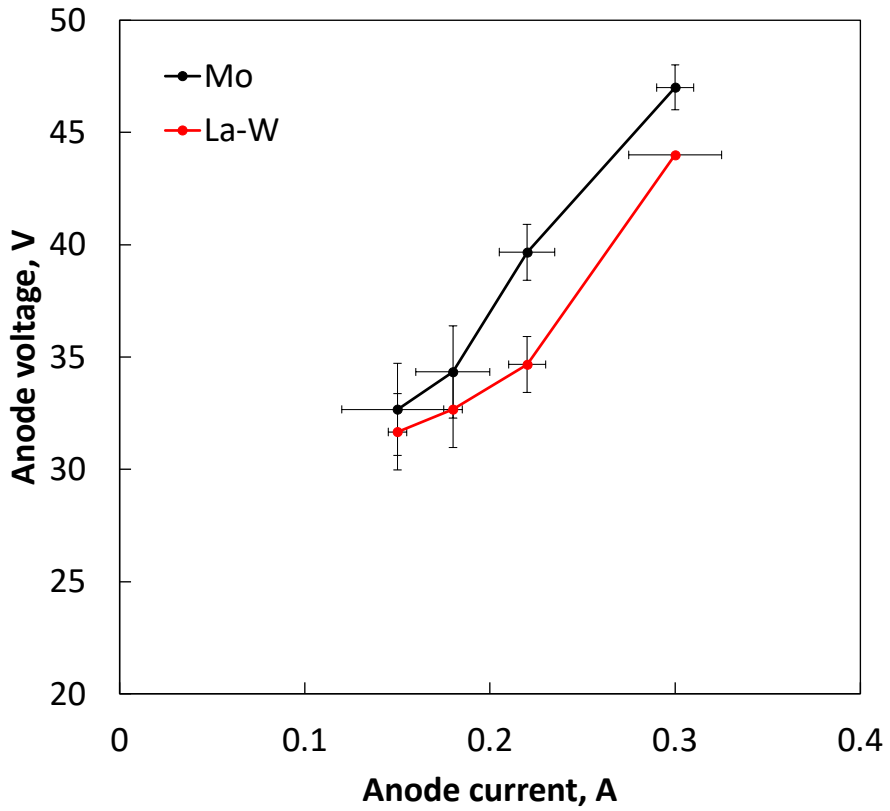

Figure A.1: Comparison of I–V characteristics of Mo and La-W nozzle.

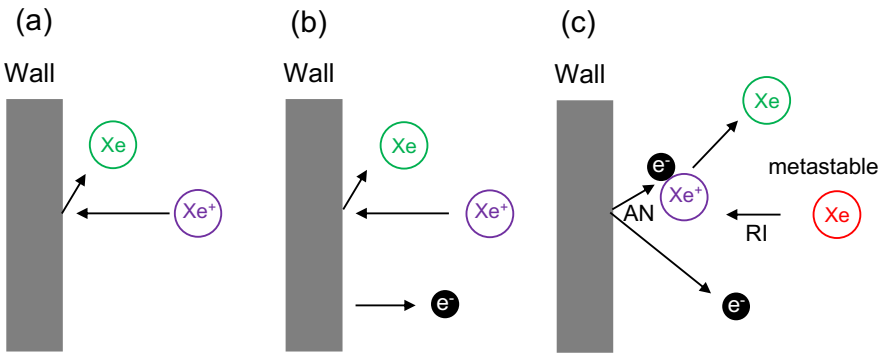

Figure A.2: Three types of flux on wall. (a) Ion current, (b) Secondary electron emission by ions, (c) Secondary electron emission by Auger de-excitation of metastable molecules.

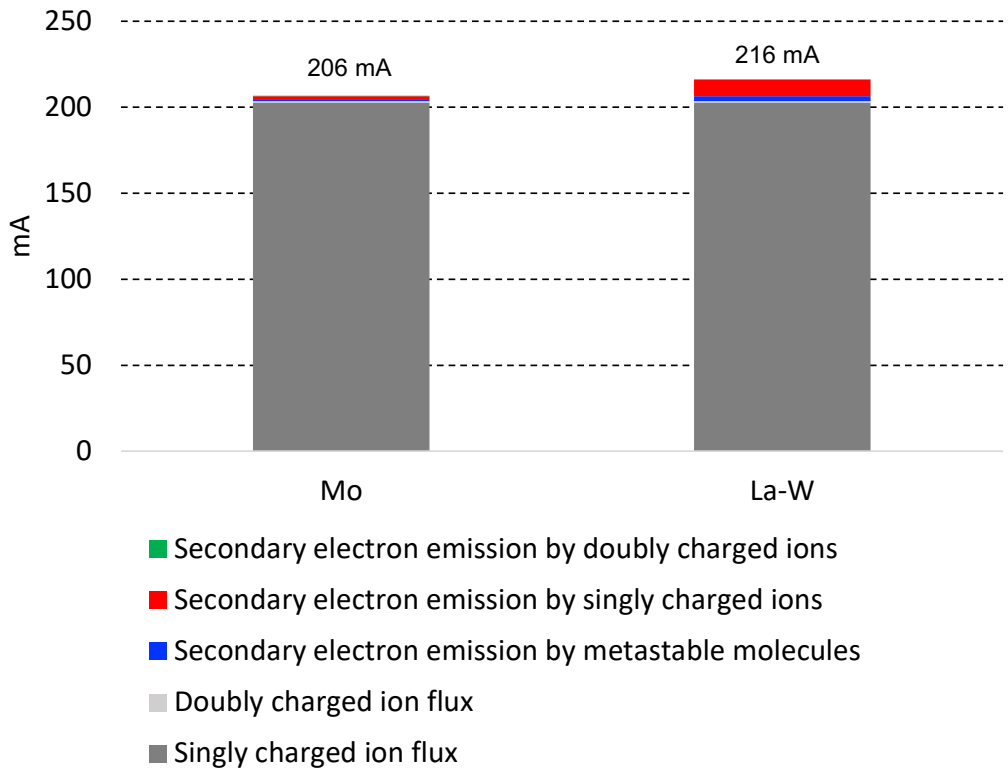

Figure A.3: Comparison of flux between Mo and La-W nozzle models.

A.4 Summary

To investigate the effect of nozzle material on performance, the I–V characteristics were compared between Mo and Th-W in diode mode operation. The results can be summarized as follows:

1. The La-W nozzle model had a voltage 1–5 V lower than that of the Mo nozzle model. The La-W nozzle model had a current 20–40 mA higher.
2. In order to discuss these differences, three types of flux were considered: ion current, secondary electron emission by ions, and secondary electron emission by Auger de-excitation of metastable molecules.
3. Secondary electron emission by singly charged ions was found to be the largest and generated a 10 mA difference.

Appendix B

Performance Analysis of 200-W Hall Thruster System

In Section 2.2, the mirror ratio and magnetic field intensity were redesigned and the I–V characteristics were measured in diode mode configuration. The improved microwave discharge cathode was coupled with a 200-W class Hall thruster to measure the I–V characteristics in coupling test operation. In appendix B, the results of the thrust performance characteristics and beam profiles are described. The differences between these characteristics and those of a hollow cathode are discussed.

B.1 Ignition characteristics

At first, experiments were conducted to investigate the relationship between the magnetic field polarity of the Hall thruster-microwave discharge cathode and the performance. It was found that the magnetic field of the Hall thruster and the magnetic field of the microwave discharge cathode interfere with each other and affect the ignition characteristics. The magnetic field of the Hall thruster was formed by an inner coil and four outer coils, forming the magnetic field around the channel. The microwave discharge cathode formed a magnetic field not only inside the discharge chamber but also outside by permanent magnets. Therefore, the magnetic field near the discharge chamber of the Hall thruster was affected by the microwave discharge cathode. There were two possible kinds of magnetic fields of the microwave discharge cathode and Hall thruster, based on the difference in polarity, as shown by type A and type B of Figure B.1. In Figure B.1, the left figures show the schematics of the magnetic field and right figures show the magnetic field measured by a teslameter. In the type A of Figure B.1, a magnetic field is formed such that the center axis of the Hall thruster and the microwave discharge cathode are connected. In the type B, a magnetic field is formed so that the outer coil of the Hall thruster and the microwave discharge cathode are connected.

Figure B.1 shows the case where the thruster center was an N pole, but the situation does not change when both the polarities of the Hall thruster and microwave discharge cathode are reversed.

The ignition process is shown in Figure B.2. Initially, cathode plasma is ignited and V_{ath} is fixed to 150 V. Next, I_{coil} is increased from 0 A to 1.5 A. In the range of 1.0-1.5 A, a thruster plasma tends to ignite. Then V_{ath} and I_{coil} are increased to the values shown in Table 2.3.

A comparison of I_{coil} vs. V_{cg} between type A and B magnetic fields at $V_{\mathrm{ath}} = 150$ V is shown in Figure B.3, which represents a comparison of plasma maintenance. V_{cg} is measured to determine ignition. When V_{cg} is not 0 V, the plasma is maintained. The results show that it is easier to ignite a plasma for type A than for type B. While for type B a plasma cannot be maintained at $I_{\mathrm{coil}} = 1.4$ A, type A maintains a plasma at $I_{\mathrm{coil}} = 1.5$ A. In addition, $|V_{\mathrm{cg}}|$ for type A is 2-6 V smaller than that for type B.

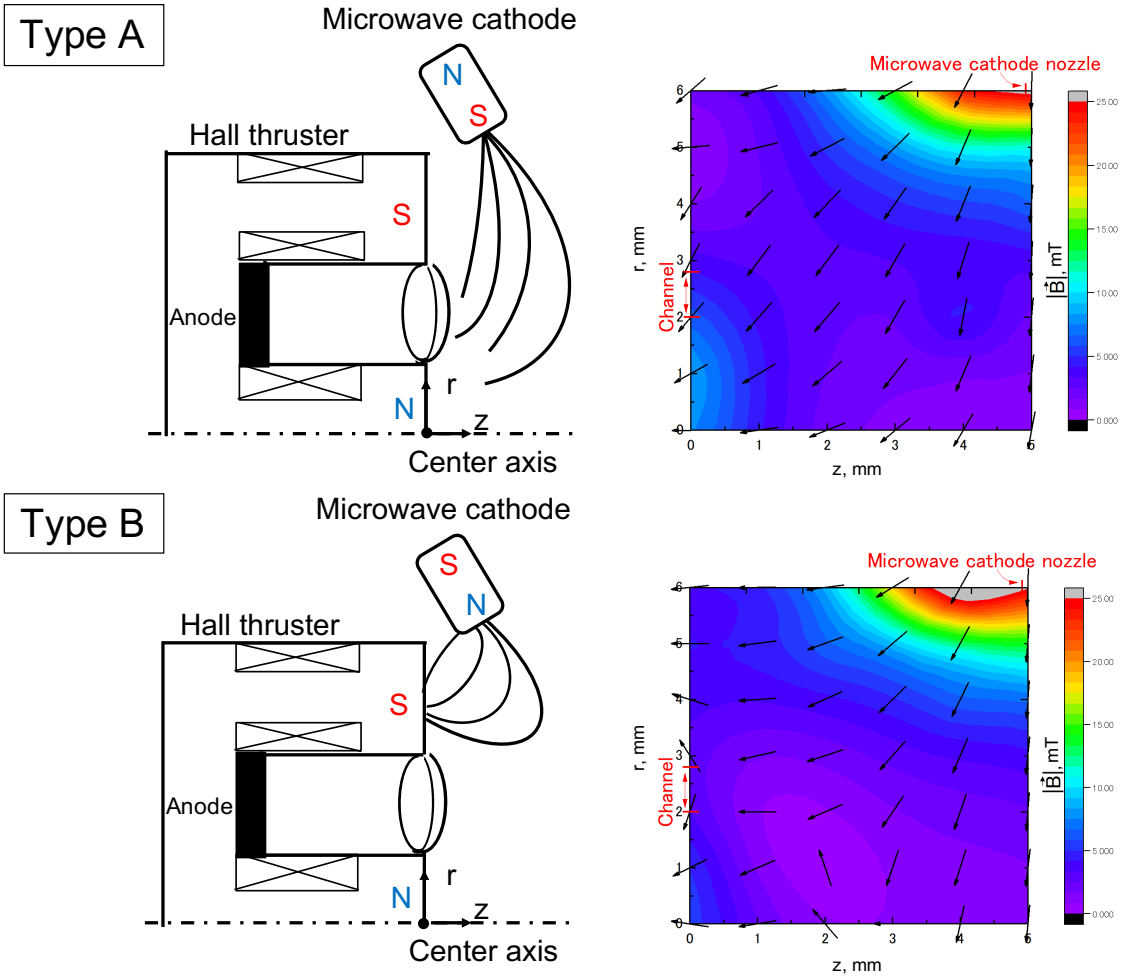

Figure B.1: Combinations of magnetic fields formed by a microwave discharge cathode and Hall thruster. The left figures are schematics and the right figures are fields measured by a teslameter.

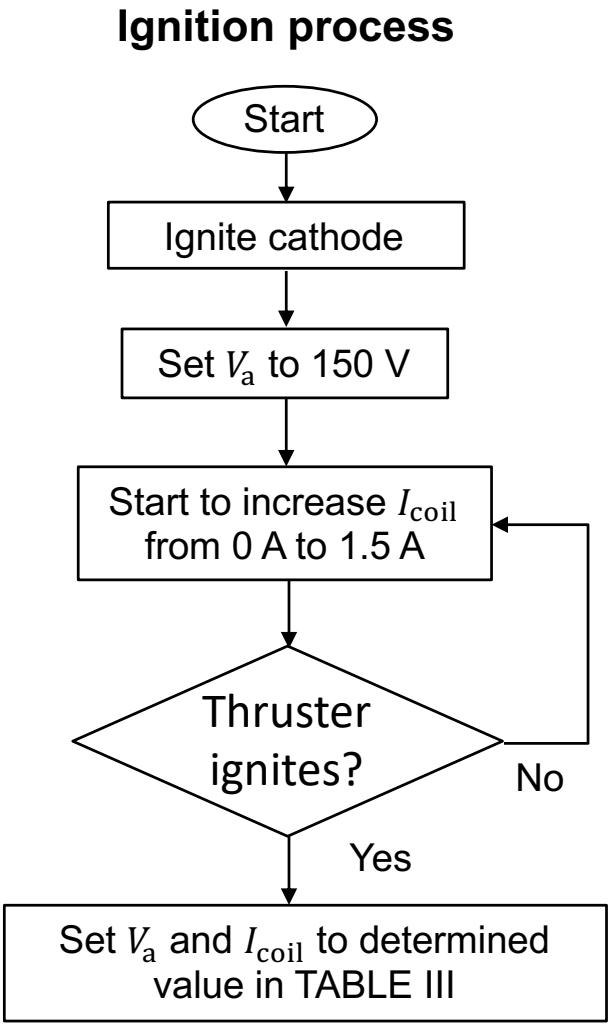

Figure B.2: Ignition process of Hall thruster - microwave discharge cathode system.

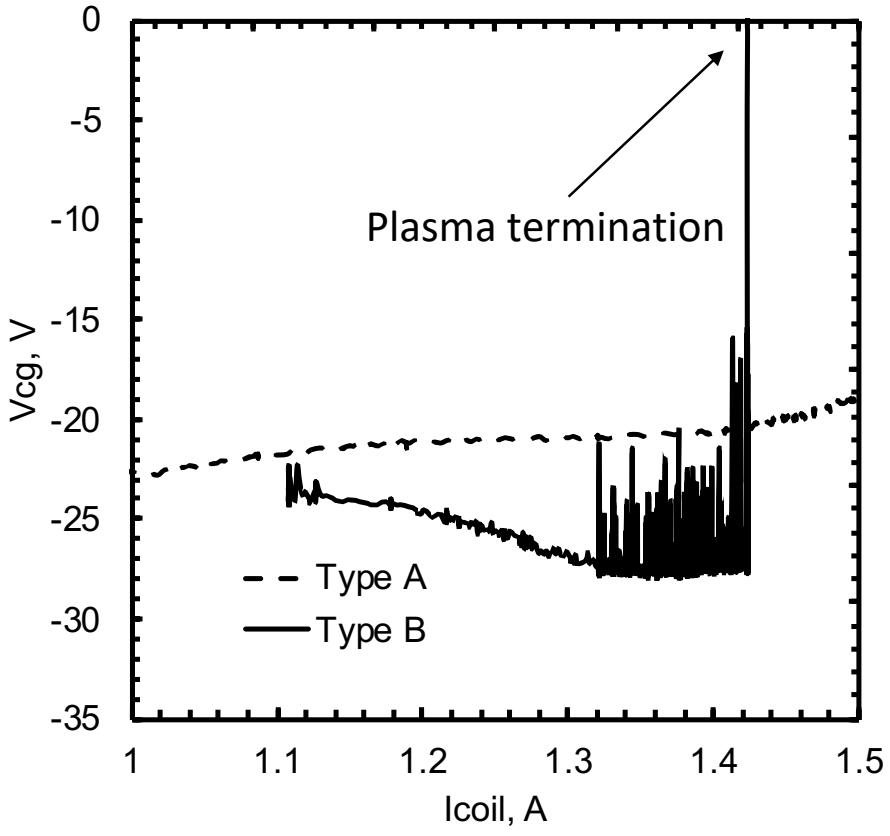

Figure B.3: I_{coil} vs. V_{cg} comparison between type A and B magnetic fields at $V_{\mathrm{ath}} = 150$ V.

B.2 Performance characteristics

The thrust F is measured by an inverted pendulum thrust stand, I_a using a current probe, V_{cg}, the ion energy distribution using an RPA, and the ion beam profile using an ion collector.

To evaluate the thrust performance, the specific impulse I_{sp} and thrust efficiency η_T are defined as

$$I_{sp} = \frac{F}{2(\dot{m}_a + \dot{m}_c)g} \tag{B.1}$$

$$\eta_T = \frac{F^2}{2(\dot{m}_a + \dot{m}_c)(P_a + P_c)} \tag{B.2}$$

Here, P_a is the anode consumption power including the coil consumption power P_{coil}, defined as follows:

$$P_a = I_a V_{ath} + P_{coil} \tag{B.3}$$

The cathode consumption power P_c is 20 W for both microwave and hollow cathodes and is defined as

$$P_c = \begin{cases} 20\,W & : \text{Microwave discharge cathode} \\ 50 - 100\,W & : \text{Hollow cathode at ignition} \\ 20\,W & : \text{Hollow cathode at steady state} \end{cases} \tag{B.4}$$

For the hollow cathode, 50-100 W for 30 minutes is required for ignition.

Figure B.4 shows the thrust performance and electron emissive characteristics for $I_{coil} = 2.0$ A. The thrust is equivalent between the microwave discharge cathode and hollow cathode. At V_{ath} = 150 V, F is 3 mN and increases to 5 mN at V_{ath} = 250 V for both types of cathode. In addition, at V_{ath} =250 V, the system power consumption $P_a + P_c$ is 202 W for the microwave discharge cathode. The specific impulse I_{sp} is 10-20% higher for the microwave discharge cathode. At V_{ath} = 150 V, I_{sp} is 370 s and it increases to 600 s at V_{ath} = 250 V for the microwave discharge cathode. The difference in I_{sp} is because the microwave discharge cathode uses 1.5 sccm xenon, while the hollow cathode uses 2.8 sccm xenon. The V_{cg} characteristic is different between the microwave discharge cathode and hollow cathode. For the hollow cathode, V_{cg} is constantly -15 V to -20 V at V_{ath} = 150 V - 250 V. On the other hand, V_{cg} of the microwave discharge cathode depends on V_{ath}; as V_{ath} increases, V_{cg} decreases. For the microwave discharge cathode, at V_{ath} = 150 V, I_a is 450 mA and is 20% larger than for the hollow cathode, while V_{cg} is -16 V and is smaller than that of the hollow cathode. At V_{ath} = 200 V, I_a is 580 mA and is 30% larger, while V_{cg} is -18 V and is equivalent to that of the hollow cathode. At V_{ath} = 250 V, I_a reaches 600 mA and V_{cg} suddenly drops to -25 V, which is an 8-V difference compared to that of the hollow cathode. These results show that the electron emission capability of the microwave discharge cathode is better or

equal to that of the hollow cathode up to $V_{\mathrm{ath}} = 200$ V. In addition, they show that the electron emission capability reaches a limit at $V_{\mathrm{ath}} = 250$ V, and that V_{cg} drops significantly negatively. At $V_{\mathrm{ath}} = 150$ V, thrust efficiency η_{T} is 5.5% for both types of cathode. However, at $V_{\mathrm{ath}} = 200$ V, η_{T} is 9 % and is higher for the microwave discharge cathode because the thrust is higher. At $V_{\mathrm{ath}} = 250$ V, η_{T} is lower because the thrust is equivalent but the power consumption is larger because of the larger I_{a}. These trends in the performance characteristics are also obtained for $I_{\mathrm{coil}} = 1.5$ A, 2.5 A.

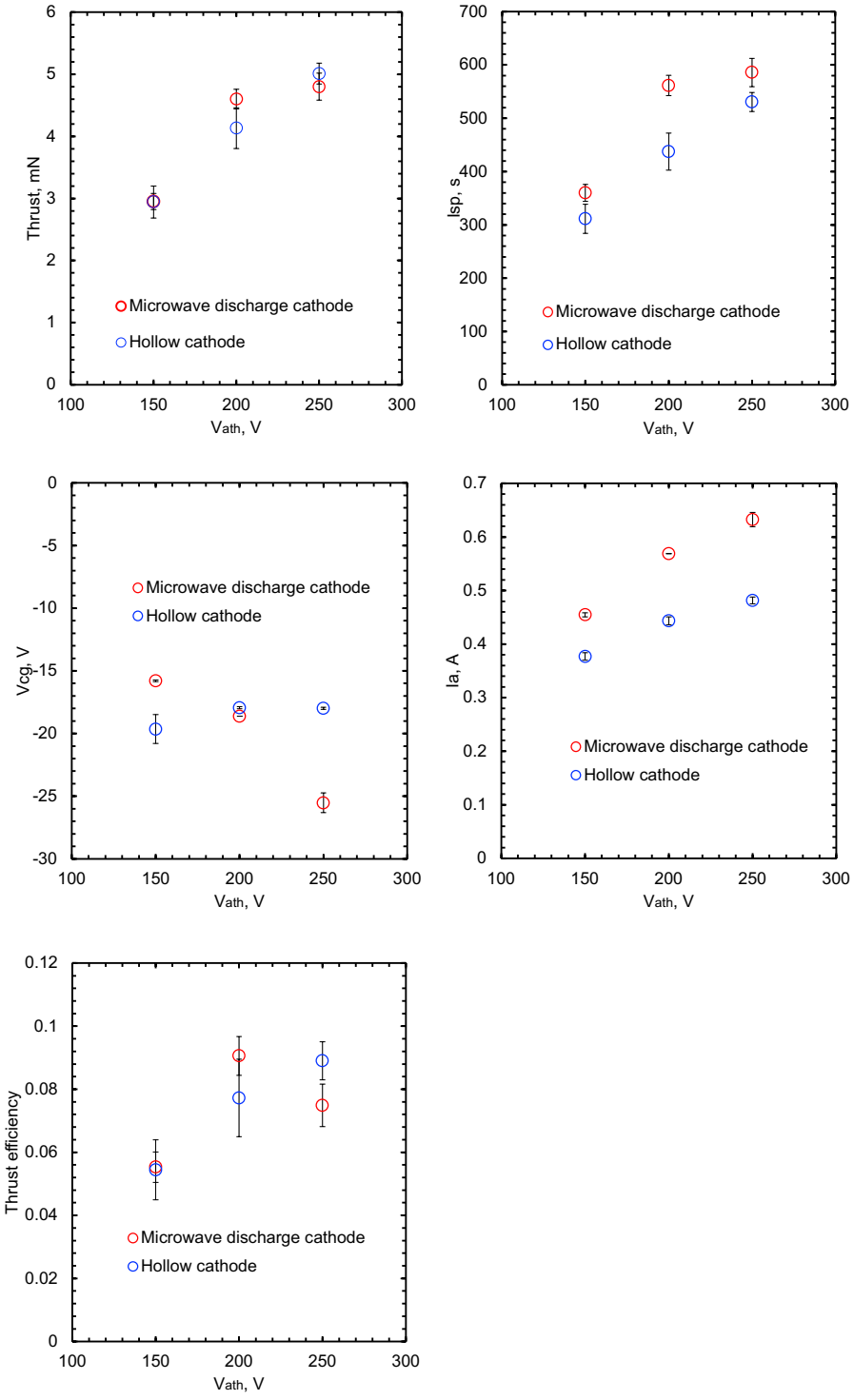

Figure B.4: Comparison of thrust F, specific impulse I_{sp}, potential difference between the cathode and ground V_{cg}, anode current I_{a}, and thrust efficiency between the microwave discharge cathode and hollow cathode at $I_{\mathrm{coil}} = 2.0$ A

B.3 Ion energy and beam profile (efficiency analysis)

To investigate the causes of the performance differences, four efficiencies, the acceleration efficiency η_a, propellant utilization efficiency η_{u}, beam energy efficiency η_{E}, and beam divergence efficiency η_{div} are calculated.[81] They are defined as follows:

$$\eta_{\mathrm{a}} = \frac{I_{\mathrm{beam}}}{I_a} \tag{B.5}$$

$$\eta_{\mathrm{u}} = \frac{I_{\mathrm{beam}} M}{e\dot{m}_a} \tag{B.6}$$

$$\eta_{\mathrm{E}} = \frac{E_{\mathrm{m}}}{eV_{\mathrm{ath}}} \tag{B.7}$$

$$E_{\mathrm{m}} = \left\{ \int f(E)\sqrt{(}E)dE \right\}^2 \tag{B.8}$$

$$\eta_{\mathrm{div}} = \left\{ \frac{\int_0^{r_0} rJ(r)dr + \int_{r_0}^{\infty} rJ(r)\cos\theta dr}{\int_0^{\infty} rJ(r)dr} \right\}^2, \tan\theta = \frac{r - r_0}{L} \tag{B.9}$$

Here, the r-axis is defined in Figure B.1 and Figure 2.15, r_0 is the thruster channel radius (= 28 mm), θ is the angle between the RPA - ion collector and thruster center axis, J is the measured current density, and L is the distance between the thruster and RPA-ion collector at r = 0 (= 0.95 m).

Figure B.5 compares the ion energy distribution function (IEDF) and ion beam profile at I_{coil} = 2.0 A,V_{ath} = 250 V of Figure B.4 between the hollow cathode and microwave discharge cathode. In the low energy region generated mainly by charge exchange, the IEDF is equivalent in the microwave discharge cathode and hollow cathode. However, the mean beam energy E_m is 9 V lower in the microwave discharge cathode than in the hollow cathode. On the other hand, the beam current I_{beam} is higher for the microwave discharge cathode. In addition, the beam profile shows that the beam focus is better for the microwave discharge cathode.

Figure B.6 compares the four efficiencies at I_{coil} = 2.0 A. In the case of the microwave discharge cathode, η_a is 3-15 % higher than that of the hollow cathode up to V_{ath} = 200 V. However, η_a of the hollow cathode is 6 % higher between V_{ath} = 200 V and V_{ath} = 250 V. As described above, η_{u} tends to be 4-10 % higher in the microwave discharge cathode due to the large I_{beam}. On the other hand, η_{E} tends to be 4-8 % lower. These trends are also obtained for I_{coil} = 1.5 A, 2.5 A. η_{div} tends to be higher in the microwave discharge cathode, at a maximum of 5% higher.

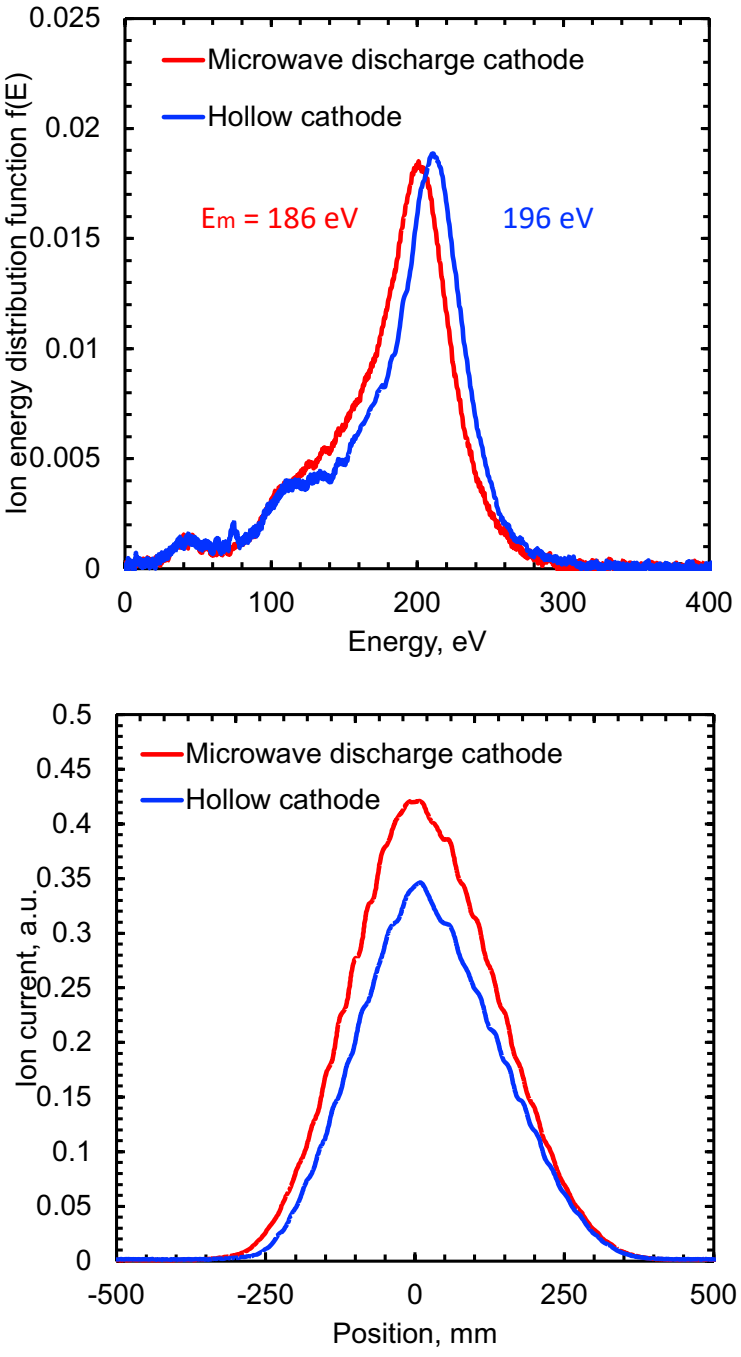

Figure B.5: Comparison of ion energy distribution (left) and ion beam profile (right) at I_{coil} = 2.0 A,V_{ath} = 250 V

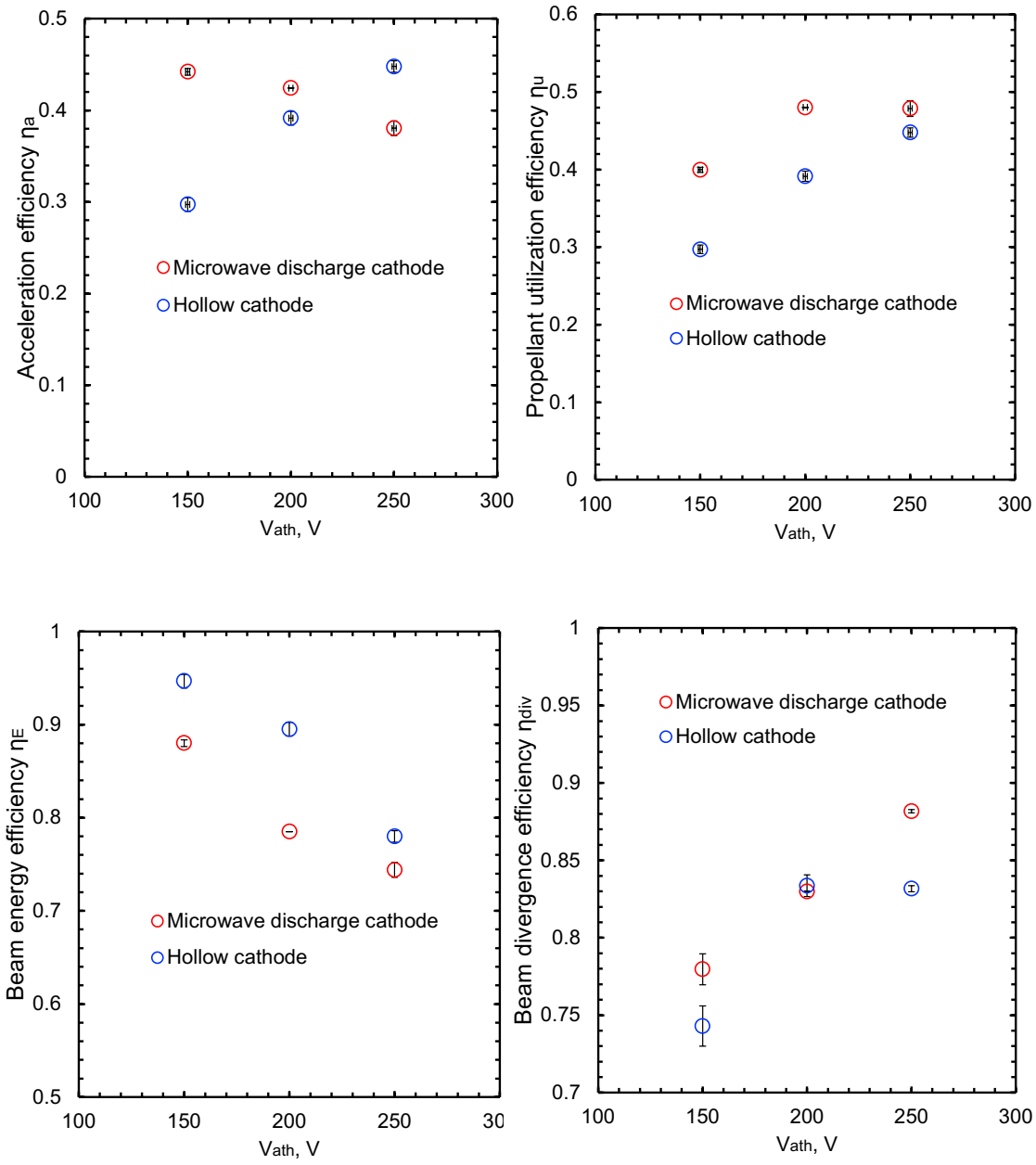

Figure B.6: Comparison of four efficiencies, acceleration efficiency η_a, propellant utilization efficiency η_{u}, beam energy efficiency η_{E}, and beam divergence efficiency η_{div} at $I_{\mathrm{coil}} = 2.0$ A.

These results suggest a difference in the plasma generation region for the two types of cathode as shown in Figure B.7. As described above, the microwave discharge cathode has a magnetic field, while the hollow cathode does not. The magnetic field of the microwave discharge cathode increases the in-channel field. Therefore, the plasma is generated closer to the anode than for the hollow cathode, and I_a becomes larger. In addition, electrons tend to be transported easily by the magnetic field of the microwave discharge cathode. Therefore, I_{beam} and I_a are larger than for the hollow cathode, and η_a and η_{u} are higher. However, over $I_a = 600$ mA ($V_{\mathrm{ath}} = 250$ V), the electron emissive capability reaches a limit, and η_a of the hollow cathode become higher. In the upper position of the plasma production region, η_{div} increases. However, because wall loss of ion momentum increases, η_{E} is lower than that of the hollow cathode. In addition, V_{cg} affects the space potential and the beam energy as a result. It is suggested that the difference of η_{E} is caused by ion energy loss at the channel wall and a cathode potential drop V_{cg}. As a result, the thrust was equivalent. The 200-W class Hall thruster was originally developed for larger propellant operation such as 10 sccm or more. Therefore, a better performance should be obtained for a smaller thruster.

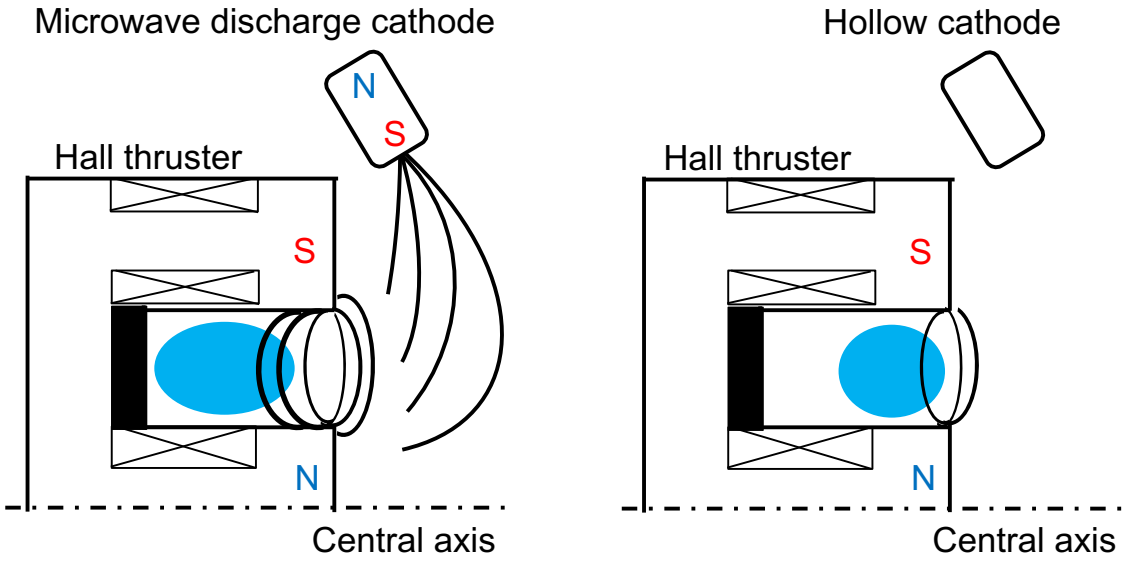

Figure B.7: Comparison of plasma production region between a hollow cathode and microwave discharge cathode

B.4 Summary

To determine whether a microwave discharge cathode is a viable alternative to a hollow cathode, coupling operation with an SPT type Hall thruster was conducted. As described in Section 2.2, the mirror ratio and magnetic field intensity were increased, and the electron current was measured in diode mode operation. An improved microwave discharge cathode was applied to a Hall thruster system and the performance and beam analysis results were compared with those for the hollow cathode. The results can be summarized as follows:

1. It was found that the magnetic polarity of the microwave discharge cathode and the Hall thruster affected the ignition and the maintenance of the plasma.
2. The hollow cathode required 20 W of heater and keeper power to emit about 500 - 700 mA of electrons, while the microwave discharge cathode required about 20 W of microwave power. The thrust was equivalent for the microwave discharge cathode and hollow cathode. However, I_{sp} of the microwave discharge cathode-Hall thruster is 10 % higher because the xenon flow rate of the microwave discharge cathode is 53% of that of the hollow cathode.
3. Since V_{cg} rapidly drops above 600 mA in the microwave discharge cathode, it was found that the performance trade-off point between the two cathodes is about 600 mA.
4. Based on the IEDF and beam profile, the propellant utilization efficiency η_{u} and beam divergence efficiency η_{div} of the microwave discharge cathode were found to be higher than those of the hollow cathode. However, the beam energy efficiency η_{E} of the microwave discharge cathode is lower.
5. These results imply a difference in the plasma generation region due to the microwave discharge cathode magnetic field. The plasma generation region of the microwave discharge cathode forms a relatively strong magnetic field in the channel of the thruster. Therefore, the plasma is generated more in the upper region relative to the case of the hollow cathode.

Appendix C

Application of a Plasma Source for Charge Removal in High Vacuum

This chapter is partially reproduced from published article,[82] with the permission of IOP Publishing. This chapter is also partially reproduced from published articles,[83][84] with the permission of Institute of Electrostatics Japan.

C.1 Background

In a vacuum, electrical charging is a major cause of failure in processes such as film deposition and semiconductor manufacturing. For example, when conveying thin films at high speed in vacuum, contact and friction charging occurs between the roll and the film, which can lead to the films becoming entangled. To solve this problem, electric charge is typically neutralized by passive discharging using the Paschen condition by cyclically lowering the vacuum pressure, which reduces production efficiency. UV neutralizers are also used, but their neutralization efficiency is lower than that for passive discharging using the Paschen condition. The microwave discharge cathode has several advantages, including easy ignition, ease of use in atmosphere, and a small plasma source. Therefore, this study investigates a charge neutralization method using a microwave discharge plasma in a high vacuum of 10^{-1} to 10^{-4} Pa.

C.2 Time constant for charge neutralization

C.2.1 Experimental setup

o evaluate the charge neutralization effect by a microwave discharge plasma in a high vacuum, the time constant was measured. As shown in Figure C.1, a 50-mm square copper plate was first charged to ±200 V. The microwave discharge plasma source was located 30 cm from the plate. An anode was installed 11 mm downstream of the microwave discharge plasma source, and the time constant was compared with and without the application of an anode voltage. In this experiment, xenon and argon were used as gases for plasma generation (argon is commonly used in vacuum equipment in ground-based industry).

The measured time constant τ_{T} includes the current flowing through the resistor R_{R}, and hence when τ_{T} is much larger than the time constant with just the resistor τ_{R}, the measured neutralization time constant due to the plasma τ_{P} becomes invalid. Therefore, τ_{P} has to be estimated. Assuming an RC circuit, τ_{T} is given by Eq. C.1.

$$\tau_{\mathrm{T}} = R_{\mathrm{T}} C \tag{C.1}$$

Here, R_T is a combined resistance, and is given by:

$$R_{\mathrm{T}} = \frac{1}{\frac{1}{R_{\mathrm{R}}} + \frac{1}{R_{\mathrm{P}}}} \tag{C.2}$$

where R_{P} is the resistance of the plasma between the plasma source and the charged plate. τ_{P} is estimated using Eq. C.3.

$$\tau_{\mathrm{P}} = R_{\mathrm{P}} C = \frac{\tau_{\mathrm{T}} R_{\mathrm{R}} C}{R_{\mathrm{R}} C - \tau_{\mathrm{T}}} \tag{C.3}$$

The experimental conditions are as shown in Table C.1.

Table C.1: Experimental conditions for measurement of neutralization time constant.

Parameter	Value
Microwave frequency	4.25 GHz
Microwave power, P_{m}	8 W
Xenon flow rate, $\dot{m}_{\mathrm{c}}$	0.2 sccm (0.049 mg/s)
Argon flow rate, $\dot{m}_{\mathrm{c}}$	0.8 sccm (0.078 mg/s)
Charged plate voltage	±200 V
Background pressure	3×10^{-3} Pa without Xe input 4×10^{-3} Pa at 0.2 sccm Xe 8×10^{-3} Pa at 0.8 sccm Ar

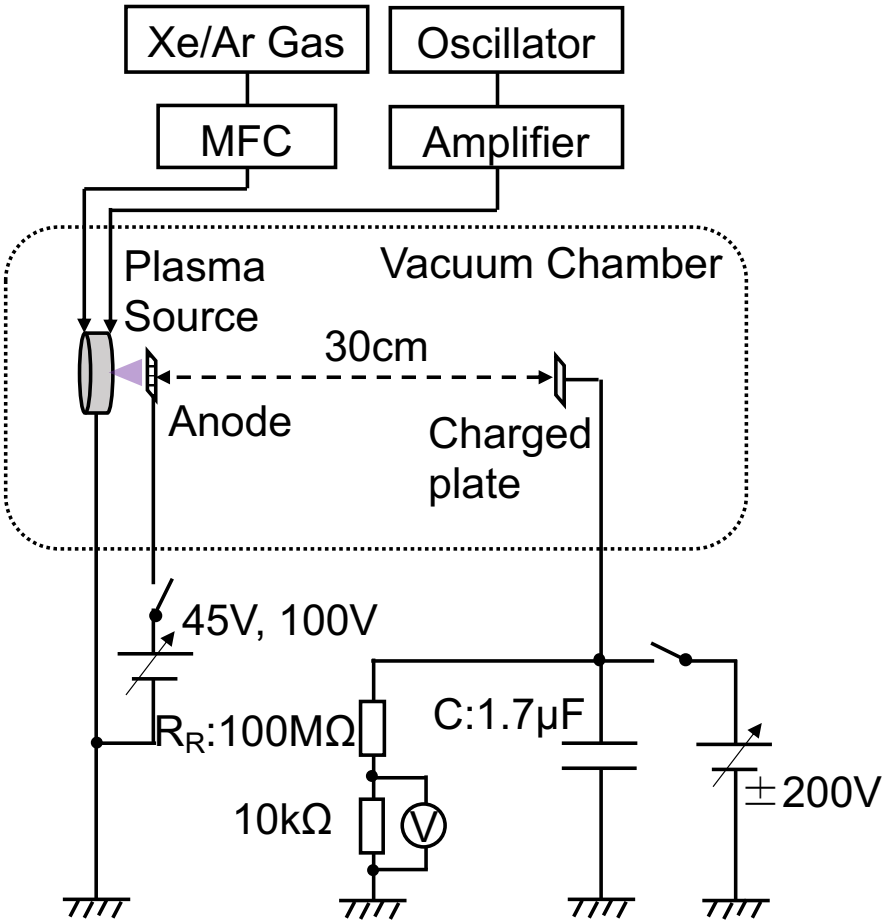

Figure C.1: Experimental setup for measurement of neutralization current density.

C.2.2 Results

Figure C.2 shows the time history of charge neutralization using 0.2-sccm xenon. The results are summarized in Table C.2. For xenon and a positively charged plate, τ_T was 0.1 s and 2 s for "Plume ON" and "Plume OFF", respectively. On the other hand, for a negative charge, τ_T was 27 s and 111 s, respectively. However, it should be noted that 111 s of τ_T is 320 s in τ_P as mentioned above. The negative charge neutralization time constant was 1 order of magnitude larger than that for a positive charge. In the case of argon, τ_P was up to 10 times larger than for xenon.

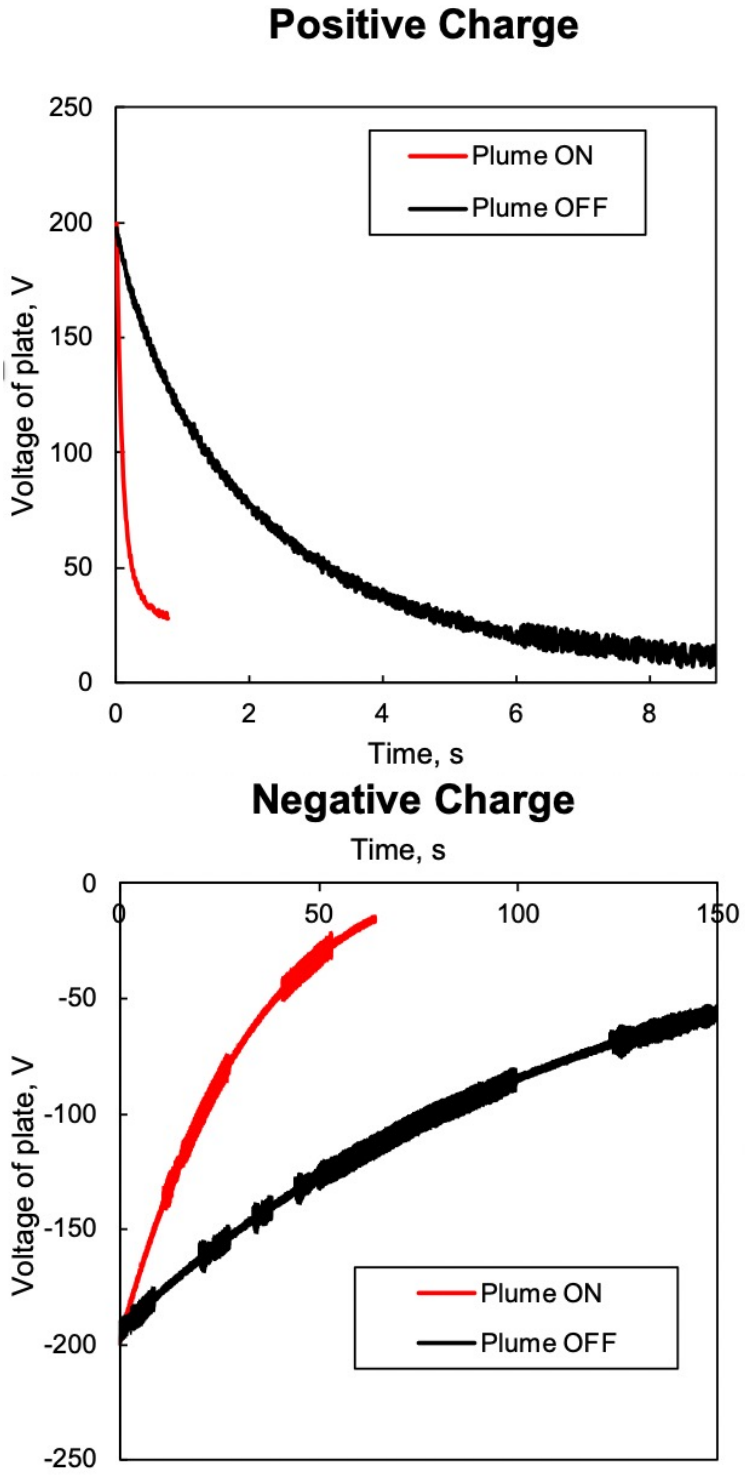

Figure C.2: Time history of charge neutralization using 0.2 sccm xenon.

Table C.2: Comparison of neutralization time constants.

Gas	Charge	Anode voltage, V	Anode current, mA	τ_{T}, s	τ_{P}, s
Xenon	Positive	45	135	0.1	0.1
Xenon	Positive	0	0	2	2
Xenon	Negative	45	135	27	32
Xenon	Negative	0	0	111	320
Argon	Negative	100	31	122	432
Argon	Negative	0	0	120	408

C.3 Distribution of charge neutralization current density

C.3.1 Experimental setup

We investigated the distribution of the charge neutralization current density generated by a plasma source in a high vacuum, as shown in Figure C.3. 50-mm square copper plates were placed at distances of 1.0, 1.5, and 2.0 m from the microwave discharge plasma source. A voltage of ±200 V was applied to the copper plates and the neutralizing current was measured. The charged plates were exposed to plasma on one side. The experimental conditions were as shown in Table C.3.

As shown in Figures C.4 and C.5, the shapes of the anode and the orifice were changed to investigate the differences in the neutralizing current density. The anode was used to generate a positive plasma column, in addition to the microwave discharge plasma in the discharge chamber, downstream of the orifice, by applying a voltage. A positive plasma column was generated by collisions between energetic electrons extracted from the discharge chamber by the applied electric field and neutral particles.

The experiments were performed with two types of orifice and two types of anode: a single-hole orifice model, which is the conventional model for microwave discharge cathodes for space use, a multiple-hole orifice model, a cylindrical electrode model (ϕ10 mm, 10 mm in length), and a ϕ20 mm electrode model. The anode current was kept constant at 135 mA. The multiple-hole orifice model and the ϕ20 mm electrode model used a punching plate with a 1-mm thick opening ratio of 32.6%.

C.3.2 Results

The charge neutralization current density distribution is shown in Figure C.6. For both positive and negative charging, it was found that the current density decreased by 1–2 orders

of magnitude when the distance from the plasma source was increased from 1 to 2 m. In addition, the positively charged neutralization current density was 3 orders of magnitude larger than for the negative charge, indicating that the negatively charged neutralization performance is rate limiting. According to Figure C.6, when a positive column was generated by the anode, the neutralization current density was larger than without the anode (single-hole orifice model). The neutralization current density was also greater for the multiple-hole orifice model. For negative charge neutralization, the neutralization current density was improved up to 5 times over the single-hole orifice model. The multiple-hole orifice model does not require an additional power supply for the anode, so the structure of the neutralizer system is simplified.

In Figure C.6, the necessary current density j_{limit} for conveying a 1-m wide film at 1,000 m/min is plotted, as determined by Eq. C.4, where V_{T} is the film conveying speed and σ is the maximum charging density in a general roll-to-roll system.[85]

$$j_{\mathrm{limit}} = \sigma V_{\mathrm{T}} = 27 \times 1000/60 = 0.45\,\mathrm{mA/m^2} \tag{C.4}$$

For positive charge, this condition was satisfied up to a distance of 2 m, even with the single-hole orifice model. Using anodes and orifices increases the neutralization current density by 1–2 orders of magnitude. For negative charge, the single-hole orifice model fulfills this condition at a distance of 1 m. Using the multiple-hole orifice, model it is possible to extend the distance up to 1.5 m.

C.3.3 Discussion

The mass difference between electrons and ions responsible for the positive charge neutralization current density is 3 orders of magnitude larger than that of negative charge. Because electrons have a smaller mass than ions, the positive charge is neutralized faster than the negative charge. Eq. C.5 shows the ratio between the ion saturation current and the electron saturation current.

$$\sqrt{\frac{T_{\mathrm{e}}}{T_{\mathrm{i}}}\frac{M}{m_{\mathrm{e}}}} = 5 \times 10^3 \tag{C.5}$$

Here, T_{e} is the electron temperature, T_{i} is the ion temperature, M is the xenon ion mass, and m_{e} is the electron mass. The positive plasma column is considered to be the cause of the large neutralization current density compared with the single-hole model. Since models with an anode generate a positive plasma column in addition to the discharge chamber plasma, they generate a large neutralization current density. Figure C.6 suggests that the high plasma conductance is the reason for the large neutralization current density for the multiple-hole orifice model. The opening area for the multiple-hole orifice was one order of magnitude larger than that for the single-hole orifice model and the thickness was five times smaller.

Therefore, it is considered that more plasma was exhausted from the discharge chamber and the neutralization current density was increased.

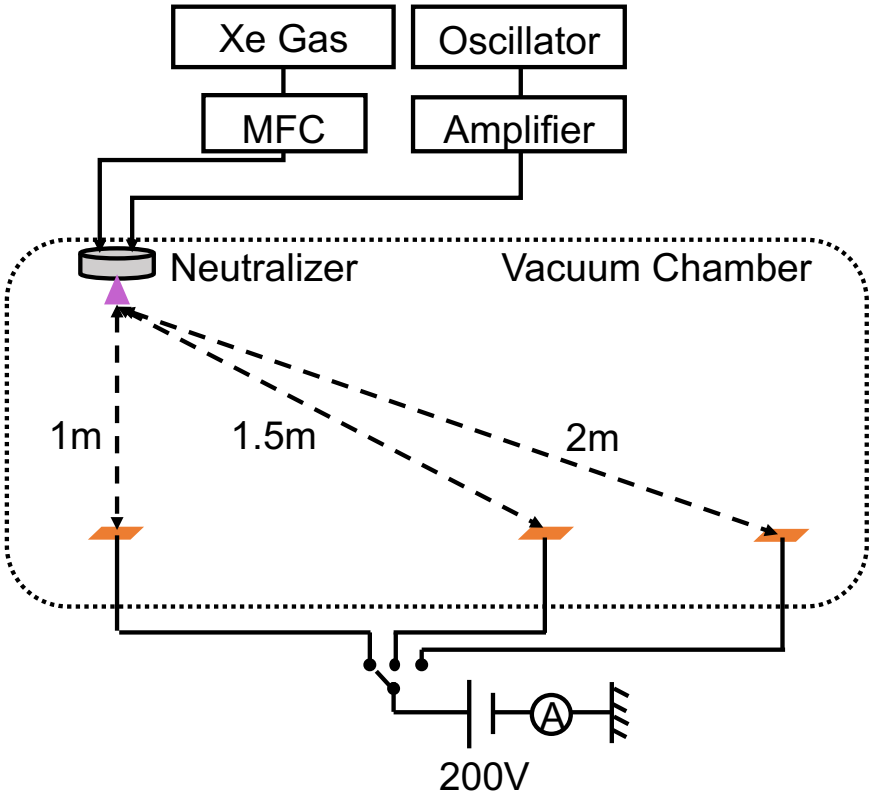

Figure C.3: Experimental setup for measurement of neutralization current density.

Table C.3: Experimental conditions for measurement of neutralization current density.

Parameter	Value
Microwave frequency	4.25 GHz
Microwave power, P_{m}	8 W
Xenon flow rate, $\dot{m}_{\mathrm{c}}$	0.5 sccm (0.049 mg/s)
Anode current	135 mA constant current
Charged plate voltage	±200 V
Background pressure	3×10^{-3} Pa without Xe input 4×10^{-3} Pa at 0.5 sccm Xe

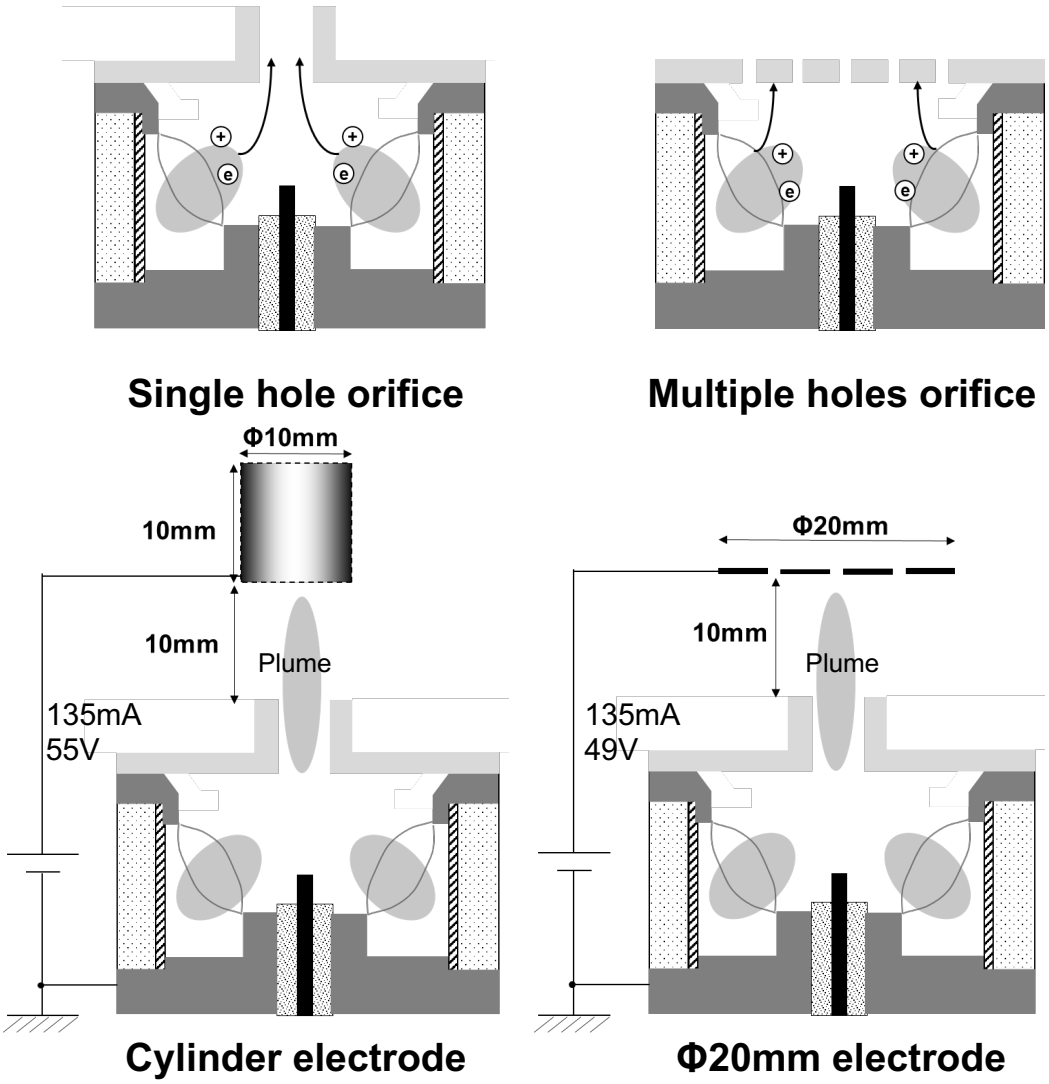

Figure C.4: Schematic diagram of microwave discharge plasma sources of neutralization current density.

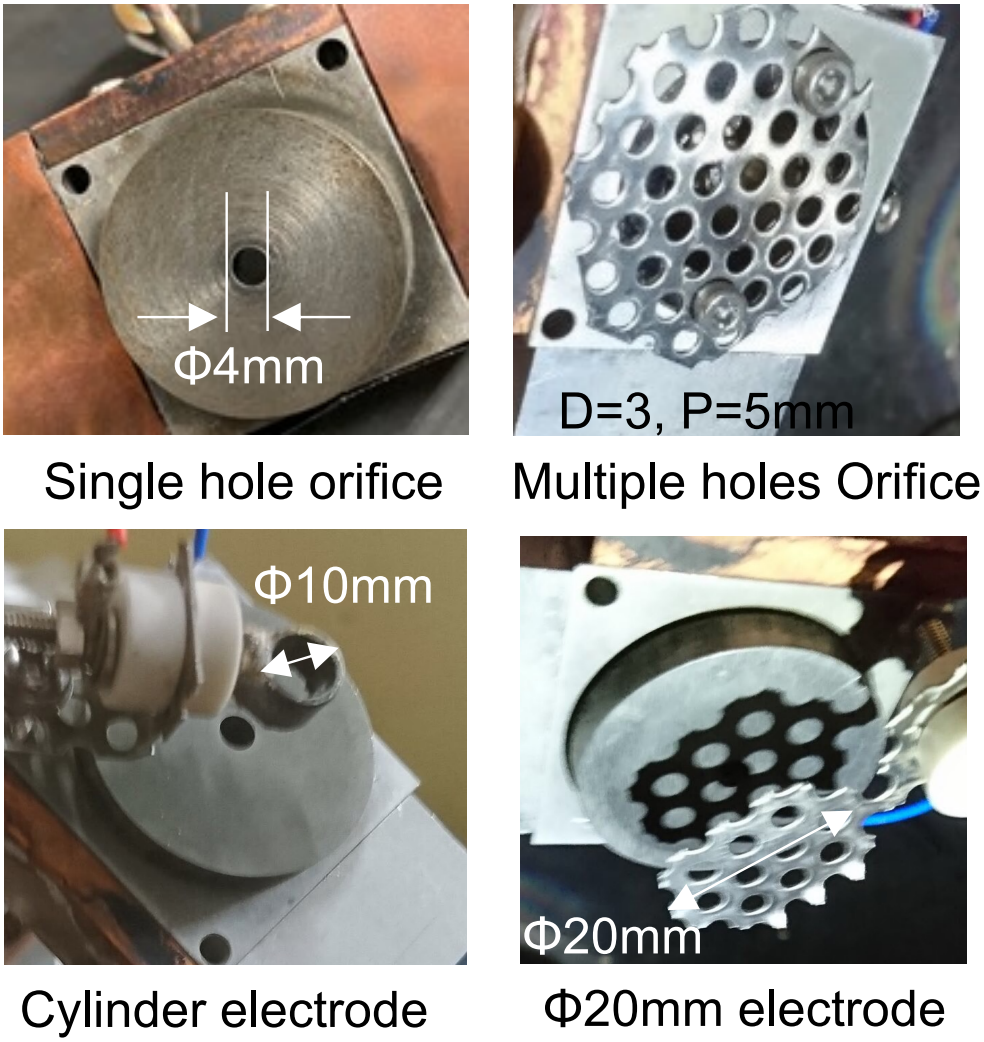

Figure C.5: Photograph of microwave discharge plasma sources of neutralization current density.

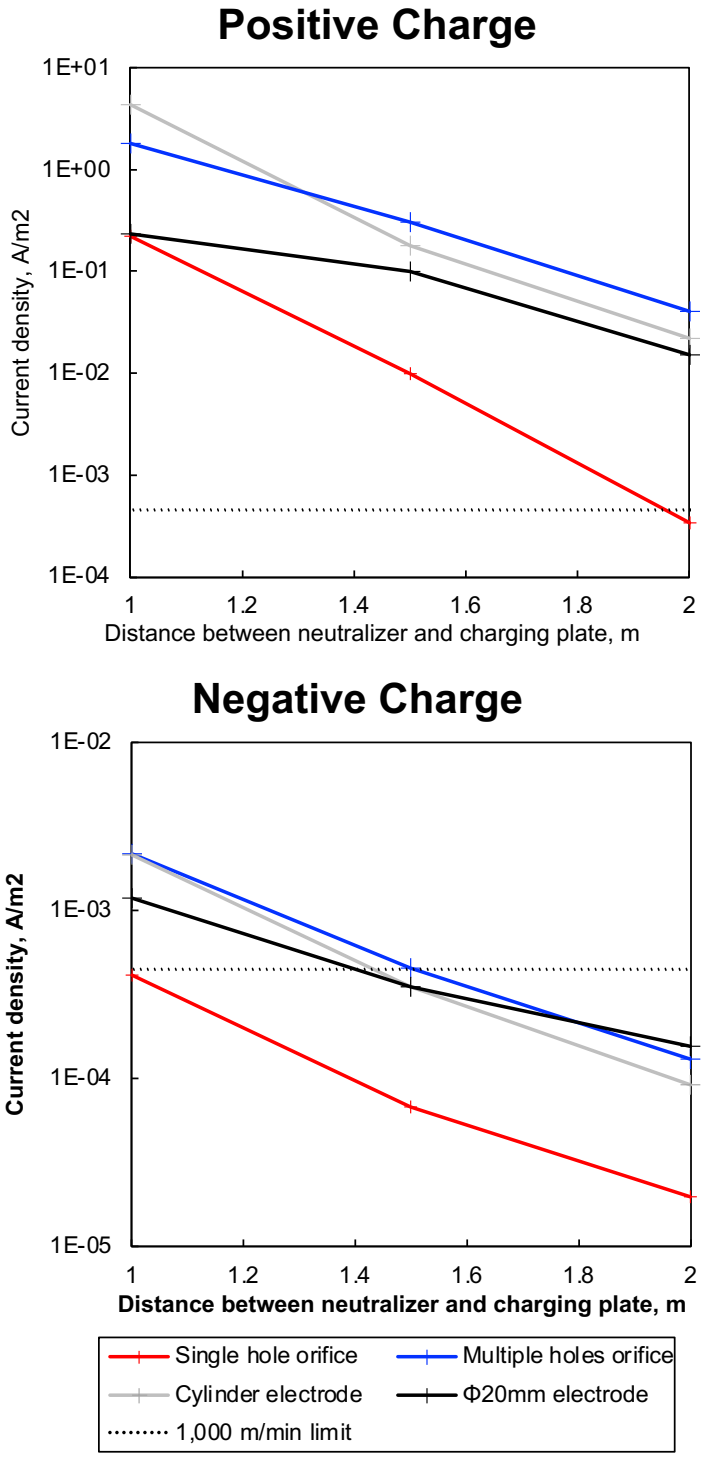

Figure C.6: Comparison of charge neutralization current density.

C.4 Neutralization demonstration in film transfer simulator

To demonstrate the charge neutralization effect for transferring film, a film transfer simulator was used. This experiment was conducted at Kasuga Denki, Inc. Figures C.7 and C.8 show the experimental setup for the neutralization demonstration in a film transfer simulator. A polypropylene film was transferred by three stainless rolls and charged by friction as they rotate. The charge potential was measured using a non-contact electrometer installed 20 mm from the film. The experimental conditions are summarized in Table C.4.

Figure C.9 shows the time history of charge neutralization of the film. Transferring the film generated a negative charge up to −1.2 kV. As shown in Figure C.9, the potential oscillated from 0 kV to −1.2 kV. Non-uniformity in the film surface charge was observed. After plasma ignition, the charge was neutralized to a plasma potential of +20 V. It was thus confirmed that the microwave discharge neutralizer system was effective in the film transfer simulator.

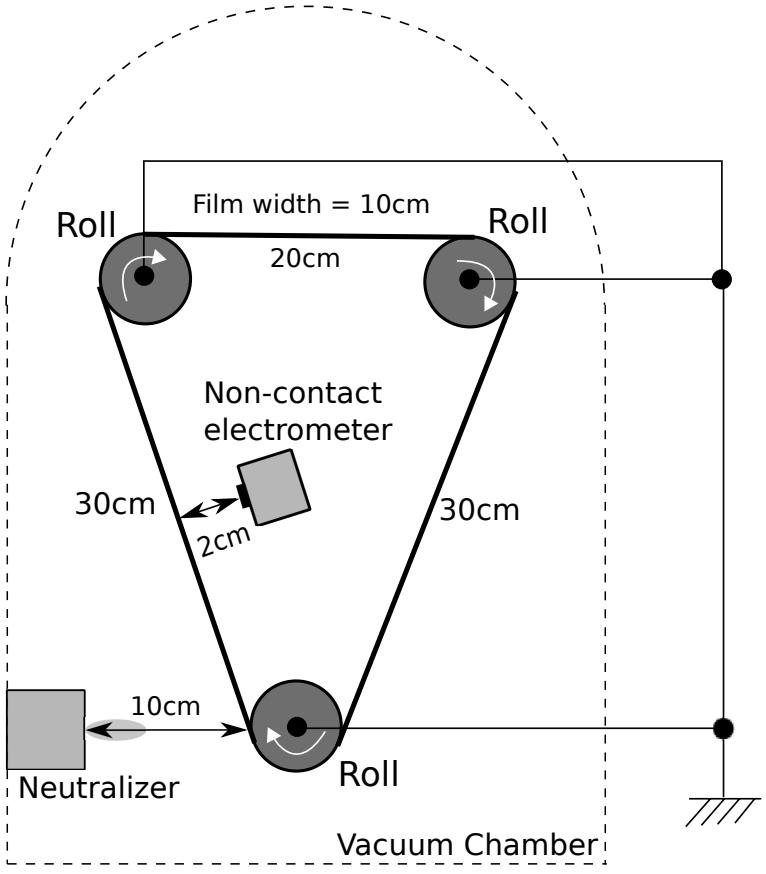

Figure C.7: Experimental setup for charge neutralization in film transfer simulator.

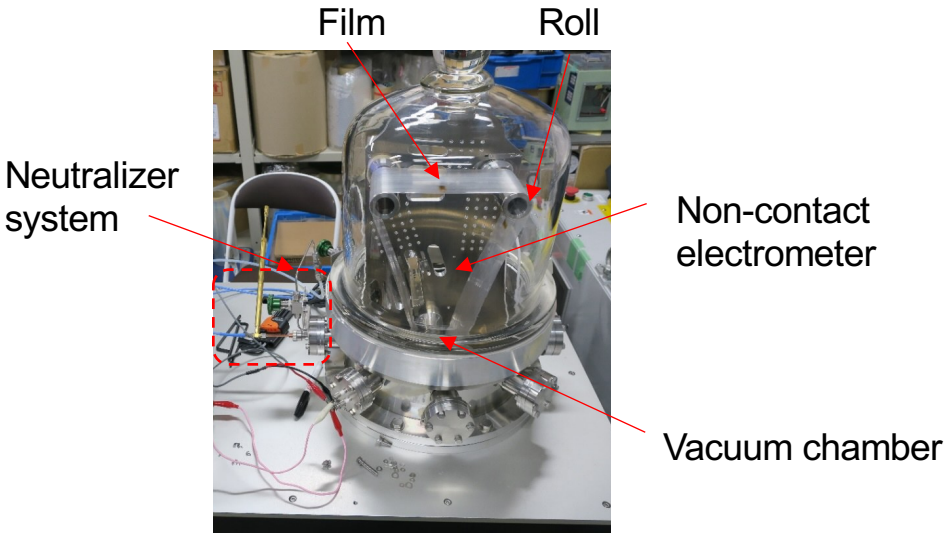

Figure C.8: Photograph of the experimental setup for charge neutralization in film transfer simulator.

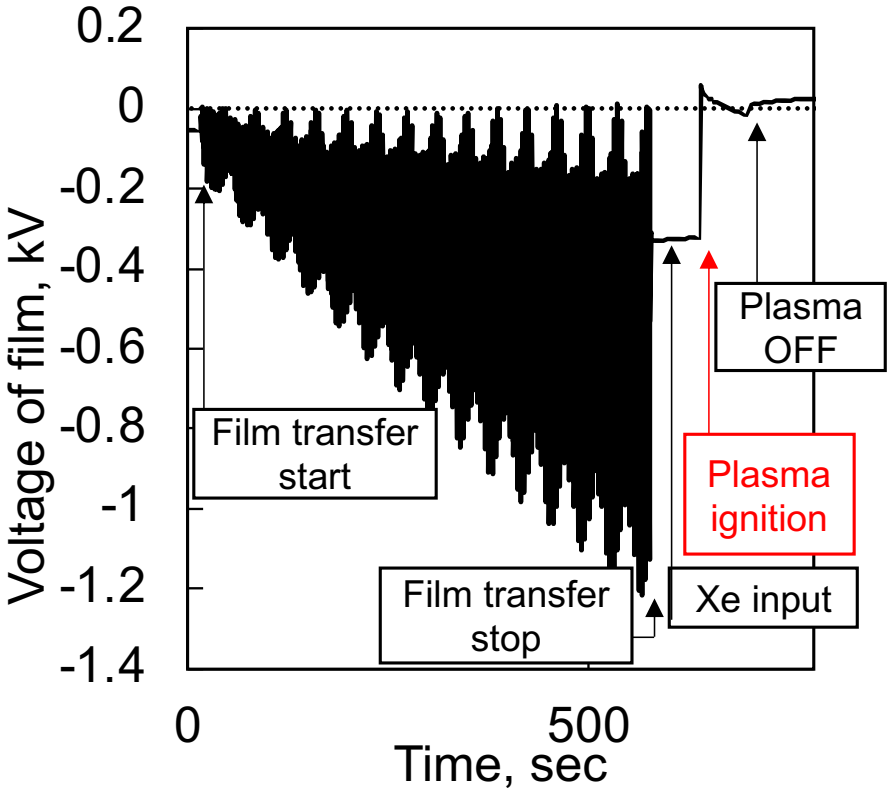

Figure C.9: Time history of charge neutralization in film transfer simulator.

Table C.4: Experimental conditions for charge neutralization in film transfer simulator.

Parameter	Value
Microwave frequency	4.25 GHz
Microwave power, P_{m}	8 W
Xenon flow rate, $\dot{m}_{\mathrm{c}}$	0.5 sccm (0.049 mg/s)
Film	Polypropylene
Film transfer speed	0.2 m/s
Background pressure	1×10^{-2} Pa at 0.5 sccm Xe

C.5 Comparison with a conventional neutralization system

The characteristics and neutralization performance were compared between this method and a conventional UV neutralizer.[86] Table C.5 shows the comparison results. Note that the neutralization time is calibrated by a capacitor. As shown in Table C.5, the microwave discharge plasma neutralization system has some advantages compared with a conventional neutralizer. The microwave discharge plasma neutralization system neutralizes positive charge 10^5 faster and negative charge 10^4 faster. In addition, the lifetime is 20 times longer.

As shown in Figure C.10, this neutralizer was developed and made into product with help from Kasuga Denki, Inc.[87]

Table C.5: Comparison between proposed microwave discharge plasma neutralization system and conventional UV neutralization system.

	This study	UV ionizer IUV-303[86]
Power consumption	∼10 W	∼100 W
Lifetime	>70,000 h	∼2,000 h
Effective neutralization distance	<2 m	<0.3 m
Head size	∼3 cm	∼ 3 cm
Neutralization from +200 V to +20 V	3×10^{-8} s	2×10^{-3} s
Neutralization from −200 V to −20 V	5×10^{-5} s	1×10^{-1} s

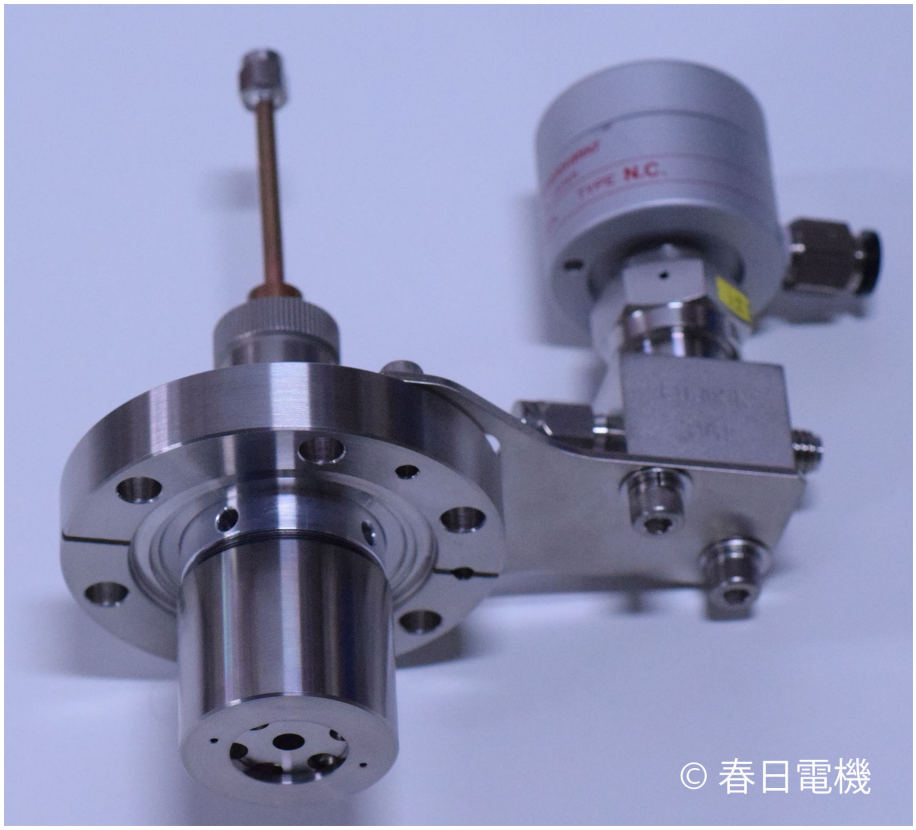

Figure C.10: Developed microwave discharge plasma neutralization system. ©Copyright 2019 Kasuga Denki, Inc.

C.6 Summary

The application of a space-qualified microwave discharge plasma source as a positive and negative charge neutralizer was evaluated. We also investigated the charge neutralization current density distribution. When a plasma source is placed within 1.5 m, it was found that film conveyance can be performed at 1,000 m/min. Furthermore, we studied the orifice and anode shape to improve the plasma transparency, and achieved a charge neutralization current density 5 times higher than for the conventional single-hole orifice type. This method was experimentally demonstrated with a film transfer simulator. These findings suggest that a $\phi 3$ cm and 10-W class microwave discharge plasma source is effective for charge neutralization in a high vacuum.

Appendix D

Application of a Plasma Source for Charged Dust Removal in High Vacuum

D.1 Background

Dust mitigation is one of the most important problems to be addressed for exploration of the Moon and Mars. Charged fine dust (regolith) attaches to mission equipment and spacesuits by an electrostatic force. When removing a spacesuit, an astronaut who inhales the lunar regolith may experience symptoms like hay fever.[88][89] Another concern is that mechanical gaps such as seals and bearings are at risk of dust contamination.[90][91][92][93] Levitated regolith will cover solar panels, heat radiators, and optical equipment, degrading performance.[94] Fine dust is also a problem in asteroid sample return missions. In the asteroid touchdown mission of explorer Hayabusa2, the optical navigation camera (ONC) confirmed that fine dust was disturbed and was caused to rise by the thruster jet. After the touchdown, the light detection level of the ONC decreased due to the coating of fine dust.

On the lunar surface, the solar wind and energetic particles arrive directly because of the low-density atmosphere. The lunar regolith is electrostatically charged and churned up at the boundary between the dayside and nightside by interaction between photoemission by UV and X-rays on the dayside and the solar wind on the nightside.[95] The charged regolith adheres to spacesuits and equipment by an electrostatic force. Methods to address this problem include fluidal methods,[96][97][98] mechanical methods,[99][100], electrodynamic methods,[101][102][103][104][89] passive methods,[93][105][106][89] and plasma methods.[107][105][108][109][110] Plasma methods use an energetic electron beam (hundreds of eV) to charge and move the particles by the Coulomb force at 10^{-1} Pa.[108] Also, a plasma jet (several kV) can be used to move particles in Martian environments of 10^{2} Pa.[110]

In the proposed method, the charged dust is neutralized and removed by Debye shielding using a plasma with low-energy electrons, of several electron volts for example. In this

study we developed an apparatus to charge dust and target surfaces in a high vacuum. In previous research, targets were charged before being introduced into a vacuum, and the targets were neutralized by the Paschen law. Neutralization of levitated charged spheres was not investigated. In this experimental study, we first removed charged regolith adhering to an insulator plate by a microwave discharge plasma in a high vacuum. The dust was charged and caused to adhere to a charged insulator plate. The microwave discharge source is an improved model. Removal of adhering dust by plasma and the prevention of adhesion of dust under a plasma environment were investigated. Second, we investigated the dust adhesion characteristics under a plasma environment. Third, we exposed levitated charged particles to a plasma. The charged particles were levitated by the Electrostatic Levitation Furnace (ELF) in JAXA.

D.2 Effect of microwave discharge plasma on charged dust

Experimental setup Figure D.1 shows a schematic diagram of the experimental setup for charged dust removal. We constructed an experimental setup to charge an insulator disk and dust in a high vacuum. If the chamber is evacuated after charging the disk and dust in the atmosphere, they will be neutralized according to Paschen's law. The rotating insulator disk, made of 1-mm thick acrylic, was installed 1 m vertically below the microwave discharge plasma source. The insulator disk rotated at 1 rps and was electrostatically charged by an insulator brush. The charge potential was measured using a non-contact electrometer installed 10 mm from the disk. The dust was a lunar simulant (FJS-1), with a range of particle diameters from a few tens of microns to several hundred microns, and was stored in a dust container. When the mixer in the dust container was operated, the dust was electrostatically charged and extracted by the charged insulator disk. The dust adhered to the lower surface of the disk because the gas jet and plasma jet should not affect the dust. The amount of adhered dust was measured using an electronic scale. The experimental conditions are summarized in Table D.1.

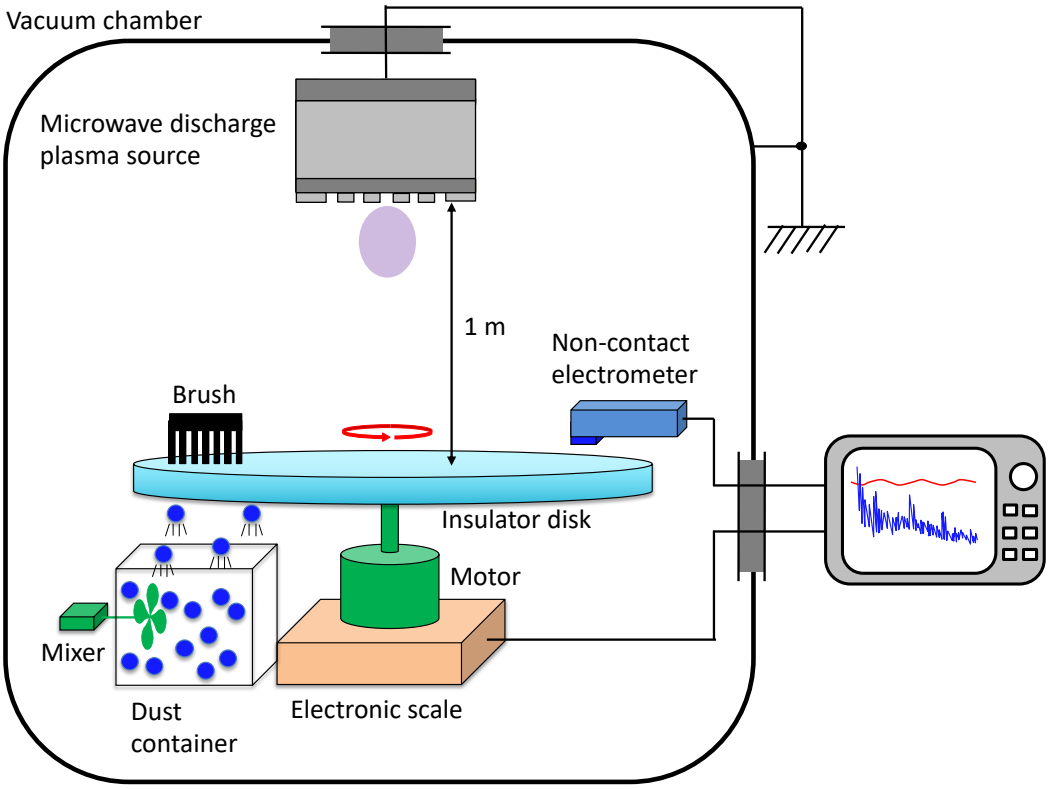

Figure D.1: Schematic diagram of experimental setup for charged dust removal.

Table D.1: Experimental conditions for charged dust removal.

Parameter	Value
Microwave frequency	4.25 GHz
Microwave power, P_{m}	8 W
Xenon flow rate, $\dot{m}_{\mathrm{c}}$	1.5 sccm (0.147 mg/s)
Dust	Lunar simulant (FJS-1)
Disk	ϕ140 mm, 1 mm, acrylic
Disk rotational speed	1 rps
Background pressure	3×10^{-3} Pa without Xe input 8×10^{-3} Pa at 1.5 sccm Xe

Removal of adhered dust Figure D.2 shows the time history of the removal of charged adhered dust by the microwave discharge plasma. In this time history, the disk was always rotated. First, the isolator disk was rotated and charged to 1.5 kV. At time $t = 5$ s, the mixer in the dust container was turned on to mix and electrically charge the dust by friction. The dust gradually adhered to the disk, and about 1.8 g of dust adhered by $t = 60$ s. At $t = 40$ s, over 3 sccm pulsed xenon was introduced, but the disk potential was not neutralized, and dust was not removed. At $t = 50$ s, a further 1.5 sccm xenon was introduced. At $t = 60$ s, the microwave power was turned on and the microwave discharge plasma ignited. Then, the dust began to be removed: 50% of the dust was removed in 5 s and 87% was removed in 50 s. It should be noted that the non-contact electrometer, which measures the potential from the electric field, does not work properly in a plasma environment because the field is shielded by the plasma, and it was therefore turned off. At $t = 160$ s, 99% of the dust was removed.

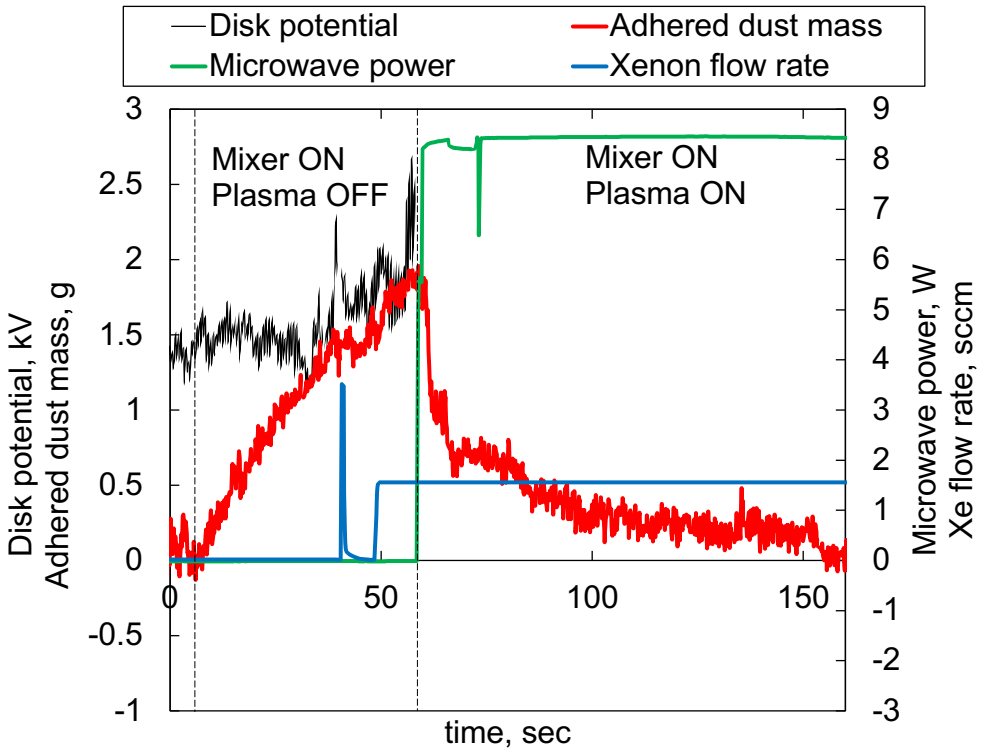

Figure D.2: Removal of charged adhered dust by microwave discharge plasma.

Mitigation of dust adhesion by the microwave discharge plasma Figure D.3 shows the time history of the mitigation of dust adhesion by a microwave discharge plasma. In this time history, the microwave discharge plasma was always generated. At $t = 10$ s, the disk started to rotate and the mixer was turned on. However, the dust did not adhere to the disk. This result suggests that the microwave discharge plasma neutralized the disk and dust, and prevented the dust from adhering to the disk. These results suggest that the adhered dust was removed by the plasma without an energetic electron beam.

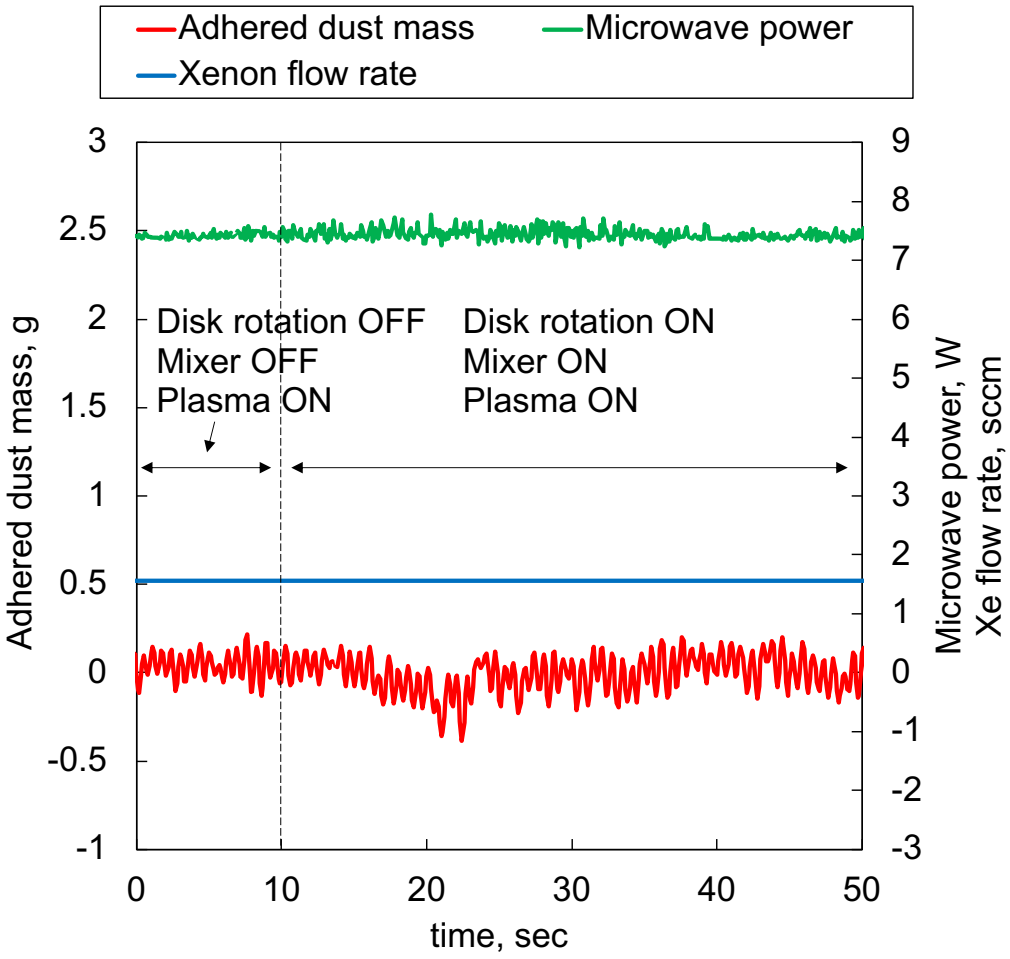

Figure D.3: Mitigation of dust adhesion by microwave discharge plasma.

D.3 Neutralization of levitated dust by microwave discharge plasma

D.3.1 Experimental setup

Figure D.4 shows the experimental setup for charge neutralization of levitated charged particles. This setup is based on the ELF in JAXA.[111] The ELF is a non-contact method developed to measure the density, surface tension, and viscosity of high-temperature materials without reactions between the container and melts. The ELF utilizes the Coulomb force between the sample and surrounding electrodes to cancel the gravitational force. A positively charged sphere was levitated between a pair of parallel disk electrodes (top and bottom electrodes), typically $d = 10$ mm apart, which control the vertical position of the sphere. At the launch of the sphere, if the top electrode has a positive potential, the sphere touching the grounded bottom electrode attracts electrons by charge polarization. Therefore, the sphere is negatively charged and starts to levitate due to the force from the electric field. In the case of a negative potential, the sphere is positively charged, and a laser can be used to maintain the charge. A CO_2 laser with a wavelength of 10.6 μm was used to melt and charge the sphere by thermal emission. We used a ϕ2 mm sphere made of glassy carbon, which is conductive. The microwave discharge plasma source was located 500 m from the sphere. The sphere and microwave discharge plasma source were observed by a camera. The potential of the top electrode was controlled depending on the vertical position, calculated by a detector. The feedback frequency of the position sensor was 600 kHz and the position error due to free fall was within 0.03 mm. The power supply for the top electrode had enough power to maintain a maximum voltage of 30 kV when the microwave discharge plasma source was in operation. The experimental conditions are summarized in Table D.2.

D.3.2 Results

Figure D.5 shows the time history of the charge neutralization of a levitated charged particle in the ELF. At first, the sphere was levitated to 1.8 mm by the Coulomb force by the top electrode with V = +11.8 kV. When the plasma as generated, the sphere started to undergo free fall. The dotted line is a fit to the free fall, and matches the measured position with an R^2 value of 0.98. When the sphere was in free fall, the electrode potential was increased to prevent the sphere from falling. The electrode potential increased up to 30 kV, and could not maintain the levitation because the plasma neutralized the sphere and shielded the electric field.

Figure D.6 shows a photograph of the charge neutralization of a levitated charged particle:

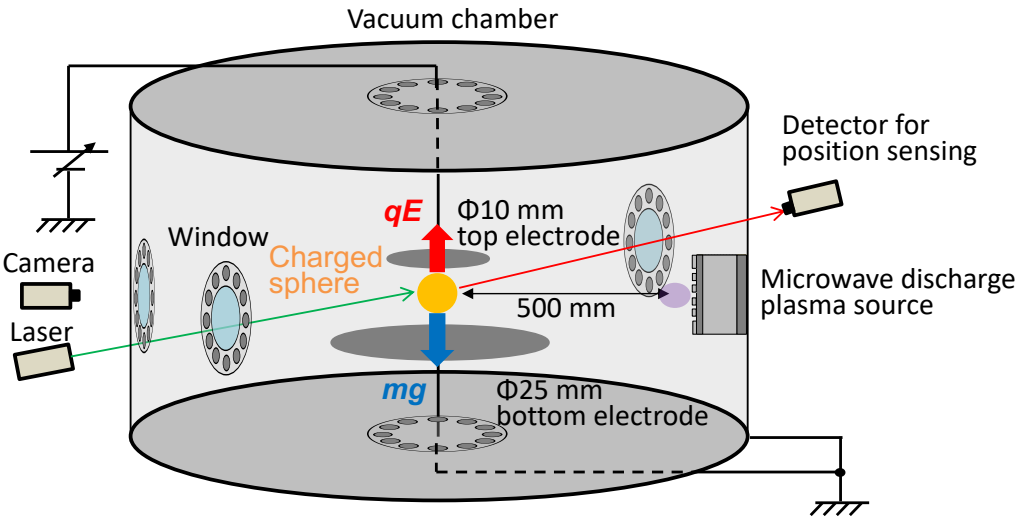

Figure D.4: Schematic diagram of charge neutralization of levitated charged particle in electrostatic levitation furnace.

Table D.2: Experimental conditions for neutralization of levitated charged sphere.

Parameter	Value
Microwave frequency	4.25 GHz
Microwave power, P_{m}	8 W
Xenon flow rate, $\dot{m}_{\mathrm{c}}$	0.8 sccm (0.079 mg/s)
Sphere	ϕ2 mm, glassy carbon
Maximum electrode potential	30 kV
Disk rotational speed	1 rps
Background pressure	3×10^{-3} Pa without Xe 1×10^{-2} Pa at 0.8 sccm Xe

before plasma ignition (a), after plasma ignition (b), after free fall (c). As shown in Figure D.6(a), the sphere levitated when the Coulomb force and gravity were balanced. As shown in Figure D.6(b), the microwave discharge plasma sources started to ignite and the sphere underwent free fall. The blue light is the microwave discharge plasma observed by the camera installed on the opposite side of the microwave discharge plasma source.

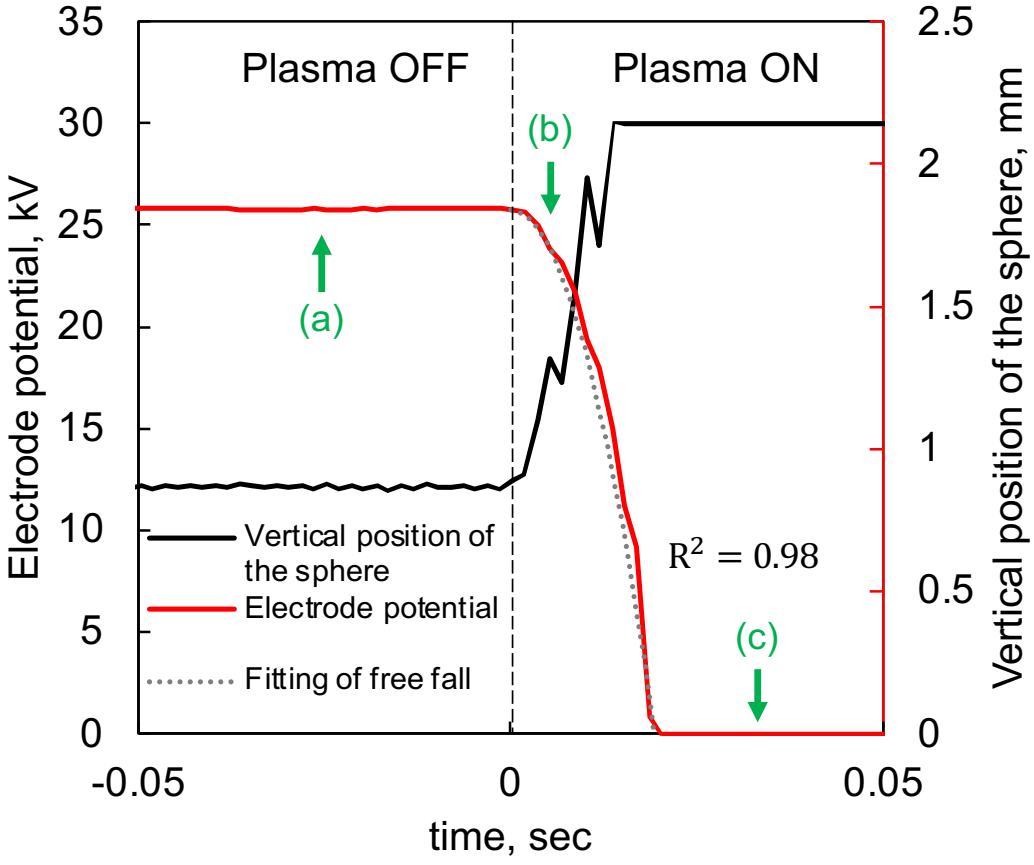

Figure D.5: Charge neutralization of levitated charged particle in electrostatic levitation furnace. The symbols correspond to those in Figure D.6

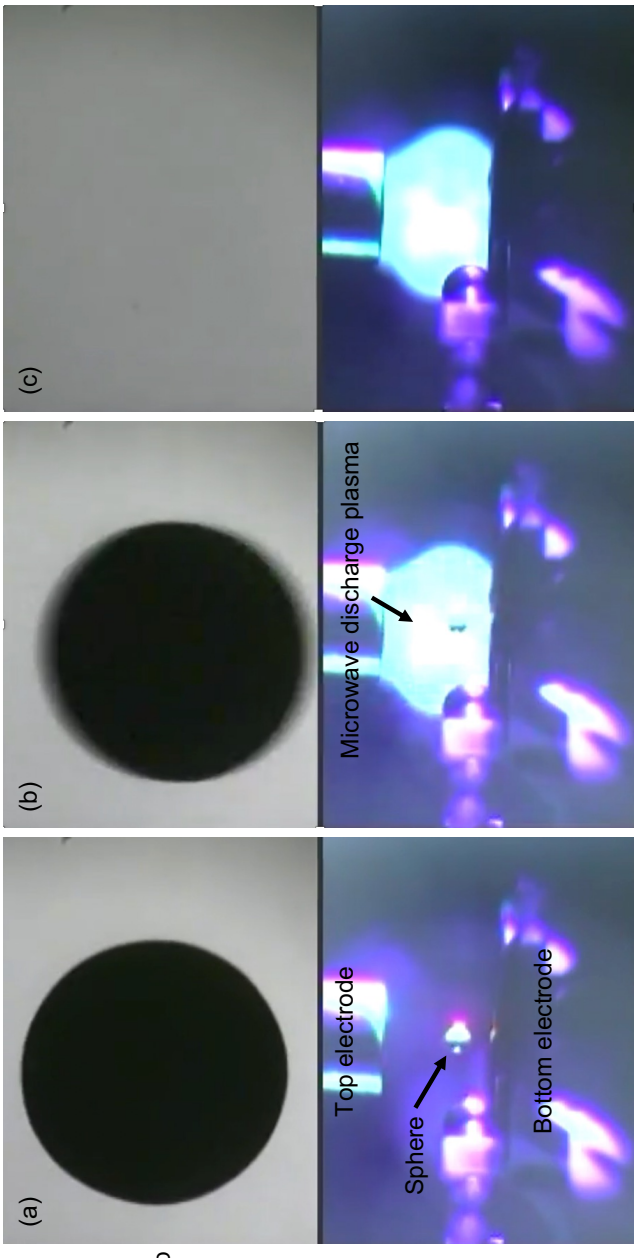

Figure D.6: Photograph of charge neutralization of levitated charged particle. The symbols correspond to those in Figure D.5: before plasma ignition (a), after plasma ignition (b), after free fall (c). The upper row is a close-up of the sphere, and is lower overall

D.4 Summary

To investigate the effects of microwave discharge plasma exposure on adhered dust and levitated dust, we conducted two experiments: charged dust removal and neutralization of a levitated sphere. For the former experiment, we developed an apparatus which can charge dust and a disk in a high vacuum. For the latter experiment, we applied the ELF to charge neutralization of the levitated sphere. The results are summarized as follows:

1. After plasma ignition, the dust began to be removed: 50% of the dust was removed in 5 s, 87% was removed in 50 s, and 99% was removed in 100 s. These results suggest that the adhered dust can be removed by the plasma without an energetic electron beam.
2. During plasma exposure, the dust did not adhere to the disk, because it was immediately neutralized and Debye shielded.
3. By plasma exposure, the levitated sphere was neutralized and underwent free fall. This is the first demonstration of the neutralization of a levitated particle.

References

[1] H Bassner, H-P Berg, and R Kukies. Recent results on qualification of the rita components for the artemis satellite. In *28th Joint Propulsion Conference and Exhibit*, p. 3207, 1992.

[2] Howard Gray, Peter Smith, and David Fearn. Design and development of the uk-10 ion propulsion system. In *32nd Joint Propulsion Conference and Exhibit*, p. 3084, 1996.

[3] Rainer Killinger, Helmut Bassner, Johann Mueller, and Ralf Kukies. Rita ion propulsion for artemis lifetime test results. In *36th AIAA/ASME/SAE/ASEE Joint Propulsion Conference and Exhibit*, p. 3273, 2000.

[4] Dan M Goebel and Ira Katz. *Fundamentals of electric propulsion: ion and Hall thrusters*. John Wiley & Sons, 2008.

[5] Hitoshi Kuninaka, N Hiroe, K Kitaoka, Y Ishikawa, K Nishiyama, and Y Horiuchi. Development of ion thruster system for interplanetary missions. In *23rd International Electric Propulsion Conference, IEPC-93-198, Seattle, USA*, pp. 13–16, 1993.

[6] Hitoshi Kuninaka, Kazutaka Nishiyama, Ikko Funaki, Tetsuya Yamada, Yukio Shimizu, and Jun'ichiro Kawaguchi. Powered flight of electron cyclotron resonance ion engines on hayabusa explorer. *Journal of Propulsion and Power*, Vol. 23, No. 3, pp. 544–551, 2007.

[7] Kazutaka Nishiyama, Satoshi Hosoda, Kazuma Ueno, Ryudo Tsukizaki, and Hitoshi Kuninaka. Development and testing of the hayabusa2 ion engine system. *Transactions of the Japan Society for Aeronautical and Space Sciences, Aerospace Technology Japan*, Vol. 14, No. ists30, pp. Pb_131–Pb_140, 2016.

[8] Ryudo Tsukizaki, Toshiyuki Ise, Hiroyuki Koizumi, Hiroyoshi Togo, Kazutaka Nishiyama, and Hitoshi Kuninaka. Thrust enhancement of a microwave ion thruster. *Journal of Propulsion and Power*, Vol. 30, No. 5, pp. 1383–1389, 2014.

[9] Bruno Victorino Sarli, Makoto Horikawa, Chit Hong Yam, Yasuhiro Kawakatsu, and Takayuki Yamamoto. Destiny+ trajectory design to (3200) phaethon. *The Journal of the Astronautical Sciences*, Vol. 65, No. 1, pp. 82–110, 2018.

[10] Dan M Goebel and Emily Chu. High-current lanthanum hexaboride hollow cathode for high-power hall thrusters. *Journal of Propulsion and Power*, Vol. 30, No. 1, pp. 35–40, 2014.

[11] James Polk, Dan Goebel, Ron Watkins, Kristina Jameson, and Lance Yoneshige. Characterization of hollow cathode performance and thermal behavior. In *42nd AIAA/ASME/SAE/ASEE Joint Propulsion Conference & Exhibit*, p. 5150, 2006.

[12] Dan Michael Goebel, JT Crow, and AT Forrester. Lanthanum hexaboride hollow cathode for dense plasma production. *Review of Scientific Instruments*, Vol. 49, No. 4, pp. 469–472, 1978.

[13] Matthew T Domonkos, Alec D Gallimore, and Michael J Patterson. An evaluation of hollow cathode scaling to very low power and flow rate. In *Proceedings of the 25th International Electric Propulsion Conference*, pp. 97–189. IEPC Cleveland, Ohio, USA, 1997.

[14] Matthew Domonkos, Alec Gallimore, George Williams, Jr, and Michael Patterson. Low-current hollow cathode evaluation. In *35th Joint Propulsion Conference and Exhibit*, p. 2575, 1999.

[15] Matthew T Domonkos, Michael J Patterson, and Alec D Gallimore. Low-current, xenon orificed hollow cathode performance for in-space applications. *Journal of propulsion and power*, Vol. 19, No. 3, pp. 438–443, 2003.

[16] Francis F Chen. *Introduction to plasma physics and controlled fusion*, Vol. 1. Springer, 1984.

[17] 谷義隆. マイクロ波放電式中和器の性能向上に関する実験的研究, 東京大学修士論文, 2016 (in Japanese).

[18] 小泉宏之, 國中均. 500ma 級マイクロ波放電式中和器の dubaisat-2 ホール推進システムへの適用. 平成 24 年度宇宙輸送シンポジウム: 講演集録, 2013 (in Japanese).

[19] Kazutaka Nishiyama, Yukio Shimizu, Hitoshi Kuninaka, Takashi Miyamoto, Miho Fukuda, and Tatsuya Nakai. Research and development status of microwave discharge ion thruster μ20. In *29th International Electric Propulsion Conference*, pp. 3–5, 2005.

[20] Kazutaka Nishiyama, Hitoshi Kuninaka, and Tatsuya Nakai. Two-dimensional characterization of microwave e-fields and beam profiles of the ecr ion thruster μ20. In *30th International Electric Propulsion Conference*, Vol. 25, 2007.

[21] Kazutaka Nishiyama, Satoshi Hosoda, Hitoshi Kuninaka, and Yasuhiro Toyoda. Operational characteristics of a microwave discharge neutralizer for the ecr ion thruster μ20. In *31st International Electric Propulsion Conference, Ann Arbor, MI, USA*, 2009.

[22] 鈴木誠二. マイクロ波放電型電子放出源に関する研究, 東京都立科学技術大学修士論文, 1997 (in Japanese).

[23] Ikkoh Funaki Ikkoh Funaki, Shin Satori Shin Satori, and Hitoshi Kuninaka Hitoshi Kuninaka. Low-power microwave electron source for ion engine neutralizer. *Japanese journal of applied physics*, Vol. 37, No. 7R, p. 4228, 1998.

[24] 佐鳥新, 船木一幸, 國中均. マイクロ波中和器の放電室内部測定. 日本航空宇宙学会論文集, Vol. 47, No. 544, pp. 197–201, 1999 (in Japanese).

[25] 小野寺範義, 竹ヶ原春貴, 西山和孝, 船木一幸, 國中均. マイクロ波放電型中和器の電子放出機構. 日本航空宇宙学会論文集, Vol. 49, No. 564, pp. 27–31, 2001 (in Japanese).

[26] Ikkoh Funaki Ikkoh Funaki and Hitoshi Kuninaka Hitoshi Kuninaka. Overdense plasma production in a low-power microwave discharge electron source. *Japanese Journal of Applied Physics*, Vol. 40, No. 4R, p. 2495, 2001.

[27] 大道渉. マイクロ波放電式中和器の耐久性に関する研究, 東京大学修士論文, 2011 (in Japanese).

[28] 谷義隆, 月崎竜童, 西山和孝. マイクロ波放電式中和器における 2 価イオンの流量依存性. プラズマ応用科学= Applied plasma science: journal of IAPS, Vol. 22, No. 2, pp. 75–80, 2014 (in Japanese).

[29] Wataru Ohmichi. *A study on the degradation mechanism and lifetime enhancement of microwave discharge neutralizers*. PhD thesis, The University of Tokyo, 2014.

[30] 森田駿也. マイクロ波放電式中和器の長寿命化に向けた実験的研究, 東京大学修士論文, 2018 (in Japanese).

[31] 西山和孝. 電子サイクロトロン共鳴型イオンスラスターの放電プラズマ. PhD thesis, 東京大学, 1998 (in Japanese).

[32] George Jarvis Williams Jr. *The use of laser-induced fluorescence to characterize discharge cathode erosion in a 30 cm ring-cusp ion thruster*. University of Michigan, 2000.

[33] Yuto Sugita, Hiroyuki Koizumi, Hitoshi Kuninaka, Yoshiki Yamagiwa, and Makoto Matsui. Number density measurement of neutral particles in a miniature microwave discharge ion thruster. *TRANSACTIONS OF THE JAPAN SOCIETY FOR AERONAUTICAL AND SPACE SCIENCES, AEROSPACE TECHNOLOGY JAPAN*, Vol. 12, No. ists29, pp. Tb_31–Tb_35, 2014.

[34] Yoshinori Nakayama and Futoshi Tanaka. Experimental visualization of ion thruster neutralization phenomena. *IEEE Transactions on Plasma Science*, Vol. 43, No. 1, pp. 269–276, 2014.

[35] OneWeb Press release. Oneweb confirms successful launch of 36 satellites, after rapid year of progress. available at `https://oneweb.net/media-center/oneweb-confirms-successful-launch-of-36-satellites-after-rapid-year-of-progress` (accessed on February 2022).

[36] Jeff Foust. Spacex passes 2,000 starlink satellites launched. available at `https://spacenews.com/spacex-passes-2000-starlink-satellites-launched/` (accessed on February 2022).

[37] George-Cristian Potrivitu, Yufei Sun, Muhammad Wisnuh Aggriawan bin Rohaizat, Oleksii Cherkun, Luxiang Xu, Shiyong Huang, and Shuyan Xu. A review of low-power electric propulsion research at the space propulsion centre singapore. *Aerospace*, Vol. 7, No. 6, p. 67, 2020.

[38] Ryan W Conversano, Dan M Goebel, Ioannis G Mikellides, Richard R Hofer, and Richard E Wirz. Performance analysis of a low-power magnetically shielded hall thruster: computational modeling. *Journal of Propulsion and Power*, Vol. 33, No. 4, pp. 992–1001, 2017.

[39] Kurt A Polzin, Thomas E Markusic, Boris J Stanojev, Amado Dehoyos, Yevgeny Raitses, Artem Smirnov, and Nathaniel J Fisch. Performance of a low-power cylindrical hall thruster. *Journal of propulsion and power*, Vol. 23, No. 4, pp. 886–888, 2007.

[40] Tomoyuki Ikeda, Kazuya Togawa, Hirokazu Tahara, and Yosuke Watanabe. Performance characteristics of very low power cylindrical hall thrusters for the nano-satellite “proiteres-3”. *Vacuum*, Vol. 88, pp. 63–69, 2013.

[41] D Dignani, C Ducci, G Cifali, P Rossetti, and M Andrenucci. Ht-100 hall thruster characterization tests results, iepc 32nd international electric propulsion conference, wiesbaden, germany. Technical report, IEPC-2011-191, 2011.

[42] Takato Morishita, Ryudo Tsukizaki, Shunya Morita, Daiki Koda, Kazutaka Nishiyama, and Hitoshi Kuninaka. Effect of nozzle magnetic field on microwave discharge cathode performance. *Acta Astronautica*, Vol. 165, pp. 25–31, 2019.

[43] Takato Morishita, Ryudo Tsukizaki, Naoji Yamamoto, Kiyoshi Kinefuchi, and Kazutaka Nishiyama. Application of a microwave cathode to a 200-w hall thruster with comparison to a hollow cathode. *Acta Astronautica*, Vol. 176, pp. 413–423, 2020.

[44] David C Meeker. Finite element method magnetics, version 4.2 (28feb2018 build), 2019.

[45] Takato Morishita, Ryudo Tsukizaki, Kazutaka Nishiyama, and Hitoshi Kuninaka. Plasma parameters measured inside and outside a microwave-discharge-based plasma cathode using laser-induced fluorescence spectroscopy. *Journal of Applied Physics*, Vol. 131, No. 1, p. 013301, 2022.

[46] Alan C Eckbreth. *Laser diagnostics for combustion temperature and species*, Vol. 3. CRC press, 1996.

[47] J. Reader A. Kramida, Yu. Ralchenko and NIST ASD Team (2020). Nist atomic spectra database (version 5.8), (national institute of standards and technology, gaithers-

burg, md, 2021). available at `https://physics.nist.gov/asd` (accessed on September 2021).

[48] David Manzella. Stationary plasma thruster ion velocity distribution. In *30th Joint Propulsion Conference and Exhibit*, p. 3141, 1994.

[49] RJ Cedolin, WA Hargus Jr, PV Storm, RK Hanson, and MA Cappelli. Laser-induced fluorescence study of a xenon hall thruster. *Applied Physics B*, Vol. 65, No. 4, pp. 459–469, 1997.

[50] George Williams, Jr, Alec Gallimore, Timothy Smith, Frank Gulczinski, III, Brian Beal, and R Drake. Laser induced fluorescence measurement of ion velocities in the plume of a hall effect thruster. In *35th Joint Propulsion Conference and Exhibit*, p. 2424, 1999.

[51] WA Hargus Jr and MA Cappelli. Interior and exterior laser-induced fluorescence and plasma measurements within a hall thruster. *Journal of Propulsion and Power*, Vol. 18, No. 1, pp. 159–168, 2002.

[52] Xingyue Duan, Mousen Cheng, Xiong Yang, Ning Guo, Xiaokang Li, Moge Wang, and Dawei Guo. Investigation on ion behavior in magnetically shielded and unshielded hall thrusters by laser-induced fluorescence. *Journal of Applied Physics*, Vol. 127, No. 9, p. 093301, 2020.

[53] Xingyue Duan, Dawei Guo, Mousen Cheng, Xiong Yang, and Ning Guo. Measurements of channel erosion of hall thrusters by laser-induced fluorescence. *Journal of Applied Physics*, Vol. 128, No. 18, p. 183301, 2020.

[54] Dan M Goebel, Kristina K Jameson, Ron M Watkins, Ira Katz, and Ioannis G Mikellides. Hollow cathode theory and experiment. i. plasma characterization using fast miniature scanning probes. *Journal of Applied Physics*, Vol. 98, No. 11, p. 113302, 2005.

[55] George Williams, Jr, Alec Gallimore, Timothy Smith, Frank Gulczinski, III, Brian Beal, and R Drake. Laser induced fluorescence measurement of ion velocities in the plume of a hall effect thruster. In *35th Joint Propulsion Conference and Exhibit*, p. 2424, 1999.

[56] Ryudo Tsukizaki, Yuta Yamamoto, Daiki Koda, Yamashita Yusuke, Kazutaka Nishiyama, and Hitoshi Kuninaka. Azimuthal velocity measurement in the ion beam of a gridded ion thruster using laser-induced fluorescence spectroscopy. *Plasma Sources Science and Technology*, Vol. 27, No. 1, p. 015013, 2018.

[57] Yusuke Yamashita, Ryudo Tsukizaki, Yuta Yamamoto, Daiki Koda, Kazutaka Nishiyama, and Hitoshi Kuninaka. Azimuthal ion drift of a gridded ion thruster. *Plasma Sources Science and Technology*, Vol. 27, No. 10, p. 105006, 2018.

[58] Mark Crofton. Laser spectroscopic study of the t5 ion thruster. In *31st Joint Propulsion Conference and Exhibit*, p. 2921, 1995.

[59] Timothy B Smith, Wensheng Huang, Bailo B Ngom, and Alec D Gallimore. Optogalvanic and laser-induced fluorescence spectroscopy of the zeeman effect in xenon. In *30th International Electric Propulsion Conference, Florence, Italy, Electric Rocket Propulsion Soc. Paper*, Vol. 229, 2007.

[60] Timothy B Smith. *Deconvolution of ion velocity distributions from laser-induced fluorescence spectra of xenon electrostatic thruster plumes*. University of Michigan, 2003.

[61] Vernon H Chaplin, Ryan W Conversano, Alejandro Lopez Ortega, Ioannis G Mikellides, Robert B Lobbia, and Richard R Hofer. Ion velocity measurements in the magnetically shielded miniature (masmi) hall thruster using laser-induced fluorescence. In *36th International Electric Propulsion Conference, University of Vienna, Austria*, 2019.

[62] Greg Severn, Dongsoo Lee, and Noah Hershkowitz. Xenon ion laser-induced fluorescence using a visible tunable diode laser near 680 nm. *Review of Scientific Instruments*, Vol. 78, No. 11, p. 116105, 2007.

[63] Christopher Dodson, Benjamin Jorns, and Richard Wirz. Measurements of ion velocity and wave propagation in a hollow cathode plume. *Plasma Sources Science and Technology*, Vol. 28, No. 6, p. 065009, 2019.

[64] GB Rybicki and AP Lightman. Radiative processes in astrophysics, wileyvch, 2004.

[65] Ursel Fantz. Basics of plasma spectroscopy. *Plasma sources science and technology*, Vol. 15, No. 4, p. S137, 2006.

[66] E Pawelec, S Mazouffre, and N Sadeghi. Hyperfine structure of some near-infrared xe i and xe ii lines. *Spectrochimica Acta Part B: Atomic Spectroscopy*, Vol. 66, No. 6, pp. 470–475, 2011.

[67] Wensheng Huang. *Study of Hall thruster discharge channel wall erosion via optical diagnostics*. PhD thesis, University of Michigan, 2011.

[68] Shuen-Cheng Hwang, Robert D Lein, and Daniel A Morgan. Noble gases. *Kirk-Othmer Encyclopedia of Chemical Technology*, 2000.

[69] George J Williams, Timothy B Smith, Matthew T Domonkos, Alec D Gallimore, and R Paul Drake. Laser-induced fluorescence characterization of ions emitted from hollow cathodes. *IEEE Transactions on Plasma Science*, Vol. 28, No. 5, pp. 1664–1675, 2000.

[70] Christopher Dodson, Daniel Perez-Grande, Benjamin Jorns, Dan M Goebel, and Richard E Wirz. Laser-induced fluorescence measurements of energetic ions in a 100-a lab6 hollow cathode plume. In *52nd AIAA/SAE/ASEE Joint Propulsion Conference*, p. 4838, 2016.

[71] G-C Potrivitu, S Mazouffre, L Grimaud, and R Joussot. Anode geometry influence on lab6 cathode discharge characteristics. *Physics of Plasmas*, Vol. 26, No. 11, p. 113506, 2019.

[72] S Mazouffre, D Gawron, and N Sadeghi. A time-resolved laser induced fluorescence study on the ion velocity distribution function in a hall thruster after a fast current disruption. *Physics of Plasmas*, Vol. 16, No. 4, p. 043504, 2009.

[73] Wensheng Huang, Brittany Drenkow, and Alec Gallimore. Laser-induced fluorescence of singly-charged xenon inside a 6-kw hall thruster. In *45th AIAA/ASME/SAE/ASEE Joint Propulsion Conference & Exhibit*, p. 5355, 2009.

[74] Vernon H Chaplin, Benjamin A Jorns, Alejandro Lopez Ortega, Ioannis G Mikellides, Ryan W Conversano, Robert B Lobbia, and Richard R Hofer. Laser-induced fluorescence measurements of acceleration zone scaling in the 12.5 kw hermes hall thruster. *Journal of Applied Physics*, Vol. 124, No. 18, p. 183302, 2018.

[75] Andrea Lucca Fabris, Christopher V Young, and Mark A Cappelli. Time-resolved laser-induced fluorescence measurement of ion and neutral dynamics in a hall thruster during ionization oscillations. *Journal of Applied Physics*, Vol. 118, No. 23, p. 233301, 2015.

[76] Kazutaka Nishiyama, Yukio Shimizu, Ikkoh Funaki, Hitoshi Kuninaka, and Kyoichiro Toki. Ground chamber measurements of the electromagnetic emissions from the hayabusa ion engine. *Journal of propulsion and power*, Vol. 23, No. 3, pp. 513–521, 2007.

[77] MY Ye and S Takamura. Effect of space-charge limited emission on measurements of plasma potential using emissive probes. *Physics of Plasmas*, Vol. 7, No. 8, pp. 3457–3463, 2000.

[78] JP Sheehan, Yevgeny Raitses, Noah Hershkowitz, Igor Kaganovich, and Nathaniel J Fisch. A comparison of emissive probe techniques for electric potential measurements in a complex plasma. *Physics of Plasmas*, Vol. 18, No. 7, p. 073501, 2011.

[79] SHUICHI Takamura, N Ohno, MY Ye, and T Kuwabara. Space-charge limited current from plasma-facing material surface. *Contributions to Plasma Physics*, Vol. 44, No. 1-3, pp. 126–137, 2004.

[80] JP Sheehan, Yevgeny Raitses, Noah Hershkowitz, and Michael McDonald. Recommended practice for use of emissive probes in electric propulsion testing. *Journal of Propulsion and Power*, Vol. 33, No. 3, pp. 614–637, 2017.

[81] Richard Robert Hofer. *Development and characterization of high-efficiency, high-specific impulse xenon Hall thrusters*. University of Michigan, 2004.

[82] T Morishita, D Koda, S Hosoda, T Mogami, K Minemura, N Nomura, and H Kuninaka. Study on charge neutralization effect by electron cyclotron resonance plasma source in high vacuum. *Journal of Physics: Conference Series*, Vol. 1322, No. 1, p. 012018, 2019.

[83] 森下貴都, 神田大樹, 細田聡史, 最上智史, 峯村和樹, 野村信雄, 國中均. マイクロ波放電式プラズマ源による高真空下除電. 静電気学会誌, Vol. 44, No. 3, pp. 128–134, 2020 (in

Japanese).

[84] 神田大樹, 森下貴都, 細田聡史, 最上智史, 峯村和樹, 野村信雄. マイクロ波プラズマ源を用いた高真空下での除電技術 (特集高真空下での静電気現象に関して: 生産現場から宇宙まで). 静電気学会誌, Vol. 43, No. 2, pp. 63–66, 2019 (in Japanese).

[85] 最上智史, 峯村和樹, 野村信雄, 細田聡史, 神田大樹, 森下貴都. マイクロ波プラズマ源を用いた真空用除電器の開発. 第 42 回静電気学会全国大会, pp. 69–70, 2018 (in Japanese).

[86] 村田雄司. 静電気除電の装置と技術. シーエムシー出版, 2004 (in Japanese).

[87] JAXA Press release. 小惑星探査機「はやぶさ 2」のイオンエンジン技術を応用した「マイクロ波プラズマ除電処理システム」の開発について (in japanese). available at `https://www.jaxa.jp/press/2019/10/20191008a_j.html` (accessed on February 2022).

[88] Roy Christoffersen and John Francis Lindsay. Lunar dust effects on spacesuit systems: insights from the apollo spacesuits. Technical report, Johnson Space Center, 2009.

[89] Kavya K Manyapu, Pablo De Leon, Leora Peltz, James R Gaier, and Deborah Waters. Proof of concept demonstration of novel technologies for lunar spacesuit dust mitigation. *Acta Astronautica*, Vol. 137, pp. 472–481, 2017.

[90] Grant A Anderson and Christine Iacomini. The design and operation of a lunar dust seal testing system. In *2010 IEEE Aerospace Conference*, pp. 1–6. IEEE, 2010.

[91] M Suzuki. Experimental study on a brush-type seal in air and in vacuum as a candidate for regolith seal applications. *JSASS-2010*, 2010.

[92] Irebert R Delgado and Michael J Handschuh. Preliminary assessment of seals for dust mitigation of mechanical components for lunar surface systems. In *40th Aerospace Mechanisms Symposium*, No. E-17280, 2010.

[93] CI Calle, CD Immer, J Ferreira, MD Hogue, A Chen, MW Csonka, N VanSuetendael, and SJ Snyder. Integration of the electrodynamic dust shield on a lunar habitat demonstration unit. In *Electrostatics Society of American Annual Meeting*, No. KSC-2010-119, 2010.

[94] Hiroyuki Kawamoto and Shusuke Hashime. Practical performance of an electrostatic cleaning system for removal of lunar dust from optical elements utilizing electrostatic traveling wave. *Journal of Electrostatics*, Vol. 94, pp. 38–43, 2018.

[95] PE Clark, SA Curtis, F Minetto, J Marshall, J Nuth, and C Calle. Sparcle: electrostatic dust control tool proof of concept. In *AIP Conference Proceedings*, Vol. 1208, pp. 549–556. American Institute of Physics, 2010.

[96] FB Tatom, V Srepel, RD Johnson, NA Contaxes, JG Adams, H Seaman, and BL Cline. Lunar dust degradation effects and removal/prevention concepts nasa technical report. Technical report, TR-792-7-207A. NASA, 1967.

[97] Ronald V Peterson and Charles W Bowers. Contamination removal by co2 jet spray. In *Optical system contamination: effects, measurement, control II*, Vol. 1329, pp. 72–85. International Society for Optics and Photonics, 1990.

[98] Kristin Wood. Design of equipment for lunar dust removal. *NASA Contractor Report*, Vol. 190014, , 1991.

[99] James R Gaier, Khrissaundra Journey, Steven Christopher, and Shanon Davis. Evaluation of brushing as a lunar dust mitigation strategy for thermal control surfaces. In *41st International Conference on Environmental Systems*, No. NASA/TM-2011-217231, 2011.

[100] James Gaier, Deborah Waters, Bruce Banks, Robert Misconin, and Mark Crowder. Evaluation of surface modification as a lunar dust mitigation strategy for thermal control surfaces. In *41st International Conference on Environmental Systems*, p. 5183, 2011.

[101] RA Sims, AS Biris, JD Wilson, CU Yurteri, MK Mazumder, CI Calle, and CR Buhler. Development of a transparent self-cleaning dust shield for solar panels. In *Proceedings ESA-IEEE joint meeting on electrostatics*, Vol. 814, 2003.

[102] CI Calle, CD Immer, JS Clements, A Chen, CR Buhler, P Lundeen, JG Mantovani, JW Starnes, M Michalenko, and MK Mazumder. Electrodynamic dust shield for surface exploration activities on the moon and mars. In *57th International Astronautical Congress conference*, No. KSC-2006-125, 2006.

[103] CI Calle, CR Buhler, JL McFall, and SJ Snyder. Particle removal by electrostatic and dielectrophoretic forces for dust control during lunar exploration missions. *Journal of Electrostatics*, Vol. 67, No. 2-3, pp. 89–92, 2009.

[104] CI Calle, CR Buhler, MR Johansen, MD Hogue, and SJ Snyder. Active dust control and mitigation technology for lunar and martian exploration. *Acta Astronautica*, Vol. 69, No. 11-12, pp. 1082–1088, 2011.

[105] Adrienne Dove, Genevieve Devaud, Xu Wang, Mark Crowder, Anna Lawitzke, and Christina Haley. Mitigation of lunar dust adhesion by surface modification. *Planetary and Space Science*, Vol. 59, No. 14, pp. 1784–1790, 2011.

[106] James R Gaier. Interpretation of the apollo 14 thermal degradation sample experiment. *Icarus*, Vol. 221, No. 1, pp. 167–173, 2012.

[107] X Wang, M Horányi, and S Robertson. Investigation of dust transport on the lunar surface in a laboratory plasma with an electron beam. *Journal of Geophysical Research: Space Physics*, Vol. 115, No. A11, 2010.

[108] TE Sheridan, J Goree, YT Chiu, RL Rairden, and JA Kiessling. Observation of dust shedding from material bodies in a plasma. *Journal of Geophysical Research: Space*

Physics, Vol. 97, No. A3, pp. 2935–2942, 1992.

[109] TM Flanagan and J Goree. Dust release from surfaces exposed to plasma. *Physics of plasmas*, Vol. 13, No. 12, p. 123504, 2006.

[110] CM Ticoş, A Scurtu, D Toader, and N Banu. Experimental demonstration of martian soil simulant removal from a surface using a pulsed plasma jet. *Review of Scientific Instruments*, Vol. 86, No. 3, p. 033509, 2015.

[111] Takehiko Ishikawa, Junpei T Okada, Paul-Francois Paradis, and Vijaya Kumar MARAHALLI. Towards microgravity experiments using the electrostatic levitation furnace (elf) in the international space station (iss). *TRANSACTIONS OF THE JAPAN SOCIETY FOR AERONAUTICAL AND SPACE SCIENCES, AEROSPACE TECHNOLOGY JAPAN*, Vol. 12, No. ists29, pp. Th_15–Th_18, 2014.